Fiber Taper-Coupled Microresonators for Applications in Sensing and Quantum Optics

DISSERTATION

zur Erlangung des akademischen Grades
doctor rerum naturalium
(Dr. rer. nat.)
im Fach Physik

eingereicht an der
Mathematisch-Naturwissenschaftlichen Fakultät I
Humboldt-Universität zu Berlin

von
Herrn MSci Markus Gregor
geboren am 25.03.1979 in Leverkusen

Abstract

The thesis deals with optical fiber tapers as a crucial tool for applications in sensing and microresonator-based quantum optical experiments.

Optical fiber tapers are essentially a standard optical fiber with a very thin-tapered waist region with a sub-micron diameter. A fraction of the optical mode is guided evanescently outside of the fiber. This forms a unique building block for nano-photonic devices. Fiber tapers are employed and investigated in three different experiments in the work presented here.

Firstly, a charged-particle trap, known as Paul trap, is used to place individual fluorescing particles onto fiber tapers. The taper acts as a probe to excite and collect fluorescence from deposited particles. It is shown that the collection efficiency is comparable or better than a high-NA microscope objective. This non-contact deposition technique can easily be extended to a wide range of particles. Such a functionalized fiber taper can be used as, e.g. advanced nano-sensor or as non-classical light source.

Secondly, a fibre taper is used as a waveguide to couple to an optical spherical microresonator. Small polystyrene spheres with a diameter of 50 μm and 31 μm are attached to a taper. This results in a thermally and mechanically well isolated microresonator system. The optical modes of the sphere, so-called whispering gallery modes, are of very high quality. Quality (Q) factors as high as 5×10^6 are measured. Microresonator systems with high Q factors, or long photon storage times, are of high interest for sensing applications due to their large matter-light interaction length. A fiber taper-coupled microsphere system can act as a sensitive thermometer. Small changes in the temperature result in change of the optical path length of the resonator mode, and therefore result in a shift of the optical resonance frequency. A shift of 3.8 GHz/K is measured for polystyrene. Furthermore, a gas sensor based on measuring the thermal conductivity is demonstrated for different volume mixtures of helium and argon.

Thirdly, a fiber taper is used to manipulate and transfer single diamond nanocrystals (DNC) onto an optical toroidal microresonator. DNC contain nitrogen vacancy (NV) defect centers which have been studied recently in the field of quantum information as a stable single-photon source. The fluorescence of a 100 nm-sized diamond nanocrystal is coupled to the toroidal resonator and is observed on a spectrometer via a fiber taper. By identifying a resonance structure in the spectrum, the coupling of the NV center to the resonator modes can be validated. A photon correlation experiment clearly reveals anti-bunching and the non-classical character of the NV light source. A photoluminescence spectrum at liquid helium temperatures resolves individual zero-phonon lines associated with individual NV centers in the DNC. These experiments are important steps towards controlled coupling of single NV centers to toroidal resonators and towards the investigation of cavity quantum electrodynamical effects in this promising microresonator system.

Keywords:
Quantum information, Microresonators, NV defect centers in diamond, Optical fiber tapers

Zusammenfassung

Diese Dissertation beschäftigt sich mit optischen Fasertapern als ein fundamentales Werkzeug für Anwendungnen im Gebiet der Sensorik und für quantenoptische Experimente.

Optische Fasertaper sind konventionelle optische Glasfasern, die eine sehr dünne Taille mit einem Durchmesser von unter einem Mikrometer besitzen. Ein Teil der optischen Mode wird evaneszent außerhalb der Faser geführt. Aufgrund dieser Eigenschaft sind Fasertaper ein wichtiger Bestandteil für nanophotonische Bauelemente. Die Fasertaper wurden in drei unterschiedlichen Experimenten eingesetzt und untersucht.

Im ersten Experiment wird eine Paul-Falle, eine Falle für geladene Teilchen, benutzt, um einzelne fluoreszierende Teilchen gezielt auf einem Fasertaper abzulegen. Der Fasertaper agiert als Sonde, um sowohl die Teilchen anzuregen als auch das Fluoreszenzlicht einzusammeln. In dem Zusammenhang kann gezeigt werden, dass die Aufsammeleffizienz verglichen mit einem Mikroskobjektiv großer numerischer Apertur gleich oder besser ist. Diese berührungslose Technik läßt sich leicht auf andere Klassen von Teilchen übertragen. Einso funktionalisierter Fasertaper kann z.B. als Nanosensor oder auch als nicht klassische Lichtquelle eingesetzt werden.

Im zweiten Experiment wird der Fastertaper als Wellenleiter eingesetzt, um an einen sphärischen optischen Mikroresonator anzukoppeln. Dazu werden Kugeln aus Polystyrol mit einem Durchmesser von $50\,\mu$m und $31\,\mu$m an den Fasertaper angehaftet. Daraus resultiert ein sowohl thermisch als auch mechanisch gut isoliertes Mikroresonatorsystem. Die optischen Moden der Kugeln, so genannte *Whispering Gallery Modes*, besitzen eine besonders hohe Qualität. Gütefaktoren von bis zu 5×10^6 können gemessen werden. Mikroresonatorsysteme mit großen Gütefaktoren und damit langen Photonenspeicherzeiten, sind aufgrund der langen Wechselwirkungszeit von Materie und Licht sehr interessant für sensorische Anwendungen. So ein fasertaper-gekoppeltes Mikroresonatorsystem kann als ein empfindliches Thermometer eingesetzt werden. Kleine Temperaturänderungen bewirken eine Veränderung der optischen Weglänge des Resonators und können so als eine Verschiebung der Resonanzfrequenz detektiert werden. Eine Verschiebung von $3.8\,$GHz/K für Polysterene wurde gemessen. Des Weiteren wird gezeigt, wie unterschiedliche Volumenmischungsverhältnisse von Helium und Argon mit diesem System basierend auf unterschiedlichen thermischen Leitfähigkeiten detektiert werden könnnen.

Im dritten Experiment wurde ein Fasertaper benutzt, um einzelne Nanodiamanten zu manipulieren und schließlich auf optischen toroidalen Mikroresonatoren zu platzieren. Die Nanodiamanten beinhalten sogenannte NV Defektzentren, die als stabile Einzelphotonenquellen im Forschungsbereich der Quanteninformation zunehmend untersucht werden. Die Fluoreszenz von $100\,$nm großen Nanodiamanten wird an einen toroidalen Mikroresonator gekoppelt und mit Hilfe des Fasertapers auf einem Spektrometer beobachtet. Indem die Resonanzen des Mikrotoroiden im Spektrum nachgewiesen werden, kann man die Kopplung der NV-Defektzentren an die Resonatormoden validieren. Die Photonenkorrelation der Fluoreszenz der NV Fehlstelle zeigt ein klares *anti-bunching* und somit die nicht-klassischen Eigenschaften der Lichtquelle. Ein Fluoreszenzspektrum bei kyrogenen Temperaturen zeigt klar die unterschiedlichen Nullphononenlinen der NV-Defektzentren im Nanodimanten. Diese Ergebnisse stellen einen wichtigen Schritt für die kontrollierte Kopplung von einzelnen NV-Defektzentren an toroidale Mikroresonatoren dar, der für die Untersuchung quantenelektrodynamischer Effekte in diesem vielversprechenden Mikroresonatorsystem bedeutsam ist.

Schlagwörter:
Quanteninformation, Mikroresonatoren, NV Defektzentren in Diamant, optische Fasertaper

Contents

Symbols and Abbreviations

a_{co}, a_{cl}	fiber core radius and fiber cladding radius
N_{co}, N_{cl}	refractive index of fiber core and cladding
ν, m	mode numbers of the HE and EH fiber modes
l,m	mode numbers of the LP fiber modes
Δ	index contrast between fiber core and cladding
β	propagation constant
M,Q	mass and charge of particles in Paul trap
Ω, U_{ac}, U_{dc}	applied voltages and oscillation frequency of Paul trap
p_x, p_y, q_x,q_y	parameters of Mathieu's differential equation
d_f, a_f	diameter and radius of fiber taper waist
d_s, a_s	diameter and radius of a microsphere sphere
N_s, N_t, N_e	refractive index of the sphere, toroid and environment surrounding the sphere or taper
$\tilde{N}$	refractive index ratio between sphere and surrounding ($\tilde{N} = N_s/N_e$)
l, m, n, p	mode numbers for spherical and toroidal microresonators: azimuthal mode number, polar mode number, radial mode number and polarization (i.e. TM or TE)
k_{th}	thermal conductivity
M	number of nitrogen vacancy centers contained in a diamond nanocrystal
c	speed of light
ϵ_0	dielectric permittivity in vacuum
μ_0	magnetic permeability in vacuum

CQED	cavity quantum electrodynamics
DNC	diamond nanocrystal
ECDL	external cavity diode laser
ESI	electro spay injection
FDTD	finite-difference time-domain
FEM	finite-element method
FP	Fabry-Pérot interferometer
FWHM	full width at half maximum
HE, EH	hybrid fiber modes
HWP	half-wave plate
NA	numerical aperture
NV	nitrogen vacancy
RIU	refractive index units
SFT	segmented Fourier transform
TM, TE	transversal magnetic modes, transversal electric mode
WGM	whispering gallery mode

Chapter 1

Introduction

Optical fiber made from silica can guide light over long distance at very low losses. Such fibers form the backbone of world wide telecom systems and are a vital tool in many scientific experiments as well. Their great advantage is that the light guided within the fiber does not interact with the surrounding of the fiber. The only access to the guided mode is by the two end-facets of the fiber.

An optical fiber taper is essentially a standard fiber that is heated and pulled apart. In this process the heated section can be thinned down to waist diameters below 1 μm while keeping the high overall transmission. A fraction of the light within the thin waist section is guided evanescently outside of the silica. Optical emitters or other photonic structures positioned near to the waist can interact with the light guided within the fiber taper. In essence, such a fiber taper provides efficient optical access to photonic structures via a standard optical fiber. This unique feature makes fiber tapers a valuable tool for sensing applications and as waveguides in microresonator-based experiments as illustrated in figure 1.1.

A fiber taper on its own can be used as an optical probe to collect the fluorescence from emitters. This has been successfully shown for quantum dots embedded in a substrate [1, 2], for optically active defect centers in diamond nanocrystals [3], sensing of organic molecules [4], or cold atoms [5].

Small changes in the refractive index surrounding the fiber taper waist have an effect on the propagating mode inside the taper and can be detected [6]. This effect can be exploited for sensing application. For instance, a hydrogen gas sensor has been implemented based on this concept [7]. The fiber taper was functionalized by a thin palladium layer that changes its refractive index when hydrogen binds to the metal.

Fiber tapers are expected to be very fragile considering their very small waist diameter of about 1 μm. However, this is not necessarily the case. They have been shown to be very resilient [8] and can even be used to manipulate diamond nanocrystals of a few hundred nanometer in diameter [9, 3]. The only caveat is the degradation of optical properties during this process.

By using a particle trap it is possible to attach single optically active particles to the taper [9]. No mechanical strain is exerted on the taper, which preserves its optical qualities. By carefully choosing suitable particles it is possible to functionalize fiber tapers for sensing applications or to fiber-couple quantum emitters.

Fiber tapers provide also an efficient way of coupling to microresonators [10]. Such fiber taper coupled microresonator systems are of high interest [11]. For instance, spherical microresonators made from silica form optical resonators of extreme high quality, with quality (Q) factors exceeding 10^9 [12]. Such a high-Q factor correlates to long photon storage times within the resonator. Since the light is confined inside the sphere by total internal reflection an evanescent field extends in the medium surrounding the sphere. This long interaction length can be exploited for sensing application [13]. A high sensitivity is guaranteed because even small changes in the resonance frequency of the resonator caused by changes in the environment can be detected due to the small resonance width (i.e. high Q factor).

A microresonator forms a sensitive thermometer, as well [14]. As the temperature changes, the dimensions of the resonator change and the resonance frequency shifts. This effect can further be exploited for gas detection by measuring the thermal conductivity of the surrounding gas [15].

An additional feature of microresonators, apart from the high Q factors, is the strong confinement of the electromagnetic fields to a small volume. As a result non-linear optical effects can be observed at low

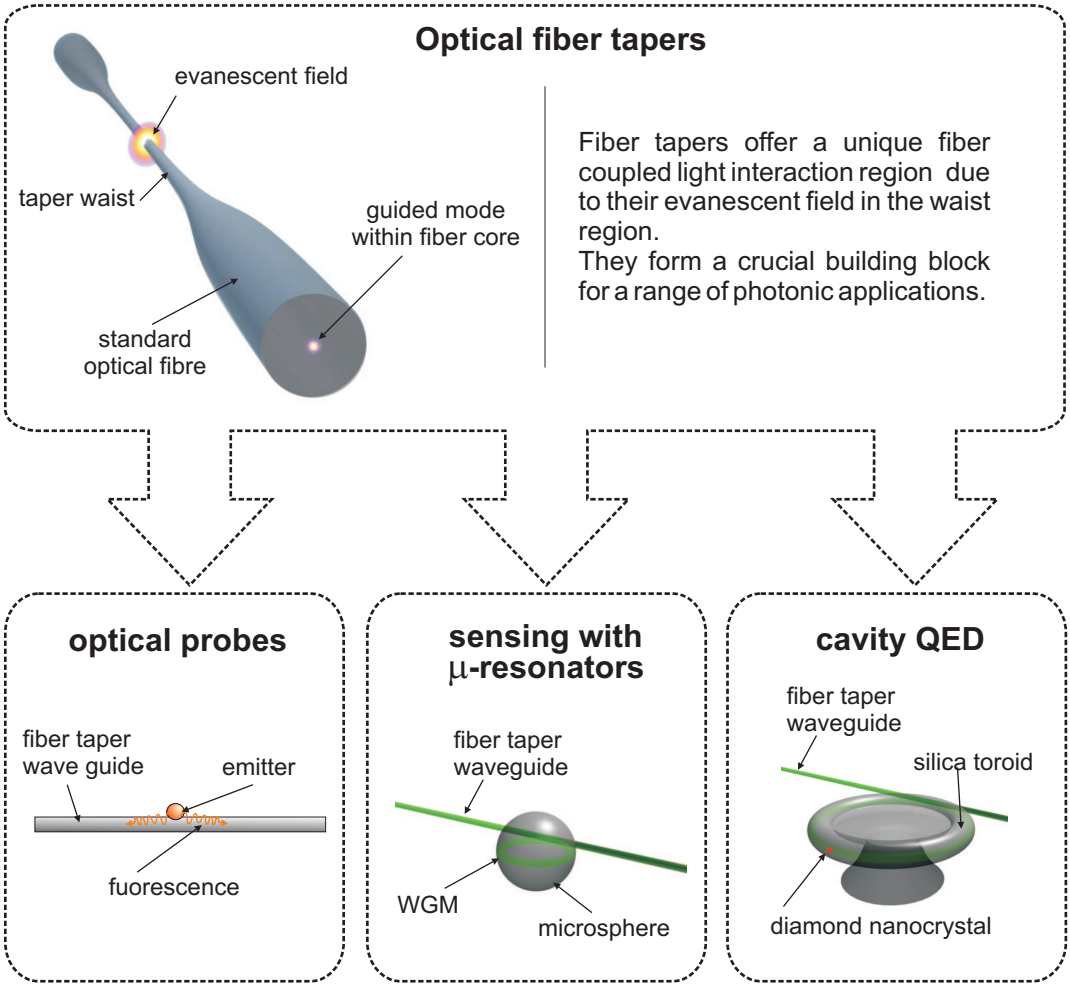

Figure 1.1: Applications of optical fiber taper as investigated in this thesis.

pump powers [16, 11].

Finally, microresonators are an attractive tool to investigate light-matter interactions in cavity quantum electrodynamic (CQED) experiments. The Purcell factor describes the change in the radiative lifetime of a dipole emitter that is influenced by the optical mode density. The Purcell factor is proportional to the ratio of the Q factor and the mode volume. This ratio is particular high for microresonators due to their small size. This allows for a very efficient coupling of quantum emitters to resonators [17]. Typical quantum emitters are atoms. However, the manipulation of single atoms requires complicated and cumbersome experimental methods. Advances have been made to use quasi-atoms like quantum dots in semiconductor structures or color defect centers in diamond nanocrystals. In particular, diamond nanocrystals can be positioned on resonators [9, 3]. If the coupling rate of the emitter to the resonator exceeds all other dissipative processes the regime of strong coupling is reached allowing for coherent interaction between the emitter and the resonator [18]. A splitting of the resonance frequencies of the resonator can be observed and this forms a basis for applications in quantum information processing [19].

Optical fiber taper help to facilitate all these microresonator experiments.

The main part of this thesis is subdivided in four chapters. A short summary of the chapters is given below.

Chapter 2: Optical fiber tapers In this chapter the guided modes within a tapered fiber are derived and discussed with respect to the electromagnetic field distribution, the evanescent guided field fraction and the propagation constant. Mode coupling within the transition region leads to a mode

interference effect that is theoretically and experimentally investigated. Furthermore the entire fiber taper drawing procedure and methods for evaluating the quality of the final tapers are introduced.

Chapter 3: Functionalizing optical fiber tapers A Paul trap is used to deposit preselected charged dye-doped polystyrene spheres onto a taper. The particles are excited through the taper and its fluorescence is collected via the taper, as well. In this chapter the theory for trapping charged particles in Paul traps is introduced. Furthermore, the collection efficiency of fiber tapers are simulated and compared with the conducted experiment.

Chapter 4: Spherical microresonators for sensing applications Polystyrene microsphere are attached to a fiber taper forming a coupled optical resonator system. A gas sensing application is demonstrated based on detecting small resonance shifts due to different heatings of the resonator in different gas environment. Thermal effects in optical spherical resonators are theoretically described and the properties of these resonator systems are studied experimentally.

Chapter 5: Coupling of quantum emitters to toroidal microresonators The efforts to couple the fluorescence of NV defect centers in a single diamond nanocrystal to a toroidal microcavity are described. A technique using a fiber taper as a mechanical device to pick and place diamond nanocrystals is developed. The coupling of the NV center to the toroidal resonator is verified by identifying resonances of the toroid in the fluorescence spectrum collected by a fiber taper. Furthermore, the system is investigated at cryogenic temperatures and the non-classical character of the emitter is investigated using a photon correlation measurement.

Finally, an outlook in chapter 6 concludes this thesis.

Chapter 2

Optical fiber tapers

2.1 Introduction

Optical fiber tapers are a unique tool for experiments in quantum optics [20], sensing [4, 5, 15] and nonlinear optics [21]. Their great advantage is to provide fiber-coupled optical access via their evanescent field surrounding the thinnest section of the taper. Optical emitters and other photonic structures, like microresonators, can efficiently interact with the optical field guided by the fiber taper. The reliable production of high quality optical tapers is of vital importance for all experiments presented in the following chapters.

In this chapter the theory governing wave guiding within optical fiber tapers is described. The main focus lies on the field distribution and modal properties that are of relevance for coupling of light in and out of the taper. The chapter will also deal with the taper manufacturing technique itself, since the fiber drawing setup was built and optimized for the experiments presented in this thesis. Finally, the quality of the fiber drawing setup, and also, the quality of a selection of different fiber tapers are investigated employing a set of optical methods.

2.2 Theory of dielectric cylindrical waveguides [22, 23]

In general, dielectric waveguides are an extensively studied field, especially after the advances made that led to optical fiber based telecommunications. The aspects discussed in this section are the theoretical ideas governing wave guiding in cylindrical dielectric structures and form the basis for the investigation of the optical properties of fiber tapers. The theoretical discussions of this chapter are based on the more extensive discussion in [22, 23].

The particular geometry of a fiber taper narrows the scope of the discussion. It is sufficient to consider only a step-like refractive index change in cylindrical waveguides since a fiber taper can be modeled as a thin silica cylinder that is air-clad. An additional advantage with respect to the theoretical considerations is the fact that the standard optical fibers used for producing fiber tapers possess a step-like index profile as well. Thus the main difference between fiber tapers and standard optical fibers is the high refractive index contrast from air to silica. This is also the reason why it is necessary to consider the full vectorial solution of the guided modes in the fiber.

2.2.1 Fundamental properties of modes

The central parameter for an individual mode is the *propagation constant*, β, that forms an eigenvalue solution of the wave equation for the particular mode. The modal fields for a translational invariant waveguide in the $\hat{\mathbf{z}}$ direction can be described as

$$\mathbf{E}_j = \mathbf{e}_j \exp(i\beta_j z)$$
$$\mathbf{H}_j = \mathbf{h}_j \exp(i\beta_j z),$$

where β_j is associated with the j^{th} mode of the waveguide. From the propagation constant, β, the phase velocity $v = \omega/\beta$ can be derived. This also implies an effective refractive index N_{eff} for an individual

mode, which may be different from the refractive indices of the waveguide material. The effective refractive index is defined as

$$N_{eff} = \frac{\beta}{k} = \frac{\beta\lambda}{2\pi}$$

where k is the wave vector given by $k = \frac{2\pi}{\lambda}$. The eigenvalue solution β for the wave equation for a guided mode can only be within the range defined by the refractive indices of the core N_{co} and the cladding N_{cl} (cf. figure 2.1), as

$$N_{cl}k \leq \beta \leq N_{co}k \quad \text{or} \quad N_{cl} \leq N_{eff} \leq N_{co}.$$

In a ray picture the light is confined by total internal reflection in the core of the fiber and this requires $N_{co} > N_{cl}$. This is a more intuitive picture and agrees with the allowed values for N_{eff} for a guided mode in the wave picture.

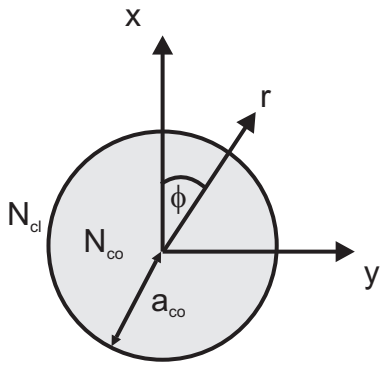

Figure 2.1: Cross-section of a two-layer, step-index fiber indicating the polar coordinates (r, ϕ) in the x-y plane. The z-axis points into the page. The fiber core with a diameter of $2a_{co}$ and refractive index N_{co} is shaded in gray. The core is surrounded by an infinite-extended cladding of refractive index N_{cl}.

Waveguide parameters

There are three important parameters referred to in waveguide theory for a two-layer step-index fiber. The *modal parameters*, U and W, describe the mode in the core and the cladding region. The parameters are positive and dimensionless. They are defined as [22]

$$U^2 = a_{co}^2(k^2N_{co}^2 - \beta^2) = k^2a_{co}^2(N_{co}^2 - N_{eff}^2) \qquad \text{for the core,} \tag{2.1}$$

$$W^2 = a_{co}^2(\beta^2 - k^2N_{cl}^2) = k^2a_{co}^2(N_{eff}^2 - N_{cl}^2) \qquad \text{for the cladding.} \tag{2.2}$$

Based on the model parameters the *waveguide parameter*, V, is defined as,

$$V = \sqrt{U^2 + W^2} = ka_{co}\sqrt{N_{co}^2 - N_{cl}^2} \tag{2.3}$$

which links the core radius a_{co}, the wavelength of the guided light and the two refractive indices of the waveguide. The waveguide parameter is also referred to as the *normalised frequency*. Finally, the *profile height* is defined as

$$\Delta = \frac{1}{2}\left(1 - \frac{N_{cl}^2}{N_{co}^2}\right) \tag{2.4}$$

describing the change in refractive index of a step index waveguide with N_{co} in the core region and N_{cl} in the cladding.

Transversal and hybrid modes

In principle there are two classes of modes that can exist inside the fiber. First of all, there are the transversal electromagnetic (TE) and transversal magnetic (TM) modes. The characteristic for these modes is that all non-transversal components of the field are zero (i.e. either $e_z = 0$ or $h_z = 0$). An illustration of this principle in the ray picture is displayed in figure 2.2 (a), showing a guided ray passing through the center of the waveguide. The polarization state can be maintained at reflections and either $e_z = 0$ or $h_z = 0$ is preserved.

The second class of modes are called hybrid modes (HE and EH). The difference in propagation compared to the transversal modes is shown in figure 2.2 (b). The guided ray no longer passes through the center of the waveguide. This skew ray no longer preserves polarization on reflection at the interfaces. It mixes TE and TM components, resulting in the name hybrid modes.

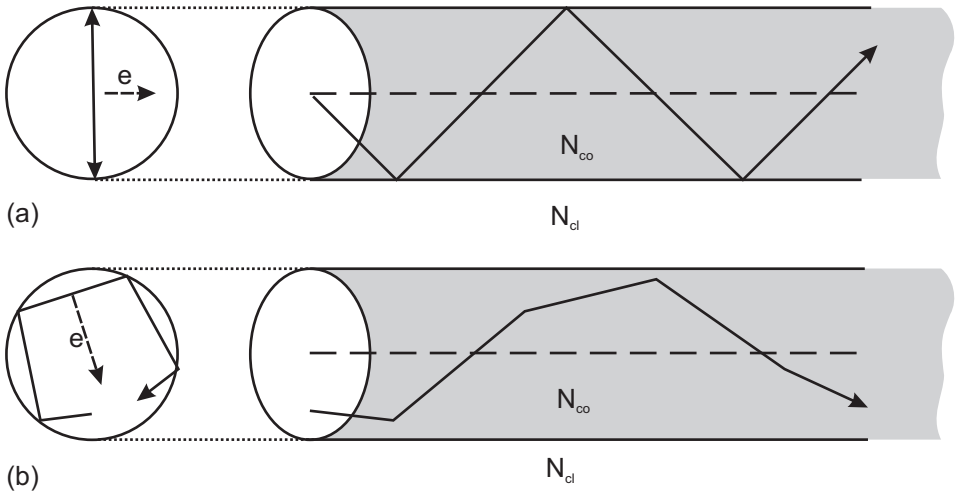

Figure 2.2: Illustration of transversal (a) and hybrid (b) modes in the ray picture. The electric field vector **e** is orthogonal to the local plane wave direction or ray. In (b), due to the skewed path of the rays through the waveguide, the electric field orientation **e** changes at every reflection. In the case of the transversal mode the reflections lie on a plane and the field orientation remains constant. Illustration is adapted from reference [23].

2.2.2 Exact vector solutions to waveguides

The exact vector solution of a mode can be derived by finding a solution to the homogeneous wave equation for the longitudinal field components e_z and h_z from which the remaining four field components can be deduced.

The **E** and **H** fields inside a dielectric waveguide have to satisfy a set of coupled homogenous wave equations of the form [22]

$$(\nabla^2 + k^2 N^2)\,\mathbf{E} = -\nabla\,(\mathbf{E}\cdot\nabla \ln N^2)$$
$$(\nabla^2 + k^2 N^2)\,\mathbf{H} = (\nabla\times\mathbf{H})\times\nabla \ln N^2.$$

By considering the geometry of the dielectric waveguide with index of refraction N it is possible to simplify the wave equation. The core-cladding interface is described as

$$N(r) = \begin{cases} N_{co} & \text{for} \quad 0 < r < a_{co} \\ N_{cl} & \text{for} \quad r > a_{co} \end{cases}$$

which means that the refractive index of the guide is constant and homogeneous apart from the step at a_{co} as indicated in figure 2.1. Thus the term $\nabla \ln N^2$ disappears, resulting in

$$\begin{aligned} \nabla_t^2 e_z + \left(N(r)^2 k^2 - \beta^2\right) e_z = 0 \\ \nabla_t^2 h_z + \left(N(r)^2 k^2 - \beta^2\right) h_z = 0. \end{aligned} \tag{2.5}$$

By replacing the transversal differential operator ∇_t^2 by the explicit polar form and introducing generally the function $\Psi(r,\phi)$ for $e_z(r,\phi)$ and $h_z(r,\phi)$ a set of differential equations for the core and cladding can be formulated as

$$\begin{aligned}\left(\frac{\partial^2}{\partial r^2}+\frac{1}{r}\frac{\partial}{\partial r}+\frac{1}{r^2}\frac{\partial^2}{\partial \phi^2}+\frac{U^2}{a_{co}^2}\right)\Psi(r,\phi)=0 \quad &\text{for the core,}\\ \left(\frac{\partial^2}{\partial r^2}+\frac{1}{r}\frac{\partial}{\partial r}+\frac{1}{r^2}\frac{\partial^2}{\partial \phi^2}-\frac{W^2}{a_{co}^2}\right)\Psi(r,\phi)=0 \quad &\text{for the cladding}\end{aligned} \tag{2.6}$$

using the definition for the modal parameters U and W defined in equations (2.1) and (2.2).

The solution $\Psi(r,\phi)$ can be separated in azimuthal and radial components. As a requirement, the azimuthal function has to be single valued for a rotation of 2π and invariant along the waveguide in the z-direction. This is fulfilled by

$$\Psi(r,\phi)=\Psi(r)\cdot\begin{cases}\sin(\nu\phi)\\ \cos(\nu\phi)\end{cases},$$

where ν is a positive integer. The substitution into equation (2.6) leads to

$$\begin{aligned}\frac{\mathrm{d}^2\Psi(r)}{\mathrm{d}r^2}+\frac{1}{r}\frac{\mathrm{d}\Psi(r)}{\mathrm{d}r}+\left(\frac{U^2}{a_{co}^2}-\frac{\nu^2}{r^2}\right)\Psi(r)=0 \quad &\text{for the core,}\\ \frac{\mathrm{d}^2\Psi(r)}{\mathrm{d}r^2}+\frac{1}{r}\frac{\mathrm{d}\Psi(r)}{\mathrm{d}r}-\left(\frac{W^2}{a_{co}^2}+\frac{\nu^2}{r^2}\right)\Psi(r)=0 \quad &\text{for the cladding.}\end{aligned}$$

The solution to this set of differential equations is a linear combination of modified Bessel functions of the first and the second kind, i.e. J_ν and Y_ν for the core and I_ν and K_ν for the cladding. Physically meaningful solutions have to converge, thus this simplifies to

$$\Psi(r)=\begin{cases}J_\nu(Ur/a_{co}) & \text{for the core}\\ K_\nu(Wr/a_{co}) & \text{for the cladding}\end{cases}.$$

In the next step the exact solutions of the fields $e_z(r,\phi)$ and $h_z(r,\phi)$ have to be determined by considering the boundary conditions for the fields' components as

$$\begin{aligned}e_z(r,\phi)=&\quad A\,f_\nu(\phi)\begin{cases}J_\nu(Ur/a_{co})/J_\nu(U) & 0\le r\le a_{co}\\ K_\nu(Wr/a_{co})/K_\nu(W) & r>a_{co}\end{cases},\\ h_z(r,\phi)=&\quad B\,g_\nu(\phi)\begin{cases}J_\nu(Ur/a_{co})/J_\nu(U) & 0\le r\le a_{co}\\ K_\nu(Wr/a_{co})/K_\nu(W) & r>a_{co}\end{cases},\end{aligned} \tag{2.7}$$

where A and B are constants. f_ν and g_ν are given by either $\sin(\nu\phi)$ or $\cos(\nu\phi)$. Now, the radial (e_r and h_r) and azimuthal (e_ϕ and h_ϕ) components of the fields are related to e_z and h_z by

$$e_r=\frac{1}{N^2k^2-\beta^2}\left(\beta\frac{\partial ie_z}{\partial r}+\sqrt{\frac{\mu_0}{\epsilon_0}}\frac{k}{r}\frac{\partial ih_z}{\partial\phi}\right) \tag{2.8}$$

$$e_\phi=\frac{1}{N^2k^2-\beta^2}\left(\frac{\beta}{r}\frac{\mathrm{d}ie_z}{\mathrm{d}\phi}-\sqrt{\frac{\mu_0}{\epsilon_0}}k\frac{\partial ih_z}{\partial r}\right) \tag{2.9}$$

$$h_r=\frac{1}{N^2k^2-\beta^2}\left(\beta\frac{\partial ih_z}{\partial r}-\sqrt{\frac{\mu_0}{\epsilon_0}}\frac{kN^2}{r}\frac{\partial ie_z}{\partial\phi}\right) \tag{2.10}$$

$$h_\phi=\frac{1}{N^2k^2-\beta^2}\left(\frac{\beta}{r}\frac{\partial ih_z}{\partial\phi}+\sqrt{\frac{\mu_0}{\epsilon_0}}kN^2\frac{\partial ie_z}{\partial r}\right). \tag{2.11}$$

where N is the corresponding refractive index. The choice of f_ν and g_ν in equation (2.7) have to be consistent with equations (2.8 - 2.11) while the continuity of the fields at the core/cladding interface $r=a_{co}$ has to be ensured. This results in only two possible combinations

$$f_\nu(\phi)=\begin{cases}\cos(\nu\phi)\\ \sin(\nu\phi)\end{cases}\quad\text{and}\quad g_\nu(\phi)=\begin{cases}-\sin(\nu\phi) & \text{even modes}\\ \cos(\nu\phi) & \text{odd modes.}\end{cases}$$

The last step is to solve the differential equation by imposing continuity of the fields at the core-cladding boundary. In the following the tangential components e_ϕ and h_ϕ to the boundary are used. A similar argument could be made for the radial components e_r and h_r. The azimuthal fields are found by substituting equation (2.7) into (2.8 - 2.11). This yields

$$e_\phi(r,\phi) = g_\nu(\phi) \begin{cases} \frac{iN_{co}^2}{U^2}\left(A\nu\frac{J_\nu(Ur/N_{co})}{J\nu(U)}\frac{\beta}{r} - B\sqrt{\frac{\mu_0}{\epsilon_0}}k\frac{dJ_\nu(Ur/a_{co})/dr}{J\nu(U)}\right) & r \le a_{co} \\ -\frac{iN_{co}^2}{W^2}\left(A\nu\frac{K_\nu(Wr/N_{co})}{K_\nu(W)}\frac{\beta}{r} - B\sqrt{\frac{\mu_0}{\epsilon_0}}k\frac{dK_\nu(Wr/a_{co})/dr}{K\nu(W)}\right) & r > a_{co} \end{cases}$$

$$h_\phi(r,\phi) = f_\nu(\phi) \begin{cases} \frac{iN_{co}^2}{U^2}\left(-B\nu\frac{J_\nu(Ur/N_{co})}{J\nu(U)}\frac{\beta}{r} + A\sqrt{\frac{\epsilon_0}{\mu_0}}kN_{co}^2\frac{dJ_\nu(Ur/a_{co})/dr}{J\nu(U)}\right) & r \le a_{co} \\ -\frac{iN_{co}^2}{W^2}\left(-B\nu\frac{K_\nu(Wr/N_{co})}{K_\nu(W)}\frac{\beta}{r} + A\sqrt{\frac{\epsilon_0}{\mu_0}}kN_{cl}^2\frac{dK_\nu(Wr/a_{co})/dr}{K\nu(W)}\right) & r > a_{co} \end{cases}$$

The constants A and B can be eliminated leading to a characteristic equation of the form

$$\left(\nu\frac{\beta}{k}\right)^2\left(\frac{V}{UW}\right)^4 = \left(\frac{N_{co}^2J_\nu'(U)}{UJ_\nu(U)} + \frac{N_{cl}^2K_\nu'(W)}{WK_\nu(W)}\right)\cdot\left(\frac{J'\nu(U)}{UJ_\nu(U)} + \frac{K_\nu'(W)}{WK_\nu(W)}\right) \tag{2.12}$$

where the prime denotes a derivative with respect to the argument. The transcendental equation defines the dependance of the parameters W and U for a two-layer step-index waveguide. Once these parameters are known, β or N_{eff} can be deduced for the given waveguide mode.

TE and TM modes

The characteristic equation (2.12) has two different classes of solutions. For the case $\nu = 0$ the azimuthal dependence disappears as $e_\phi = 0$. As a result either the longitudinal magnetic $h_z = 0$ or electric $e_z = 0$ fields disappear. These families of modes are called TM and TE, respectively. The resulting characteristic equation for these modes is given by

$$\frac{N_{co}^2J_1(U)}{UJ_0(U)} + \frac{N_{cl}^2K_1(W)}{WK_0(W)} = 0 \qquad \text{for TM and}$$

$$\frac{J_1(U)}{UJ_0(U)} + \frac{K_1(W)}{WK_0(W)} = 0 \qquad \text{for TE.}$$

These equations can be evaluated numerically and possess discrete solutions. The solutions of U form a series and are associated with the mode number m, i.e. TM_{01}, TM_{02}, TM_{03} ... TM_{0m} or TE_{01}, TE_{02}, TM_{03} ... TM_{0m}.

Hybrid modes

The other class of solutions of the characteristic equation (2.12) is given for $\nu \neq 0$. Equation (2.12) can also be seen as a second degree equation in x

$$N_{co}^2x^2 + xb(N_{co}^2 + N_{cl}^2) + (N_{cl}^2b^2 - c) = 0$$

with the parametrization $x = J_\nu'(U)/(UJ_\nu(U))$, $c = (\nu N_{eff})^2(V/UW)^4$ and $b = K_\nu'(W)/(WK_\nu(W))$. The roots of the quadratic equation are given by

$$x = -b(1-\Delta) \pm \sqrt{b^2\Delta^2 + c/N_{co}^2}.$$

There exist two families of hybrid modes: one associated with the positive (+) solution and the negative (−) solution of the root. Now it is conventional to call the negative solutions HE modes and positive solutions EH modes. These modes posses an azimuthal dependance. Also, the e_z and e_h field components of the modes are non-zero. Therefore these modes are called hybrid. The individual modes are identified by two mode numbers, i.e. $HE_{\nu m}$ or $EH_{\nu m}$. The mode number m is associated with the discrete solutions which again form a series.

2.2.3 Weakly guiding approximation

The exact vectorial solution introduced above is, in particular important, for a dielectric waveguide with a high refractive index contrast as is the case for air-clad fiber tapers. For standard optical fibers, like the ones used in telecommunication applications, the refractive index contrast is very small. For instance, the refractive index difference between the core and the cladding for the widely used SMF28e (Corning inc.) fiber is only 0.36% [24] at 1550 nm.

In general, the intensity of light transmitted or reflected at a dielectric boundary depends on the relative refractive indices of the dielectrics as well as the polarization state of the light. A first formal description was given by Fresnel, and the corresponding refection and transmission coefficients are named accordingly [25]. For a small change in the refractive index (i.e $N_{cl} \approx N_{co}$) the coefficients for orthogonal polarization states are approximately the same. This leads to a nearly TEM like propagation of the wave within the waveguide with negligible longitudinal field components. The resulting transversal fields are related to each other by $\mathbf{H}_t \approx \sqrt{\epsilon_0/\mu_0}\, n\, \hat{\mathbf{z}} \times \mathbf{E}_t$. Thus it is sufficient to find a scalar solution for a linear polarized mode of the waveguide. This is called the *weakly guiding approximation*.

Following the same argument of the previous section it is possible to to derive a scalar wave equation based on equation (2.5) as $(\nabla_t^2 k^2 N^2 - \beta^2) F_l(r,\phi) = 0$, where

$$e_x \text{ or } e_y = F_l(r,\phi) = \Psi(r) \left\{ \begin{array}{c} \cos(l\phi) \\ \sin(l\phi) \end{array} \right\}.$$

The azimuthal mode number, l, must be an integer for the azimuthal part of $F_l(r,\phi)$ to be single valued. As a next step the transversal Laplacian ∇_t^2 in polar coordinates is applied to $F_l(r,\phi)$ resulting in

$$\frac{\mathrm{d}^2\Psi_l(r)}{\mathrm{d}r^2} + \frac{1}{r}\frac{\mathrm{d}\Psi_l(r)}{\mathrm{d}r} + \left(k^2 N(r)^2 - \beta^2 - \frac{l^2}{r^2}\right)\Psi_l(r) = 0.$$

The solutions to this wave equation determine the propagation constant, β, for the linear polarized mode family $\mathrm{LP_{lm}}$ and are written as

$$\begin{aligned} \Psi_l(r) &= J_l(Ur/a_{co})/J_l(U) \qquad r \le a_{co} \\ \Psi_l(r) &= K_l(Wr/a_{co})/K_l(W) \qquad r > a_{co}. \end{aligned}$$

By requiring $\Psi_l(r)$ and the derivative of $\Psi_l(r)$ be continuous across the boundary at a_{co} the parameters U can be found, and thus β. This results in

$$\frac{UJ_l'(U)}{J_l(U)} = \frac{WK_l'(W)}{K_l(W)}$$

which is equivalent to the following form

$$\frac{UJ_{l\pm1}(U)}{J_l(U)} = \frac{WK_{l\pm}1(W)}{K_l(W)}.$$

For a given l and V there are multiple solutions U_m of this transcendental equation which form a series and are associated with the mode number m. Thus a particular mode can be identified by $\mathrm{LP_{lm}}$.

The propagation constant and electric field distribution of the $\mathrm{LP_{01}}$ mode and $\mathrm{HE_{11}}$ mode are similar [26]. Therefore, the $\mathrm{LP_{01}}$ is sometimes used as an approximation for the $\mathrm{HE_{11}}$, since the scalar solution is numerically less complicated.

Mode cut-off

Not all modes exist for a given wavelength and waveguide geometry. The particular frequency at which a mode stops to be guided is called the *cut-off frequency*. By considering the asymptotic limits of the characteristic equations (2.12) as $U \to V$ the cut-off frequency can be found. This limit can also be restated as $N_{eff} \to N_{cl}$ which may be more intuitive, since a requirement for wave guiding is $N_{eff} > N_{cl}$. The cut-off criteria for the different mode classes are given by

TE_{0m} and TM_{0m}: $J_0(U) = 0$

$\mathrm{HE}_{\nu m}$: $\begin{cases} J_1(0) = 0 & \nu = 1 \text{ (incl. } U = 0) \\ \frac{UJ_{\nu-2}(U)}{(\nu-1)J_{\nu-1}(U)} = -\frac{2\Delta}{1-2\Delta} & \nu > 1 \end{cases}$

$\mathrm{EH}_{\nu m}$: $J_\nu(U) = 0 \quad (U \neq 0)$

It is important to note that the fundamental mode, HE_{11}, is not cut off and thus even if the fiber is continuously thinned the fundamental mode is still guided.

By considering the zero crossing of the Bessel function the single mode criterion for an air-clad fiber taper is $a_{co}/\lambda = 0.37$. For instance, the single mode regime at a wavelength of 532 nm is reached for a taper smaller than 0.4 μm in diameter. In contrast, a taper of 1.2 μm in diameter, as was routinely used in our experiments, is highly multimode with 12 modes at 532 nm. A summary of the cut-off points for the first 27 modes is given in appendix A, table A.3.

2.2.4 Numerical solution

The propagation constant, β, has to be numerically calculated by solving the corresponding transcendental equation for the particular mode under consideration. Figure 2.3 illustrates this procedure for the hybrid modes. The left and the right hand side of equation (2.12) is plotted in the same diagram. The intersection points between both curves provide all U solutions to the transcendental mode equation. There are efficient numerical algorithms to calculate the intersection point to high degree of precision. However, it is still necessary to manually preselect and provide the algorithm with a good approximation of U as a starting point.

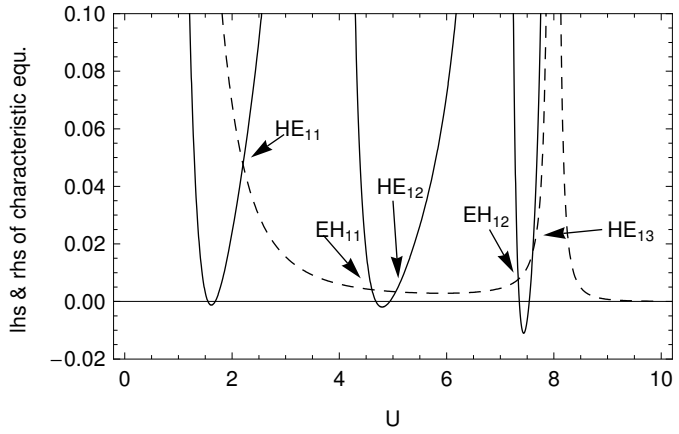

Figure 2.3: First five eigenvalues of the hybrid modes with $\nu = 1$ given by the intersection points of the right hand side (solid) and left hand side (dashed) of equation (2.12) ($\Delta = 0.26$, $N_{co} = 1.44$, $N_{cl} = 1$, $V = 8$).

Figure 2.4 shows the numerical solution of U as a function of the normalized frequency V for several vector modes. The cut-off points of the individual modes are indicted by the black dots. In a two-layer, step-index fiber there will always be a fundamental mode, HE_{11}. This is nicely illustrated by the continuous range of solution for all positive V. For comparison to the vector modes, the solution U for the first two LP modes are plotted. The similarity of the fundamental LP_{01} mode and the HE_{11} mode is perceived [26]. Note that the solutions presented in figure 2.4 are not universal, since they depend on profile height Δ as defined in equation (2.4).

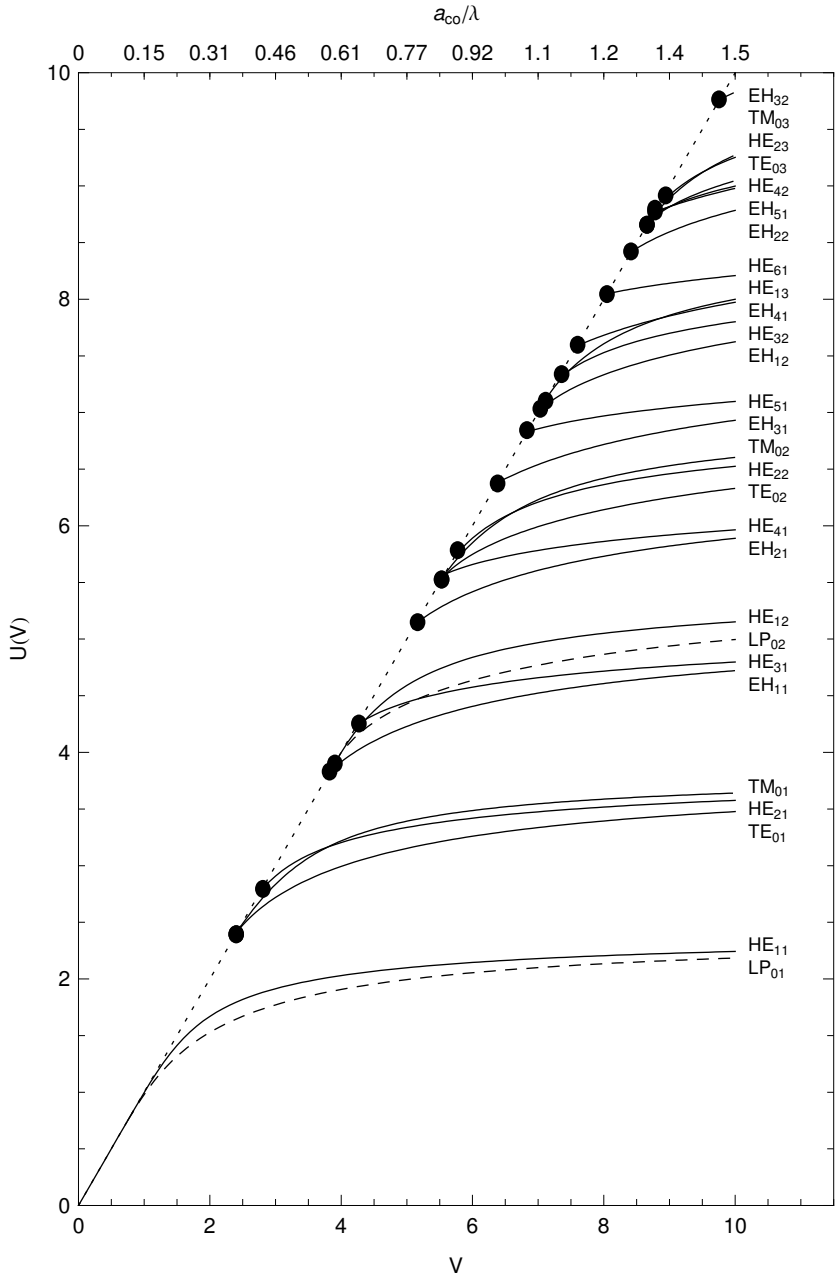

Figure 2.4: Numerical solution for the first 26 vector modes (solid) and first two linearly polarized modes (dashed) for an air-clad fiber taper (i.e. $\Delta = 0.26$, $N_{co} = 1.44$, $N_{cl} = 1$). The cut-off points are represented by the black dots on the line $U = V$. The top axis shows the dependence of U on the normalized core radius a_{co}/λ using equation (2.3).

It is convenient to plot the mode solutions U in terms of the effective refractive index N_{eff} as a function of the normalized core radius a_{co}/λ as shown in figure 2.5. This representation can be helpful for phase matching considerations of fiber taper and microresonator modes.

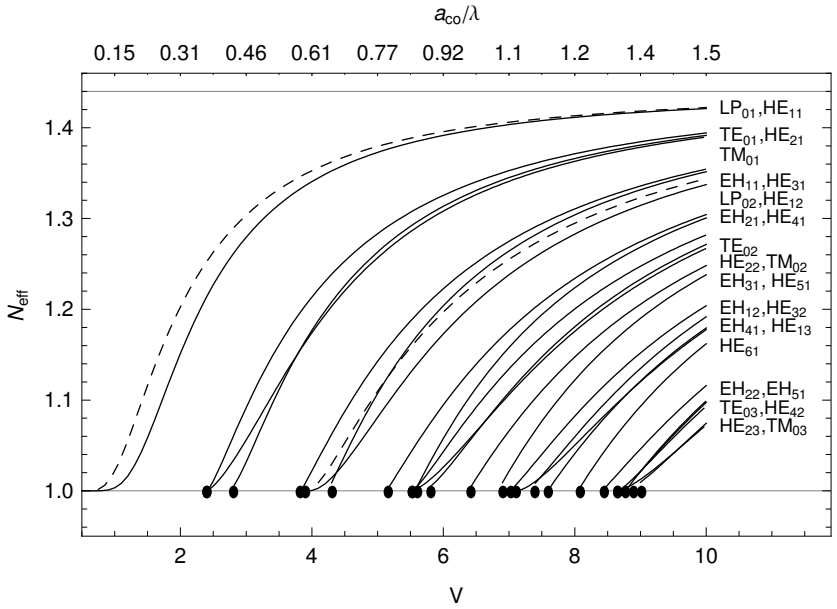

Figure 2.5: Numerical solution of $N_{eff}(V)$ based on the results presented in figure 2.4 using $N_{eff}(V) = N_{co}\sqrt{1-2\Delta(U/V)^2}$. Black dots indicate the mode cut-off points. The order of the plotted modes reverses with respect to figure 2.4.

2.3 Optical properties of fiber tapers

In the previous section solutions to the wave equation for a two-layer step index fiber were found. These results will now be applied to optical fiber tapers. Two main aspects are considered: Firstly, the evanescent decay of the fields outside the taper region. The extent of the evanescent field is of importance for all fiber taper based sensing applications and also for coupling to optical microresonators. Secondly, the transition region from the taper waist to the unstretched fiber is considered. In particular, the adiabaticity criterion [23, 27], describing the intermodal coupling between the taper modes within the transition region, is introduced, and the resulting effects of intermodal interference are examined.

2.3.1 Modal power density

The power density is given by the Poynting vector projected onto the axis of propagation $\hat{\mathbf{z}}$ [22], i.e.

$$D(r,\phi) = \frac{1}{2}(\mathbf{E}\times\mathbf{H}^*)\cdot\ \hat{\mathbf{z}} = \frac{1}{2}\frac{e_r h_\phi - e_\phi h_r}{C},$$

where the field components e_r, h_ϕ, e_ϕ and h_r were derived in section 2.2.2 and are summarized in appendix A.1. The normalization constant C is obtained by integrating the Poynting vector over the entire cross sectional plane S_∞ of the fiber

$$C = \frac{1}{2}\left|\int_{S_\infty}(\mathbf{E}\times\mathbf{H}^*)\cdot\hat{\mathbf{z}}\,dS\right|.$$

The solution of this integral for the core and cladding region can be found in appendix A.2.

The modal power density for the fundamental, HE_{11}, mode is shown in figure 2.6 (a) and (b). The main power of the mode is guided within the central region of the core. A slight asymmetry of the mode is visible due to its polarization state. The discontinuity at the silica-air interface is noticeable and

particularly prominent in the 3D surface plot. In plot (c) and (d) of figure 2.6 the power density of the EH_{11} and HE_{22} mode are depicted. For these modes the power density varies strongly with the position on the surface of the fiber. This important feature has to be considered if the taper is used to couple light into a microresonator or even, in sensing applications, to excite molecules on its surface.

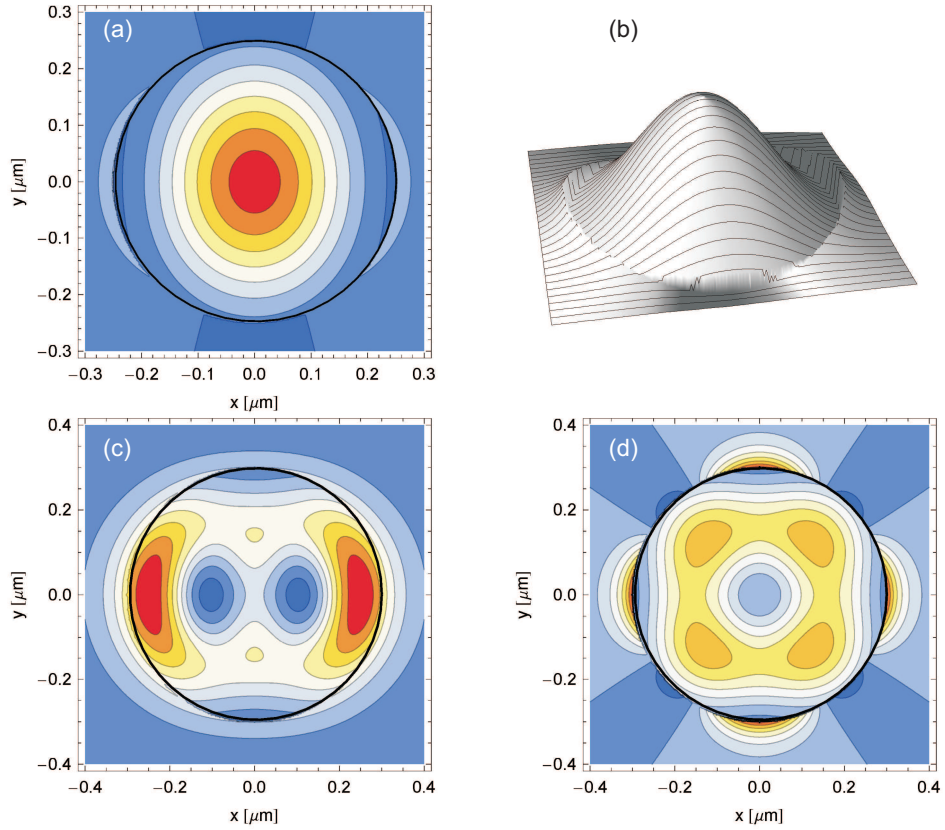

Figure 2.6: Selection of power density contour plots for (a) HE_{11} ($a_{co} = 0.25\,\mu$m), (b) three dimensional surface plot of (a), (c) EH_{11} ($a_{co} = 0.3\,\mu$m), and (d) HE_{21} ($a_{co} = 0.3\,\mu$m). The power density is plotted in a normalized linear scale of arbitrary units. Regions of highest power density are coded in red while regions of lowest intensity are shown in blue. The glass taper ($N_{co} = 1.44$) is surrounded by air ($N_{cl} = 1$) with resulting $\Delta = 0.26$ at 780 nm.

2.3.2 Fraction of power guided in core

The evanescent field protruding into the space surrounding the fiber taper is interesting for a wide range of applications. Therefore it is of great importance to be able to calculate the relative power contained in the evanescent part of the guided mode. The fractional power, η, guided in the core of the fiber is given by

$$\eta = \frac{\text{power guided in core}}{\text{total guided power}},$$

which corresponds to the fractional power guided in the evanescent field as $1 - \eta$.

This leads to the general expression for η based on a calculation of the energy flow through the core area and the total energy flow by integrating the Poynting vector for these surfaces

$$\eta = \frac{\frac{1}{2}\int_{S_{co}} (\mathbf{E} \times \mathbf{H}^*) \cdot \hat{\mathbf{z}}\, dS}{\frac{1}{2}\int_{S_\infty} (\mathbf{E} \times \mathbf{H}^*) \cdot \hat{\mathbf{z}}\, dS} = \frac{C_{co}}{C_{co} + C_{cl}}.$$

The normalization constants C_{cl} and C_{co} for the different modes are given in appendix A.2.

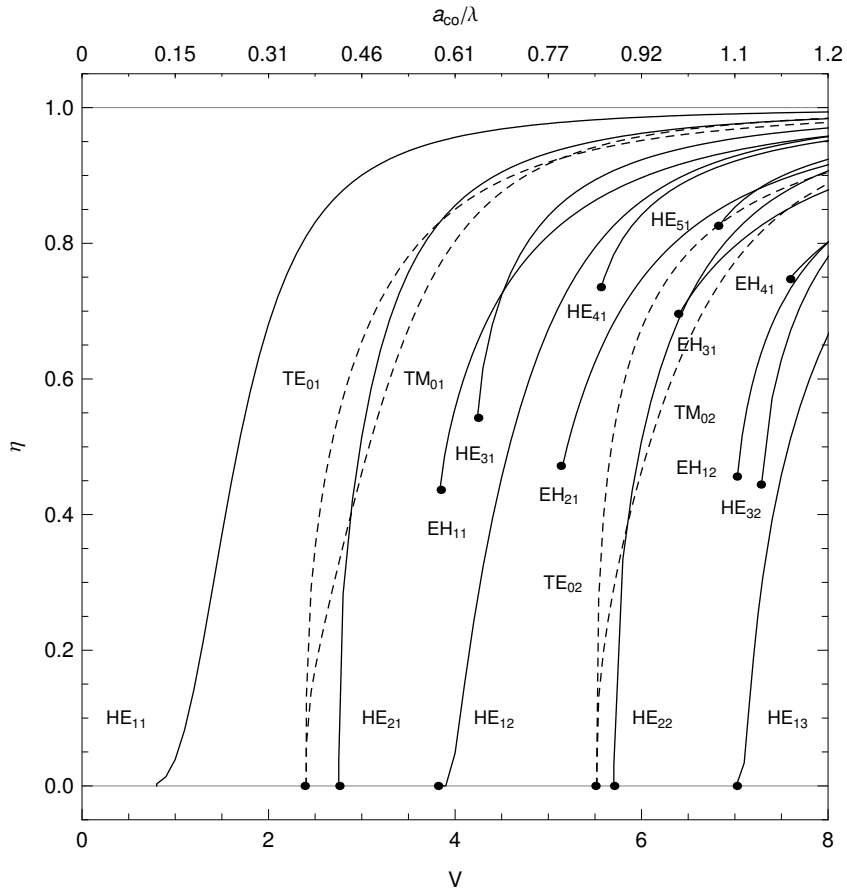

Figure 2.7: Fractional power guided in the core $\eta(V)$ for the first 18 modes. The cut-off points are indicated by black dots. The top axis shows the dependence of U on the normalized core radius a_{co}/λ using equation (2.3). Hybrid modes are plotted as solid lines. TM and TE modes are plotted as dashed lines. The profile height Δ is 0.26.

Figure 2.7 shows the fractional power guided within the fiber taper for the first 18 modes. For decreasing taper diameters or smaller wavelengths ($V \to 0$) less power is guided within the taper and more by the evanescent field surrounding the taper. For instance, in order to guide 50% of the total power of the fundamental HE_{11} mode outside of the taper the ratio radius to wavelength has to be smaller than 0.24. This would result in very thin tapers, which are very difficult to produce. Higher-order modes are of advantage in this respect, as a higher percentage of the power is guided outside the taper for larger V. This is in agreement with the intuitive understanding that higher-order modes are less tightly bound to the waveguide.

2.3.3 Adiabaticity criterion for the transition region

The waist diameter is of great importance for applications as it determines β to achieve optimum phase matching to resonators as well as the extension of the evanescent field needed for sensing applications.

The thin waist of the taper is connected via a transition region to the unstretched fiber and transfers the standard fiber mode to the modes of the tapered waist, as seen in figure 2.8. The thining rate $da(z)/dz$ determines the quality of the transfer. If the transition is to steep light from the fundamental mode is coupled to higher modes and will ultimately be scattered from the taper for single mode fibers. To avoid this effect an adiabaticity criterion [23, 27] is formulated as

$$\left|\frac{\mathrm{d}a(z)}{\mathrm{d}z}\right| \leq \frac{a(z)|\beta_1 - \beta_2|}{2\pi}, \tag{2.13}$$

where $a(z)$ is the diameter of the transition region, and β_1 is the propagation constant of the fundamental

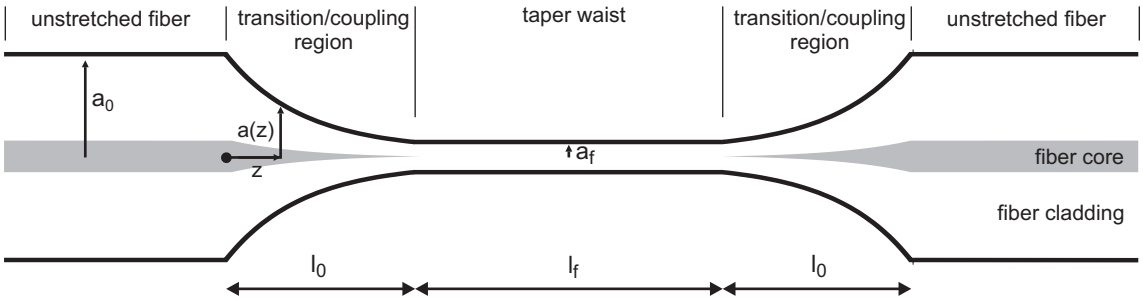

Figure 2.8: Illustration of the different zones of a fiber taper.

mode. β_2 is the propagation constant of the next higher order mode which is most likely (from a geometrical consideration) to accept most of the scattered light from the fundamental mode.

The fundamental idea behind the adiabaticity criterion is the concept of *local modes*. Since the diameter varies along the taper, the mode solution is not translationally invariant, as it was assumed in the derivation of the solution of the vector and scalar modes (cf. sections 2.2.3 and 2.2.2). However, if the variation of the taper diameter is sufficiently small the vector or scalar mode solution may be used locally. This is the case if the diameter of the taper $a(z)$ does not vary significantly within the *beat length* z_b of two taper modes, where the beat length is defined as $z_b = 2\pi/|\beta_1 - \beta_2|$. The energy transfer between local modes is associated with very low losses and is called adiabatic.

2.3.4 Interferometric effects between guided taper modes

The previous section introduced the concept of an adiabatic change of the fiber diameter at the transition zone. This very gradual change minimizes the intermodal coupling and subsequent loss of light from the fundamental mode to higher modes. However, if light is coupled into higher modes of the fiber taper mode interference occurs.

The basic concept is illustrated in figure 2.9 by an analogy to a Mach-Zehnder interferometer. A fraction of the light guided in the fundamental FM_1 mode is coupled into the FM_2 mode at the transition region of the taper, indicated as a beamsplitter in the diagram. As both modes propagate along the fiber taper waist both accumulate a different phase due to different modal propagation constants $\beta_{1,2}$. Finally reaching the second transition region of the taper, both modes couple and interfere with each other. This simple picture can easily be extended to multiple taper modes, since the taper waist may guide multiple modes (cf. section 2.2.3).

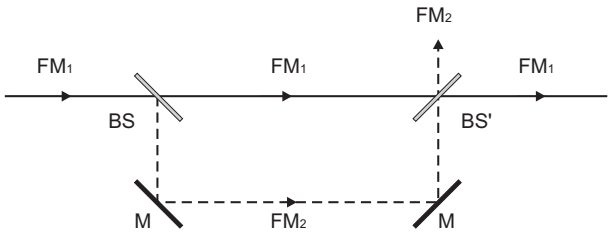

Figure 2.9: Mach-Zehnder interferometer as a model for interfering modes in a fiber taper consisting of beamsplitters (BS) and mirrors (M). The different paths for two different fiber modes (FM) are indicated.

By using this model it is possible to describe the interference by calculating the transmitted power P_T through this interferometer

$$P_T(\lambda) = P_0 \left[T(\lambda)T'(\lambda) + R(\lambda)R'(\lambda) - R(\lambda)R'(\lambda)\cos\left(\phi_1(\lambda) - \phi_2(\lambda)\right)\right],$$

where R and T is the coupling strength between the modes FM_1 and FM_2. Since the interferometer may not be symmetric an additional T' and R' for the second transition zones has to be used. The mode coupling constants can be calculated using mode coupling theory [22]. The accumulated phase of the two modes is represented by ϕ_1 and ϕ_2.

The difference in the phases can be rewritten in terms of the propagation constants for the two modes, as $\Delta\phi_{12} = \phi_1(\lambda) - \phi_2(\lambda) = (\beta_1 - \beta_2)l$, where l is the distance between the mode coupling regions. Since the taper diameter is changing with z, the propagation constant $\beta(z)$ for a mode changes as well. Therefore, the change in the propagation constants has to be integrated along the entire fiber radius profile $a(z)$ as [28]

$$\Delta\phi_{12}(\lambda) = 2\left(\int_0^{l_0} \Delta\beta_{12}(\lambda, a(z))\mathrm{d}z + \Delta\beta_{12}(\lambda, a_f)\frac{l_f}{2}\right).$$

The definition for the distances and diameters are given in figure 2.8.

In principle, these considerations allow one to calculate the spectral transmission spectrum of a fiber taper. A difficulty arises for thin fiber tapers of a few micrometers in diameter, as shown in figure 2.8. The gray region in the center of the fiber represents the fiber core of the unstretched fiber. In the taper waist region the fiber core index contrast has disappeared completely and the fiber is transformed from core guiding to an air-clad fiber. This mode transition is difficult to model precisely. There have been some efforts in interpreting the phaseshift $\Delta\phi_{12}$ for the taper waist region [28] and for thicker tapers [29] as a function of the drawn distance.

2.4 Fabrication of sub-micron fiber tapers

2.4.1 Properties of silica

Fiber tapers are fabricated from standard, single-mode optical fibers made from fused silica. In order for these fibers, to guide light the refractive index of the small core region is slightly increased with respect to the surrounding cladding. This can be achieved by adding dopants, like germanium to the silica. Thus it is important to know the physical properties of deformation for silica at different temperatures.

Fused silica is a glass and, therefore, does not undergo a sudden phase transition into a molten low-viscous state at a fixed melting temperature. The viscosity of silica changes rather exponentially with the temperature, as shown in figure 2.10. In order to soften the fiber, it has to be heated to temperatures of $1350 - 1500\,^{\circ}\mathrm{C}$. However, at the same time, the temperature over the heating zone must be free from variations since this would result, varying in a viscosity and, therefore, a different local elongation rate when the fiber is drawn.

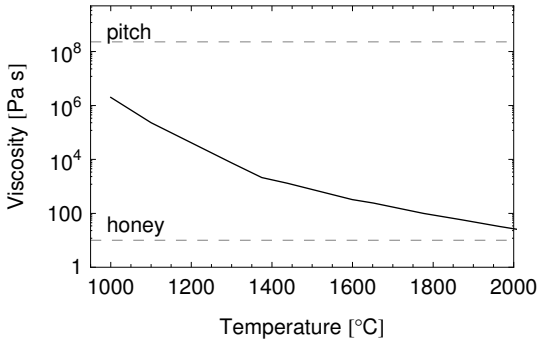

Figure 2.10: Viscosity of pure silica [30]. For illustration purposes typical viscosities for pitch and honey are indicated by the dashed lines as an additional reference.

2.4.2 Shape of fiber tapers

Theoretical considerations regarding the mode transition in the taper (cf. section 2.3.3) for optimal transmission properties demand precise control of the fiber taper diameter $a(z)$ during the drawing procedure.

The first theoretical approach describing a method for generating an arbitrary taper shape is presented by Birks *et al.* [27]. It is based on the assumption that the silica fiber is plastically deformable only

within a clearly defined heated section, the *hot zone*. In order to generate an arbitrary shaped taper, the extension of the hot zone is varied with time. The fiber drawing setup built as part of this thesis work has a constant hot zone. Thus, this theoretical model is applied to this special case only.

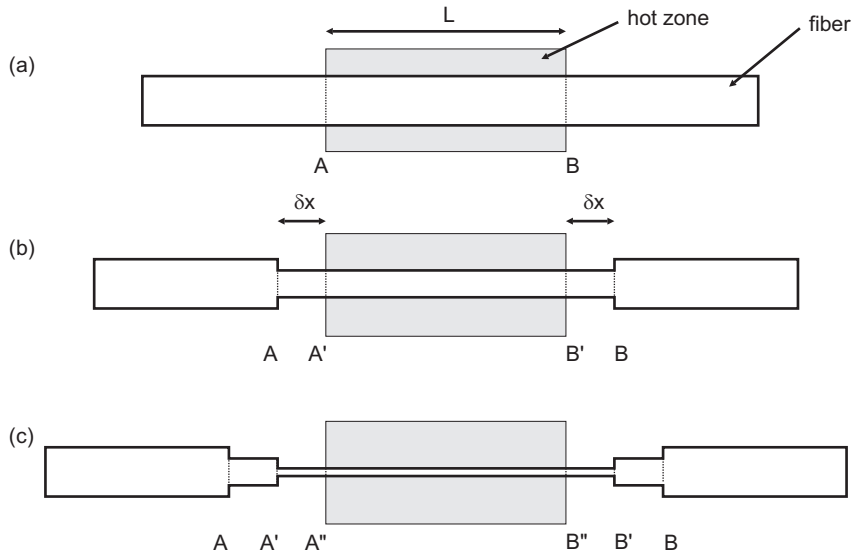

Figure 2.11: Schematic illustrating the thinning of the fiber at three consecutive time steps (a)-(c).

Figure 2.11 (a) displays a short section of the fiber. The gray shaded area represents the hot zone with a constant length L. The length of the taper waist at a given time must be equal to the length of the hot zone at that time. Therefore, as the hot zone is constant, $l_f = L$ must hold.

As the fiber is slowly pulled apart only the section of the fiber within the hot zone is deformed (cf. figure 2.11 (a)-(c)). It is assumed that the mass and therefore also the volume is conserved during the pulling process. For a small pulling distance δx the resulting equation conserving the volume of the taper is

$$\pi(a_f + \delta a_f)^2(L + \delta x) = \pi a_f^2 L, \tag{2.14}$$

where a_f is the waist diameter, and δa_f is the change in the radius and negative. By rewriting equation (2.14) in differential form and integrating for the initial condition $a_f(0) = a_0$ the spatial dependance of $a_f(x)$ is derived

$$a_f(x) = a_0 \exp\left(-\frac{1}{2}\int_0^x \frac{1}{L(x')}\mathrm{dx}'\right).$$

Since $L = \text{const}$, this leads to

$$a_f(x) = a_0 \exp\left(-\frac{x}{2L}\right).$$

The taper waist radius as a function of the drawing distance $a_f(x)$ is central for designing a fiber taper drawing stage.

Finally, it is also of interest to find the resulting radius profile of the transition region $a(z)$. By considering that if the fiber is stretched by a total amount x_0 the transition zone lengths have to be $l_0 = x_0/2$, it follows that

$$a(z) = a_0 \exp\left(-\frac{z}{L}\right).$$

It is important to point out that, in this model, the rate of change of the radius of the fiber $\frac{\mathrm{d}a(z)}{\mathrm{d}z}$ depends only on one parameter, i.e. the length of the hot zone, L. In conclusion, small hot zones result in steeper profiles, which may be a limitation for producing adiabatic tapers.

2.4.3 Heater

The central part of any fiber drawing stage is the heater. It heats a section of the optical fiber up to the temperature at which the silica starts to soften and fiber pulling is possible.

A homogenous and constant temperature distribution within the hot zone of the heating element is of vital importance. Due to the required high temperatures of 1350−1500 °C this becomes a challenging task. Small changes in the temperature distribution result in a significant change in the viscosity. Furthermore, air currents in the vicinity of the taper have to be minimized. In order to be able to provide fiber tapers on demand, a high degree of repeatability and stability is required.

There are various approaches to construct such a heater. CO_2 lasers have been used for fiber taper drawing [31]. The most successful methods producing highest quality tapers are based on a gas flame [32, 4] or on ceramic heaters [33].

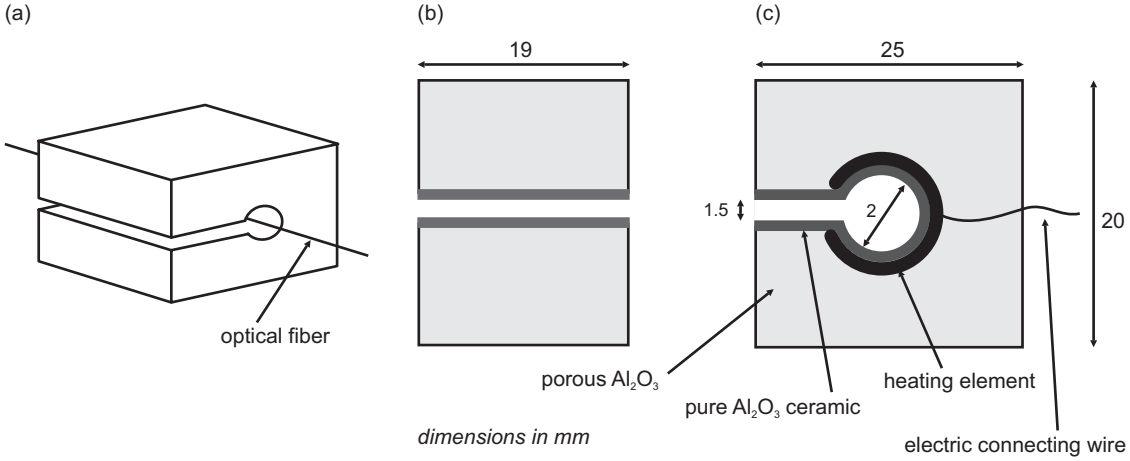

Figure 2.12: (a) Schematic drawing of the heater geometry. The position of a fiber within the heater is indicated. (b) Front view of the heater, showing the slit through which the fiber is inserted. (c) Side view of the heater illustrating the position of the heating element and the different ceramic materials used. Dimensions are given in millimeters.

The heater used in the fiber drawing setup is a commercially available electric ceramic heater (NTT Advanced Technology, Japan) used for producing fiber couplers. Figure 2.12 (a) shows a schematic drawing of the heater. The position of the fiber within the heater is indicated. Figure 2.12 (b-c) provide the dimensions of the heater and its composition. The temperature profile within the heater can be found in appendix B as a reference, since the exact temperature distribution is an important factor for the reproducibility of the drawing process.

2.4.4 Fiber drawing setup

The fiber drawing setup consists of three main components: (a) a computer controlled fiber drawing stage, (b) a ceramic heater and (c) an inverse microscope. The different components will be discussed below. A schematic drawing of the setup is shown in figure 2.13 and a corresponding photograph in figure 2.14.

(a) The central part of the setup is the pair of high precision translation stages (M-111.1DG, Physik Instrumente, Germany). The stages are connected to a PC and can be controlled by a LabVIEW based control software, which allows one to control the translation speed and acceleration of the stages. The translation stage on the right of the setup is mounted onto a solid aluminum block, whereas the other stage is placed on a 5-axes manual positioning stage (Thorlabs, USA), that allows for careful alignment of the translation stages relative to each other. Two magnetic V-groove fiber holders (Thorlabs, USA) are mounted on top of the stages. The fiber can additionally be fixed by two fiber clamps at each side mounted to the optical table. To monitor the transmission of the fiber during the drawing procedure, a He-Ne laser is coupled into the fiber. The transmission is observed on a photodiode and recorded simultaneously on the PC.

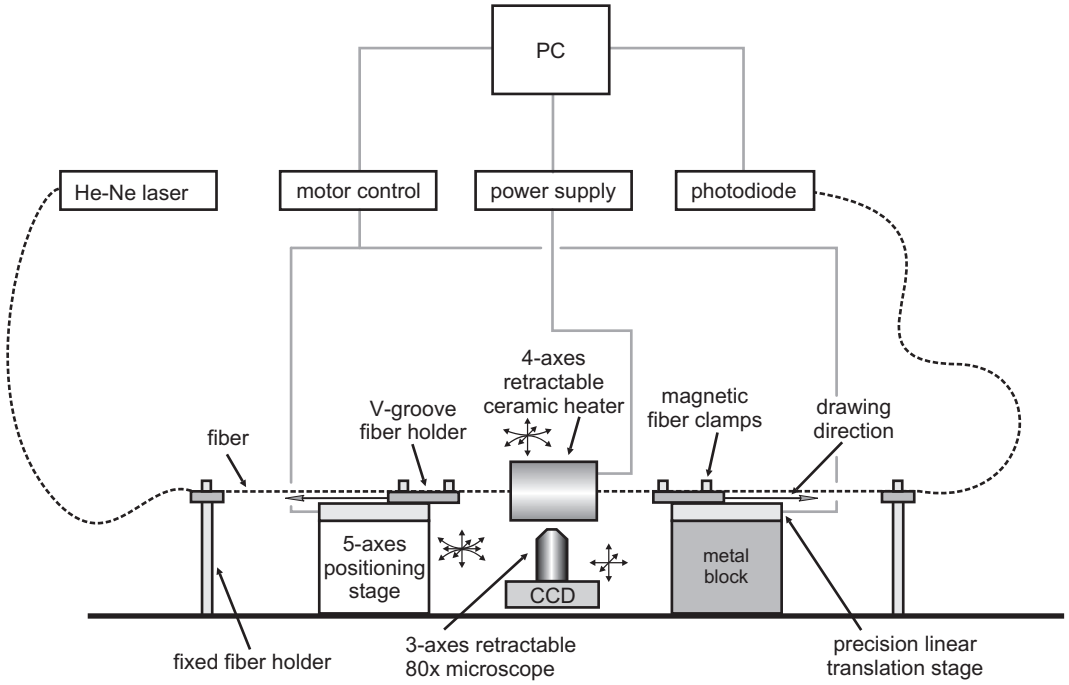

Figure 2.13: Schematic of the fiber drawing setup indicating the optical, mechanical and electrical interplay of the setup.

(b) The ceramic heater itself is braced in a custom made aluminium holder. The heater is not in direct contact with the aluminium. A high temperature silicone is used as a spacer. Since the heater transfers a substantial amount of heat to the aluminium holder an additional heat sink is added. For positioning the heater, it is mounted onto a 4-axes positioning stand. An additional 50 mm translation stage is used to manually move the heater over the fiber or retract it.
The electrical power for the heater is provided by a computer controlled switching power supply (Voltcraft, Germany).

(c) A custom-made inverse microscope is placed below the fiber between the drawing stages. It consists of a 80x microscope objective (Olympus, 80x, NA = 0.75) which is mounted to a standard optical tube system (Thorlabs, USA). The inline illumination is coupled into the optical path via a pellicle beamsplitter (Thorlabs, USA). The white light is provided by a fiber optical cable (Edmund Optics, USA) to the tube system. The image is captured by a low-cost USB camera connected to the PC. The microscope is held by a 3-axes translation stage (Thorlabs, USA) with micrometer precision. In order to distance the microscope lens as far as possible from the heater an additional vertical translation stage with a lower resolution and larger translation distance (Edmund Optics, USA) is added. A small aluminium plate can be positioned right above the microscope objective for additional protection from the heater. The resolving power of the microscope at a wavelength of 500 nm for this imaging system is about 400 nm following the Rayleigh criterion $\Delta x = \frac{1.22\lambda}{2\mathrm{NA}}$.

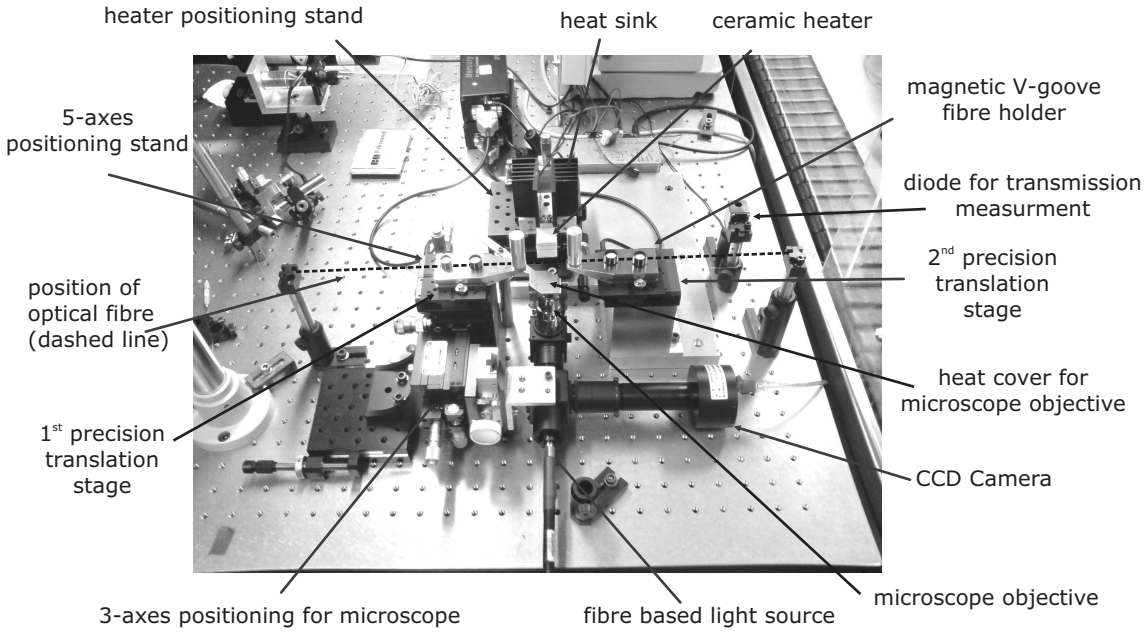

Figure 2.14: Photograph of experimental setup used for the fiber taper fabrication.

2.4.5 Procedure of taper drawing

The typical fiber drawing procedure for producing tapers with a waist diameter of about 1 μm is described below. Since the translation distance of the drawing stages is not sufficient to produce such a thin taper in a single step the fiber has to be drawn twice in a two-step process.

1. The heater is carefully heated up at two different heating rates. In order to avoid structural tensions inside the ceramic due to inhomogeneous temperature distribution a maximum heating rate of 50 °C/min is quoted by the manufacture. To be well within this limit the voltage is increased up to 8 V at a rate of 0.4 V/min and up to the final voltage of 14.8 V at a slower rate of 0.2 V/min.

2. A standard optical fiber is polymer coated to provide additional protection of the silica waveguide. A plastic blade stripping tool (NTT, Japan) is used to remove approximately 10 cm coating from the midsection of the fiber. The exposed silica is cleaned using ethanol wipes and carefully mounted to the v-groove fiber holders using the magnetic clamps.

3. A He-Ne laser is coupled into one end of the fiber and the other is placed in front of a photodiode.

4. The heater is manually moved over the fiber and the automated drawing procedure is started. The fiber is heated and thermally stabilized for 150 s. Then both translation stages start drawing the fiber at a speed of 100 μm/s for a distance of about 8 mm (single stage translation). This reduces the fiber waist diameter down to about 20 μm. The transmission through the fiber is automatically recorded during this procedure.

5. The heater is manually retracted and the inverse microscope can be used to check the diameter and quality of the fiber taper.

6. The fiber needs to be repositioned for the final drawing step. The magnetic fiber clamps on the side of the fiber are lifted and the translation stage is moved to the center position. The fiber is then fixed again by the clamps. This procedure is then applied to the other side of the fiber as well.

7. The heater is manually moved over the fiber and the automated drawing procedure is started again with the same parameters, but the drawing distance is increased to 12 mm.

8. The heater is manually retracted and the final taper diameter can now be measured by the inverse microscope. If the taper diameter does not have the desired size, the last three steps can be repeated until the desired width is obtained.

9. The taper is put under tension by moving the stages for an additional 50 μm (each side) in order to minimize sagging and movements due to air turbulence in later applications. This step is also necessary to obtain a clear image of the fiber taper waist using the inverse microscope.

10. The finished taper is then carefully glued onto a U-shaped holder made from glass fiber-reinforced plastic that is positioned by a portable stand below the fiber. The best results are obtained using a UV-curing glue.

2.5 Experimental characterization of fiber tapers

2.5.1 Fiber drawing

Figure 2.15 illustrates the fiber waist radius and transmission during a typical drawing procedure as described in section 2.4.5. The taper is drawn for 7 mm, repositioned and then finally drawn for another 15 mm. The drawing procedure is regularly stopped and the inverse microscope is used to measure the waist diameter. Figure 2.15 (a) clearly shows the exponentially decreasing waist radius. During the drawing the transmission through the taper has been recorded (c.f. figure 2.15 (b)). An increasingly faster oscillating signal can be observed in the taper transmission due to the mode interference effects (c.f. section 2.3.4). There is also a slight drop of transmission during the repositioning of the taper. This drop can be minimized by a skilled operator. The large transmission drop at the end of the drawing procedure in this measurement is due to dust contamination creating a large scattering center on the surface of the taper. Such a contamination would render the taper unusable for further experiments.

The success probability for the production of fiber tapers is quite high. On average one in three drawing attempts will produce a good taper.

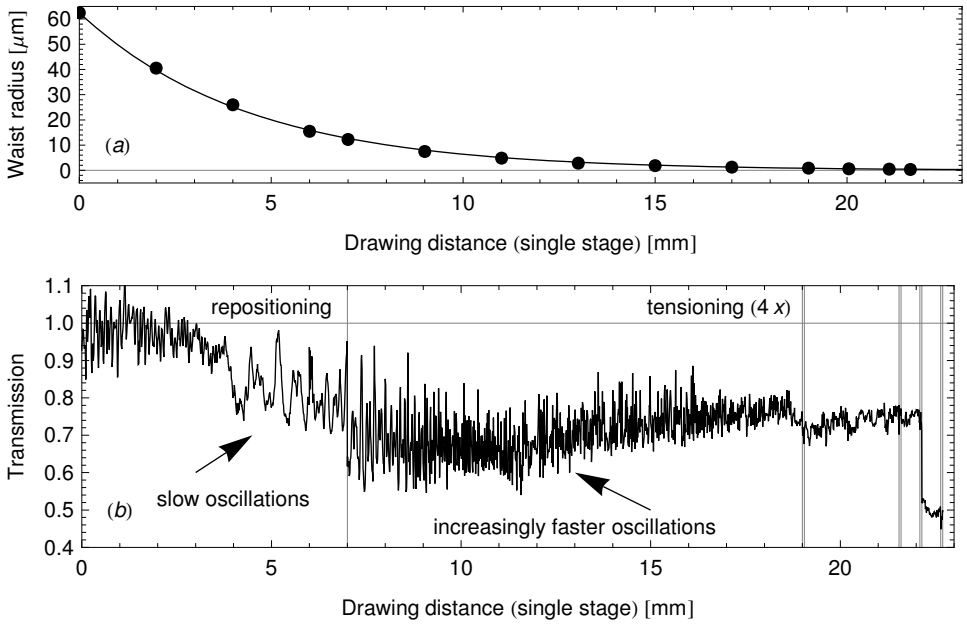

Figure 2.15: Waist diameter and transmission during the standard drawing procedure. The drawing distance corresponds to the translated distance of a single translation stage only. Final waist diameter: 0.7 μm, fitted exponential decay constant: $\alpha = 0.22\,\mathrm{mm}^{-1}$ for $a(z) = 62.5\,\mu\mathrm{m}\exp(-\alpha z)$, fiber type: telecommunication single-mode test fiber (TF) (Corning), heater power: 14.19 V, 5.272 A.

Figure 2.16 shows a microscope image of a typical taper. The image also illustrates the limitation in resolution of the inverse microscope. The theoretical limit is about 400 nm. For precise measurements of the taper diameter an electron microscope [32] or diffraction based methods [34] can be used.

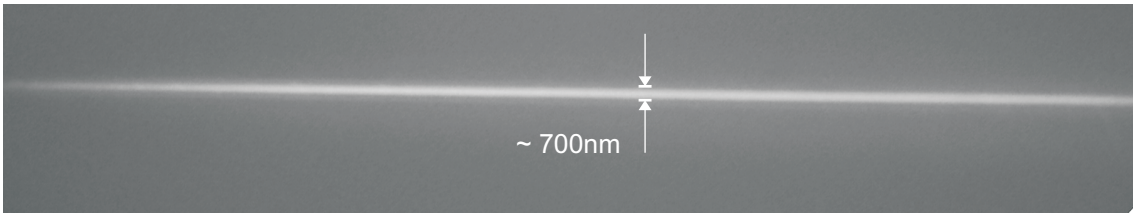

Figure 2.16: Microscope image of the waist section of a typical fiber taper of about 700 nm in diameter.

A photograph of the finished taper including U-shaped holder is shown in figure 2.17. The fiber waist is too thin to be visible in the photograph. However, the UV-glue spots fixing the taper to the holder and the unstretched fiber are visible. The fiber ends are folded into a ribbon and glued to the holder to provide further protection from mechanical stress to the fragile uncoated fiber section.

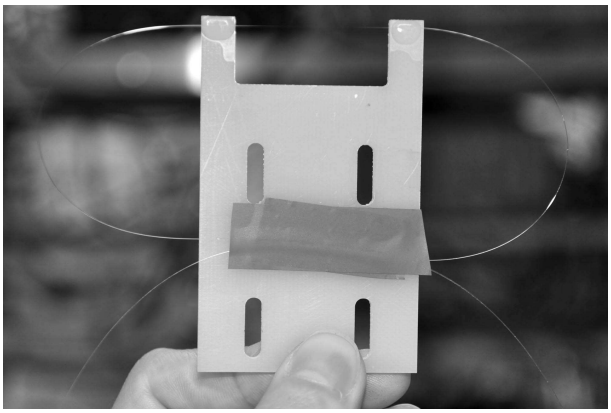

Figure 2.17: Photograph of a typical fiber taper mounted on the glass fiber-reinforced plastic U-shaped holder.

2.5.2 Fiber taper profile

The taper profile provides information about the shape of the transition region as well as the length and diameter of the taper waist. Consequently, the taper profile determines the adiabaticity of the taper and therefore its transmission. The taper waist diameter provides important information regarding the propagation constant and the extent of the evanescent field.

The change of the taper waist diameter has already been presented in figure 2.15 (a). However, it is also of interest to determine the entire taper profile of a completed taper. The results of such a measurement are shown in figure 2.18. After the drawing procedure the taper remained in the fiber drawing stage. The inverse microscope was then moved along the taper and its diameter was recorded. The measured profile shows nicely the predicted exponentially decreasing taper radius. The decay constant, α, for the measured taper profiles in figure 2.15 and 2.18 agree nicely and support the conclusion that the length of the heat zone is indeed constant and of the same length for both tapers. This result can be related to the measured heat profile of the used heater displayed in figure B.1. The heat profile shows that a nearly constant temperature distribution exists only for a few mm at the center of the heater.

A number of drawing parameters, including the temperature and the drawing speeds, have been varied in order to study their effect on the steepness of the transition region. However, only negligible changes in α have been observed.

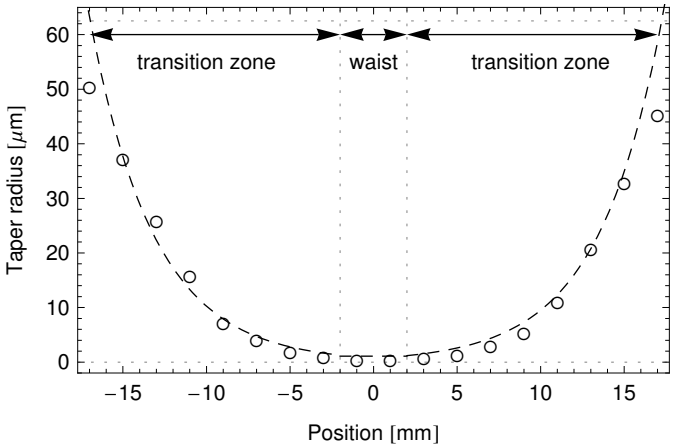

Figure 2.18: Typical taper profile. The transition zone and taper waist are indicated. The transition zone is fitted to an exponential function $a(z) = 62.5\,\mu\text{m}\exp(-\alpha z)$, and $\alpha = 0.26\,\text{mm}^{-1}$ is found. The deviation from the exponential decay of the fiber radius at both ends of the taper is associated with an error in measurement of larger fiber radii. The waist length is 4 mm and the taper waist diameter is 1.2 μm.

2.5.3 Transmission

A crucial parameter for the performance of a fiber taper is the transmission. In figure 2.19 the transmission of different fiber types at wavelengths of 632 nm and 1330 nm as a function of the drawing distances are shown. For this measurement the fiber tapers are not repositioned, but instead the maximal possible drawing distance of the stages was used. This procedure has proven to be sufficient in order to evaluate the suitability of a particular type of fiber for producing fiber tapers. If a significant drop in the transmission is observed due to a non-adiabatic transmission zone, this occurs at the first few mm of the drawing procedure only.

Figure 2.19 shows the transmission for (a) SMF28 (Corning) fiber, a widely used telecommunication single mode fiber and (b) a telecommunication single-mode test fiber (TF) (Corning), that is mainly used in the experiments, at the standard telecommunication wavelength of 1330 nm. The final transmission at a drawn distance of 15 mm is 97% and 95%, respectively, which can be considered to be adiabatic. This also emphases the optical similarity between both fibers.

The remaining transmission plots in figure 2.19 are recorded using a He-Ne laser at 632 nm. The transmission at this wavelength region is of greater importance for applications involving fluorescence detection of NV diamond defect centers (discussed in chapter 5.2). By comparing the different fibers it is obvious that some are more suitable than others. For instance it has not been possible to produce fiber tapers with acceptable transmission using the S630 (Nufern) fiber. This is attributed to the special design of this fiber. The core of the fiber is made from pure silica while the cladding of the fiber is doped to have a smaller refractive index. In the transition zone the guided modes couple to radiation modes and are scattered. This scattering phenomenon is nicely illustrated by the microscope image in figure 2.20.

In terms of transmission, there is no significant difference between the remaining fiber types shown in figure 2.19. The best transmission is obtained using the SM450 (Fibercore) fiber. However, due to the high cost of this fiber, the less expensive TF is used. With an average transmission between 60% and 70% as shown in figure 2.15 (d) for the TF fiber, this seems to be an acceptable trade-off.

All transmission signals show the typical intermodal interference oscillations that increase in frequency with smaller taper diameter [28].

2.5.4 Spectral transmission properties

Fiber tapes may be used as a probe for collecting fluorescence from quantum emitters. Therefore it is of interest to measure the spectral transmission of a fiber taper before it is used in further experiments.

The emission of a white LED (Luxeon III, $I = 80\,\text{mA}$) is coupled into the fiber taper. The transmitted

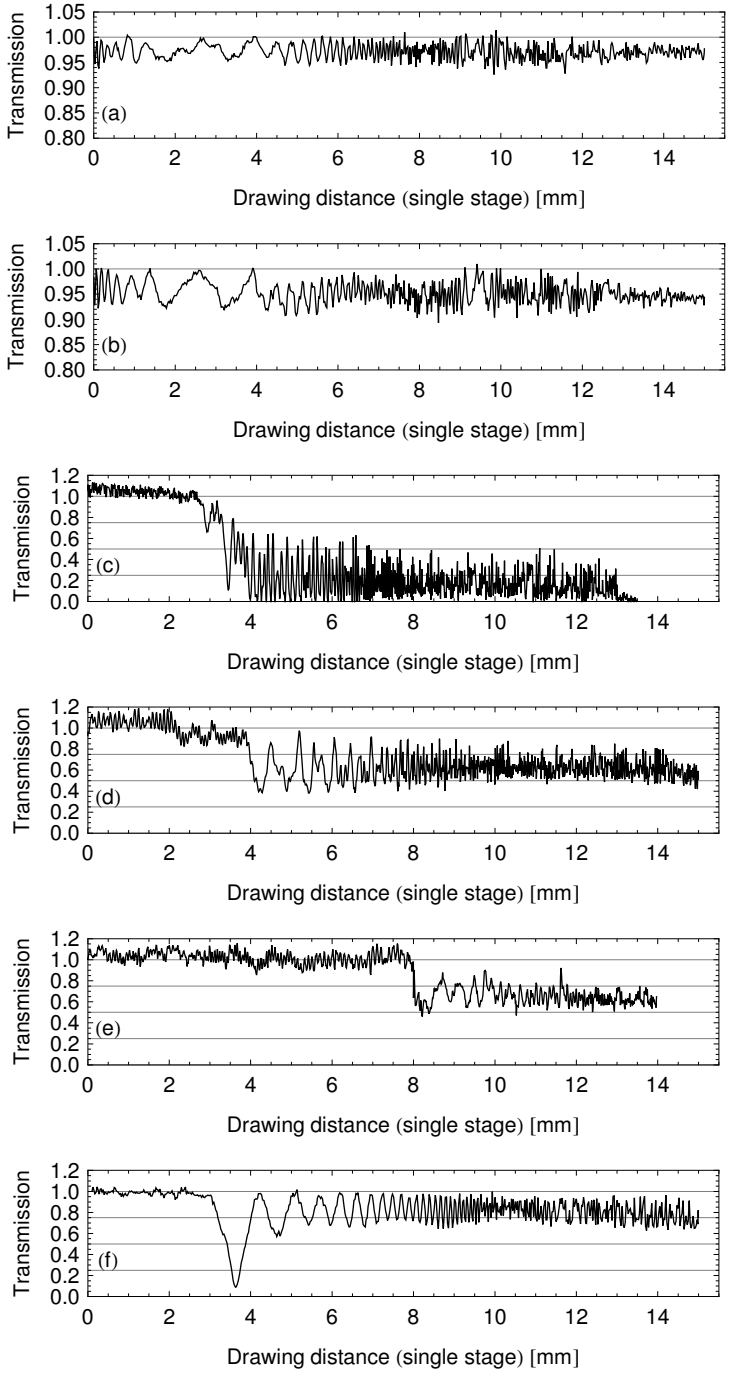

Figure 2.19: Comparison of the fiber taper transmission recorded during the drawing procedure. (a) SMF28 (Corning), $\lambda = 1330\,\text{nm}$, (b) telecommunication single-mode test fiber (TF) (Corning) , $\lambda = 1330\,\text{nm}$ (c) S630 (Nufern), $\lambda = 633\,\text{nm}$, (d) TF (Corning), $\lambda = 633\,\text{nm}$, (e) 980HP (Corning), $\lambda = 633\,\text{nm}$, (f) SM450 (Fibercore), $\lambda = 633\,\text{nm}$.

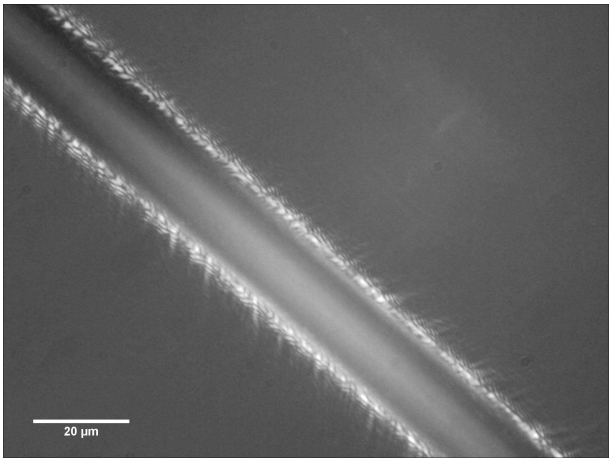

Figure 2.20: Microscope image of scattered modes at the transition region of a fiber taper. A AS100/110 UVAN (Fibretech, GmbH) multimode UV guiding fiber with 100 μm core diameter is used. The laser wavelength is 632 nm.

light is then analyzed by a spectrometer (Spectra Pro 500i, Acton Research). The results are presented in figure 2.21 for a selection of different fiber types.

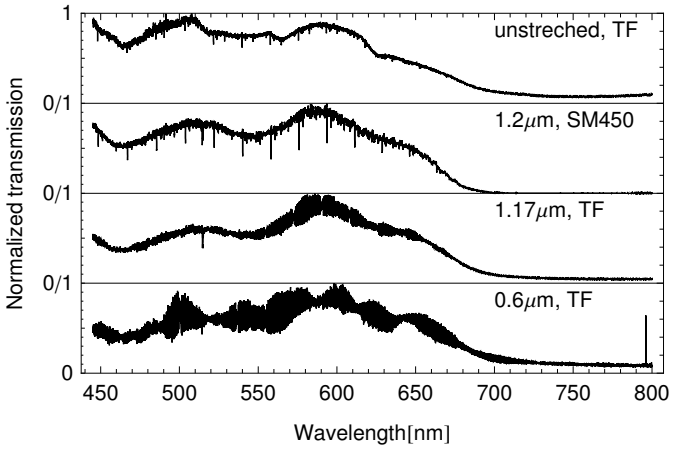

Figure 2.21: Spectral transmission for different waist diameters and fibers types. The transmission is normalized with respect to the white LED light source. For definitions of fiber types see figure 2.19.

The lower three spectra in figure 2.21 show the typical spectral transmission of fiber tapers. The envelope of the spectral transmission of a taper is very similar to the unstretched fiber. The low transmission at wavelengths above 700 nm may originate from the presence of HO^- ions in the glass [35] that have absorbtion peaks at 720 nm.

By comparing fiber taper spectra to the transmission of a unstretched, plain fiber the oscillations in the transmission signal attributed to the intermodal interference effects can be identified as discussed in section 2.3.4.

Further investigations into the fast oscillations in a white-light transmission spectrum are shown in figure 2.22 (a) and (b) by performing a segmented Fourier transform (SFT) (cf. appendix C). Two prominent bands are visible in the SFT indicating the presence two oscillating signals within the transmission signal. By considering the discussion in section 2.3.4, at least three different fiber taper modes must be involved leading to this interference effect. By an additional careful examination of the SFT, further oscillating signals can be seen in between the prominent bands, corresponding to additional interfering taper modes. Since the contrast is much lower compared to the prominent bands the coupling in the transition region of the taper into these modes must be weaker.

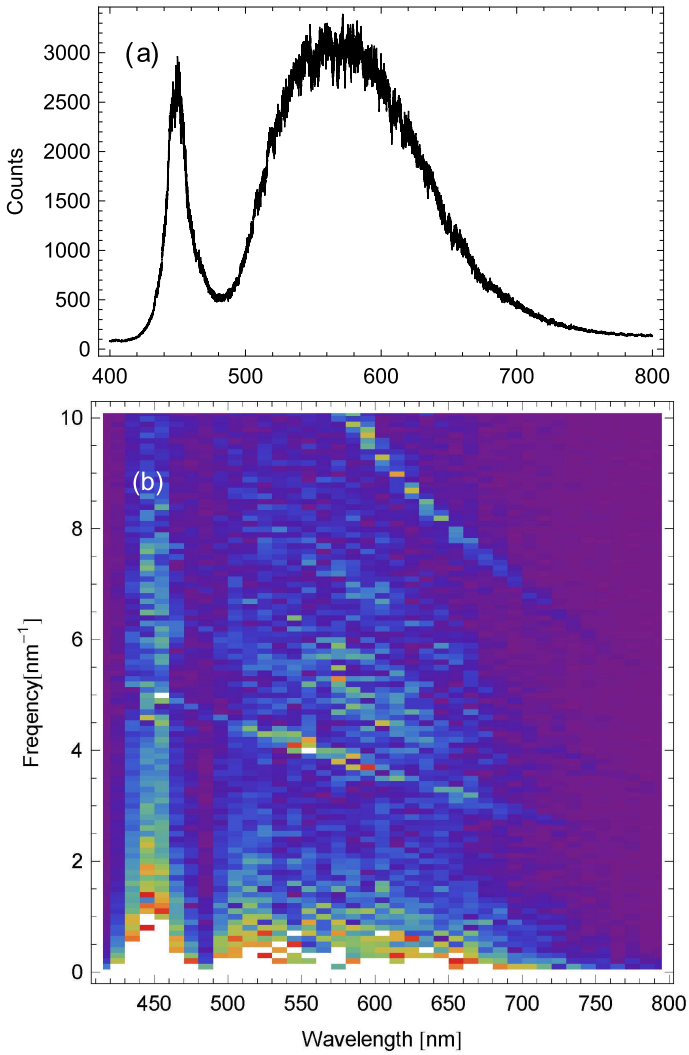

Figure 2.22: (a) Unnormalized transmission spectrum of a white light LED source through a $1\mu m$ thick fiber taper. (b) Corresponding segmented Fourier transform (SFT).

The SFT of the spectral transmission spectrum is a valuable tool. It can be used as an indicator for the quality of the taper and its adiabaticity. Additionally it allows one to distinguish interference effects originating from the taper and other sources, like microresonators (as discussed later in chapter 5.3.2).

2.5.5 Aging effects

Aging is an important issue concerning optical fiber tapers. In particular very thin tapers with diameters of a few micrometers and below seem to be subjected to this phenomenon [36, 37]. The typical changes in the transmission spectrum of a sub-micron fiber is shown in figure 2.23. On the day of production the taper shows a well modulated spectrum due to mode interference effects. As the time progresses this modulation frequency changes and after 13 days the overall transmission has dropped dramatically. In particular, shorter wavelengths are suppressed quicker than longer wavelengths.

These aging effects are correlated to (a) mechanical stress, (b) water vapor and (c) contamination by dust from the environment. This particular taper was used over this period of 13 days for contact coupling to a toroidal microresonator. These attempts involved a large amount of mechanical stress for the taper as it is was moved across the surface the toroid. Since the taper is not enclosed in a protective gas environment it is subject to water vapor. A thin water film on the surface or even water diffusion into the taper have an adverse effect on the transmission properties of the taper. The influence of water vapor can be reduced by placing the taper within a vacuum chamber [36, 37].

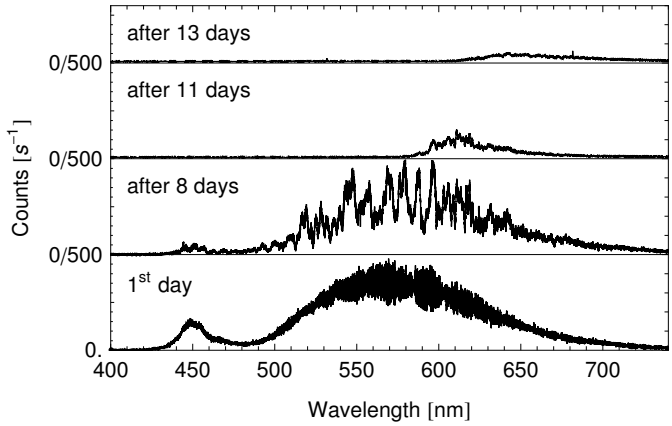

Figure 2.23: Transmission spectra of a taper with a diameter of 900 nm illustrating aging effects over a time period of 13 days. The transmission spectra show the un-normalized spectral transmission of the white LED with corresponding broad peaks at 450 nm and 550 − 600 nm.

2.6 Conclusion

Optical fiber tapers, and, in particular, thin fiber tapers with a diameter similar to the guided wavelength (c.f. figure 2.7), guide a substantial fraction of the optical power in the evanescent field and form the basis for applications in sensing and microresonator experiments.

A theoretical description of the modes and fields within a cylindrical dielectrical waveguide has been introduced in order to determine the propagation constant, β, of the mode as the well as fractional optical power guided outside of the taper. The calculation showed, that for a substantial amount of the power in the fundamental fiber mode to be guided in the evanescent field, the diameter of the taper has to be substantially smaller than the wavelength of the guided light.

Fiber tapers with waist diameters of about one μm are highly multimode in the visible wavelength region resulting in an interference effect between the individual modes. Methods involving a Fourier transform are used to identify these effects in spectral transmission spectra. This knowledge is of particular importance for fiber taper-coupled microresonator systems.

The mechanical setup allows for the reliable production of adiabatic fiber tapers with a transmission of about 95% and waist diameters below one μm. These results are excellent for a manufacturing method

based on a ceramic heater. Only much more involved setups using a moving flame approach [32] have been able to produce tapers with a significantly higher transmission.

In summary, this reliable production method for optical fiber tapers combined with the insight of the optical properties lay the foundations for the experiments described in the following chapters.

Chapter 3

Functionalizing optical fiber tapers

3.1 Introduction

Optical fiber tapers are a versatile tool for sensing applications. A significant fraction of the light guided through the tapered region is contained in the evanescent field and thus interacts with the medium surrounding the taper.

There are two different sensing approaches: One is based on detecting phase shifts in the propagation mode due to changes in the dielectric environment of the taper [6]. The other uses the evanescent field for highly sensitive absorbance measurements of single atomic layers [4]. Even the fluorescence of a small number of atoms in a magneto-optical trap can be detected [5]. The evanescent fields around the taper form a trapping potential that may be used to trap single atoms [26]. A different sensing concept is to functionalize the surface of a fiber taper in order to make it optically sensitive to changes in the environment. This has been shown for humidity [38, 39], hydrogen [7] or ammonia [40] sensors.

In this chapter, a technique for functionalizing a fiber taper by deposition of individual micrometer-sized particles is presented. Optimum control of functionalization is obtained if only a single active particle is placed on a fiber taper. It was possible to mechanically pick up, for instance, single diamond nanocrystals with fiber tapers from different substrates [20, 3]. However, the method introduced in this chapter is a non-contact technique for assembling such a sensor element by landing a preselected microparticle on the tapered region of a fiber with the help of a segmented linear Paul trap.

A Paul trap uses an oscillating electric field in order to trap charged particles [41]. Linear Paul traps are widely-used tools to confine single ions for high resolution spectroscopy [42] or as quantum registers [43] for quantum information processing [44]. Another application concerns controlled implanting of trapped ions [45]. However larger particles, ranging from a few nanometers [46] to micrometers [47] have also been trapped and investigated. The Paul trap used in these experiments has been built as part of the diploma thesis by Alexander Kuhlicke [48]. The collaboration between Alexander Kuhlicke, Oliver Benson and myself resulted in a publication [9] and are presented in this chapter.

3.2 Theory of the Paul trap

This section introduces the central theoretical ideas related to trapping charged particles using a Paul trap. It focusses on the basic concepts important to understand the principle of this trapping concept. This section is based on a more comprehensive and detailed description that can be found in [48].

A particle trap uses appropriate restoring forces to contain particles within a certain region of space. A possible approach is to use electric fields acting on charged particles. A simple argument shows that *static* electric fields are not suitable for trapping particles in all three dimensions. In the simplest case, the restoring force grows linearly with the distance to the center of the trap giving a parabolic potential $\Phi = ax^2 + by^2 + cz^2$. However, the requirement on such a potential is to fulfill the Laplace equation, i.e. $\Delta\Phi = 0$. This is only possible if $a + b + c = 0$, which means that at least one coefficient has to be negative. A three-dimensional confinement is not possible.

By introducing *oscillating* electric fields radial confinement can be achieved. This approach is used in radio frequency traps, so-called Paul trap [41]. The potential for the xy-plane of a Paul trap with a

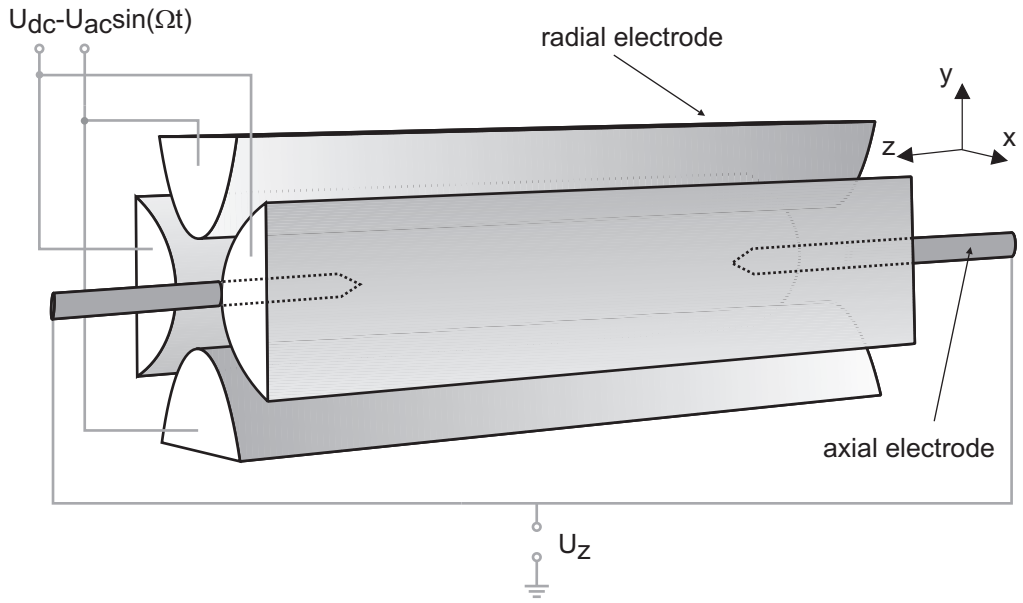

Figure 3.1: Illustration of the geometry of an ideal linear Paul trap showing the four radial and the two axial electrodes. The electric wiring for applying the electric fields is indicated. The illustration is adapted from [48].

linear geometry, shown in figure 3.1, is given by

$$\Phi(x, y, t) = (U_{dc} - U_{ac} \cdot \cos(\Omega t)) \cdot \frac{x^2 - y^2}{2r_0^2}, \tag{3.1}$$

where a dc voltage, U_{dc}, in series with an ac voltage, U_{ac}, is applied to the linear, radial electrodes and Ω is the angular frequency of the oscillation. The opposing electrodes are connected and have a minimal distance of $2r_0$ between them as indicated in the schematic drawing of the trap geometry.

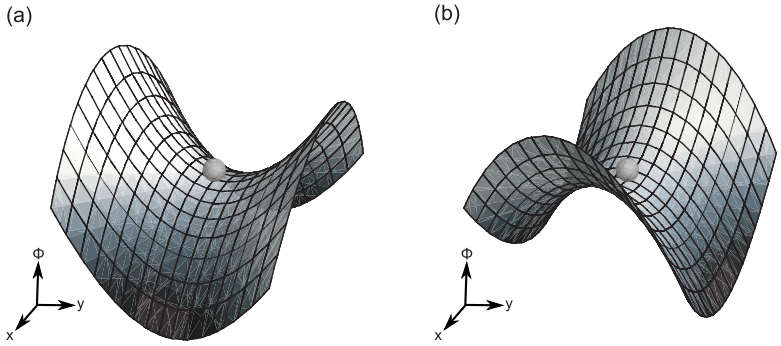

Figure 3.2: Illustration of the electric potential in the xy-plane at time $t = t_0$ (a) and $t = t_0 + \pi/\Omega$ (b). The small sphere indicates the time averaged minima of the potential and the position of the trapped particle within the trap.

The two-dimensional trapping potential Φ can be visualized as a rotating saddle potential. Figure 3.2 (a) shows such a potential at $\Phi(x, y, t = t_0)$ and after a rotation of half a period $t = t_0 + \pi/\Omega$ in (b). The small sphere sitting in the center of the saddle represents a trapped particle. By an intuitive argument, the particle remains stationary if the correct rotation frequency is chosen. The time average of Φ forms a quasi potential with a minimum at its center.

The trapping force in the axial or z-direction has to be introduced by an additional static trapping potential created by another dc-voltage applied to the axial electrodes, which are shown in figure 3.1 (see section 3.4.1 for the experimental implementation).

These considerations lay the basis for trapping particles. However, in order to decide if a particular particle can be trapped the equation of motion has to be solved. The force acting on a charged particle can be calculated by considering the electric field as,

$$\vec{E} = -\nabla\Phi. \tag{3.2}$$

The equation of motion for a particle of mass M and charge Q is then

$$M \cdot \frac{d^2\vec{r}}{dt^2} = Q \cdot \vec{E} \tag{3.3}$$

By choosing the right parametrization the equation of motion can be reformulated in the normal form of the Mathieu differential equation [48]

$$\frac{d^2u(\tau)}{d\tau^2} + (p_u - 2q_u\cos(2\tau))u(\tau) = 0 \quad u \,\epsilon\, \{x, y\}. \tag{3.4}$$

The parameters are then given by

$$\tau = \frac{\Omega t}{2}, \qquad p_x = -p_y = 4\frac{Q}{M}\frac{U_{dc}}{\Omega^2 r_0^2}, \qquad q_x = -q_y = 2\frac{Q}{M}\frac{U_{ac}}{\Omega^2 r_0^2} \tag{3.5}$$

It is interesting to note that the particle's charge Q and mass M appear as a ratio in the parameters.

The Mathieu differential equation is often chosen for describing harmonic problems involving an additional oscillating parameter. By numerical integration of the differential equation and observing the amplitude of the particle's motion within the trap is is possible to deduce parameter ranges that correspond to confined trajectories. Such stable regions are shown in figure 3.3. The stability regions for the x- and y-direction are indicated. Only if both regions coincide, as in the middle of the diagram, is radial trapping possible.

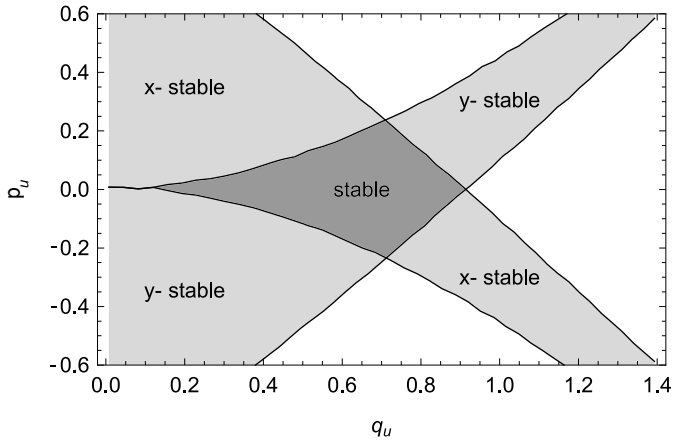

Figure 3.3: First region of stability for a linear Paul trap. The plot is adapted from [48].

The calculated stability diagram refers to particles in vacuum without considering gravitational forces. If a Paul trap is operated in air an additional damping term has to be introduced, which results in an enlargement of the stability region [49] allowing for easier trapping and increased storage time. A more detailed discussion can be found in [48].

3.3 Theoretical considerations for optical properties of particle functionalised fiber tapers

3.3.1 Excitation efficiency of dipole emitters

The main feature of a taper is the evanescent field that extends from the waist of the taper into the surrounding medium, as discussed in chapter 2.3.2. The energy contained in this field can be used to

optically excite particles or molecules [4] placed on the surface of the fiber taper. Therefore, it is of high interest to calculate the optical power available for excitation.

The fraction of the energy guided outside of the taper is plotted in figure 3.4 for the fundamental HE_{11} mode for different taper diameters and different wavelengths. For an efficient excitation using the pump wavelength of 514 nm of an argon-ion laser, a taper diameter well below 1 μm has to be used. In particular, if a particle of size comparable to the taper diameter is placed onto the taper surface, only a small fraction of the evanescent field overlaps with the particle. However, the excitation efficiency can be optimized by adjusting the orientation of the seeded linear polarization, since the power density outside of the taper depends on the orientation of the polarization [50] (cf. also figures 2.6).

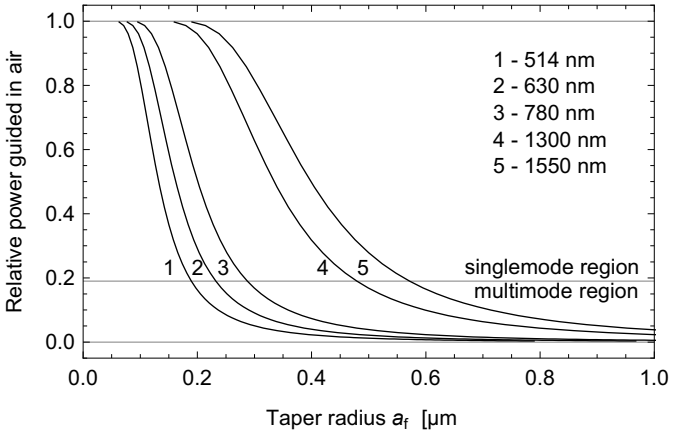

Figure 3.4: Fractional power guided outside an air-clad fiber taper for different wavelengths for the fundamental HE_{11} mode at an index contrast of $\Delta = 0.259$.

It is important to point out that the tapered geometry also increases the power density inside the guiding dielectric. This may lead to undesired non-linear optics effects [21] and to an additional increased background fluorescence of the waveguide material, thereby limiting the applicability.

3.3.2 Collection efficiency of dipole emitters

The central aspect of a functionalized optical taper is its ability to collect the fluorescence from active particles placed onto its surface. In this section the collection efficiencies for this problem, based on a finite-difference time-domain (FDTD) simulation, are presented and compared to the collection efficiency of a microscope objective.

A good approximation for the spatial emission of an optically active particle used for functionalizing fiber tapers is to consider the time averaged power dP radiated by a dipole per solid angle $d\Omega$ in the far-field, given by [25]

$$\frac{dP}{d\Omega} = \frac{\omega^4 p_0^2}{32\pi^2 \epsilon_0 c^3} \sin^2(\theta) \tag{3.6}$$

where θ describes the angle between the radiation direction and the orientation of the dipole centered at the origin of a spherical polar coordinate system (cf. figure 3.5 (a)), ω is the radiation frequency, p_0 is the normalized power. A dipole shows the well-known beacon like emission pattern. The strongest optical transitions in molecules or atoms often show a dipole like emission. If multiple optical molecules or atoms with random orientations contribute towards the fluorescence of a particle the spatial average over all three possible dipole orientations has to be considered.

A conventional approach to collect fluorescence efficiently from a small radiating object is to use a microscope objective with a high numerical aperture (NA). The NA parameter is a geometrical description of the maximal opening angle of the cone of light the objective is able to collect, as illustrated in figure 3.5 (b) and can be expressed as

$$NA = N_e \sin(\alpha)$$

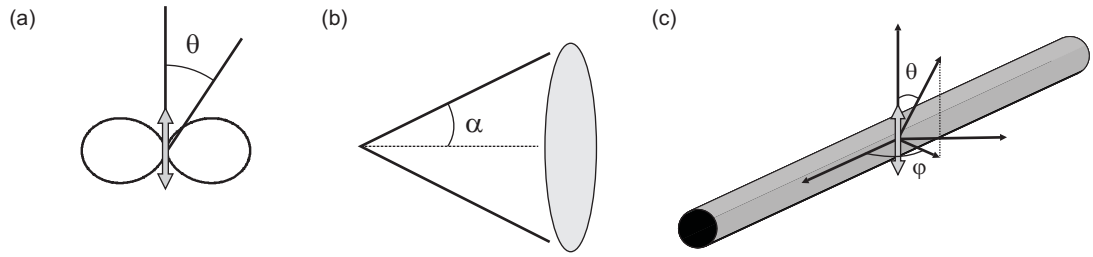

Figure 3.5: (a) Typical far-field emission characteristics of an oscillating dipole (gray). (b) Collection efficiency of a lens described by the numerical aperture NA $\sim \sin(\alpha)$. (c) Orientation in conventional spherical polar coordinates (θ, φ) of a dipole (double sided gray arrow) on the surface of a silica cylinder as used in the discussed FDTD simulation.

where N_e is the refractive index of the surrounding medium. The collection efficiency of such a microscope objective for a radiating dipole can be estimated by integrating the power radiated into the solid angle corresponding to the cone spanned by the numerical aperture of the microscope objective. There are three orthogonal orientations in space. Thus, it is convenient to consider the dipole to be parallel $P_\parallel$ to and perpendicular $P_\perp$ to the optical axis of the microscope objective. The integrals for the parallel and perpendicular orientations of the dipoles, normalized by the total radiated power P_T are given by,

$$\frac{P_\parallel}{P_T} = \frac{1}{48}\left(24 - 27\cos(\alpha) + 3\cos(3\alpha)\right) \tag{3.7}$$

$$\frac{P_\perp}{P_T} = \frac{1}{32}\left(16 - 15\cos(\alpha) - \cos(3\alpha)\right) \tag{3.8}$$

$$\frac{2P_\perp + P_\parallel}{3P_T} = \frac{1}{2}\left(1 - \cos(\alpha)\right) \tag{3.9}$$

where α is related to the numerical aperture. The collection efficiency of a randomly orientated dipole is given by the average of the two perpendicular and the parallel orientations, i.e. $(2P_\perp + P_\parallel)/(3P_T)$. A plot of the collection efficiency can be found in figure 3.6.

In order to compare the collection efficiency of a functionalized taper to a microscope objective an FDTD simulation is performed. Commercial software (Lumerical inc., Canada) for solving electromagnetic problems based on the FDTD method is used.

Since a simulation of the entire taper with a length of a couple of centimeters would require too much computational resources, only a small section of the taper waist is modeled as a 40 μm long silica cylinder. This approach seems to be reasonable considering the size of the particle with respect to the length of the taper waist. This model further assumes taper adiabaticity, i.e. all the light emitted into one end of the silica cylinder is also emitted at the end facet of the fiber taper. The funtionalizing particle attached to the taper is represented as a radiating dipole on the surface or at a distance of 100 nm from the silica cylinder. Two distances are chosen in order to account for the finite size of the few hundred nanometer-sized particles. The coupling efficiency is calculated by considering the energy flow through selected surfaces in the model. The energy flow through a surface S is given by

$$P_S = \frac{1}{2}\int_S \mathrm{Re}\left(\mathbf{E} \times \mathbf{H}^*\right) \cdot d\mathbf{S}. \tag{3.10}$$

The quantity $\mathbf{E} \times \mathbf{H}^*$ is the Poynting vector, as already discussed in 2.3.1, describing the energy flow of an electro-magnetic field. By integrating the Poynting vector across a surface, the total energy flow across this surface is found. The factor $\frac{1}{2}$ arises from the time average of the field.

The silica cylinder and the taper are completely enclosed in a rectangular box of planar surfaces. The coupling efficiency, η_t, for the taper is given by the ratio of the power transmitted through the end facet of one side of the silica cylinder $P_{\text{end facet}}$ to the total power radiated through all surfaces $P_{\text{all surfaces}}$, i.e.

$$\eta_t = \frac{P_{\text{end facet}}}{P_{\text{all surfaces}}}. \tag{3.11}$$

The results of these simulations for different parameters are shown in figure 3.6 (b). The coupling efficiency for all three different dipole orientations are calculated separately (solid lines) and then averaged (dashed

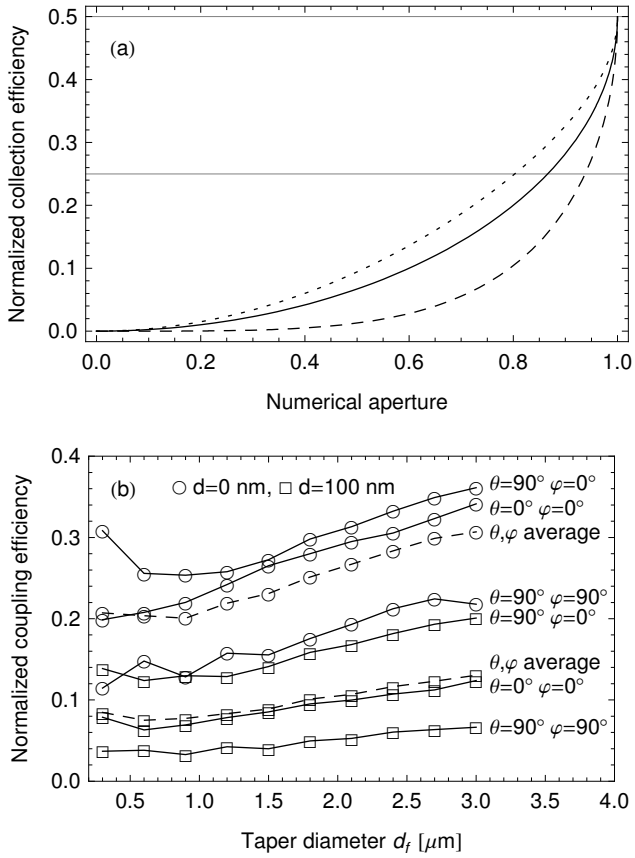

Figure 3.6: (a) Calculated collection efficiencies as a function of the numerical aperture for a parallel (dashed, equation (3.7)) and perpendicular (dotted, equation (3.8)) orientation of the dipole with respect to the optical axis of the microscope objective (cf. figure 3.5 (a)-(b)). The solid line gives the collection efficiency of a randomly oriented dipole (equation (3.9)). (b) Simulated collection efficiency (equation 3.11) of a dipole (different orientations, θ, φ, positioned on the surface or at a distance of 100 nm from the surface) into a 40 μm long taper section of varying diameter as illustrated in figure 3.5 (c). Other simulation parameters: dipole radiation wavelength 610 nm, unit cell size 43 nm. Boundary conditions are implemented as perfectly matched layers.

lines) for a randomly orientated dipole. Also, the distance of the dipole from the taper is considered by placing the dipole onto the surface and at a distance of 100 nm from the taper. The length of the simulated fiber section of 40 μm has been chosen to balance the computational resources and the decay of radiating modes in the fiber. Additional simulations for different section lengths have shown that errors in the coupling efficiency due to the specifically chosen length can be neglected.

The simulations show that the highest coupling efficiency is achieved if the dipole radiates along the extension of the taper. Thus, if a single photon source, e.g. a diamond nanocrystal or a quantum dot, is placed onto such a taper, it is important to consider the orientation of the dipole transition for obtaining the highest possible coupling efficiency. Additional simulations suggest an exponential decay of the coupling efficiency with increasing separation distance between taper and dipole. The coupling efficiency halves within 100 nm. This has to be considered if, for instance, a single photon source contained in a dielectric matrix is coupled to a fiber taper, since the matrix may increase the distance between the single photon source and taper.

There has been some effort to calculate analytically the coupling efficiency of the fluorescence of individual atoms to a guided mode of optical tapers. Kien *et al.* have calculated the coupling efficiency of a cesium atom to be up to 28% for a taper of 200 nm in diameter [51]. This value agrees well with the results from this FDTD simulation.

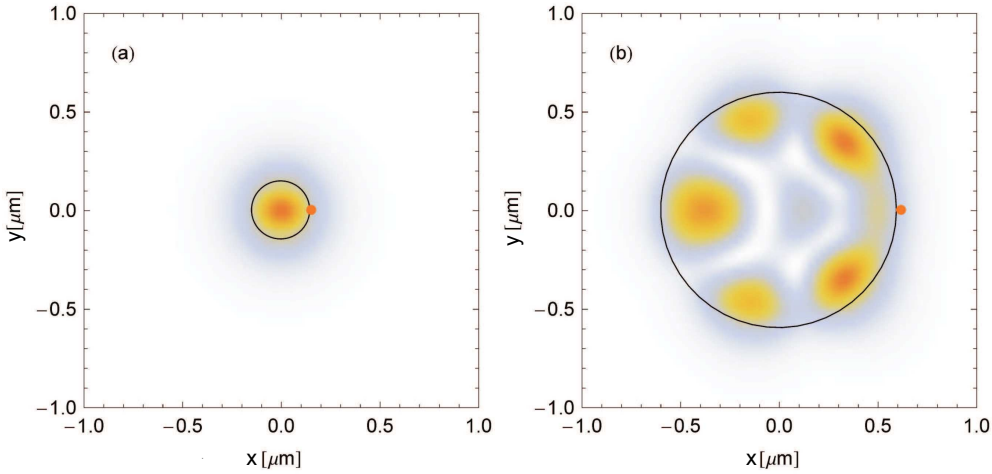

Figure 3.7: Power density mode profile excited by the radiating dipole at a distance of 40 μm from the surface for a silica cylinder of 300 nm (a) and 1.2 μm (b) in diameter. The outline of the taper is indicated by the black circle. The position of the dipole is shown as an orange dot. The dipole orientation with respect to the taper is $\theta = 0°$, $\varphi = 0°$. All other simulation parameters are as quoted in the caption of figure 3.6.

By scrutinizing the results in figure 3.6 it is possible to estimate the coupling efficiency of an optical fiber taper with respect to a conventional microscope objective. An optimal coupling efficiency of $\eta_t \approx 0.3$ can be achieved using a fiber taper, and this compares with a high NA microscope objective with NA > 0.8. This already emphasizes the advantages of fiber coupled access and is complemented by a robust geometry allowing access to complicated structures.

Furthermore, the simulation in figure 3.6 (b) indicates that the coupling efficiency is proportional to the cylinder's diameter. This would suggest that thicker tapers would result ultimately in a better coupling efficiency. However, this might not necessarily be the case as the number of guided modes in a thin air-clad fiber is smaller than the number of guided modes in an optical fiber as discussed in chapter 2.2.3. A density plot of the guided modes in the silica cylinder can be found in figure 3.7. As expected, for a thin cylinder with diameter of 300 nm the power is guided by the fundamental mode only. Whereas, if the cylinder diameter increases the coupled power is distributed over multiple modes. This effect will increase with increasing cylinder diameter. As examined in chapter 2.3.4 not all modes are adiabatically transformed in the transition region of the taper. Thus, some of the power in higher guided modes of the air-clad fiber will be lost in the transition region. The simple proportional relation between coupling efficiency and taper diameter is not expected to hold. In fact, detailed numerical simulations are mandatory for each specific geometry.

In principle, it is possible to increase the effective coupling efficiency of an optical fiber taper by adding an additional mirror to one end of the fiber. As a consequence the entire collected fluorescence is emitted via the other end of the fiber.

3.3.3 Scattering from small particles

By placing a particle onto a taper an additional scattering center is introduced that reduces the transmission through the fiber. It is envisioned to place multiple particle acting as sensors onto a single taper. Furthermore, it is expected that the particle size will have a major influence on the overall transmission. It is therefore important to understand the loss mechanism and to be able to predict the effective transmission through such a functionalized taper.

The reduction in transmission due to the placement of a particle is calculated using a FDTD simulation. The fibre taper waist is again represented by a silica cylinder. In order to be able to account for different sized particles the problem is modeled by a silica cylinder piercing a larger polystyrene sphere. The diameter of the polystyrene sphere is increased in successive FDTD simulations. At the lower limit, the diameter of the sphere is equal to the diameter of the taper and no loss in transmission should by visible. With increasing sphere diameter the silica cylinder is encompassed by an increasingly thicker

layer of polystyrene representing particles of different size. This modeling geometry is illustrated by the inset in figure 3.8 and also by the microscope image of a particle in figure 3.15 (b).

The transmission of the fundamental mode (HE_{11}) through the silica cylinder is then calculated by

$$T_t = \frac{P_{\text{end facet}}}{P_{\text{seeded mode}}} \tag{3.12}$$

where $P_{\text{end facet}}$ and $P_{\text{seeded mode}}$ is given by equation (3.10).

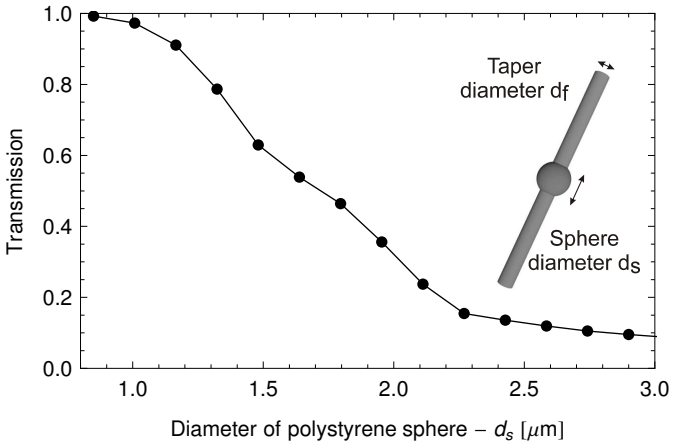

Figure 3.8: Results of an FDTD simulation of the transmission of the HE_{11} mode at 532 nm in a silica cylinder with a diameter $d_f = 850\,\text{nm}$, and a length of $100\,\mu\text{m}$ piercing a polystyrene sphere of diameter d_s. The unit cell size of the simulation is 33 nm and perfectly matched layers are used as boundary conditions.

Figure 3.8 shows the results for a particular silica cylinder with a diameter of $d_f = 850\,\text{nm}$. For a thin layer of polystyrene surrounding the taper ($< 150\,\text{nm}$) the drop in transmission is only on the order of a few percent. This correlates with the power guided in the evanescent field of the taper. For larger sphere diameters the polystyrene layer increases and a rapid loss in transmission can be observed. This can be understood, if one considers that the polystyrene layer introduces a larger perturbation to the dielectric waveguide and thus the entire mode propagation is distorted leading to an increase in scattering.

A similar result is obtained by Uzunoglu *et al* [52]. There, an analytical approach is used to model the change in transmission through an air-clad fiber as a sphere of varying size is coupled to the fiber.

3.4 Experimental setup

3.4.1 Segmented Paul trap

In order to prepare and select single particles for subsequent placement, we use a segmented linear Paul trap. Such a trap confines charged particles in a two-dimensional oscillating electric field created by a geometry of four main electrodes, as discussed in section 3.2. Confinement in the remaining direction along the trap's symmetry axis is typically obtained with the help of additional auxiliary electrodes, e. g., rods [53], rings [54] or segments of the main electrodes [55]. In the last case segmentation can be used to define well-separated trapping and spectroscopy regions. Transport between these regions is obtained by changing the voltage applied to the individual electrodes [56, 57].

A schematic of the used segmented trap can be seen in figure 3.9. The trap has a total length of 70 mm and consists of four cylindrical electrodes made of brass tubes mounted on glass fiber rods, which act also as a cable guide. The opposing electrodes are electrically connected. A radio-frequency (rf) voltage is applied to one pair of electrodes while the other pair is held to ground, resulting in the same potential as shown in figure 3.2. The ground electrodes are subdivided into twelve segments with lengths of 2, 5, and 7 mm. A varnish painted on the end facets of the segments provides electrical insulation. The electrodes with an outer diameter of $2R = 4\,\text{mm}$ have a minimum distance to the center of the trap of $r_0 = 3\,\text{mm}$. A sinusoidally varying rf-voltage is produced by a function generator and amplified to a voltage amplitude

of typically $U_{ac} = 1\,\mathrm{kV}$ with a frequency of $\Omega = 2\pi \cdot 5\,\mathrm{kHz}$. The additional direct current (dc) voltages are provided by laboratory power supplies and are applied to the segments by a switch box. Typical values are $U_{2,4-12} = 20\,\mathrm{V}$ and $U_{1,3} = 0-40\,\mathrm{V}$. The electrodes are mounted on two insulating plates inside an air-tight box allowing sufficient optical access. The trap is operated under ambient conditions. Air-friction results in damping of the particle motion [49] establishing a wider stability-region, i.e. the possibility to trap particles with a wider mass-range compared to vacuum conditions. Based on the parameters quoted above and an estimated charge of $10^4\,e \approx 10^{-15}\,\mathrm{C}$ per particle it is theoretically possible to trap polystyrene spheres within the range from 25 nm up to 4 μm in size [48]. This range can be extended by changing the trapping frequency, Ω. With this trap, particle storage times on the order of several hours can easily be achieved.

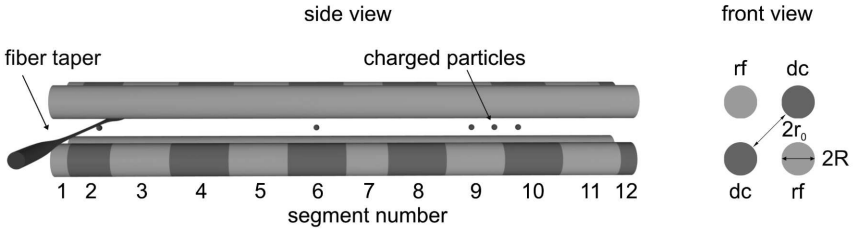

Figure 3.9: Schematic of the Paul trap geometry: The trap consists of two rf-electrodes and two dc-electrodes. The dc-electrodes are subdivided into twelve segments with lengths of 2, 5 and 7 mm. The total length of the trap is 70 mm. Segments 1-3 constitute the spectroscopy region, where the fluorescence measurements and the deposition on the optical fiber taper are performed. Loading of the trap occurs from the righthand side (segments 10-12.) The segmentation allows confinement of several particles at once, isolation of single particles, and their transfer within the trap.

The segmented geometry provides different regions in the trap for different purposes. The particles are inserted at one end of the trap (segments 10-12, figure 3.9) whereas at the other end, the spectroscopy region (segments 1-3, figure 3.9), fluorescence measurements and the deposition on the fiber taper are performed. This subdivision protects the fiber taper from unwanted deposition and, in addition, avoids contamination of the electrodes in the spectroscopy region by charged particles, which would modify the trapping potential in an uncontrolled way.

3.4.2 Insertion of particles via electrospray injection

Charging and insertion of particles occurs by a technique called electrospray ionisation injection (ESI) [58] as illustrated in figure 3.10. Any kind of particle, which can be brought in suspension (e.g. water, ethanol) can be injected with this method. A high voltage of about 2 kV is applied to the metallic capillary (inner diameter of 110 μm) of a syringe containing the suspension. Charged droplets leave the metal capillary along a potential gradient oriented towards the trap. The droplets reduce in size due to evaporation. When the Coulomb repulsion exceeds the surface tension, fission of the droplets (Coulomb explosion) occurs [59]. Finally, when the remaining solvent is completely evaporated, the charged particles are captured by the linear trap.

3.4.3 Optical setup including the Paul trap

The optical setup is designed to be flexible. It offers free optical beam access to the trap and provides for easy incorporation of the fiber taper. This has been achieved using the setup illustrated in figure 3.11.

Dye-doped polystyrene beads (Invitrogen, USA, FluoSpheres F8801) are used as model particles. They can efficiently be excited via a fiber coupled argon-ion laser operating at 514 nm or a frequency doubled Nd:YVO_4 laser at 532 nm. In order to preselect a desired particle before placing it onto the taper it is necessary to investigate its optical properties while it is still hovering inside the trap. By flipping mirror FM2 and keeping mirror FM1 upright it is possible to excite a trapped particle through the microscope objective. During initial fluorescence studies the fiber taper is removed from the trap and covered, in

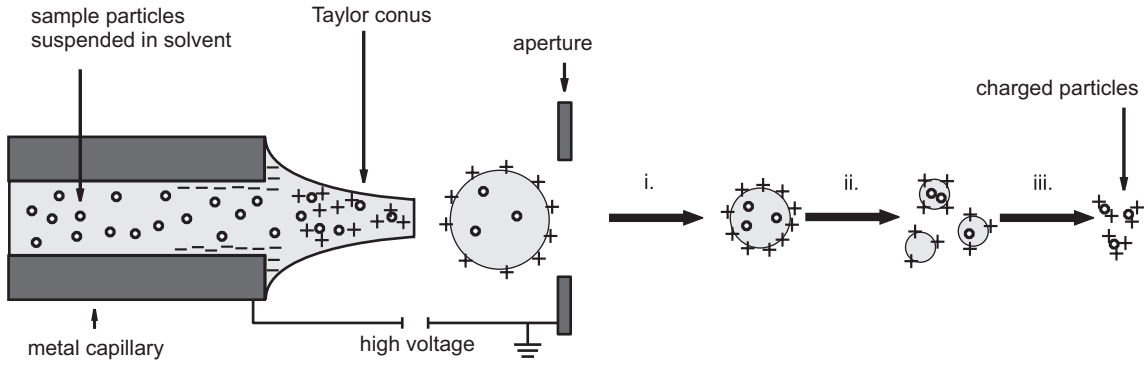

Figure 3.10: Illustration of electrospray injection: i. evaporation of solvent until Rayleigh limit is reached, ii. Coulomb explosion, iii. evaporation of residual solvent and further Coulomb explosions. Illustration is adapted from [48].

order to avoid unwanted contamination. A low power microscope objective with a magnification of 4× and $NA = 0.1$ is optimal to find a particle within the trapping region due to its large field of view combined with a large depth of field. The position of the trap can be controlled by motorized translation stages in order to bring particles in the trap center into focus. The fluorescence of a particle is collected by the same microscope objective. A dichroic mirror and additional long pass filters are used to suppress the pump light before the fluorescence is imaged on a sensitive CCD camera (ORCA-ER, Hamamatsu) or dispersed by a spectrometer (Spectra Pro 500i, Acton Research) with a cooled CCD camera (LN/CCD-1340/100-E/1, Roper Scientific). After deposition of a suitable particle, the taper also provides optical access. This can easily be achieved by flipping mirror FM1 and keeping mirror FM2 in the upright position. The flexible setup allows rapid switching between both detection methods.

A photodiode was added to the setup in order to measure the change in fiber transmission while a particle is placed on the taper. In this case mirror FM1 has to be flipped and mirror FM3 has to be upright. As indicated in the figure, the Paul trap and the taper are contained in an airtight box, in order to reduce air turbulence.

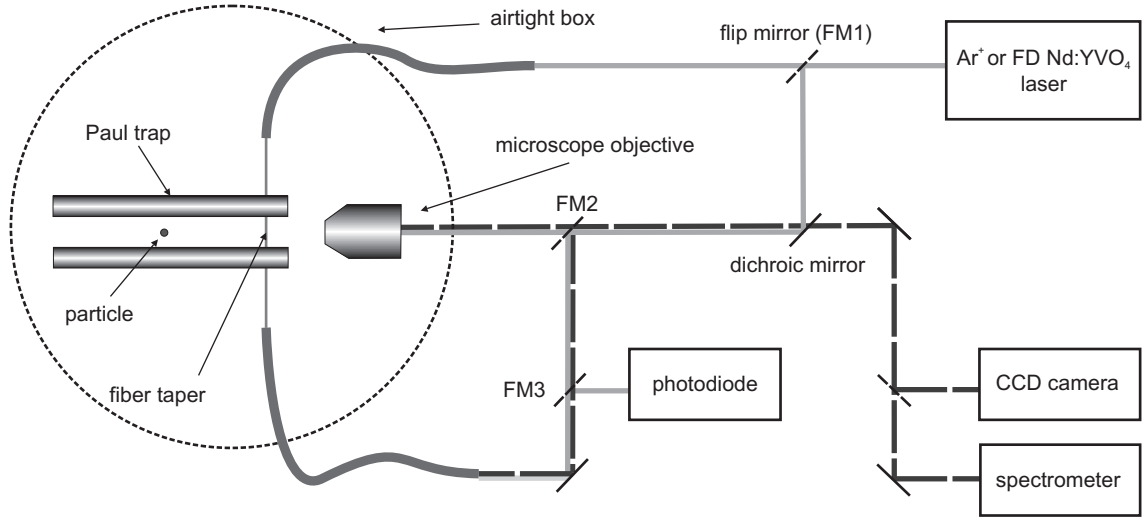

Figure 3.11: Schematic of optical setup: solid gray and dashed black lines indicate the optical paths for the excitation laser and fluorescence detection, respectively. By flipping either mirror FM1 or FM2 it is possible to excite and detect particles hovering in the trap through the microscope objective or to measure deposited particles directly through the optical fiber taper. FM3 allows measurement of the change in transmission via a photodiode as a particle is placed onto the taper.

3.5 Deposition and spectroscopy of a single particle

In this section the placement of a spectroscopically pre-selected particle is presented [9].

3.5.1 Manipulation procedure

The deposition process for a single dye-doped polystyrene bead is illustrated in figure 3.12. Initially, a suspension of 100 nm-sized dyed-doped polystyrene spheres in ethanol is prepared by sonication and loaded into the ESI-syringe for injection. The concentration of the suspension is chosen to be 2×10^7 particles/ml. The particles were negatively charged by a voltage of 1.7 kV applied to the ESI and injected in the trap.

Several particles can be loaded into the trap simultaneously and can then be transferred between different trapping regions in the segmented trap as described in section 3.4.1. An additional He-Ne laser (not shown in figure 3.11) beam is directed along the axial center of the trap in order to observe the particles via light scattering. In this way trapped particles can be imaged on the CDD camera. This greatly facilitates the manipulation procedure.

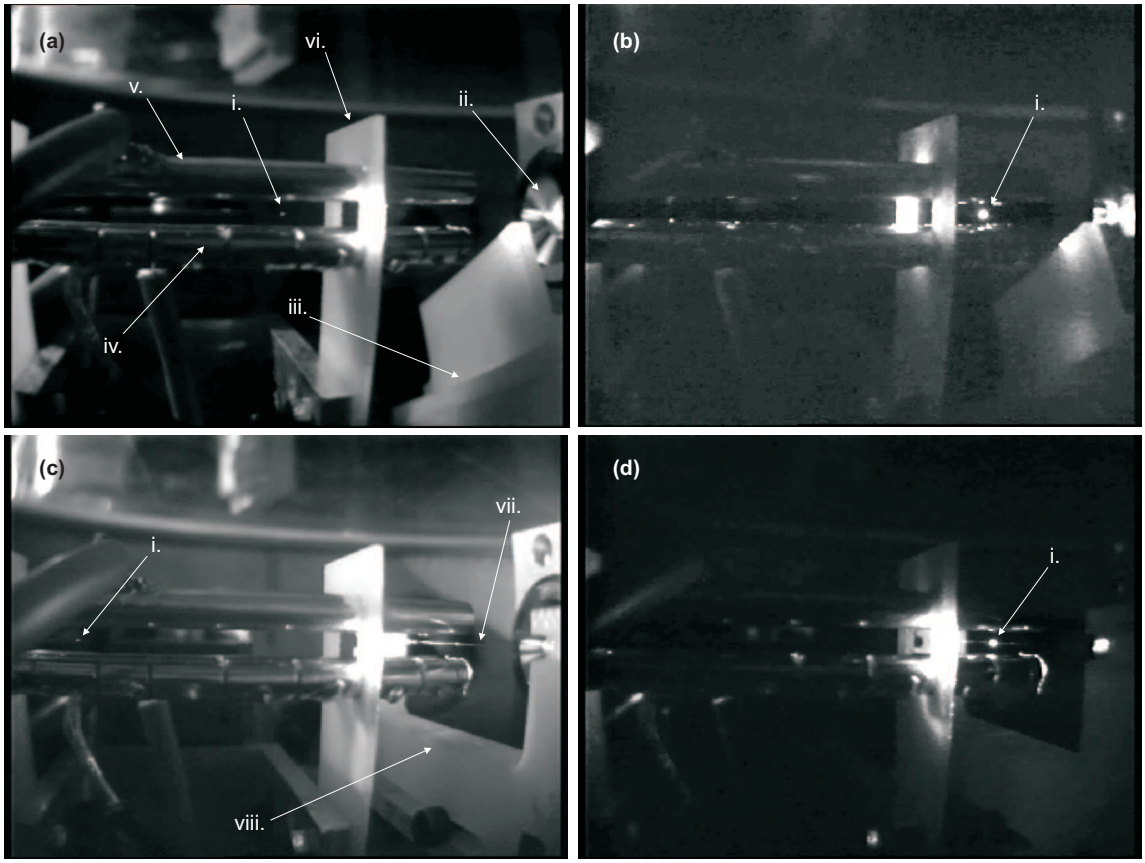

Figure 3.12: (a) Particle, after electrospray injection, trapped between electrodes, (b) particle moved into spectroscopy region of the trap, (c) optical fiber taper is uncovered and moved into trap, (d) particle has landed onto fiber taper. Annotation: *i.* trapped particle, *ii.* microscope objective, *iii.* cover for optical taper, *iv.* segmented electrode, *v.* high-voltage electrode, *vi.* holder for electrodes, *vii.* fiber optical taper (seen due to light scattered out of a guided fiber mode), *viii.* U-shaped holder for optical fiber taper. A short movie clip of the process can be found at [60].

A single trapped particle can be seen in figure 3.12 (a) hovering in the middle of the trap. In the next step the particle is moved into the focus of the microscope objective as shown in figure 3.12 (b). A photoluminescence spectrum of the particle is recorded (cf. section 3.5.2). This procedure allows one to preselect a particle based on its spectral properties. If a particle is not considered to be suitable, it can be easily ejected by switching off the axial confinement potential at the end of the trap. Then, another

particle from the storage region at the other side of the trap can be transported to the spectroscopy region to repeat the measurement. Once a suitable particle is found, all other particles are removed from the trap and the selected particle is moved into the storage region, before the fiber taper is uncovered and moved slowly into the trap as seen in figure 3.12 (c). The fiber taper can be observed via scattered light from an argon-ion laser beam coupled into the taper. In figure 3.12 (c) the fiber taper can be identified as a thin line glued into a U-shaped holder. The taper used for this experiment has a diameter of 700 nm. Such a thin diameter was chosen in order to increase the evanescent field as well as to ensure a high coupling efficiency of fluorescence light into the fundamental mode of the taper, as discussed in section 3.3.1 and 3.3.2. When the taper is placed within the trap, the selected particle is transported back to the spectroscopy region. By adjusting the trap position with respect to the taper and changing the electrode voltages it is possible to move the particle close to the taper, where it is eventually attracted to and lands on the taper. Once the particle is placed it can be observed as a bright scattering center on the taper as shown in figure 3.12 (d). We found that only negatively charged particles can be attracted by the taper. This is due to positive charges on the glass surface since a repulsive effect could be observed for positively charged particles.

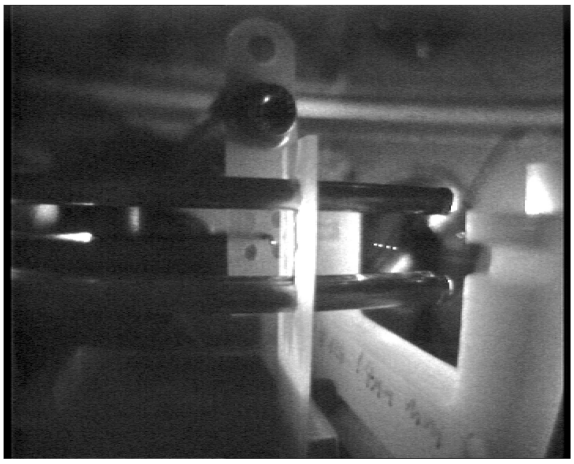

Figure 3.13: Four particles placed evenly spaced onto a fiber taper. The distance between the particles on the taper is roughly 2 mm.

The reliable procedure of selection and placement of particles can be repeated also for one and the same taper as shown in figure 3.13. Four particles are evenly spaced along the taper, where the minimal distance between the particles is given by Coulomb repulsion due to their similar initial charge from the ESI process. This also illustrates the potential of this deposition technique. The lateral precision of the deposited particles is limited by the motion of the particle induced by the alternating trapping potential. For the presented trap configuration this motion is on the order of $1 - 2\,\mu$m. However, as seen in figure 3.13, the surface charge distribution on the taper has a major influence. In future experiments particle deposition may be guided by modifying the charge distribution, for instance, using focused UV light to remove electrons from the surface. This would also allow a precise deposition on more complicated structures than optical fiber tapers.

3.5.2 Spectroscopy inside the trap and on the taper

One of the advantages using a Paul trap for placing particles is the possibility to spectroscopically preselect a particle before it is deposited onto the taper. The fluorescence spectrum of a particle hovering in the spectroscopy region of the trap is recorded in figure 3.14 (a) by the microscope objective as seen in figure 3.12 (b).

Once the particle is placed on the taper, it provides optical access to the particle (cf. figure 3.12 (d)). By coupling the argon-ion laser into the taper it is possible to excite the deposited particles on the surface via the evanescent field of the taper. At the same time, the taper collects the fluorescence of the dye-doped particle. Figure 3.14 (b) shows the fluorescence spectrum measured via the fiber taper. Obviously, both spectra, taken by the microscope and the fiber (figure 3.14 (a) and (b)) coincide and

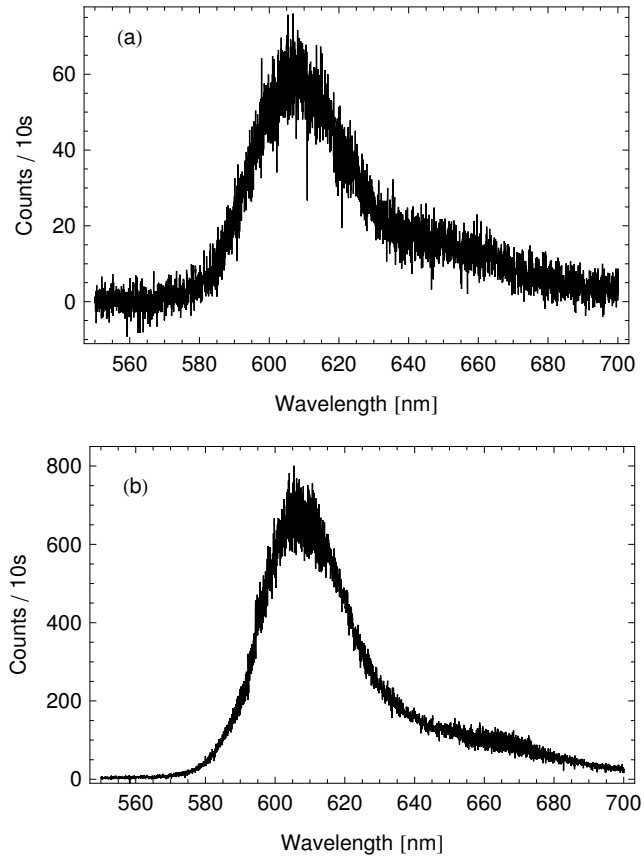

Figure 3.14: (a) Fluorescence spectrum of a trapped dye-doped particle measured via a microscope objective, (b) fluorescence spectrum of the same particle deposited onto and detected via a fiber taper of 700 nm in diameter. The excitation power was $P_{\text{ext}} = 30\,\mu$W at 514 nm.

show the typical emission characteristics of the dye used for doping the particle.

3.5.3 Transmission loss during deposition

The deposition process is also investigated for a single particle in more detail. In order to do this the transmission is measured by a frequency doubled Nd:YVO_4 laser at 532 nm through a fiber taper of 850 nm in diameter during the deposition. Figure 3.15 (a) shows a sudden decrease in transmission corresponding to additional scattering by the deposited particle. The transmission changes to 46%, which indicates that, in this experiment the single trapped and deposited particle corresponds in fact to a cluster of several 100 nm-sized polystyrene beads. For smaller objects of a few hundred nanometer in diameter (corresponding to a single bead) a much smaller change in transmission of the order of a few percent would have been expected, as discussed in section 3.3.3. The size of the deposited particle cluster in this experiment was measured subsequently using a microscope. Figure 3.15 (b) shows the microscope image indicating a particle size of $\approx 1.5\,\mu$m. The observed loss in transmission agrees with the calculated loss for a particle of this size as shown in figure 3.8. The correspondence is convincing when taking into account deviations of the bead cluster from a perfect sphere as well as possible guidance of light via higher order, modes which are subject to higher scattering losses.

3.5.4 Comparison of excitation and fluorescence collection efficiencies

In addition to the robustness and flexibility of a single active particle coupled to a fiber taper, there is also an improved fluorescence yield compared to collection via a simple microscope objective. This is

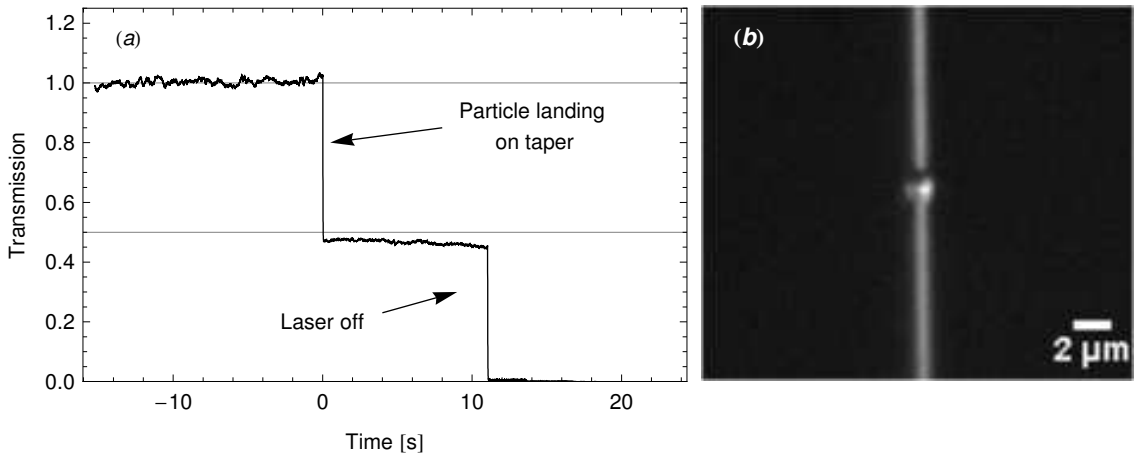

Figure 3.15: (a) Transmission at 532 nm while depositing a single 1.5 μm-sized particle consisting of a cluster of polystyrene beads on a 850 nm diameter taper, (b) microscope image of the deposited particle.

clearly seen by comparing the different count rates of the spectra in figure 3.14 (a) and (b) for collection via the microscope objective and the tapered fiber, respectively. In both cases the same pump power of 30 μW at 514 nm was used, but the fluorescence signal collected through the taper is 11 times larger than the signal collected through the microscope objective. An order of magnitude estimation can be performed to explain this difference.

One aspect concerns excitation efficiency. The focal spot of a free beam after our microscope objective has been calculated using the Gaussian beam propagation method [61] for the lens system used to have a theoretical minimum diameter of 17 μm. For a 1.5 μm sized particle the areal overlap is only 0.8%. A similar argument can be made for the particle attached onto the fiber by considering the evanescent field surrounding the taper. For a taper 700 nm in diameter at a wavelength of 515 nm about 4% (cf. figure 3.4) of the power is guided outside the taper and is available for exciting the particle. In our case the overall transmission through the taper, including coupling and fiber losses, was measured to be 6.3%. Multiplying this by the fractional evanescent field we found a value of 0.25% to be compared to the areal overlap in the free beam excitation. Thus, excitation via the tapered fiber should be approximately 3 times less efficient.

The other aspect concerns the collection efficiency of the fluorescence emission. The microscope lens with $NA = 0.1$ collects only 0.25% of the emission of an arbitrarily oriented dipole (cf. figure 3.6 (a)). When comparing to the collection via the fiber one has to take into account that only a thin layer around the taper will couple evanescently to the guided mode in the taper. In a cluster of dye-doped beads those closest to the surface will couple most efficiently while the coupling efficiency exponentially decreases with the distance from the fiber surface. Based on our FDTD simulations for a 700 nm taper the collection efficiency of emission from an arbitrarily oriented dipole on the surface and at a distance of 100 nm from the surface is 21% and 8%, respectively (cf. figure 3.6(b)). Thus, as an estimation, the emission from a 100 nm layer around the taper with an average coupling efficiency is considered to be 15%. For such a taper and a spherical cluster of 1.5 μm in diameter enclosing the taper, approximately 5% of the total fluorescence of the cluster is collected. This is about 20 times larger than collection via the microscope objective.

By combining the estimation for the excitation and the enhanced fluorescence collection a factor of 7 in improvement for the fluorescence signal for the particle on the fiber taper compared to the detection via a microscope objective is expected. This is slightly underestimated, but a convincing order-of-magnitude agreement with the observed factor of 11.

3.6 Conclusion

As mentioned in the introduction it is possible to pick up single, nano-sized diamond crystals using fiber tapers [20, 3]. There has also been considerable efforts to manipulate nano-sized objects using different

probe based techniques [62, 63, 64], which are promising for adaptation to deposit particles onto fiber tapers.

However, it is important to point out that the method presented here is non-contact. Thus no mechanical stress and damage occurs to the taper. Also, in principle, the Paul trap can be operated in vacuum which offers a very clean environment and is important for maintaining the optical quality of the taper. Further contamination of the taper due to parasitic particles transferred during mechanical contact techniques can be avoided since only trapped and spectroscopically preselected particles are deposited.

The measured collection efficiency of light from fluorescence particles deposited on the taper exceeded free beam detection via our microscope objective by an order of magnitude. The corresponding FDTD simulations suggests that an optical fiber taper can collect light as efficiently as a high-NA microscope objective.

Chapter 4

Spherical microresonators for sensing applications

4.1 Introduction

Microspherical resonators support optical modes with very high photon storage times corresponding to a high quality (Q) factor [16, 12] (cf. section 4.2.1). An analogous acoustical phenomenon was discovered by Lord Rayleigh [65] at the St. Paul's cathedral in London (cf. figure 4.1 (a)). A very prominent feature of the cathedral is the dome with a diameter of 34 m. Sound is reflected at the interior of the dome in such a way that people at distant point on the dome's gallery can whisper to each other. In analogy optical modes with a high Q factor are called *whispering gallery modes (WGM)*.

An illustration and photograph of such microspherical resonators coupled to a fiber taper waveguide are shown in figure 4.1 (b) and (c).

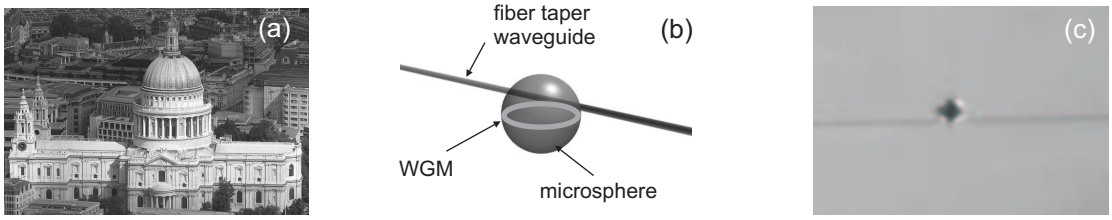

Figure 4.1: (a) St. Paul's cathedral in London, schematic drawing (b) and microscope image (c) of a fiber taper coupled microsphere resonator. The depicted polystyrene microsphere has a diameter of 50 μm.

The long interaction time and strong field confinement associated with WGM's in the microresonator are ideal to study light-matter interactions, like non-linear optical effects. For example, it was possible to demonstrate Raman lasing within a silica microspheres at a very low pump power threshold [66]. By doping a glass resonator with erbium and ytterbium it is also possible to construct a compact microlaser [67].

At the same time, microsphere resonator systems are very interesting for sensing applications due to the long interaction length of the evanescent field protruding from the sphere into the immediate surrounding (cf. figure 4.3). Small changes in refractive index cause a resonance frequency shift that can easily be detected. This has been shown for small refractive changes in liquids [68] or even the label-free detection of binding events of biomolecules [69, 70]. Such biosensors can also be operated in the stimulated regime by using the changes in the lasing properties of dye doped microspheres [71]. Even single molecule detection has been observed [72]. Here, in particular, analyzing the sensing mechanism is crucial, since apart from influences of refractive index, thermal heating effects may be important as well.

A double-ring resonator has been used to detect changes in the surrounding gas composition [73]. Another approach for gas sensing is based on resonant detection, e.g. of trace gases [74].

A challenge is to couple light efficiently in and out of a high quality resonator. The most successful techniques use evanescent field based couplers, i.e. glass prisms [75] or fiber tapers [10]. In these setups

the microsphere and the coupler are mounted to individual stages in order to be able to control the relative position very carefully for obtaining an optimal coupling position. This type of setup is mechanically involving and in parts cumbersome.

As part of this thesis a coupling method is demonstrated where the polystyrene microspheres as microresonators [76] are directly attached to the optical fiber taper [15, 77, 78]. No further alignment is necessary. In this way a mechanically and thermally well-isolated resonator system is formed, since the microsphere is supported by the thin glass fiber only. Furthermore, the optical stability of the resonator system is significantly enhanced.

In this chapter the optical properties of such a resonator system are investigated. Here the main focus lies on a sensing application for gas detection. It is demonstrated that the resonance frequency of the attached microsphere shift with temperature and therefore constitute a sensitive thermometer.

A successful gas sensing method is presented by measuring the thermal conductivity of the gas surrounding the sphere. Some of the coupled laser light is absorbed by the sphere and results in heating of the sphere. The resulting rise in temperature can be measured, and it is found to be proportional to the specific thermal conductivity of the surrounding gas.

The collaboration between the diploma student Christroph Prylik, Rico Henze, Andreas Wicht, Achim Peters, Oliver Benson and myself resulted in a publication[15] and are presented in this chapter.

4.2 Properties of spherical microresonators

The resonances in dielectric spheres and microspheres have been widely explored [79]. In the following sections the main optical properties are introduced in order to provide a background for sensing applications. The selection of topics is limited to aspects related to the work presented here.

4.2.1 General properties of microresonators

In the following a set of parameters is introduced that is commonly used to characterize optical microresonators. These are the *quality factor*, the *free spectral range*, the *finesse* and also the *mode volume*.

Quality factor

The quality factor (or Q factor) is a key parameter to describe the losses in a resonator [61]. It is defined as

$$Q = 2\pi \frac{\text{stored energy}}{\text{energy loss per cycle}}.$$

This means that a high-Q resonator has a rather small decay constant of its stored energy. In the context of optical resonators this relates to the photon storage time, τ, within the resonator for a given resonance frequency, ν_0, so that

$$Q = 2\pi\nu_0\tau = \frac{\nu_0}{\Delta\nu} = \frac{\lambda_0}{\Delta\lambda}.$$

By considering the time-frequency uncertainty $\Delta\nu \cdot \tau = \frac{1}{2\pi}$ the quality factor can be related to a spectral line width (FWHM) $\Delta\nu$ in frequency space. This can also be expressed in terms of the wavelength, as shown above. Thus, very narrow resonances correspond to high quality resonators. A rigorous derivation of these relations can be found, for instance, in [61].

There are different factors that influence and limit the total observable Q factor. It can be decomposed in

$$\frac{1}{Q_{\text{total}}} = \frac{1}{Q_{\text{mat}}} + \frac{1}{Q_{\text{WGM}}} + \frac{1}{Q_{\text{sur}}} + \frac{1}{Q_{\text{cont}}} + \frac{1}{Q_{\text{cou}}} \tag{4.1}$$

where Q_{mat} are losses in the resonator material, Q_{WGM} is due to scattering losses due to the curved resonator, Q_{sur} is related to surface imperfections, Q_{cont} are contaminations of the surface or even of the resonator dielectric and, finally, Q_{cou} are losses due to coupling.

Very high Q factors of up to 10^9 for silca spheres have been reported [80]. The spherical and toridal microresonators investigated in this work have Q factors in the range from $10^5 - 10^6$. This corresponds to photon storage times of up to 0.4 ns at 780 nm.

Free spectral range

Another important parameter of a resonator is the free spectral range, which describes the spectral distribution of the modes supported by the resonator. The frequency spacing between two modes of a simple Fabry-Pérot resonator is given by $c/(\textit{optical path length})$ where c is the speed of light. This can easily be extended to a spherical resonator by,

$$\nu_{\mathrm{fsr}} = \frac{c}{2\pi\, N_s\, a_s}, \tag{4.2}$$

where a_s is the radius of the sphere and N_s the index of refraction for the material of the sphere. This is a good approximation in the ray-optics picture for the free spectral range, however, for a precise result Mie theory [81] has to be applied. For high-Q modes an effective refractive index, N_{eff}, can be used in equation (4.2) to take care of the confinement of the optical mode below the surface of the resonator.

The polystyrene spheres used in this work are 31 μm and 50 μm in diameter. The corresponding free spectral ranges are 1.9 THz and 1.2 THz. At 780 nm this corresponds to 3.9 nm or 2.4 nm.

Finesse

The finesse of a resonator describes the number of photon roundtrips per decay time of the photon in the resonator. Equivalently, the finesse describes to what extent the neighboring resonances overlap due to their finite linewidth and thus how well individual modes can be distinguished. This quality is reflected by the ratio of the free spectral range to the linewidth, as

$$\mathcal{F} = \frac{\nu_{\mathrm{fsr}}}{\Delta\nu} = Q\frac{\nu_{\mathrm{fsr}}}{\nu_0}. \tag{4.3}$$

The finesse of spherical dielectric microresonators is inherently very large due to the high Q factors and large free spectral ranges. This makes them very attractive for applications, as optical filters, microlasers, or as a tool in cavity quantum electrodynamics (CQED, cf. chapter 5.1.1) experiments, to name just a few. The spherical resonators used here have finesses up to 5000.

Mode volume

Finally, the mode volume describes the volume of an optical mode inside the resonator. It is of special interest for microresonators since the field is contained within such a small volume so that non-linear and QCED effects are strongly enhanced as discussed in chapter 5.1.1. The mode volume is [16]

$$V_{mode} \approx \frac{\left(\int_V \epsilon(\vec{r})|E|^2 d^3\vec{r}\right)^2}{\int_V |E|^4 d^3\vec{r}} \tag{4.4}$$

where the $\epsilon(\vec{r})$ is the dielectric constant of a homogeneous, isotropic material at the point $\vec{r}$, V is the integration volume, and $\vec{E}$ the electric field.

4.2.2 Optical modes in spherical resonators

This section describes the field distributions of the optical modes supported by a dielectric sphere. A selection of different distributions are presented in order to illustrate the properties of this class of resonators.

Scalar mode solution

In general, the fields describing the resonance modes in spheres are vector fields. However, the orientation of the polarization in the direction of propagation can be assumed to be constant. For an air clad silica sphere of 25 μm it has been shown numerically [82] that 99.8 % of the energy contained in a mode is confined either in the E_θ or H_θ component. This percentage increases for larger spheres. Based on this argument a valid approximation is to use a scalar and separable representation for the solution of the spherical Helmholtz equation. Thus, the components of the fields E_θ (TE) or H_θ (TM) are given in spherical coordinates (r, θ, ϕ) by

$$\Psi_{l,m,n}(r,\theta,\phi) = C\psi_r(r)\psi_\theta(\theta)\psi_\phi(\phi), \tag{4.5}$$

with mode numbers l,m,n. The radial modes are denoted by n. The azimuthal mode number, l, describes the number of complete wave periods contained within a roundtrip along the mode. The polar mode number is given by m. There exist a maximum of $2l-1$ possible values of m. Since for a perfect sphere all m mode resonances are degenerate, this results in a maximum degeneracy of $2l-1$ for a given l. Due to residual eccentricity of real polystyrene resonators this degeneracy is lifted, as will be discussed in section 4.2.3.

In the case of the optical modes, additionally the polarization state p has to be considered, i.e. TE or TM modes. Thus a set of four mode numbers (n, l, m, p) can be used to describe a particular resonance.

The solution of the individual components can be found [82] as

$$\begin{aligned}
\psi_\phi(\phi) &= \exp[\pm im\phi] \\
\psi_\theta(\theta) &= \exp\left[-\frac{m}{2}\theta^2\right] H_{l-m}(\sqrt{m}\theta) \\
\psi_r(r) &= \begin{cases} j_l(kN_s r) & r \le a_s \\ j_l(kN_s R_0)\exp[-\alpha_s(r-a_s)] & r > a_s \end{cases}
\end{aligned}$$

The coefficients are

$$\begin{aligned}
C &= \{\sqrt{\frac{\pi}{m}} 2^{l-m-1}(l-m)! a_s^2 [\left(1+\frac{1}{\alpha_s a_s}\right) j_l^2(kN_s a_s) \\
&\quad - j_{l-1}(kN_s a_s) j_{l+1}(kN_s a_s)]\}^{-1/2} \\
\alpha_s &= \sqrt{\beta_l^2 - k^2 N_e^2} \qquad \beta_l = \frac{\sqrt{l(l+1)}}{a_s} \qquad k = \frac{2\pi}{\lambda}.
\end{aligned}$$

The exact solution of the polar dependance involves the associated Legendre Polynomials P_m^l. For small polar angles $\theta \approx 0$, as relevant to the experiments presented here, P_m^l can be represented by the Hermite polynomials H_{l-m}. The radial distribution inside the sphere with refractive index N_s is described by the spherical Bessel function j_l. Outside of the sphere (i.e. $r > a_s$) the field decays exponentially from the sphere in the radial direction with the constant α_s. Such an exponentially decaying field is an evanescent field. The refractive index of the environment surrounding the sphere is given by N_e. C is a normalization constant found by the volume integral $\Psi^2_{n,l,m}$ over all space divided by the equatorial path length $2\pi a_s$. Finally, the resonance frequency of the individual modes has to be found. This topic is dealt with in more detail in the following section 4.2.3.

For completeness, the characteristic equation belonging to the introduced scalar field representation is given by $(p\,\alpha_s + \frac{l}{a_s}\, j_l(kN_s a_s) = kN_s j_{l+1}(kN_s a_s)$, where $p = 1$ ($p = N_s^2/N_e^2$) for the TE (TM) modes. The characteristic equation is found by matching the tangential fields outside and inside at the sphere's surface.

Mode field distribution

In the remaining part of this section different properties of the resonator modes are illustrated by plotting them based on the introduced representation.

Figure 4.2 (a) shows the electric field across the equatorial plane of the resonator as the mode propagates close to the surface along the curvature of the sphere. The individual field maxima and minima are clearly visible and the resonance condition is conserved as, in this case, the field reproduces after it has propagated for 25 wavelengths. In a geometric optics picture this can be understood as a ray that is contained in the sphere and is totaly internally reflected at the boundary from the sphere to the surrounding vacuum. This plot also nicely illustrates, the analogy to a *whispering gallery* as was observed by Lord Rayleigh [65] in the gallery of St. Paul's cathedral in London for the propagation of a sound wave along its gallery (cf. figure 4.1 (a)). The black circle in the plot indicates a cut through the equatorial plane of the sphere. Here, the evanescent field protrudes from the sphere outwards into the vacuum. This effect is even more evident in figure 4.2 (b) showing the second radial mode of the sphere.

A plot of the radial intensity distribution of the WGM with $n = 1$ for polystyrene spheres with a diameter of 31 μm, one of the diameters used in the experiments, can be found in figure 4.3 (a). Here, the evanescent field is shown in gray. In Figure 4.3 (b) the intensity distribution for the $n = 5$ mode is plotted. As the radial mode number increases the highest intensity of the mode is more and more concentrated towards the center of the sphere.

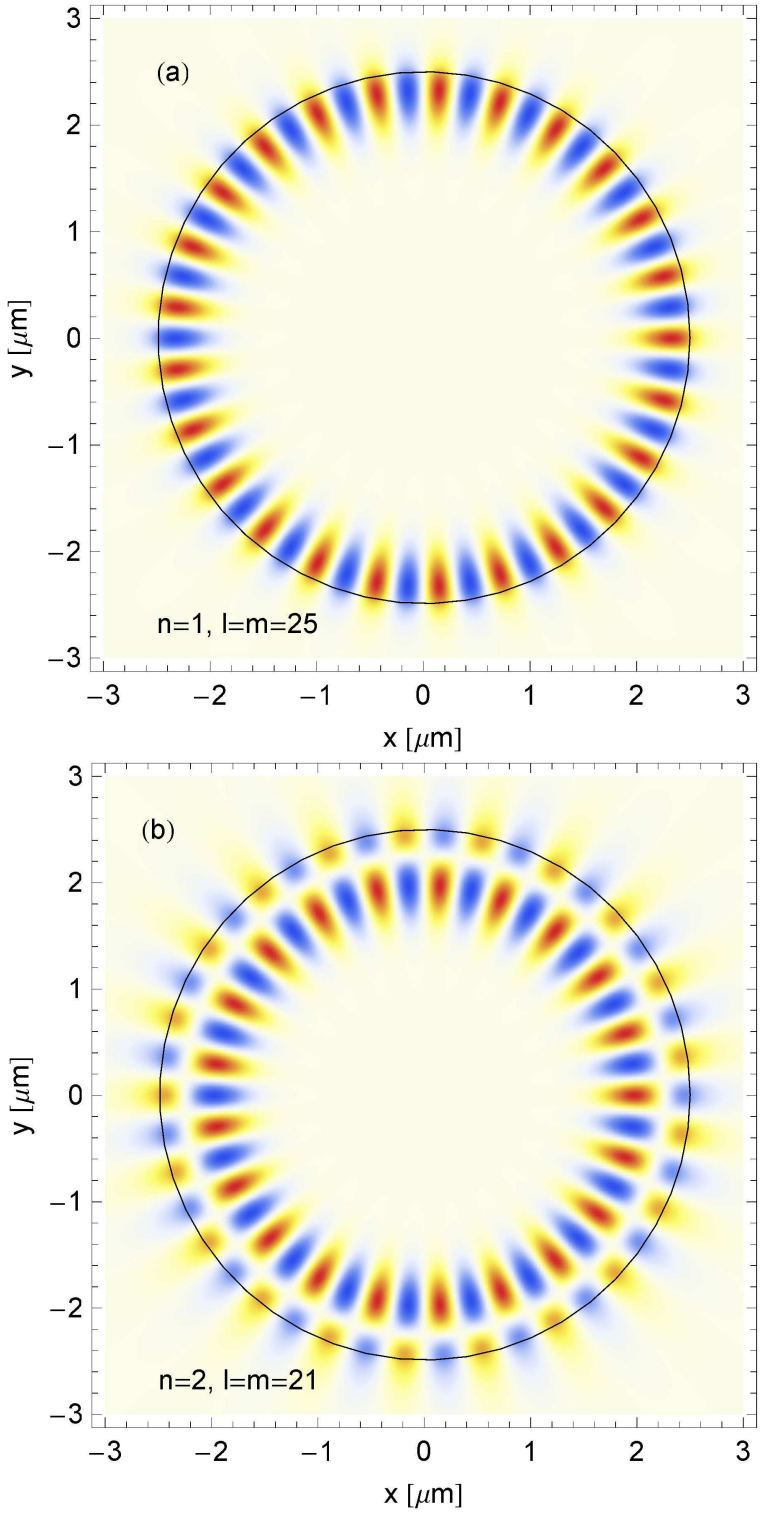

Figure 4.2: Electric fields E_θ (and H_θ) across the equatorial plane for a polystyrene sphere ($N_s = 1.578$) 5 μm in diameter in vacuum ($N_e = 1$). (a) $n = 1, l = m = 25$ (fundamental mode, WGM), (b) $n = 2, l = m = 21$. The black circle indicates the dimension of the sphere. The color code represents the strength and orientation of the electrical field in arbitrary units on a linear scale. Field-free regions are drawn in white.

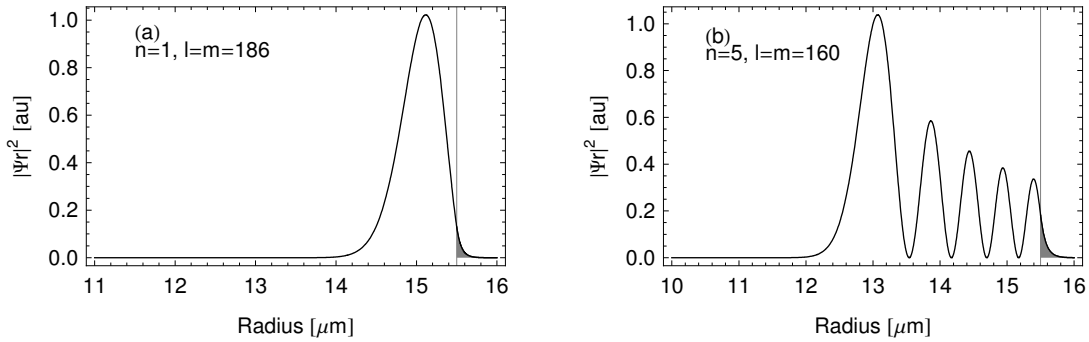

Figure 4.3: Radial field intensity $|\psi_r(r)|^2$ for a polystyrene sphere ($N_s = 1.578$) 31 μm in diameter in vacuum. (a) $n = 1, l = m = 186$, (fundamental mode, WGM), (b) $n = 5, l = m = 160$. The thin vertical line indicates the surface of the sphere. The evanescent field is shaded in gray.

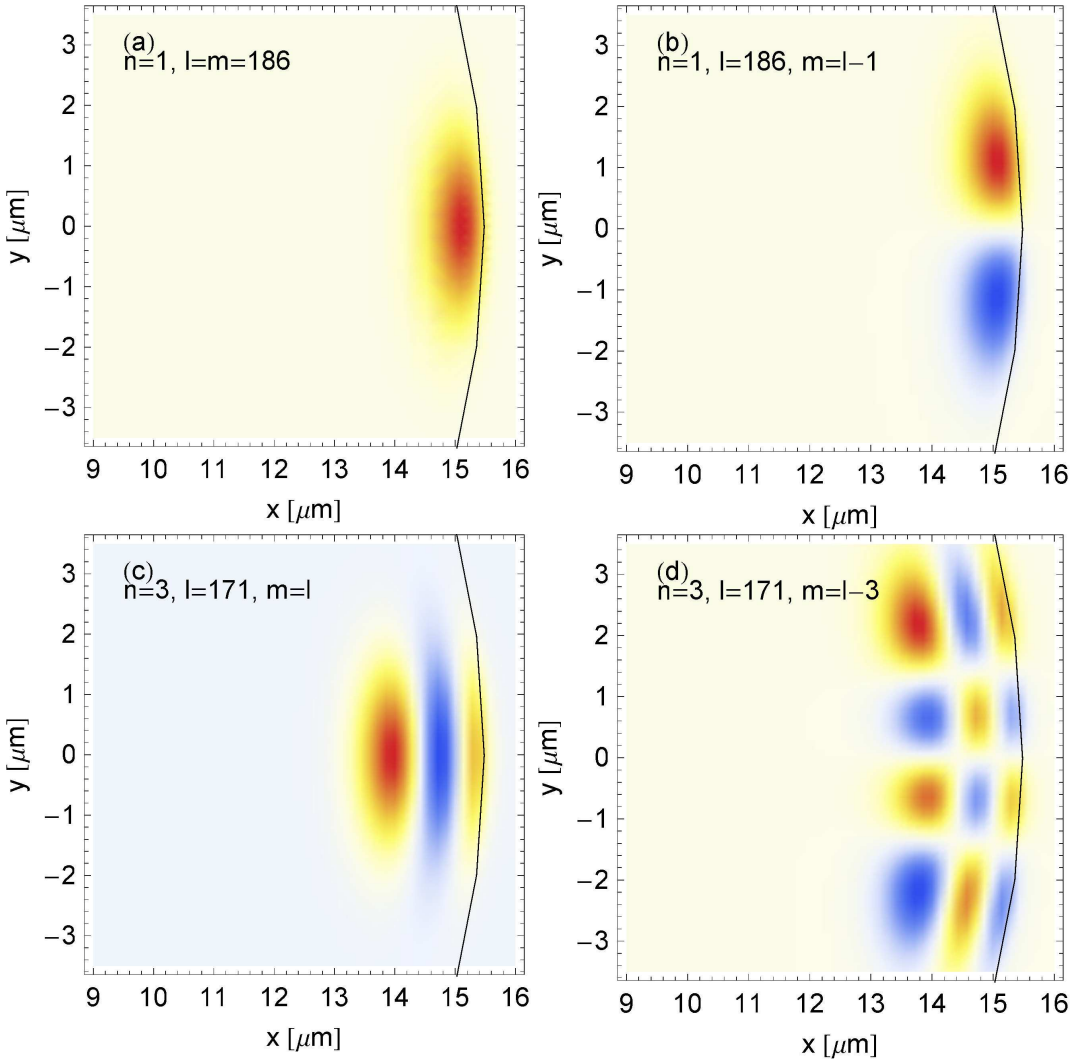

Figure 4.4: Electric fields E_θ (or H_θ) across the polar plane for a polystyrene sphere ($N_s = 1.578$) 31 μm in diameter. (a) $n = 1$, $|m| - l = 0$ (fundamental mode), (b) $n = 1$, $m - l = -1$, (c) $n = 3$, $m - l = 0$, and (d) $n = 3$, $m - l = -3$. The color code represents the strength and direction of the electrical field in arbitrary units on a linear scale. Field-free regions are drawn in white.

Finally, it is instructive to look at the polar dependance of the optical modes. The mode with $n = 1$, $l = m$ is called the *fundamental mode* as it possesses the smallest mode volume and the highest Q factor. However, as mentioned, this mode is frequency degenerate for a perfect sphere. Thus as $|m|$ decreases more and more polar mode components develop. This is illustrated in figure 4.4 (a) and (b). The lower two plots in figure 4.4 (c) and (d) show the mode structure as the radial mode number is increased. The optical fields become rapidly more complex.

4.2.3 Spectral properties of spherical resonators

In the previous section the mode distribution was introduced based on a separable scalar solution. However, in this section a vectorial solution will be presented studying the properties of the resonance frequencies. This is necessary since approximations, like the one made in the previous section tend to become imprecise for smaller ($< 20\,\mu$m) spheres, which are of interest for sensing applications.

Vectorial mode solution

The scattering of plane waves off dielectric spheres has been of great interest since the early studies by Mie [81] that formed the basis for the investigation of a number of light scattering phenomena. The scattering amplitude can be expanded as [83]

$$\frac{2}{x^2}\sum_{l=1}^{\infty}(2l+1)(|a_l|^2+|b_l|^2), \tag{4.6}$$

where the scattering coefficients are given by

$$a_l = \frac{j_l(x)[\tilde{N}xj_l(\tilde{N}x)]' - N^2 j_l(\tilde{N}x)[xj_l(x)]'}{h_l^{(2)}(x)[\tilde{N}xj_l(Nx)]' - N^2 j_l(Nx)[xh_l^{(2)}(x)]'} \tag{4.7}$$

and

$$b_l = \frac{j_l(x)[Nxj_l(Nx)]' - j_l(Nx)[xj_l(x)]'}{h_l^{(2)}(x)[Nxj_l(Nx)]' - j_l(Nx)[xh_l^{(2)}(x)]'}. \tag{4.8}$$

Only the relative refractive index $\tilde{N}$ has to be considered given by $\tilde{N} = N_{\text{sphere}}/N_{\text{environment}} = N_s/N_e$. The variable x is known as the size parameter given by $x = 2\pi a_s N_e/\lambda$, where a_s is sphere radius. l is the azimuthal mode number. j_l denotes the spherical bessel function and $h_l^{(2)}$ is the second order Hankel function.

The scattered spectrum shows narrow resonance peaks corresponding to the WGM modes (c.f. section 4.2.2) inside the sphere. These resonance frequencies can be found as they correspond to the poles of the coefficient a_l and b_l. This leads to the transcendental characteristic equation

$$\frac{[\tilde{N}xj_l(\tilde{N}x)]'}{j_n(\tilde{N}x)} = \frac{[xh_l^{(2)}(x)]'}{h_l^{(2)}(x)} \tag{4.9}$$

for the magnetic mode (TM) and

$$\frac{[\tilde{N}xj_l(\tilde{N}x)]'}{N^2 j_n(\tilde{N}x)} = \frac{[xh_l^{(2)}(x)]'}{h_l^{(2)}(x)} \tag{4.10}$$

for the electric mode (TE). For a given azimuthal number l and relative refractive index $\tilde{N}$ it is possible to find the corresponding size parameter x, which might be complex. The real part is associated with the resonance frequency, whereas the imaginary part describes scattering losses of the resonator [83, 84]. Thus, it corresponds to the linewidth of the resonance and, therefore, the Q factor. There might be more than one solution to these equations. The n^{th} root is associated with the radial mode number n of the sphere. Thus it is appropriate to consider $x_l^{(n)}$.

In figure 4.5 (a) and (b) the first complex poles are shown corresponding to the TM and TE WGM, respectively, with $n = 1$ for a polystyrene sphere ($N = 1.578$). The plots illustrate that the Q factor for

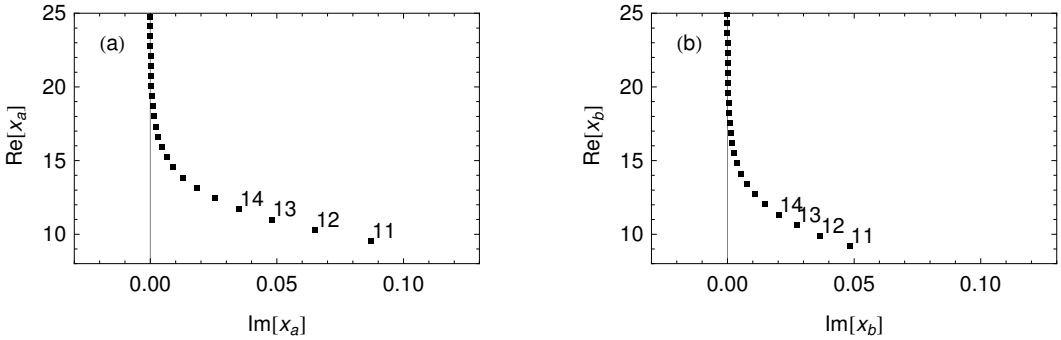

Figure 4.5: Complex poles of the scattering amplitudes a_l (a) and b_l (b), as given by equation (4.9) and (4.10). The numbers indicate the solution for a given mode number l for the radial mode number $n = 1$ at $N = 1.578$.

the TM are smaller compared to the corresponding TE Mode. The important feature to notice is that the size parameter for spheres with mode number $l < 25$ start to have larger complex components, which results in smaller Q factors due to diffraction losses caused by the high curvature of small spheres. This has to be taken into consideration as a limiting factor for the resulting sensitivity of a sensor system. Thus, $x \approx 20$ at 780 nm corresponds to sphere sizes smaller than 5 μm, when diffraction losses have to be considered. A more comprehensive discussion of the derivation, vectorial field distributions and observed optical effects associated with Mie scattering in dielectric spheres can be found in [85, 86, 76].

Asymptotic approximation

The calculation of the resonance frequencies based on the Mie scattering theory, as introduced in the previous section, can be quite cumbersome and numerically involving. Alternatively it has been shown that the resonance frequency can be expanded in an asymptotic expansion in powers of $(l + 1/2)^{-1/3}$ [87, 88]. The first eight terms of this expansion are listed by Schiller [89]. The relative accuracy for modes $l > 50$ is better than 10^{-4}.

The size parameter, $x_l^{(n)}$, for the radial mode n and azimuthal mode l is given by

$$x_l^{(n)} = \frac{l+1/2}{\tilde{N}} - \frac{\zeta_n}{\tilde{N}} \left(\frac{l+1/2}{2} \right)^{1/3} + \sum_{k=0}^{k_{max}} \frac{d_k(\tilde{N}, \zeta_n)}{(l+1/2)^{k/3} (\tilde{N}^2 - 1)^{(k+1)/2}}, \tag{4.11}$$

where ζ_n is the n^{th} zero of the Airy function. The relative refractive index $\tilde{N}$ is defined as in the previous section to be $\tilde{N} = N_s/N_e$. The first coefficients of the expansion are listed in appendix D. As in the previous section, the resonance frequencies can be calculated by considering $\nu_l^{(n)} = x_l^{(n)} c/(2\pi N_e a_s)$ for the size parameter $x_l^{(n)}$

Modesplitting for imperfect spheres

So far only the special case of a perfect sphere has been considered. However, the chemically grown polystyrene spheres are not perfectly symmetric and the process of manually attaching the spheres to tapered fibers results in further deformation. Therefore it is a good approximation to consider the polystyrene spheres as spheroidal with an eccentricity $\epsilon = (a_{pol} - a_{eq}) \cdot 3/(a_{pol} + 2a_{eq})$, where a_{pol} is the polar and a_{eq} the equatorial radius of the spheroid. The $(2l - 1)$ mode degeneracy is lifted and the resonance frequency is given by [90]

$$\frac{\Delta\nu_{n,l,m}}{\nu_{n,l,m}} = \frac{\epsilon}{6} \left[\frac{3m^2}{l(l+1)} - 1 \right] \tag{4.12}$$

For $l \gg 1$ and if $l - |m|$ is small the spacing between the individual m-modes can be considered to be nearly constant and scales with the eccentricity of the spheroid and l, as $\Delta\nu \approx \epsilon\nu_{n,l,m}/l$. For a prolate spheroid ($\epsilon > 0$) the resonance frequency increases, and decreases for an oblate spheroid ($\epsilon < 0$).

The microspheres investigated in this work lie within equidistant frequency spacing range considering that $l \approx 186$ and 304 for a sphere 31 μm and 50 μm in diameter at 780 nm.

4.2.4 Efficient optical fiber taper coupling to spherical microresonators

The optical mode structure of spherical resonators has been introduced in the previous section. In order to be able to excite these optical modes a waveguide has to be coupled to the resonator. This is achieved by placing a fiber taper close to the sphere. A thorough physical insight into this coupling process is of crucial importance for the performance of the resonator system.

Simple coupled-cavity model

A simple scalar model describing a ring cavity coupled to a waveguide may be used to gain a deeper understanding of the coupling parameters and the shape of the resonances.

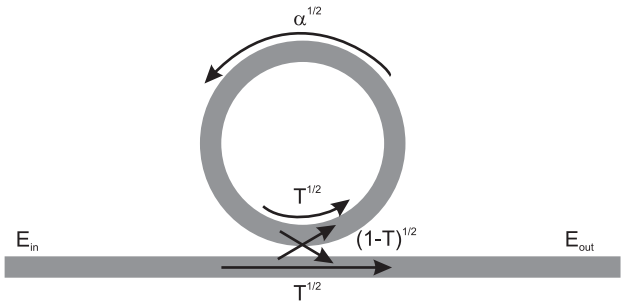

Figure 4.6: Simple model of a ring cavity coupled to a waveguide.

Figure 4.6 shows an illustration of a simple coupled-cavity model. The electric field transmission across the coupling junction is denoted by $\sqrt{T}$, while the coupling into and out of the cavity is given by $\sqrt{1-T}$ and a phase shift of π is to be considered. The resonator loss is expressed by the round-trip transmission constant α. The acquired phase for a round-trip is ϕ.

The transmission through the system can now be calculated by summing over the electric field coupled back into the waveguide for the consecutive round trips as [91]

$$\frac{E_{out}}{E_{in}} = \sqrt{T} - \frac{1-T}{\sqrt{T}} \sum_{j=1}^{\infty} \left(\sqrt{\alpha\, T} e^{i\phi}\right)^j,$$

where j denotes the round trip number. A closed form of the electric field transmission can be found by rewriting the sum as a geometric series leading to

$$\frac{E_{out}}{E_{in}} = \frac{\sqrt{\alpha\, T} e^{i\phi} - T}{\sqrt{T}(\sqrt{\alpha\, T} e^{i\phi} - 1)}.$$

The transmitted power through the waveguide-coupled resonator system is then given by

$$P_T = \left|\frac{E_{out}}{E_{in}}\right|^2 = \frac{\alpha + T - 2\sqrt{\alpha\, T}\cos(\phi)}{1 + \alpha\, T - 2\sqrt{\alpha\, T}\cos(\phi)},$$

where the round trip phase, ϕ, is given by $\phi = 2\pi \frac{NL}{\lambda}$ and thus P_T depends on the wavelength, λ, the cavity length, L, the cavity transmission, α, and the coupling quality in form of the transmission T. This expression is equivalent to the results presented by Cai *et al.* [91].

A plot of the transmission through the coupled resonator system is shown in figure 4.7. It can easily be seennthat the solid transmission curve corresponds to a higher Q factor compared to the dashed and dotted transmission curve. An expression of the finesse of the system is given by [91]

$$\mathcal{F} = \frac{4\sqrt{\alpha T}}{(\sqrt{\alpha T} - 1)^2}$$

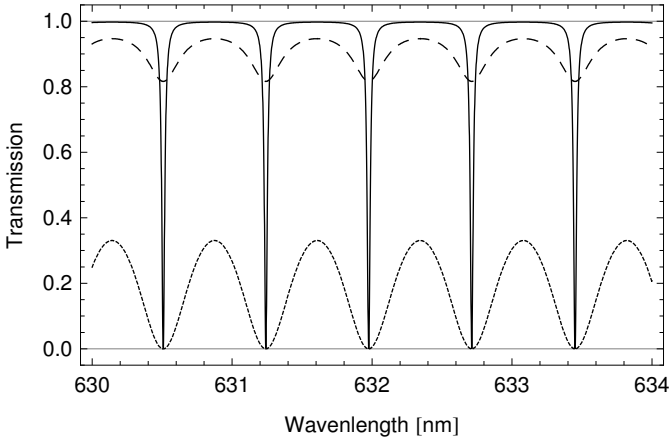

Figure 4.7: Transmission through a simple waveguide-coupled silica ring resonator of 120 μm in diameter using $\alpha = 0.9$, $T = 0.9$ (solid), $\alpha = 0.9$, $T = 0.1$ (dashed) and $\alpha = 0.1$, $T = 0.1$ (dotted).

and shows clearly that the finesse of a coupled resonator system depends on the loss within the resonator, but at the same time on the coupling strength to the cavity, as can be confirmed in figure 4.7. This result is in agreement with equation (4.1) for the total Q factor taking into account the individual contributions.

The model has a caveat, as it assumes that the fields within the resonator couple exclusively to a single mode of the waveguide. This, however, may not be necessarily the case if the waveguide supports multiple modes. The particular case when the resonator couples to a single mode within a multimode waveguide is called *ideality* and has been studied for a taper-coupled microsphere system in detail [10].

The transmission plots in figure 4.7 also nicely illustrate *critical coupling*, which is reached if the transmission through the waveguide drops to zero. This is the case, when the electric field coupled back out of the resonator into the waveguide exactly cancels the field within the waveguide. The coupling parameter K is introduced as [91],

$$K = 1 - \frac{(\sqrt{T} - \sqrt{\alpha})^2}{(1 - \sqrt{T\alpha})^2}.$$

Critical coupling is reached for $K = 0$. A system with $K > 1$ is called *over-coupled* and a system with $K < 0$ is called *under-coupled*. In both cases, the transmission does not drop to zero.

In order to reach critical coupling in an experiment, the distance between the waveguide and the resonator may be varied in order to change the coupling T, since the loss within the resonator, α, is an intrinsic parameter of the cavity and may not be changed as easily. The optimal distance has been investigated in much detail for a fiber taper coupled microsphere [91].

Phase matching

The coupling coefficient, κ, between the waveguide and the resonator is given in the simple model by $(1 - T)$. In order to calculate this value accurately from first principles the mode overlap between the waveguide and the resonator has to be determined. In the case of a high-Q resonator the coupling coefficient is small. Thus, it can be assumed that the modes in the waveguide and resonator are unperturbed and the optical coupled mode approach [92] is suitable. The coupling coefficient is given by the following overlap integral

$$\kappa_{s,f} \propto \int_A \left(N_f^2 - N^2(\vec{r})\right) \vec{E_s} \cdot \vec{E_f}\, dA \tag{4.13}$$

where $\vec{E}_{f,s}$ represents the unperturbed optical modes of the fiber taper and the resonator, respectively. $N^2(\vec{r})$ denotes the refractive index profile of the composite system. The integration is performed over the cross-sectional area. This approximation assumes an invariant cross-sectional coupling geometry, neglecting the curvature of the spherical resonator. One aspect of the overlap integral is the phase relation between the fields inside the sphere and the fiber taper. In order to maximize the integral the

propagation constant for the fiber β_f and the sphere β_s have to be equal. This requirement is called *phase matching* and can be rewritten as

$$\beta_f - \beta_s = \Delta\beta = 0. \tag{4.14}$$

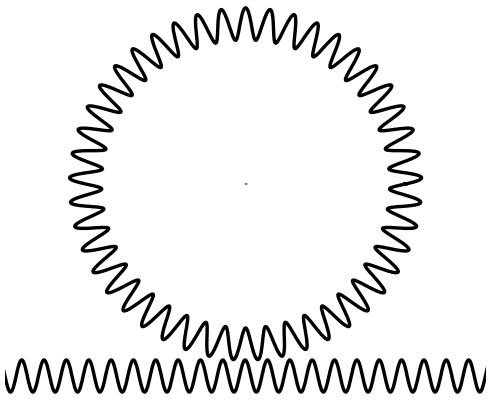

Figure 4.8: Illustration of phasematching process between the resonator's and taper's phase [93].

An intuitive illustration of phase matching is shown in figure 4.8. The mode propagating in the fiber and inside the sphere are represented by sine-waves. The fields inside the resonator and the waveguide are phase matched. This can easily be confirmed by observing the coinciding phases at the coupling region. However, the illustration also hints at the problems arising in phasen matching a straight waveguide to a curved resonator geometry. Perfect alignment of the phases is only given for the point of smallest distance between waveguide and resonator. Starting form this point, the phase matching degrades for the remaining coupling region. In order to account for this effect the phase matching condition for curved resonator design [94, 93] can be approximated by

$$\beta_{\mathrm{eff,s}} \simeq \beta_{\mathrm{s}} \left(1 - \frac{a_f}{4a_s}\right), \tag{4.15}$$

where a_f and a_s are the radii of the taper waist and sphere, respectively. It is assumed that the waveguide and the resonator are in contact.

Figure 4.9 (a) shows the calculated effective refractive indices, N_{eff}, for the first three radial modes of polystyrene microspheres as a function of the sphere's diameter. Based on these effective refractive indices the required taper diameter can be found. The phase matching condition can be restated as N_{eff} as $\beta = (2\pi N_{eff})/\lambda$. The refractive indices for pure polystyrene and silica are represented by thin gray lines. The fiber diameter for the simple, uncorrected phase matching (i.e. $N_{\mathrm{eff},f} = N_{\mathrm{eff},s}$) can be determined by matching $N_{\mathrm{eff},s}$ in figure 4.9 (a) to $N_{\mathrm{eff},f}$ in figure 2.5. Only the fundamental WGM modes ($n = 1$) of spheres with a diameter $< 20\,\mu$m have an effective refractive index of $N_{eff} < 1.44$. This illustrates the limits of phase matching between two different materials with different refractive indices.

The required phase matching taper diameters are shown in figure 4.9 (b). The curved geometry is taken into consideration by solving the transcendental equation (4.15). The results suggest that perfect phase matching between the fundamental fiber mode HE_{11} and the fundamental WGM ($n = 1$) is only possible for very small spheres with $2a_s < 9\,\mu$m. Phase matching for higher radial modes ($n > 2$) is possible for larger spheres. However, in this case the overlap of the electric fields may be the limiting factor (and not the phase matching) since confinement of the modes is higher (cf. figure 2.7 and figure 4.3).

In conclusion, perfect phase matching of the fundamental modes of the fiber taper and spheres with the size used in the experiments in this thesis (i.e. $31\,\mu$m and $50\,\mu$m) is not possible. In section 4.5.1 it is experientially shown that the coupling efficiency and losses within the resonator still allow for nearly critical coupling of certain resonator modes. This indicates that the overall coupling strength, $\kappa_{s,f}$, given by the overlap integral is not limited by imperfect phase matching. A detailed numerical analysis based on coupled mode theory for the particular coupled-resonator geometry would be needed to investigate the influence of the phase matching and the mode overlap in more depth.

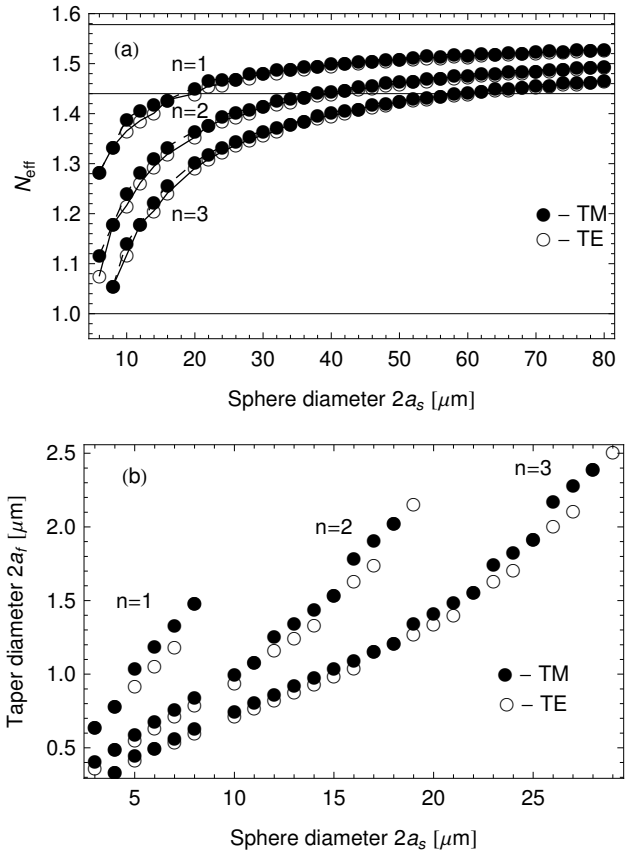

Figure 4.9: (a) Effective refractive index N_{eff} of the first three radial modes of a polystyrene sphere using equation (4.11). The horizontal lines indicate the refractive indices of air ($N \approx 1$), silica ($N = 1.44$) and polystyrene ($N = 1.59$). (b) Fiber taper diameter required to phase-match a polystyrene microsphere. The fundamental mode HE_{11} is matched using equation (4.15) to the spherical modes shown in (a).

Contact coupling for ellipsoidal resonators

In the previous section it was argued that coupled mode theory can be used to calculate the coupling strength, $\kappa_{s,f}$. These calculations are beyond the scope of this thesis. Nevertheless, it is instructive to look at some results obtained by this method. Humphrey *et al.* [95] used coupled mode theory to calculate the coupling coefficient for a microspherical resonator made from silica. The sphere is in contact with the fiber taper and slightly prolate. This is exactly the configuration of the microresonator system investigated in this thesis with the only difference being the material. Figure 4.10 shows the calculated mode spectrum. The mode splitting due to the eccentricity of the sphere is clearly visible. Additionally, the varying coupling strength for the split modes is shown. The results are very intriguing, since they agree qualitatively very well with the experimental results discussed in the following sections (cf. section 4.5.2, in particular).

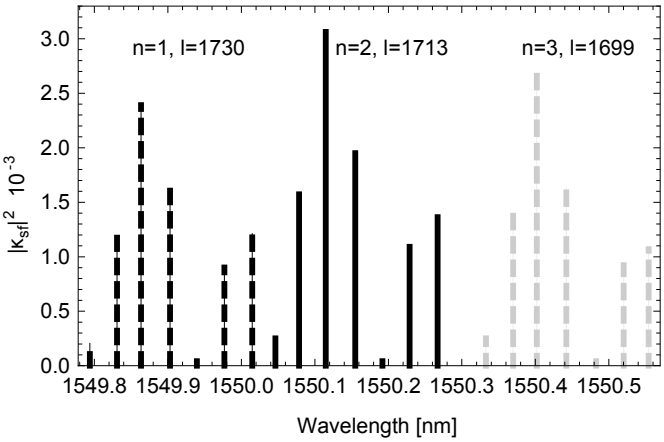

Figure 4.10: TE mode spectrum of contact-coupled taper-microsphere resonator system. The $n = 1$, $l = 1730$ (dashed) and $n = 2$, $l = 1713$ (solid) and $n = 3$, $l = 1699$ (dashed, gray) modes are shown. $a_s = 300\,\mu$m, $a_f = 1.68\,\mu$m, prolate sphere $\epsilon = 0.29$, $\theta_{off} = \pi/76$. Reproduction from reference [95].

4.3 Theoretical considerations for sensing applications

In the previous section, theoretical foundations of spherical microresonators were laid. In the following these concepts are applied to sensing applications.

4.3.1 Temperature sensing

Frequency stability as a function of the temperature is of great importance for resonator systems. In this respect microresonator systems have a great advantage due to their size. They have the potential to be very stable since such a small volume can easily be temperature controlled to high degree of precision.

Shifts in the resonance frequency of the resonator are caused by small changes in the optical path length of the resonator mode. There are two parameters influencing the optical path length, ℓ, and, therefore, the resonance frequency of a microspherical resonator as the temperature changes. The linear thermal expansion coefficient, α, determines the overall change in size of the sphere. The other parameter is the change in refractive index, β, with the temperature.

A simple argument can be made to estimate the temperature-dependent relative resonance frequency shift $\Delta\nu/\nu_0$ of a resonator. The resonance frequency ν_0 is given by considering the integer number of wave periods m contained inside a resonator of length ℓ by $\nu_0 = mc/\ell = mc/(2\pi d_0 N_0)$. Based on this, the relative shift is given by [14]

$$\frac{\Delta\nu}{\nu_0} = -\frac{\Delta d}{d_0} - \frac{\Delta N}{N_0}. \tag{4.16}$$

The change in the diameter of the sphere and the change in the refractive index can be described as,

$$d = d_0 + \Delta d = d_0(1 + \alpha \Delta T), \tag{4.17}$$
$$N = N_0 + \Delta N = N_0 + \beta \Delta T. \tag{4.18}$$

By substituting equation (4.17) and equation (4.18) into equation (4.16) the expression for the frequency shift as a function of temperature change is obtained

$$\frac{\Delta \nu}{\Delta T} = \left(-\alpha - \frac{\beta}{N_0} \right) \nu_0. \tag{4.19}$$

It is worth noting that the temperature-dependent frequency shift does not depend on the size of the resonator, but only on the material properties, like the linear expansion and the change in the refractive index at a give frequency ν_0. At first, this result seems to be counterintuitive, since larger resonators should experience a larger absolute change in the resonator length and should, therefore, experience a larger frequency shift.

Figure 4.11 illustrates why this is not the case. It shows two spherical resonators where the left resonator has half the diameter of the right one. A WGM is sketched as a sine-wave inside the resonator. It is important to note that the wavelength for both indicated WGMs is the same. The change in size with temperature of the right resonator will be twice as large as for the left resonator. However, the total number of wave periods l contained inside the resonator is also twice as large. Therefore, the change in length per period is the same in both cases and is independent of the absolute size of the resonator.

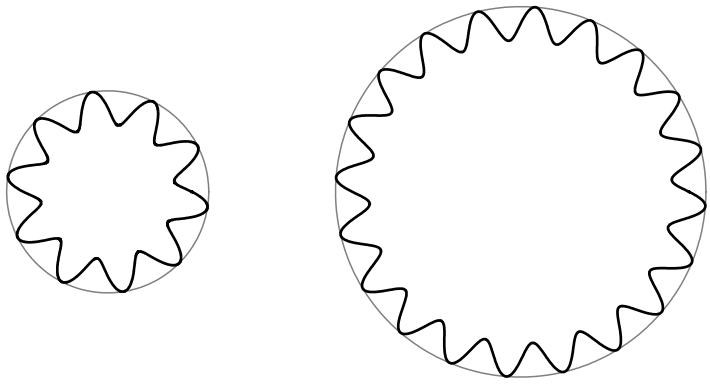

Figure 4.11: Illustration of the independence of the resonance shift from the diameter of the resonator. The wavelength of the WGM modes (sine-waves trapped inside the resonator) is the same for both resonators. The diameter of the right resonator is twice the diameter of the left resonator and, therefore, contains twice as many wave periods.

Obviously, this approximation is only valid if the optical path length of a spherical resonator scales linearly with its diameter. The mode distribution of a WGM in small spheres extends outside the resonator due to the large curvature and a linear relation is no longer valid. In these cases one has to resort to a calculation of the precise resonance frequency for different temperatures based on the asymptotic approximation introduced in equation (4.11). Theoretical curves are shown in figure 4.12. For different sphere sizes and modes the frequency shift for a change in temperature of 1 K is calculated. The temperature dependent frequency shift does not scale linearly with the size of the sphere, as expected. However, $\Delta\nu/\Delta T$ is nearly constant for larger spheres. The line in the plot indicates the value of 3.475 GHz/K calculated using equation (4.19). The difference between this value and the asymptotic approximation of the Mie theory for a large sphere of diameter 250 μm is smaller than 0.5%. By using the Mie approximation the resonance shift for the polystyrene spheres used in this experiment of diameter 50 μm and 31 μm is 3.32 GHz/K and 3.37 GHz/K, respectively.

An additional interesting point to investigate is the linearity of the frequency shift with temperature. Figure 4.13 (a) shows the calculated resonance frequency of a 31 μm sized sphere for a temperature range relevant to the experiment in this chapter. For this temperature range the frequency shift can

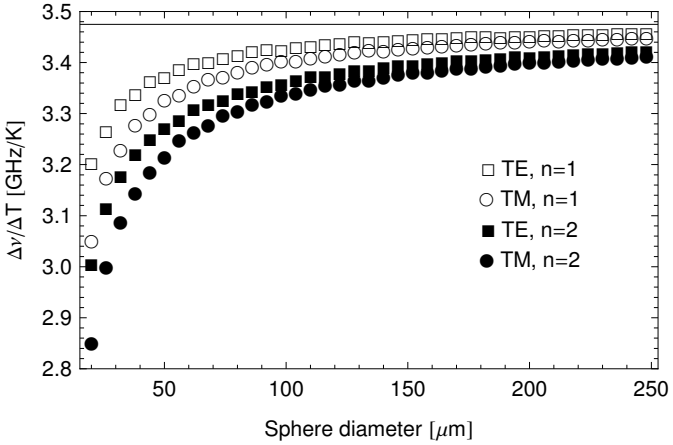

Figure 4.12: The variation of the coefficient for the thermal induced frequency shift $\Delta\nu/\Delta K$ for a polystyrene sphere with different diameters. The line at 3.475 GHz/K indicates the limit for very large spheres as calculated by equation (4.19) and evaluated for polystyrene (cf. table 4.1).

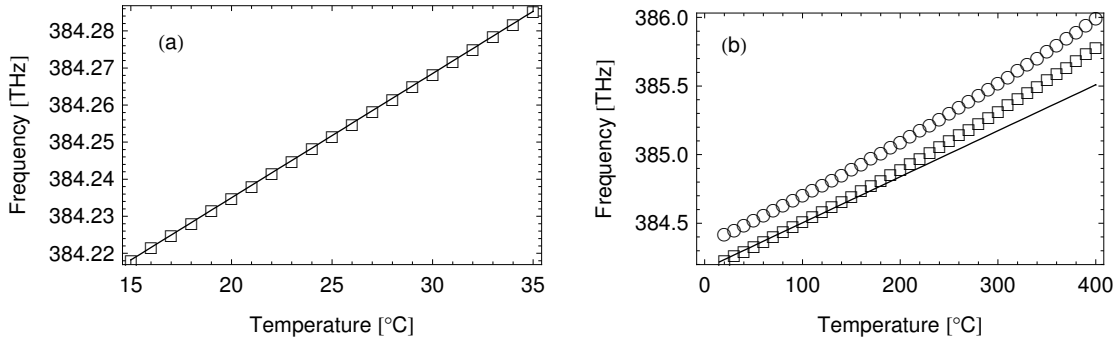

Figure 4.13: (a) Temperature-dependent frequency shift of the $n = 1, l = 187$ (TE) mode for a polystyrene sphere with a diameter of 31 μm. (b) Temperature-dependent frequency shift for $n = 1, l = 187$ (TE) mode (squares) and $n = 1, l = 306$ (TE) polystyrene sphere with a diameter of 50 μm (circles). The solid line indicates the linear limit with a slope of 3.35 GHz/K.

Table 4.1: Theoretical values for the temperature induced resonance shift for silica, PDMS, and polystyrene based on equation (4.19) at 780 nm.

material	α [K^{-1}]	β [K^{-1}]	N_0	$\Delta\nu/\Delta T$ [GHz/K^{-1}]
silica [14]	$6. \times 10^{-7}$	8.5×10^{-6}	1.45	-2.48
polydimethylsiloxane [96]	2.7×10^{-4}	-1×10^{-4}	1.41	-76.5
polystyrene	(6.7 ± 0.1) $\times 10^{-5}$[98]	$-(1.2 \pm 0.05)$ $\times 10^{-4}$[99, 100]	1.578 ± 0.001 [97]	3.475 ± 1.3

be considered to be linear. However, in figure 4.13 (b) it becomes obvious that frequency shift with temperature is not linear, in general.

Table 4.1 shows the numerical results based on equation (4.19) for silica, PDMS and polystyrene. For silica and polystyrene the calculated values for $\Delta\nu/\Delta T$ are in the range of a few GHz/K. A shift in this order of magnitude can easily be measured and makes silica and polystyrene attractive materials for temperature sensing. The promising material PDMS has been included for reference, as the application for temperature sensing has been shown using a toroidal microresonator geometry [96].

4.3.2 Thermal conductivity sensing

Even though the polystyrene microresonators used in these experiments are optically transparent in the visible spectrum, there exists some residual absorption. This leads to a pronounced heating of the sphere when laser light is coupled into a WGM [101, 102, 103].

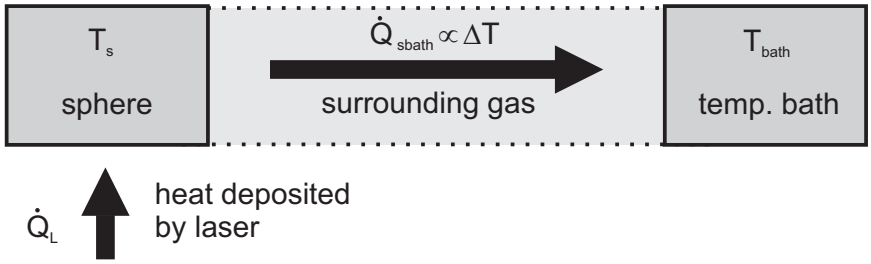

Figure 4.14: Schematic of the heat transfer from the laser to the sphere, to the surrounding gas and then to the temperature bath that is kept at constant temperature.

Figure 4.14 illustrates the heat flow in our system schematically. The absorption of the pump light launched into a mode of the microspherical resonator causes a heat transfer $\dot{Q}_L$ to the sphere. The deposited heat is dissipated to the surrounding environment at a rate of $\dot{Q}_{sbath}/A$ per given area A, which depends on the thermal conductivity k_{th} of the surrounding gas. In steady state a certain temperature gradient $\Delta T/s$ across a given length s is maintained. Due to energy conservation, i$\dot{Q}_L = \dot{Q}_{sbath}$, from which follows

$$\dot{Q}_L = k_{th}\frac{A}{s}\Delta T. \tag{4.20}$$

This means the temperature of the sphere is a linear function of the pump power depending only on the thermal conductivity k_{th} as A/s is constant for a given resonator. Exploiting now the pronounced sensitivity to temperature changes, as discussed in the previous section, the thermal conductivity of the gas surrounding the sphere can be determined. By changing the laser power, the heating rate $\dot{Q}_L$ can be adjusted. The temperature change ΔT can be measured by observing the resonance shift of a WGM. Then, it is possible to deduce changes of the thermal conductivity k_{th} of the surrounding gas. Since A/s cannot be measured the resulting values of k_{th} have to be calibrated to the conductivity of a known gas.

4.3.3 Heuristic model for nonlinear thermal effects within microspherical resonators

In the previous section heating effects due to absorption within the microresonator have been introduced and a steady state for the heating rate was assumed. In the following, however, non-linear, non-stationary thermal effects on the resonance lineshape will be discussed based on a heuristic model.

Non-linear thermal effects have been studied in more detail by Schmidt *et al* [104] using a taper coupled silica microsphere. A set of coupled differential equations describing the temperature and optical fields of the sphere separately as the laser is scanned across a resonance have been used. These equations depend on quite a large number of different parameters, like mode volume, coupling efficiency, Q factor, absorption efficiency, etc. Additionally to the nonlinear thermal effects the influence of nonlinear optical effects, namely the Kerr effect, have been studied. Schmidt *et al* were able to show that it is possible

to distinguish the non-linear optical and thermal effects, based on the resonance lineshape at different wavelengths and sweeping speeds of the probe laser.

In the following, a qualitative model for the influence of the thermal heating effects on the resonance lineshape is developed. It is based solely on the dynamic temperature change of the sphere. This model is in particular valid for spheres with low Q factors. The temperature of the sphere as a function of the time $T_s(t)$ can be described by a differential equation

$$C_s \frac{\mathrm{d}T_s(t)}{\mathrm{d}t} = -k_{th}\, T_s(t) + \kappa\, L\left[v_\nu\, t, (\Delta\nu/\Delta T)\ T_s(t)\right]. \tag{4.21}$$

The change in the temperature $\frac{\mathrm{d}T_s(t)}{\mathrm{d}t}$ is given by the dissipation of heat to the environment (1^{st} term) and the absorption of heat as the laser is swept across the optical resonance (2^{nd} term). In particular, C_s is the heat capacity of the sphere, k_{th} is the thermal conductivity of the gas surrounding the sphere, v_ν is the sweeping speed of the probing laser, κ describes the heat coupling efficiency into the resonator, which is proportional to the optical mode coupling strength, and the laser power, and $\Delta\nu/\Delta T$ is as introduced in chap. 4.3.1. Close to the resonance of the WGM a larger amount of heat is introduced to the sphere compared to an off-resonance situation. This is accounted for by considering a Lorentzian resonance lineshape L of the form

$$L(\nu, \nu_0) = \frac{\left(\frac{1}{2}\Gamma\right)^2}{(\nu - \nu_0)^2 + \left(\frac{1}{2}\Gamma\right)^2}, \tag{4.22}$$

where the FWHM linewidth is given by Γ for a resonance centered at ν_0. $L(\nu, \nu_0)$ quoted here is normalized to $L(\nu, \nu_0) = 1$ for $\nu = \nu_0$ which is slightly different compared to the conventional form of the Lorentzian lineshape.

A solution to the differential equation is plotted in figure 4.15. The plots (a) and (c) show the time evolution of temperature of the sphere as the laser is scanned across a resonance for two differen scan directions. The dotted line indicates the heat Q_L deposited by the laser as the heat flux is proportional to the shape of the optical resonance. The solid line is the numerical solution for the sphere's temperature $T_s(t)$ based on the differential equation (4.21). The arrows in the diagram indicate the thermal frequency shift direction of the sphere and the frequency scan direction. In figure 4.15 (a) the directions coincide, which results in a strong heating of the sphere, as the optical resonance shifts with the scan of the laser. The absolute heating time is increased. The opposite is the case if the direction of the resonance shift and laser scan are opposite, as shown in 4.15 (c).

If the time evolution of the temperature of the sphere, $T_s(t)$, is known, it can be used to calculate the temperature dependent transmission Θ through the fiber taper coupled microresonator system

$$\Theta(\nu) = 1 - L\left(\nu, (\Delta\nu/\Delta T)\ T_s(\nu/v_\nu)\right). \tag{4.23}$$

The resulting resonant lineshapes are shown in the lower plots of figure 4.15 (b) and (d) as a solid line. Figure 4.15 (b) corresponds to the case where the laser scan direction and the direction of temperature-dependent resonance shift coincide, discussed in plot (a). It can be seen that the resonance width increases strongly and it becomes asymmetric compared to the temperature independent resonance, shown as the dasehd line for reference. A similar observation applies to figure 4.15 (d) corresponding to the second case, discussed in plot (c), where the the laser scan direction and the direction of temperature-dependent resonance shift are opposite. Here, however, the resonance linewidth is reduced due to the relative smaller passing time of the laser scan and temperature shift.

Finally, the potential of this effect for possible sensing applications is investigated. In figure 4.16 the expected optical resonances for different thermal conductivities are plotted. The plots (a) and (b) show the expected asymmetric lineshape for the coinciding and opposite scan and shift direction, respectively. The decreasing thermal conductivity results in a stronger non-linear thermal effect. This shows that this effect is sensitive to the thermal conductivity. However, it also shows the limitations for sensing approaches based on the observation of lineshape, since the lineshape depends non-linearly on the thermal conductivity and also a variety of different parameters. It would be difficult to isolate the effect of the thermal conductivity, while controlling the other parameters efficiently.

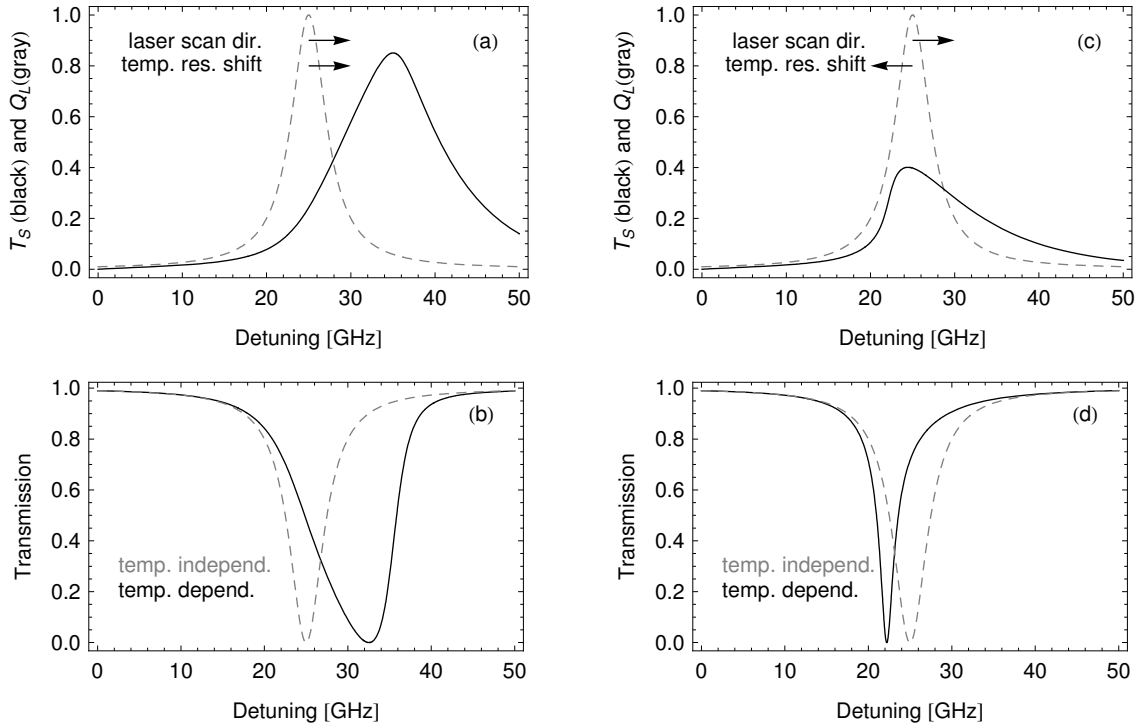

Figure 4.15: (a) and (c) deposited heat Q_L (dashed) and the calculated temperature (equation (4.21)) of the sphere (solid). The arrows in the plot indicate the relative direction of the laser frequency scan and the temperature induced resonance drifts. In (a) the directions coincide and in (b) they are opposite. (b) and (d) are the corresponding optical resonance lineshapes (solid) taking the sphere's temperature calculated in (a) and (c), respectively, into account. The temperature independent resonance (dashed) is shown for reference. The simulation parameters are: $\Gamma = 5\,\mathrm{GHz}$, $C_s = 2\,\mathrm{J/K}$, $k_{th} = 0.35\,\mathrm{W/K}$, $\kappa = 0.35\,\mathrm{GHz/s}$,$v_\nu = 1\,\mathrm{GHz/s}$ and $\Delta\nu/\Delta T = \pm 10\,\mathrm{GHz/K}$. The resonance frequency ν_0 is offset to 25 GHz.

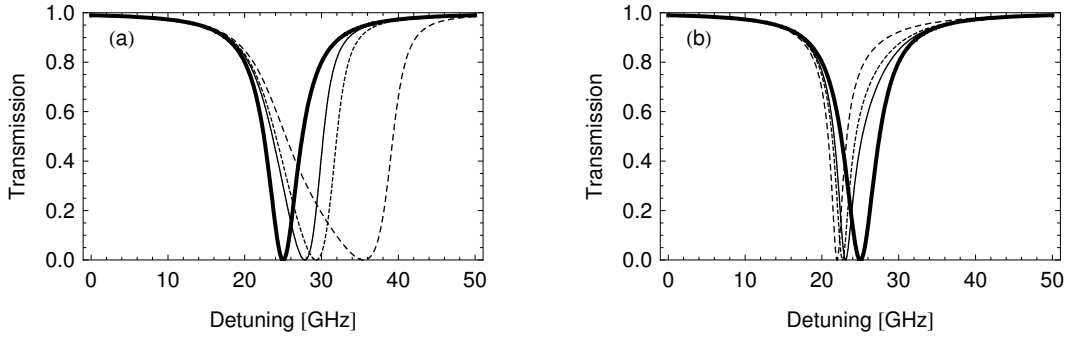

Figure 4.16: Optical resonance lineshape for different thermal conductivities k. (a) The laser frequency shifts in the same direction as the thermal induced drift of the resonance and in plot (b) the directions are opposite. The thermal conductivity k is chosen to be $1\,\mathrm{W/K}$(solid), $0.6\,\mathrm{W/K}$(dashed), and $0.2\,\mathrm{W/K}$(long dash). All other parameters are as quoted in the caption of figure 4.15. The thick line shows the temperature independent resonance for comparison.

4.3.4 Refractive index sensing

A different sensing approach is based on the idea of detecting changes in the refractive index of the material surrounding the sphere. The resonance frequency depends strongly on the relative refractive index N_s/N_e . Resonance shifts can be recorded with high precision and speed, which makes this technique very appealing for sensing applications. Such approaches have been shown to work for resonators submerged in liquids [68] or biomolecule sensing using high-Q resonators [13, 69].

In this section the feasibility of gas sensing based on refractive index sensing is discussed. The results obtained in section 4.2.3 are numerically evaluated for small changes in the surrounding refractive index. This allows one to gain an overview of the influence for the different parameters involved and also allows for an estimation of the expected resonance shift. Figure 4.17 shows the relative resonance shift, $\Delta\nu/\Delta N_e$, for spheres of different sizes as the refractive index, N_e, is changed from 1.000 (vacuum) to 1.001.

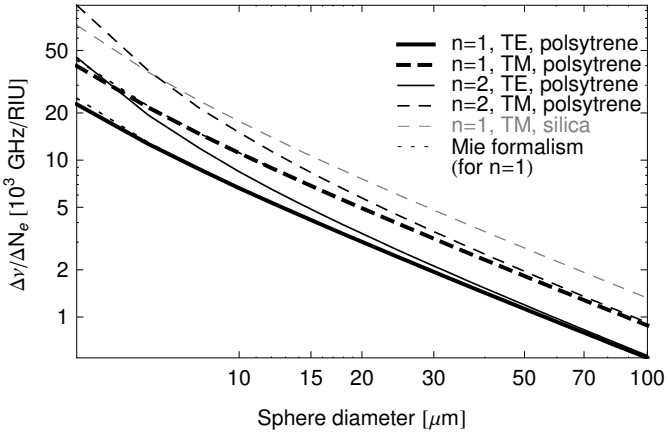

Figure 4.17: Relative resonance shift $\Delta\nu/\Delta N_e$ for a change in the refractive index from $N_e = 1.000$ to 1.001 dependent on the diameter of the sphere. The different parameters for the individual curves are displayed in the plot legend. The dotted curve (called Mie formalism in the plot legend) uses the more precise formalism for calculating the resonance frequency based on the Mie theory introduced in chapter 4.2.3. A difference to the asymptotic approximation can only be observed for $2a_s < 5\,\mu$m.

The following qualitative conclusion can be drawn with respect to a larger frequency shift and increased sensitivity for sensing applications. A higher sensitivity is obtained with:

- a smaller sphere diameter,
- a TM mode instead of TE mode,
- higher radial modes, and
- a material of low refractive index for the sphere.

However, the limiting factor is the Q factor as it determines the detection resolution of the resonance shifts. Thus, there is a trade-off, as smaller spheres and higher radial modes have lower Q factors.

Table 4.2: Refractive index [105] and thermal conductivity [106] for selected gases.

gas	k_{th} $[\mathrm{Wm^{-1}K^{-1}}]$	N
helium	0.1567	1.000035
argon	0.0179	1.000281
air	0.0262	1.000277

Finally, it is interesting to investigate the order of magnitude for the resonance change expected for the experimental setup considered in this work. In table 4.2 the refractive indices for a selection of gases are listed. The absolute change in refractive index for the two gases used in the experiments, i.e., going from argon to helium is $\Delta N = 0.246 \times 10^{-3}$ RIU (refractive index units). This results in resonance frequency shifts of 277 MHz (TE, $n = 1$) and 449 MHz (TM, $n = 1$) for a polystyrene sphere of 50 μm in diameter. For a 31 μm sphere this results in 460 MHz (TE, $n = 1$) and 749 MHz (TM, $n = 1$).

A more sophisticated refractive index sensing approach is to detect *relative* changes between individual modes instead of measuring the *absolute* shift of a single mode. The great advantage is that other effects influencing the absolute position of the resonance frequency, like thermal shifts, cancel out. In this respect, it is important to consider the relative shifts for TE and TM modes and modes for spheres of different size. For instance, the difference in the relative shift between the TE ($n = 1$) and TM ($n = 1$) for a 31 μm sphere is about 172 MHz. The same idea can also be applied to two modes of different spheres attached to the same taper.

4.4 Experimental methods

4.4.1 Optical setup for measuring whispering gallery modes

The central tool for measuring the resonance properties of the microresonators is a tuneable laser with a narrow linewidth. Such a laser is coupled into the fiber taper to which a microsphere is attached. Optical resonances in the sphere can be investigated by tuning the laser frequency and monitoring the transmission through the microsphere coupled resonator system. A schematic of the experimental setup illustrating the optical components is shown in figure 4.18.

A suitable class of lasers for these kind of experiments are external cavity diode lasers (ECDL). These lasers are commercially available in a variety of wavelengths. The laser used here (Velocity TLB-6312, New Focus, USA) can be coarse tuned from 765 nm to 781 nm. Additionally, it is possible to fine tune the laser mode-hope-free for 75 GHz while maintaining a linewidth of less than 300 kHz. This is achieved by rotating the end mirror of the external cavity resonator while keeping the grating within the resonator, as a wavelength selective element, fixed. This external resonator design is called the Littman-Metcalf [107, 108] configuration. A dc motor and a piezo actuator are attached to the rotating mirror for coarse and fine tuning, respectively. The ECDL has a fine tuning bandwidth of up to 2 kHz. For a continuous linear frequency scanning of the laser frequency a voltage ramp is applied to the piezo.

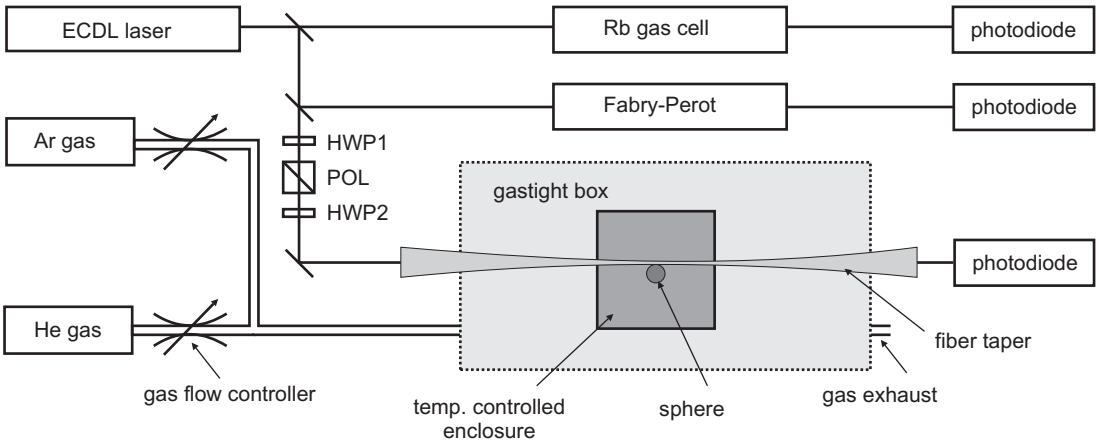

Figure 4.18: Experimental setup consisting of the optical components for measuring resonance shifts of the microresonator, the enclosures for the taper coupled microsphere and the gas mixing and delivery system. HWP and POL are abbreviations for a half-wave plate and polarizing beamsplitter, respectively.

The sensing approach is based on the absolute shifts of microresonator resonances. Therefore it is very important to measure the position of these resonances with a high degree of accuracy, which is limited by the frequency precision of the probing ECDL. A Fabry-Pérot interferometer is used to monitor

the linearity of the frequency scan and the atomic absorption in a rubidium gas cell is employed as an absolute frequency reference.

The Fabry-Pérot (FP) interferometer consists of two plane parallel mirrors with a reflectivity 90 % at 770 nm (PR770/90/AR, Laser Components GmbH, Germany). The mirror substrates are one inch in diameter and are placed in mirror mounts. In order to increase the stability of the interferometer the mirror mounts are connected by an optical cage system (Thorlabs GmbH, Germany). The interferometer is further thermally isolated from the optical table by a fiber glass reinforced stand and housed in a two centimeter thick enclosure of foamed polystyrene. The distance between the mirrors is 138.9 ± 0.1 mm, which results in a free spectral range of 1.079 ± 0.001 GHz. The theoretical finesse for a FP interferometer with reflectivities $R > 0.5$ can be approximated by $\mathcal{F} = \pi\sqrt{R}/(1-R)$. For $R = 0.9$ a maximal finesse of 29.8 can be expected. The theoretical value is rarely achieved due to mirror surface imperfection, non-perfect parallel alignment, a finite mirror size and other loss mechanisms. The linewidth of a single FP resonance was measured to be be 150 MHz (cf. figure 4.20) at 780 nm, which results in a finesse of 7.2. For our experiment a low finesse is of advantage, since the position of the resonance peaks can be resolved more precisely. The spectral resolution is about one order of magnitude higher than the linewidth of the FP peaks.

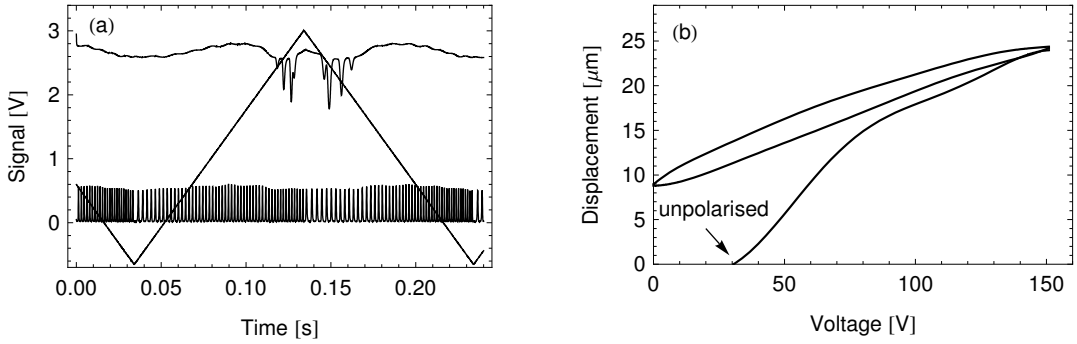

Figure 4.19: (a) Voltage ramp (solid line) and transmission signal through the FP (bottom) and the Rb cell recorded with a photodiode (top). (b) Hysteresis of piezo displacement as a function of the applied voltage for the piezo ceramic used in the ECDL [109].

The FP interferometer acts as a ruler in frequency space. Figure 4.19 illustrates the need for this tool nicely. The plot shows the unprocessed voltage signal of the piezo driving voltage ramp, the individual peaks of the FP transmission and the absorption of the Rb gas cell at the top. The hysteresis of the piezo results in a non-linear variation of the frequency with the applied voltage. This can be seen by the unequally spaced FP peaks and also by the nonsymmetrical Rb absorption depending on the laser scanning direction. In the following work all resonance spectra are linearized based on the individual position of the FP peaks.

In order to be able to compensate drifts of the probe laser an absolute frequency reference is needed. This can be achieved by employing an atomic resonance. In this experiment the absorption of a natural abundance of rubidium contained in a 5 cm long gas cell (Toptica AG, Germany) without any buffer gas is used. The gas cell was placed within a foamed polystyrene enclosed compartment on the optical table. The typical absorption spectrum is shown in figure 4.20. Four individual dips can be seen and are associated with the two isotopes in rubidium. The energy scheme of the resonance transition (D2-line) close to 780.24 nm [14, 110] is given in appendix E. The two absorption dips of each of the isotopes, ^{87}Rb and ^{85}Rb, are separated by 6.83 GHz and 3.04 GHz, respectively, as indicated in figure 4.20. The individual transitions of the subdivided hyperfine sub-level is not observed since the transitions are Doppler-broadened due to the thermal movement of the atoms in the cell. For instance, the weaker ^{85}Rb absorption has a full width at half maximum (FWHM) linewidth of about 650 MHz. The frequency precision given by this linewidth is sufficient for measuring absolute resonance shifts expected in the conducted experiments. If higher accuracy is required, Doppler-free spectroscopy may be used [110].

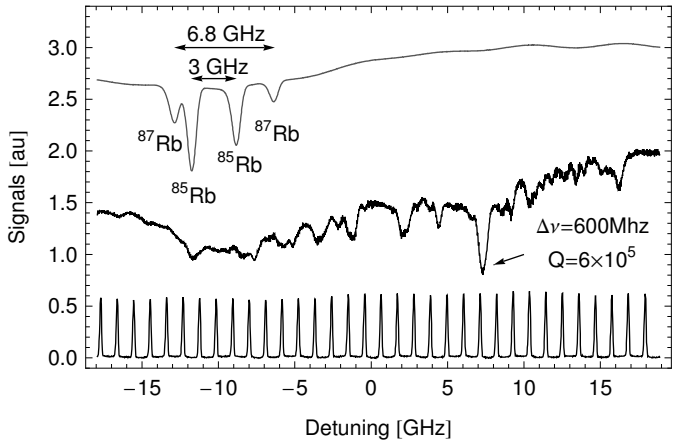

Figure 4.20: Transmission signals of the Rb gas cell (top), of the taper-coupled microresonator system (polystyrene sphere of 31 μm in diameter, taper diameter 1.2 μm) (middle), and of the plane-plane Fabry-Pérot interferometer (bottom).

Laser and Fabry-Pérot stability

The optical setup designed to measure resonance frequency shifts of microresonators can also be used to estimate the frequency stability of the FP interferometer and the probe laser itself.

Figure 4.21 shows the typical drift of the laser and the FP. The ECDL has a very good long term stability of 40 kHz/s. A voltage ramp with a frequency of 5 Hz is applied to the laser. This results in a single sweep time for measuring the resonance spectrum of 100 ms. The laser drift within this timeframe can be neglected. The same argument applies to the FP drift with a stability of 130 kHz/s. This is a good result, considering the simple design of the FP resonator and thermal insulation. The sampling rate for this measurement was 0.1 Hz. For investigating the stability at a higher bandwidth a laser lock technique is more suitable, but not necessary for the sensing approach introduced in this work.

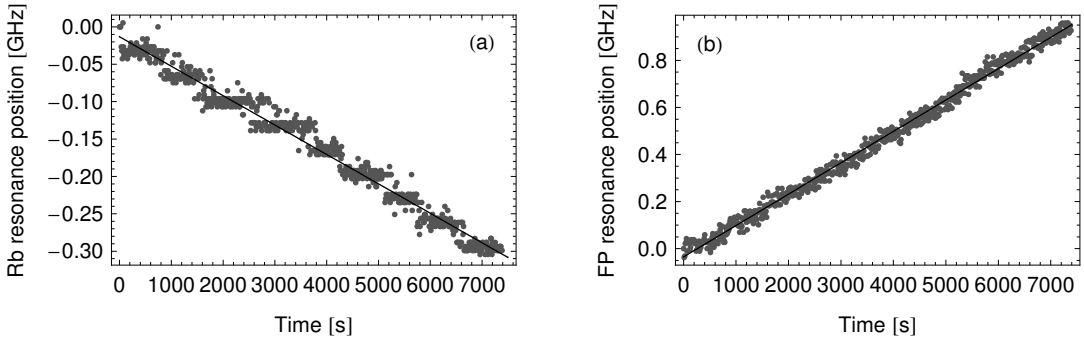

Figure 4.21: (a) Position of the rubidium dips corresponding to the absolute frequency drift of the ECDL laser. A drift of 40 kHz/s over a time period of 7000 s is observed. The steps of the measured frequency result from the finite resolution of the data acquisition equipment used. In (b) the drift of the FP interferometer is plotted for the same measurement. The drift is compensated for by the probe laser drifts. The resulting stability is of the order of 130 kHz/s over a period of 7000 s. Every 10 s a reading is taken.

4.4.2 Technique for attaching polystyrene microsphere onto optical fiber tapers

We use microspheres made from chemically grown polystyrene with diameters of 31 μm and 50 μm (Microparticles GmbH, Germany) which are dispersed in ethanol. A few drops of the dispersion are applied

onto a cover slide. After evaporation of the solvent individual spheres can be picked up from the remaining reservoir, as seen in figure 4.22(a). The optical quality of the individual spheres may vary. In particular surface contamination occurs due to residues dissolved in the ethanol. An indication of the quality can be gained by using a polarization filter in front of the reflected-light microscope (Olympus SZ11). The contrast of the ring structure around the individual spheres is enhanced for spheres with higher optical quality (cf. figure 4.22(b)).

For manipulation a specially formed glass tip is used. With the help of a focused CO_2 laser a standard glass fiber is formed to end with an acute tip (see figure 4.22 (c)-(e)). This fiber tip is mounted onto a manual three axis translation stage for precise positioning. An individual sphere from the cover slide can be picked up by slightly moving the fiber tip probe across the sphere until it sticks to the probe. The sphere can then be transferred in the same way onto an optical fiber taper. A tilted mirror indicated in figure 4.22 (d) and (e) facilitates observation during this procedure. Figure 4.22 (c) shows a 50 μm sphere attached to a taper of 1.2 μm in diameter.

For certain applications it is often necessary to tune a resonance to a particular frequency. For instance, in the experiments presented here it is desirable to tune a WGM resonance close to the atomic resonance frequency of rubidium. This can be achieved by carefully adjusting the position of the sphere on the taper using the fiber tip, while the resonance spectra are observed at the same time. This has proven to be a valuable approach of coarse tuning the resonator system. This tuning method relies on the eccentricity or imperfection of the sphere that results in small changes of the resonance frequency.

A photo of the setup during placement and manipulation of the spheres is shown in figure 4.22 (g). The taper is indicated as a dotted red line. The cover slide acting as a reservoir for the spheres is visible just in front of the taper. The fiber tip probe is connected to the 3D-positioning stage on the right side (outside of the picture). The microscope has been removed for this picture.

The taper-microresonator system proved to be robust against subsequent manipulation and transfer within the lab, and it remained in a stable configuration over weeks. The particular reason why a polystyrene sphere adheres to the fiber tip probe or even to the very thin fiber has not been completely resolved. During the manipulation electrostatic effects may play an important role. Long term adhesion has to be attributed to surface effects between the polystyrene and silica. The adhesion may be enhanced by a water film created by condensed water vapor from the surrounding air.

One of the great advantages of our pick-and-place approach is that multiple spheres of different sizes can also been attached to the same taper, as will be discussed in section 4.5.7.

4.4.3 Temperature control, containment box, and gas conditioning

The photo in figure 4.22 (g) shows the U-shape copper heater enclosure in the retracted position. The copper enclosure is temperature stabilized by a PID control loop using a PT100 temperature sensor and a peltier element placed underneath the enclosure. A piezo motor driven, linear translation stage is used to move the enclosure over the taper (cf. figure 4.22 (f)). An additional thin copper cover is placed onto the U-shaped copper heater in order to reduce any thermal effects due to convection. Small slits at the side allow the taper to enter the enclosure.

The entire taper-resonator system and the copper enclosure for the temperature control (see figure 4.22 (g) and (f)) is contained in a hermitically sealed box made of 1.5 cm thick perspex. The cover lid is only 3 mm thick allowing for a good optical access for the microscope. The base plate of the box is made from aluminium, acting as a breadboard for placing securely the optical and mechanical components within the box. It also provides the inlets for the gas which enters though four rows of mounting holes. The inner dimensions of the chamber are 17.8 cm $\times$ 15.9 cm $\times$ 11.3 cm.

The gas delivery systems are based on two standard pressure controllers that are directly connected to the gas cylinders allowing one to control the gas flows individually. The flow rate is determined by a set of electrical mass flow meters that were individually calibrated for argon and helium. A specific mass flow ratio is manually set by controlling the valves connected to the gas cylinders.

A gas flow rate of 0.4 l/min has proven to be suitable for

flushing the containment box. Here a trade-off has to be made, since a high gas flow rate would reduce the time taken to exchange the gas volume inside the box. This would improve the precision of the measurement, since the drifting time of the resonator is reduced. However, at the same time a high gas flow introduces unwanted turbulence to the system, degrading the stability of the system.

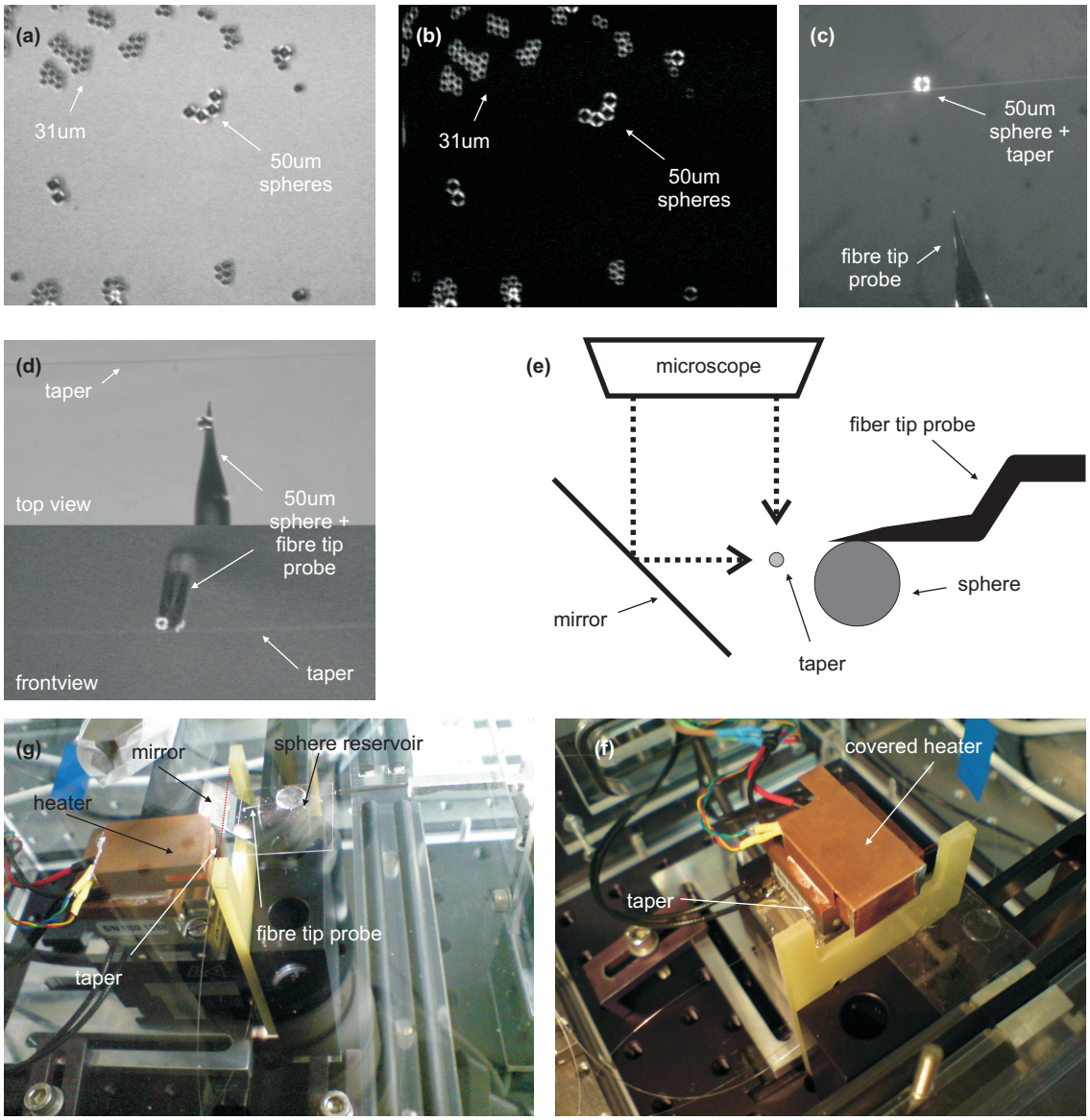

Figure 4.22: (a) 50 μm and 31 μm polystyrene spheres on a glass cover slide acting as a resonator reservoir. (b) The optical quality of the resonator can be estimated by using a polarization filter in front of the microscope lens as surface roughness or contamination results in a decreased scattering of polarized light. (c) Placed 50 μm sphere on 1.2 μm taper. (d) Top and front (horizontal) view using a 45 ° mirror behind the taper as indicated by (e). A 50 μm sphere is attached to the fiber tip probe. (f) Photo of experimental setup during placement of spheres. (g) Photo of the fiber taper enclosed by the heater and additional copper cover as used to perform optical resonance measurements. The taper is indicated by a dashed red line in the photos for clarity. Scale in the microscope images (a)-(d) can be estimated by the size of the individual spheres.

Finally, it is important to estimate the time taken to reach a target gas concentration for a given gas flow rate. A simple differential equation can be used to describe the gas concentration $c(t)$ in the chamber as

$$\frac{dc(t)}{dt} = \frac{\dot{R}_{in}}{V} c_{in} - \frac{\dot{R}_{in}}{V}. \tag{4.24}$$

The perspex box encloses a volume V of about 3.23 l. The gas flow rate into the box $\dot{R}_{in}$ is 0.4 l/min, which also has to be the out-flow rate, $\dot{R}_{out}$, due to mass flow conservation. For simplicity, a pure in-gas flow, for instance $c_{in} = 100\%$ helium, and an initial box concentration, i.e. $c(t = 0) = 0\%$ helium (100% argon), is assumed. This model also assumes that the flow rates are sufficiently low for the gas to form a homogenous mixture throughout the entire volume. For the presented experiments a minimal flushing time of 30 min is maintained for exchanging gas mixture ratios in the containment box. Now, it is possible by solving the equation to estimate the helium concentration after 30 min of flushing. The expected helium concentration is 97.6%. Thus, the resulting error in the gas mixture concentration for the conducted measurements can be neglected.

4.5 Experimental results

In this section the experimental results for the fiber taper coupled microsphere system are presented.

4.5.1 Spectra of TM and TE modes for an entire free spectral range

A frequency scan over multiple free spectral ranges of the investigated resonator is a valuable piece of information for gaining a better understanding of the coupling condition, mode structure and quality of the resonator.

In figure 4.23 the resonance spectrum of a 31 μm sphere in diameter can be seen. The spectrum is recorded by coarsely scanning the ECDL laser over a range of 16 nm. By rotating the HWP2 by an angle of 45 ° it is possible to excite the two orthogonal polarization modes of the sphere. The plot shows that is is possible to selectively excite the TM or TE modes of the sphere with a high contrast. However, at some places the coupling to the other polarization state can not completely be suppressed, for instance at 777.5 nm for the red polarization curve.

In general it is quite difficult to identify the individual modes precisely. It can be assumed that narrow resonances belong to the fundamental, $n = 1$, modes and then resonances with wider linewidths to higher radial modes. A clear identification of the modes is difficult, due to the facts that, firstly, the degeneracy of the $l - |m|$ modes is lifted because of the non-perfect spherical shape of the polystyrene bead and this results in a number of additional superimposing resonances. Secondly, the coupling to the individual modes may differ from mode to mode due to the geometrical alignment and the phasematching condition, which changes with wavelength.

However, a repeating structure can be identified for some modes. This has been indicated for the individual set of modes by different dashed vertical lines that are spaced by a free spectral range of 2.075 THz. Using this frequency spacing and the asymptotic approximation for the resonance frequencies (cf. section 4.2.3) it is possible to estimate the diameter of the sphere to be 29.7 μm. This size is still in agreement within 5% of the specifications considering fabrication tolerances and shrinkage due to drying of the polystyrene sphere.

In general, this result shows that a microsphere attached to fiber taper shows a promising mode-structure with clearly defined high-Q modes. The transmission contrast is surprisingly high for a contact coupled microresonator system. Some modes are almost critically coupled (i.e. at 771.2 nm), as discussed in section 4.2.4.

4.5.2 Typical resonance spectra of individual WGMs

A frequency scan for multiple free spectral ranges provides an overview of the mode spectrum of the resonator system, as discussed in the previous section. For an investigation of the development of individual features of the mode spectrum or resonance frequency shift with time this scanning method is too

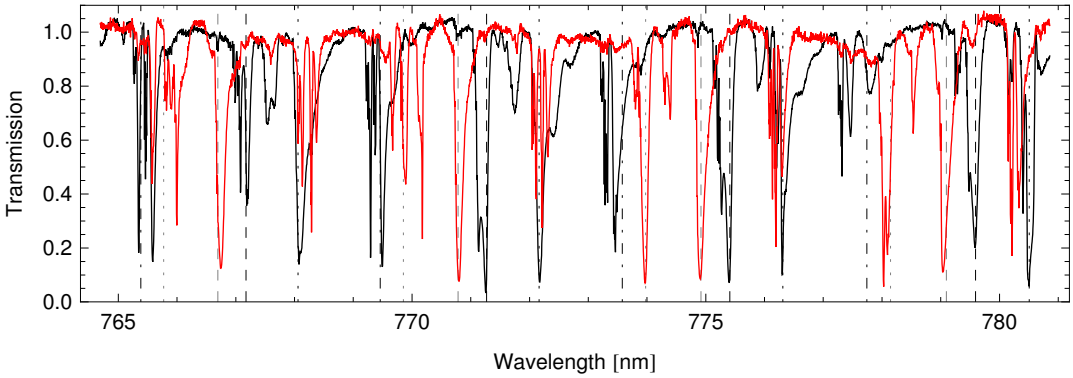

Figure 4.23: Transmission spectrum from a taper-coupled 31 μm polystyrene sphere for two orthogonally linear polarization orientations (black and red) coinciding with TM and TE modes of the sphere. Clearly a repetitive mode structure is visible (cf. differently dashed vertical lines). However, it is difficult to identify the individual modes. The distance between these lines corresponds to a free spectral range of 2.075 THz, which corresponds to a sphere diameter of 29.7 μm. The spectra are normalized to the taper transmission.

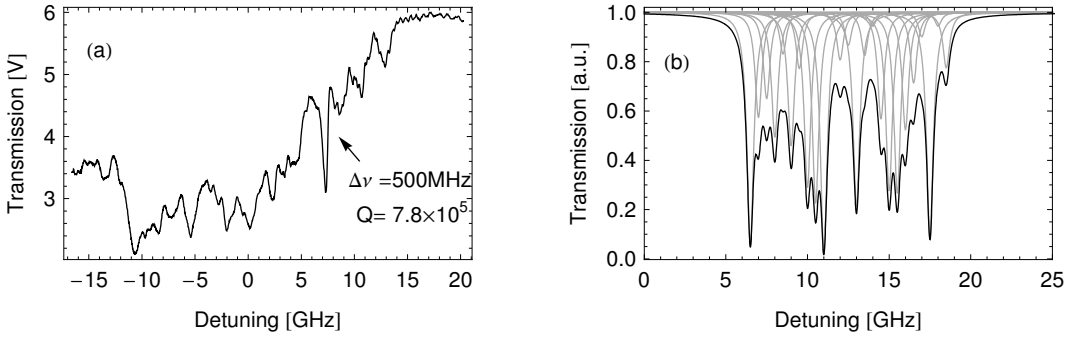

Figure 4.24: (a) Typical resonance spectrum of a 31 μm sphere attached to a taper. Small dips correspond to the nondegenerate $l - |m|$ modes. High-Q resonance with $Q = 7.8 \times 10^5$ is shown. (b) Illustration of 25 superimposed lorentzian lineshapes of 500 MHz linewidth with random coupling strength and equal frequency spacing.

imprecise. A more suitable option is to use the piezo-based scan mode of the laser since it provides a higher accuracy and bandwidth, as introduced in section 4.4.1.

Figure 4.24 (a) displays typical resonances for a polystyrene sphere attached to an optical taper. A particular high quality resonance with a Q factor of 7.8×10^5 is measured. A large number of additional smaller dips can be identified corresponding to the eccentricity split WGM resonances. An illustration of the theoretically complex spectrum can be seen in figure 4.24 (b). A number of equally spaced lineshapes with random coupling strength are plotted and superimposed, producing a mode structure that is qualitatively very similar to the observed spectrum.

Waterfilms on spheres

It is observed that the contrast of the mode structure degrades in time and this happens within hours up to days. This effect is attributed to water vapor in the surrounding air which condenses and creates a water film on the surface of the sphere and taper, as illustrated in figure 4.25. This introduces additional scattering at the coupling region and degrades the coupling.

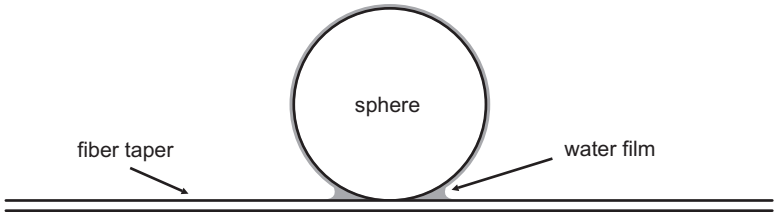

Figure 4.25: Illustration of a waterfilm due to water vapor contained in air.

Figure 4.26 (top) shows the degraded resonance structure of a taper coupled sphere that was contained in the laboratory atmosphere. The improvement of contrast for the individual modes after four hours of dry argon flushing is evident in figure 4.26 (bottom). The individual modes start to reappear and the Q factor increases.

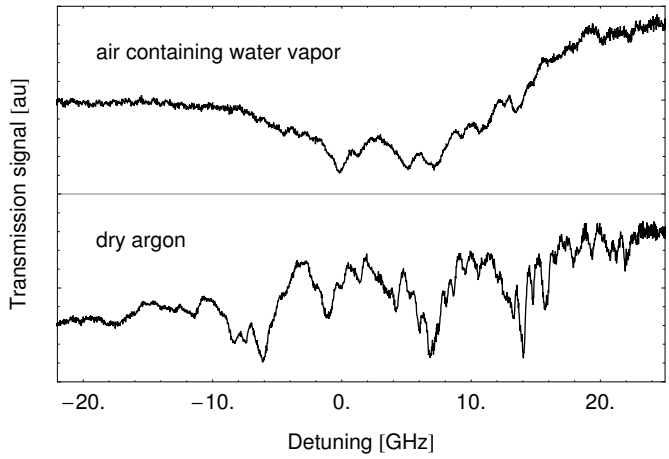

Figure 4.26: Top: Degraded mode spectrum observed after approximately a day after preparation of sphere and fiber in ambient air atmosphere. Bottom: Same spectrum taken after 4 h of argon flushing with assisted heating to 35 °C.

4.5.3 Thermal tuning of whispering gallery modes

The microsphere resonator and a small section of the taper is placed within a small temperature controlled copper enclosure in order to provide a well defined thermal environment. The temperature of this enclosure is varied in steps while the position of a narrow WGM resonance is tracked, as shown in figure

4.27. The plot shows how the resonance shift corresponds to the temperature change. It is important to point out the overall obtained frequency stability for a time period of 4000 s (> 1 h). It results from the well controlled thermal environment and the resonator system's inherent mechanical stability.

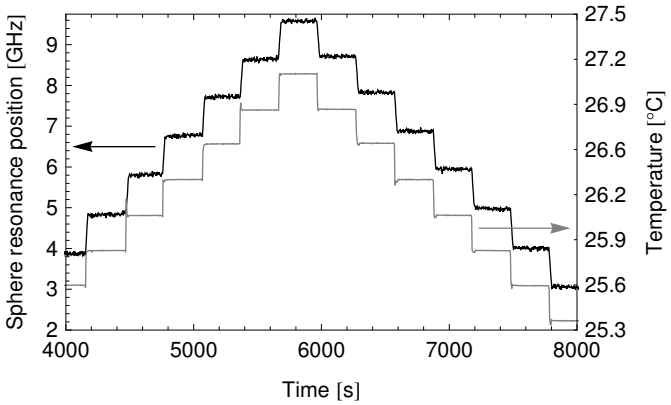

Figure 4.27: Position of a sharp resonance (black) (cf. figure 4.20) as the temperature of the copper enclosure is changed incrementally (gray) for a sphere 31 μm in diameter attached to a 1.2 μm diameter taper.

By plotting the frequency shift versus the measured temperature change the frequency shift in GHz/K can be determined. A corresponding plot can be found in figure 4.28. A linear fit reveals a shift of 3.80 ± 0.01 GHz/K for a polystyrene sphere of 31 μm diameter. This result agrees well with the calculated value of 3.475 ± 1.3 GHz/K (cf. table 4.1).

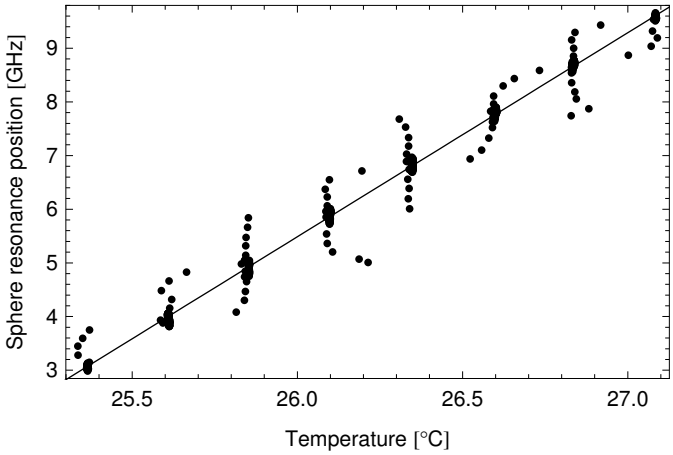

Figure 4.28: Measured temperature versus the induced resonance position for the measurement presented in figure 4.27. A linear fit is used to estimate the coefficient $\Delta\nu/\Delta T$ to be 3.80 ± 0.01 GHz/K for a coupled power of $P_{Pump} = 5\,\mu$W. At this power level the pump does not induce measurable heating of the sphere, as confirmed in additional measurements of $\Delta\nu/\Delta T$ for different pump powers. Points scattered off the fitted line indicate the approach towards a steady state temperature after the incremental increase (decrease) of the temperature at the copper heater.

These results show that a microresonator system can act as a sensitive thermometer. The temperature resolution is expected to be in the range of a few tens of milikelvin considering that a tenth of the resonance linewidth can be resolved.

4.5.4 Gas sensing by measuring local thermal conductivity

Some of the light contained in a WGM is absorbed by the sphere. This results in heating of the microsphere and, thus, a change of temperature depending on the thermal conductivity of the surrounding gas, as

discussed in section 4.3.2. In this section a set of measurements is presented that shows the ability to measure the thermal conductivity of binary volume mixtures of argon and helium.

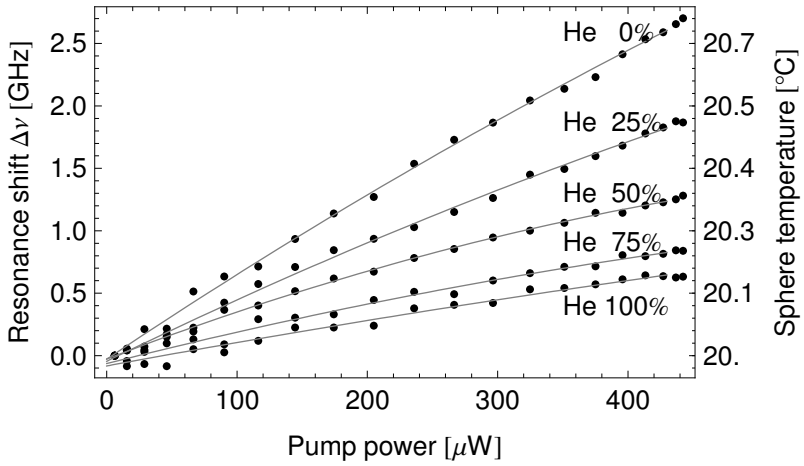

Figure 4.29: Laser heating induced resonance shifts for volume mixtures of helium and argon as indicated. The quoted pump power is the power in the taper taking coupling and transmission losses into account. The solid lines are fits of the form $a_0 + a_1 P + a_2 P^2$. The nonlinearity arises from a temperature dependent shift in the absorption spectrum. The temperature scale is calculated based on a shift of 3.8 GHz/K.

As discussed in section 4.4.3 the coupled microresonator system is contained in a gas tight box that is connected to a gas delivery system. In our experiment we continuously flush the box with a controllable volume mixture of helium and argon at a rate of 0.4 l/min. The box is flushed for 30 min between the measurements, expecting an exchange of 97.6% of the gas volume within this time (cf. section 4.4.3). The difference in the thermal conductivity of these mixtures can now be determined by changing the laser power (and thus Q_L, cf. equation (4.20)) while measuring the resonance shift (corresponding to a new ΔT). The combination of the half-wave plate (HWP1) and the polarizer (POL) is used to attenuate the laser. This allows for a quick variation of the laser power while at the same time maintaining the coupling efficiency into the fiber. In figure 4.29 the relative shift of the resonances is plotted for different helium-argon mixtures while the copper enclosure is kept at a fixed temperature of 20 °C and the laser is continuously tuned across a 54 GHz window. A smaller frequency shift, indicating a smaller temperature rise of the sphere for an increasing helium concentration, is visible, as expected, due to the higher thermal conductivity of helium.

The inverse of the linear fit coefficient, a_1, in figure 4.29 is proportional to the thermal conductivity k_{th} and is plotted as a function of the gas mixing ratios in figure 4.30.

The thermal conductivity of a binary mixture of helium and argon is not given by a simple linear interpolation according to the thermal conductivities of the pure gases, but rather by a non-polynomial relation measured for instance by Thornton et al [111]. This is to be expected since, in general, the thermal conductivity of a gas depends on quantities like diffusion coefficient, molar mass and scattering cross section of the individual atoms or molecules. These parameter do not scale linearly if the composition of a gas is changed [112].

The thermal conductivity for the helium-argon mixture [111] is plotted in figure 4.30 as a solid line for comparison. The relative thermal conductivities measured for the different gas mixture ratios agree well with the expected values from literature.

4.5.5 Non-linear lineshape dependance on thermal conductivity

The heating of the microsphere during a single frequency scan has an influence on the observed lineshape of the resonance. This is due to the fact that the microsphere heats up sufficiently fast for the resonance frequency to shift thermally, while the laser still scans the resonance, as introduced in section 4.3.3.

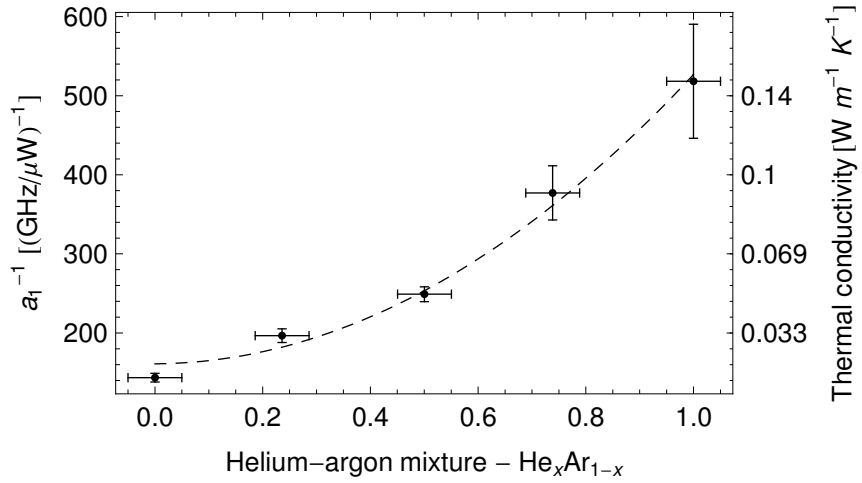

Figure 4.30: $1/a_1$ is proportional to the thermal conductivity k_{th} and is plotted for the different gas mixtures. The solid line corresponds to the measured thermal conductivities at 18 °C and 1 bar according to reference [111].

This effect can be studied best for a single resonance lineshape. Due to the contact coupling and eccentricity of the sphere there usually exists an large number of closely spaced $n = 1$ modes. A better option is to use a $n = 2$ mode, which has a lower Q factor, but has a well defined lineshape. Such a typical mode can be found in figure 4.31. The individual plots are composed to show the resonance lineshape for the two cases where either the laser scan and thermal shift direction coincide or are opposite. For the plots from (a) to (f) the surrounding gas is changed starting from air, which is exchanged for a mixture of argon and helium with increasing helium content. Argon possesses the lowest thermal conductivity and helium the highest from the used gases (cf. table 4.2). This can be seen in the shape of the resonances. For argon the linewidths for the two cases differ the most. As the thermal conductivity increases with higher helium concentration this difference in linewidth reduces, since the heat deposited by the laser can be dissipated much quicker and the resulting thermal shift reduces.

The simple model introduced in section 4.3.3 provides a good qualitative description of the lineshape depending on the thermal conductivity. However, a quantitative fit using this model is not satisfactory and a much more involved model [104] would have to be used.

Considering the non-linear lineshape seems to be an intriguing idea for a sensing application, since a single measurement reveals changes in the surrounding thermal conductivity. However, the linewidth is not a linear function of the thermal conductivity of the surrounding gas. Therefore, the applicability of this approach is limited.

4.5.6 Influence of refractive index changes

So far only the influence of the different thermal conductivities of the used gases, helium and argon, are discussed. In section 4.3.4 the influence of the change in the refractive index are theoretically reviewed. The expected effects for an absolute or relative resonance shift are of the order of a few hundred MHz. During the experiments these effects could not clearly be identified as the gas temperature for different mixing ratios could not be sufficiently stabilized. Considering that a change of a tenth of a degree in temperature results in a resonance shift of 380 MHz the requirements on the gas delivery system become apparent. Without using a much more advanced gas delivery system refractive index effects can not clearly be identified.

4.5.7 Differently sized spheres coupled to the same taper

The technique developed for attaching polystyrene spheres to a thin optical taper has, so far, only been used to place a single sphere onto a taper. In principle there is no limitation on the number of spheres

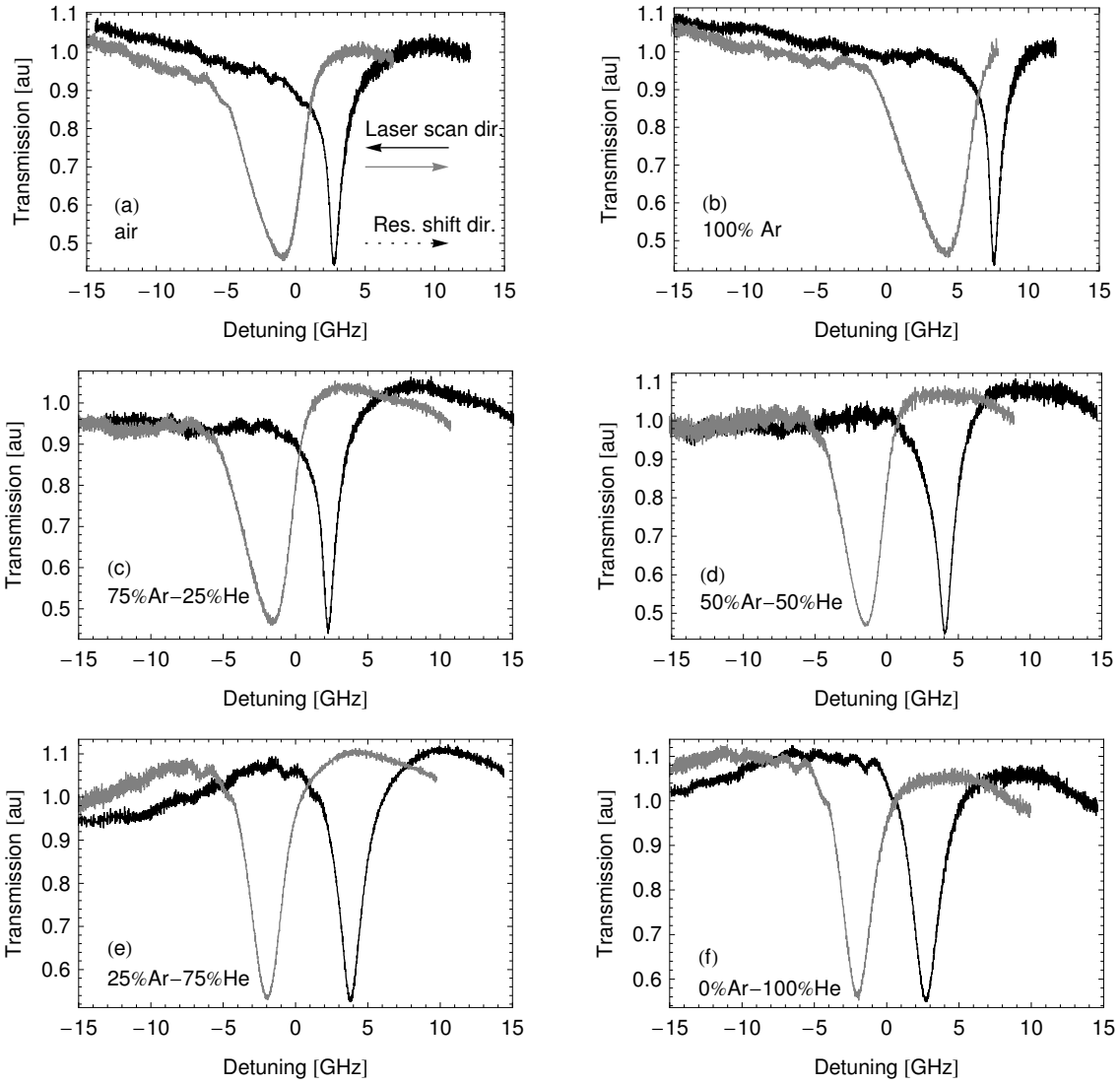

Figure 4.31: (a)-(f) Change in the resonance lineshape for an $n = 2$ mode of a $31\,\mu$m polystyrene sphere attached to a $1.2\,\mu$m taper as the surrounding air is exchanged for binary mixtures of argon and helium. For resonances plotted in gray the direction of the thermal frequency shift and laser scan direction coincides, and for resonances plotted in black they are opposite (cf. arrows in (a)). The experimental curves can be compared to the theoretical model depicted in figure 4.16. The laser power was $P_P = 1.46\,\mathrm{mW}$.

that can be transferred to the taper. In the following, the case of two attached spheres is investigated in more detail.

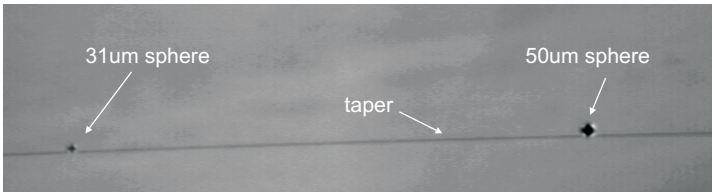

Figure 4.32: A 31 μm and a 50 μm sphere are placed onto the same taper. The scale can be estimated by the size of the two spheres.

The microscope image in figure 4.32 shows a section of a fiber taper and two attached polystyrene spheres of 31 μm and 50 μm in diameter, that are placed one after the other using the technique described in section 4.4.2.

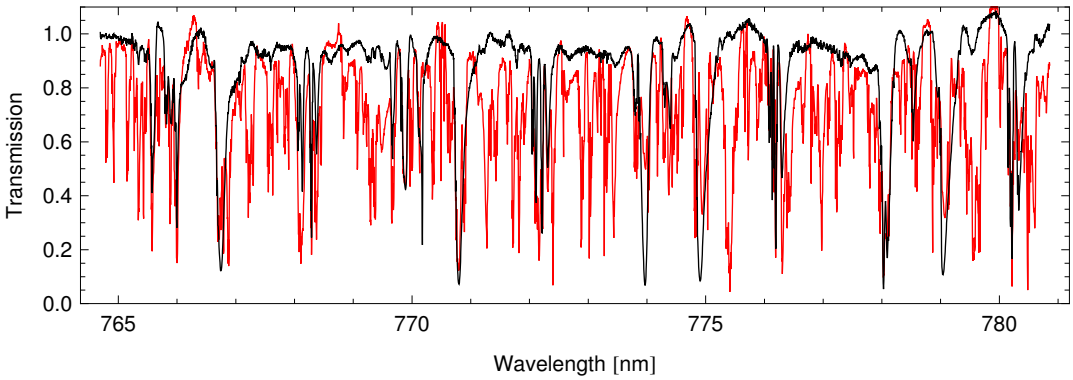

Figure 4.33: Comparison of two transmission spectra for a 31 μm and a 50 μm sphere attached to the same taper (red) and the 31 μm sphere only (black) for the same linear polarization.

A suitable method for investigating the mode structure of this more complex, multiple resonator system is to perform a frequency scan over several free spectral ranges of the resonator. Such a transmission spectrum is shown in figure 4.33. The gray line shows the transmission for both spheres attached to the fiber taper, whereas for the black spectrum the 50 μm sphere has been removed. By comparison the modes associated with the individual spheres can be identified. The mode density of the larger 50 μm sphere is much higher than for the smaller 31 μm sphere. This is due to the different coupling conditions, as well as the smaller free spectral range for larger spheres. However, it is difficult to identify individual modes due to multiple superimposed resonances caused by the eccentricity splitting.

Such a 'chaotic' resonance spectrum can be the basis for a frequency reference. If the entire transmission spectrum is known it is possible to identify a given frequency based on the "fingerprint"-like local structure.

Since individual modes of the resonator can be associated to the different resonators, this technique could be used for more complex sensing tasks involving multiple spheres. Firstly, a refractive index sensor based on two differently sized spheres can be envisioned. When using two spheres, one can be exploited to account for thermal drifts, whereas the other sphere merely detects local changes of the dielectric environment. Further, functionalized spheres with chemically or biochemically [70] active layers which respond to certain gases [113] or binding events via a shift of their index of refraction can be utilized to assemble highly specific gas or bio sensors.

4.5.8 Long term stability

The passive stability of such a resonator system is of crucial importance for sensing applications based on frequency shifts. In this section two stability measurements are presented: one for the average resonance

stability of the setup, as it is observed many times in the laboratory and a single measurement showing a much enhanced stability indicating the potential of the integrated geometry of this resonator setup.

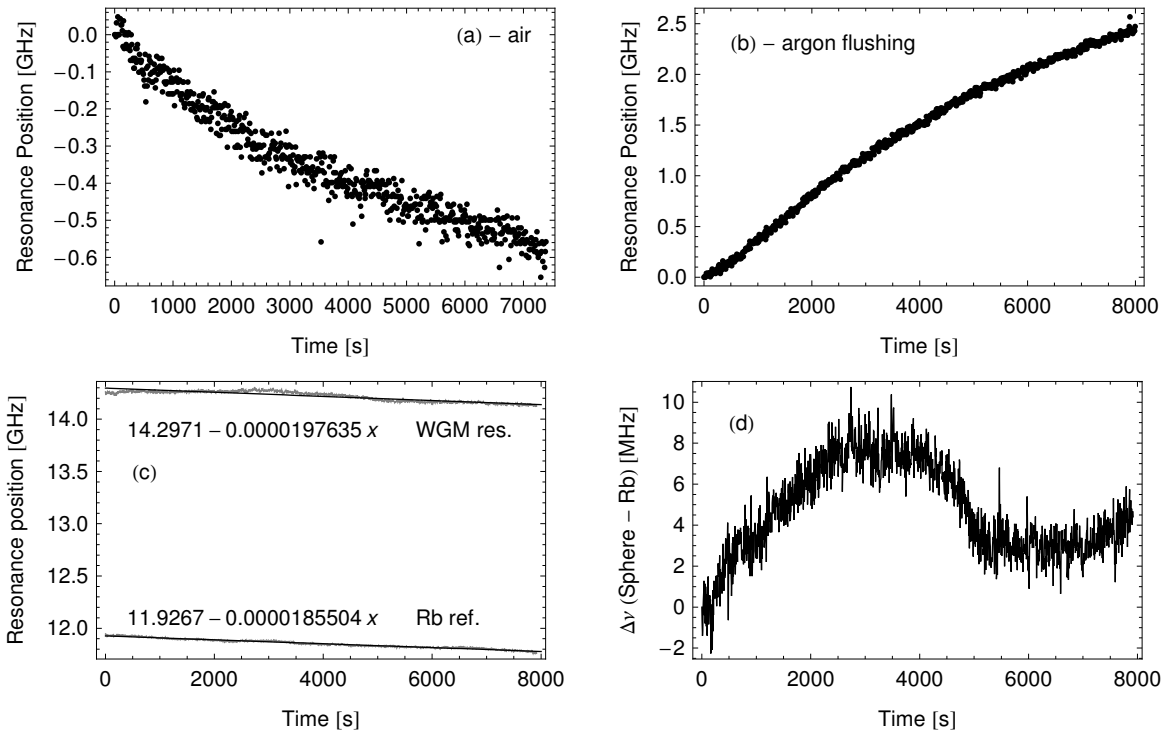

Figure 4.34: (a) and (b) resonance position of a single WGM measured for a time period of $> 2\,\mathrm{h}$ for a $31\,\mu\mathrm{m}$ sized sphere in air and while flushed with argon at a rate of $0.4\,\mathrm{l/h}$, respectively. The temperature of the copper enclosure is stabilized to $20\,^{\circ}\mathrm{C}$. The pump power is $P_P = 25\,\mu\mathrm{W}$.
(c) Measured electronic transition in Rb and WGM resonance of the sphere in air are shown for a period of $2.2\,\mathrm{h}$. The results of linear fits are shown revealing an average shift of $1.2\,\mathrm{kHz/s}$ over a time period of $2.2\,\mathrm{h}$. The system was allowed to settle over the weekend and the copper enclosure was temperature stabilized to $23.18\,^{\circ}\mathrm{C}$. The pump power is $P_P > 1\,\mathrm{mW}$. (d) shows the relative drifts of the Rb resonance compared to the sphere's resonance.

Figure 4.34 (a) and (b) show the shift in the resonance for a $31\,\mu\mathrm{m}$ diameter sphere contained in the temperature stabilized environment of the copper enclosure. The resulting passive stability for the sphere in air is about $80\,\mathrm{kHz/s}$ over a time of $2\,\mathrm{h}$. If the containment box is flushed continuously with argon, as needed as part of the gas sensing, the passive stability reduces to $300\,\mathrm{kHz/s}$ over a time of $2.2\,\mathrm{h}$. These stabilities are more than sufficient for the presented sensing approach in section 4.5.4.

The highest observed stability for these resonator systems is displayed in 4.34 (c) and (d.) The system showed a remarkable passive frequency stability with a drift less than $1.2\,\mathrm{kHz/s}$ over a time period of $2.2\,\mathrm{h}$ in air. This high stability may be attributed to a thermal passive locking effect [102].

4.6 Conclusion

The simplicity of the integrated resonator system is highly attractive, since once the sphere is attached to the taper, no further positioning mechanics frequently required for coupling in conventional microresonator systems is needed. A fiber optical access to the resonator is given by the optical fiber taper.

The measurements demonstrate that our integrated and alignment-free, taper-microsphere system acts as a sensitive thermometer with a temperature drift of $3.8\,\mathrm{GHz/K}$. Such an integrated high-Q microresonator system has applications in thermal sensing of small gas volumes with a fast response time due to the small heat capacity of the $31\,\mu\mathrm{m}$ microsphere. A temperature-sensitivity of a few tens of milikelvin can be achieved, as a tenth of one linewidth shift at Q factors ranging from 10^5 to 10^6 can be resolved.

Due to the thermal sensitivity and heating effects inside the sphere it is possible to determine gas concentrations based on changes in the thermal conductivity. This has been demonstrated for the first time for different volume mixtures of helium and argon. The expected change in the thermal conductivity for the binary gas mixtures could be well reproduced.

The system showed a remarkable passive frequency stability with a drift of less than 80 kHz/s over a time period of 2 h in air and this is increased by a factor of four when the box is flushed by argon. This can be attributed to the geometry of the microresonator system. Mechanical vibrations and the thermal environment can be well controlled.

The attachment of two spheres with different sizes to the taper has been successfully been demonstrated. The individual modes of the two spheres have been distinguished in the mode spectrum. This approach allows one to attach an arbitrary number of resonators and, therefore, to couple a large number of microspheres to a single taper.

Chapter 5

Coupling of quantum emitters to toroidal microresonators

5.1 Introduction

Toroidal microresonators [114] are a valuable system to study cavity quantum electrodynamics (CQED) effects due to their high Q factors and small mode volume. It is particularly fascinating to couple single quantum emitters to these cavities in order to investigate their potential for applications in quantum information processing [19].

Nitrogen vacancy (NV) color centers in diamond are stable single photon emitters even at room temperature [115] and are ideally suited for applications in nanophotonics or quantum technologies [116]. Diamond nanocrystals (DNCs) can be regarded as carrier particles of these NV centers, allowing easy manipulation and they have been coupled to spherical microresonators [117] using coatings [118] and a single DNC pick-up technique [119].

In this chapter a technique for transferring preselected DNCs from a donor fiber acting as a DNC reservoir onto a toroidal microresonator using a fiber taper is presented. The DNC's fluorescence coupled to the toroid is investigated and non-classical light emission from the coupled toroid-fiber system is demonstrated.

The mircotoroids used in these experiments has been produced as part of the diploma thesis by Tim Schröder [140] and Rico Henze. The collaboration between Rico Henze, Tim Schröder, Oliver Benson and myself resulted in a publication[20] and are presented in this chapter.

5.1.1 Quantum information processing with cavities and atoms

One of the intriguing applications for NV centers in DNCs coupled to toroidal microresonators is quantum information processing. This section offers a brief introduction to this application based on cavity quantum electrodynamical effects (CQED). An in-depth discussion is out of the scope of this thesis; however, a more detailed review can be found in references [11, 120].

Photons are a possible implementation of a qubit, the fundamental unit of quantum information. The great advantage of photons is at the same time their biggest draw back: Photons interact very weakly with their environment. Thus, photons preserve their quantum state for a long period of time while, at the same time, propagating at the speed of light. These features make them a very promising candidate for transporting quantum information over long distances and thus photons are also called "flying qubits".

The challenge lies in creating a way to let individual photons interact. In principle, there are two options. One is to find a system with an extremely large non-linearity, so that an interaction of light with light can be obtained even at the single photon level. Another option is to transfer the quantum information encoded in a photon to another system, e.g. an electronic excitation which is more appropriate to mediate interaction. Single optical emitters, like atoms, quantum dots, or color centers in diamonds, can be used for both options. A requirement is to establish a long enough interaction between the photon and the emitter, i.e. to realize an efficient quantum interface. At this point microresonators can be used to facilitate a highly enhanced interaction time between photon and emitter. With microresonators,

the so-called strong interaction regime of CQED can be realized. This regime corresponds with a true quantum interface, i.e. an excitation can coherently exchange between an emitter and an optical mode of the microresonator.

More precisely, in the strong coupling regime, the emitter-cavity coupling rate g is faster than any other dissipative rate of the system, like the photon decay rate of the cavity or the emission rate of the emitter into free space and other cavity modes. The presence of an emitter coupling strongly to the cavity splits the cavity's transmission spectrum into two distinct resonances. These two states form eigenstates of the cavity-emitter system, which can no longer be factorized into cavity and emitter components. By controlling the coupling it is now possible to control the reflectivity of a cavity as shown in the case of a quantum dot in a photonic crystal cavity [121]. The same ideas have been used to show efficient routing of single photons by a caesium atom coupled to a toroidal microresonator [122]. The eigenstates of the cavity-emitter system can also be used as a quantum gate to perform computations [19]. Such an implementation would constitute a flying qubit interface.

However, even in the less stringent regime of weak coupling in CQED, the interaction between the photon and emitter is enhanced. This is useful for enhanced phase shifts, enhanced absorbtion or enhanced emission. The emission rate of a dipole depends on the optical mode density. In the weak coupling regime of QED a microresonator supports an enhanced emission in its resonant modes. The ratio of the emission rates of a dipole radiating into a specific mode and the emission rate in free space is called the Purcell factor, F_P. Its definition for a cavity with quality factor Q, mode volume V, and refractive index N is given by

$$F_P = \frac{3}{4\pi^2}\left(\frac{\lambda}{N}\right)^3\left(\frac{Q}{V}\right).$$

Optical microcavities, like microspheres and toroids, may provide a large Purcell factor due to their high Q factors and small mode volume. The Purcell factor also indicates the quality of the coupling of a dipole emitter to a cavity. By monitoring the change in the spontaneous emission the optimal coupling position for an emitter on a microresonator can be found. A crucial application of the Purcell factor is in the improvement of the emission rate and directionality of single photon sources [123].

5.2 Optical properties of NV defects in diamond

Color centers in diamond have attracted much attention as single photon emitters [115] in recent years. In particular, the NV center that is formed by a nitrogen atom and an adjacent vacancy within a carbon crystal (cf. figure 5.1 (a)) has been widley studied [124].

NV centers are one of the most common, naturally-occurring defect centers in diamond and are responsible for the yellow coloring in gems. NV centers can be artificially produced in thin film diamond samples by electron radiation and subsequent annealing [125]. Diamond nanocrystals (DNCs) can be obtained, for instance, by grinding bulk diamond.

One of the remarkable aspects of the negatively charged $NV^{(-)}$ centers is their electronic structure. A term scheme of the three lowest energy levels is shown in figure 5.1 (b). The ground state ^{3}A and the excited state ^{3}E are both triplet states. This allows for the storage of quantum information in the individual spin states. Optical readout schemes have been demonstrated [126, 127]. The energy difference between the ground and excited state is 1.945 eV [128] which corresponds to a wavelength of 637 nm. This transition is referred to as the zero-phonon line (ZPL) since only the phonon ground states are involved. The lifetime of this transition in a bulk sample is measured to be 11.6 ns [128]. The lifetime depends on the surrounding matrix. Thus the lifetime may be reduced due to strain in DNCs [129, 130]. In this context a shift of the ZPL resonance wavelength may also be observed. Additionally, there exists a meta stable excited singlet state ^{1}A. The intersystem crossing rate is measured to be 2.6% [125]. Since the energy difference between the ^{3}E and ^{1}A is relatively small, the depopulation of the meta stable ^{1}A to the ^{3}E state is temperature dependent and has to be taken into account for low temperature experiments. The electron spin configuration of NV centers can be optically detected, leading to applications as nano-magnetic probes [126, 127].

NV centers can be optically excited using frequency doubled Nd:YAG lasers at 532 nm or an argon-ion laserline at 514 nm. A typical fluorescence spectrum of a DNC at room temperature is shown in figure 5.2. The prominent vibronic sidebands lead to a broad spectrum. At low temperatures a substantial

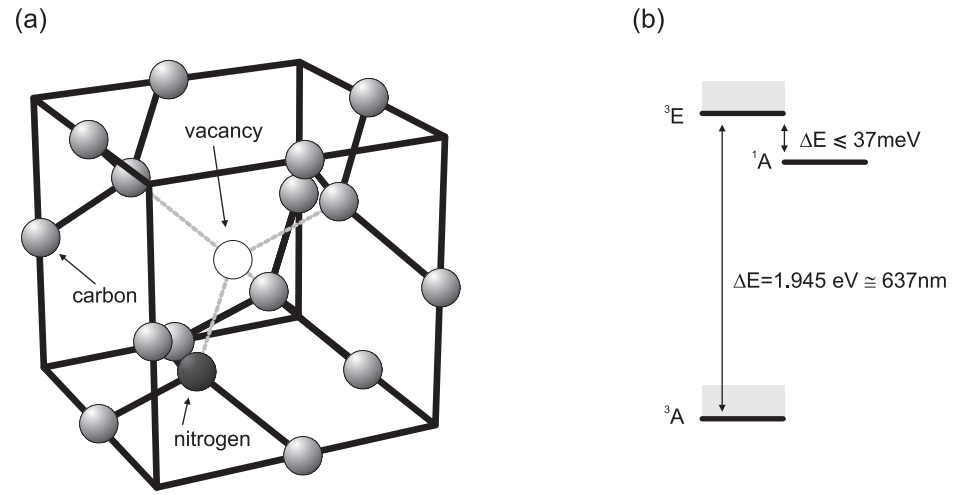

Figure 5.1: Structure (a) and schematic (b) representation of the energy level scheme of the $NV^{(-)}$ center [125]. The gray shaded areas in (b) correspond to phonon states.

reduction of the sidebands and an enhancement of the zero phonon line (cf. figure 5.24) is observed. This is a vital prerequisite to couple only the narrow ZPL transition to a narrow cavity resonance.

In this context, it is important to point out that NV centers are optically stable, i.e. no photobleaching or blinking is observed. Additionally the size and positionalibility make NV centers in diamond nanocrystals viable candidates for CQED experiments [64].

5.2.1 NV centers as single photon sources

Single photon sources are of great importance for applications in quantum cryptography or computing. The first experiments that lay the groundwork for experiments investigating the statistical characteristics of a photon source were conducted by Hanbury-Brown and Twiss [133] by measuring the intensity correlation of the form $\langle I(t_0)\, I(t_0+\tau)\rangle$ of stellar light. The important insight of Hanbury-Brown and Twiss is that coherence properties of light, usually associated with the phase of the electromagnetic wave, are also contained in the intensity fluctuation of the fields. This implies further that in the photon picture, the occupancy of photons must be statistically related to the photon source.

The intensity correlation is a second order correlation since it involves the intensities, i.e. the squared electric field amplitudes. The second order correlation function, $g^{(2)}$, is defined as

$$g^{(2)}(\tau) = \frac{\langle : I(t_0) I(t_0+\tau) : \rangle}{(\langle : I(t_0) : \rangle)^2},$$

where t_0 is some fixed time and $t_0+\tau$ is a time span with respect to t_0. $<: \ldots :>$ indicates the time average of normally ordered operators.

Photons emitted by thermal sources, like incandescent lamps, tend to bunch. There will be a high correlation between the intensity fluctuations within the coherence time of the source, i.e. $\tau < \tau_{coh}$. For thermal light the correlation function at $\tau = 0$ tends to $g^{(2)}(0) = 2$. A different class of light source is formed by the laser. The light emitted by a laser has a high phase stability. The emerging photons are uncorrelated and are statistically described by the Poisson distribution forming a coherent state. The resulting correlation function is a constant of the form $g^{(2)}(\tau) = 1$. The remaining class of light sources are quantum emitters. If the standard deviation of the probability distribution describing the number of photons contained in a particular mode is smaller than a Poisson distribution this light source is called sub-Poissonian distributed or a non-classical light source. The corresponding correlation function is given by $g^{(2)}(\tau) < 1$. In contrast to the bunching of photons emitted from thermal sources the photons of quantum emitters are anti-bunched. This is nicely illustrated for $\tau = 0$, where the correlation function $g^{(2)}(0) = 0$, as observed for single photon sources such as single atoms or NV centers in diamond. Thus, by measuring the second order correlation function, it is possible to identify the class of light source.

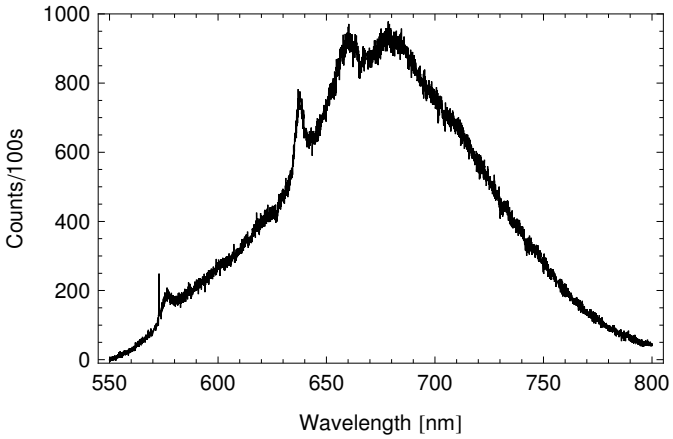

Figure 5.2: Typical fluorescence spectrum of NV centers in a diamond nanocrystal at room temperature. The zero phonon line (ZPL) at 637 nm for the $NV^{(-)}$ center and the prominent vibronic side bands at longer wavelengths are visible. The two additional narrow peaks at 575 nm and 572.5 nm are related to the ZPL of the neutrally charged $NV^{(0)}$ center [131] and a Raman scattering signal. The Raman shift in diamond is 1331 cm^{-1} [132]. This corresponds to a shift of 39.9 THz. Thus, for a pump wavelength of 532 nm the Stokes sideband appears at 572.5 nm. The spectrum is recorded using the optical setup described in section 5.4.2.

The $g^{(2)}$-function for an ensemble of M identical, two-level emitters is given by [134]

$$g^{(2)}(\tau) = 1 - \frac{\exp(-k|\tau|)}{M}, \tag{5.1}$$

where $k = k_{ex} + k_{em}$ is the decay rate based on the excitation rate k_{ex} and spontaneous emission rate k_{em} of the emitter. Usually, in the case of optically pumped NV centers, the intense pump field leads to instantaneous excitation of the NV center. Thus k_{ex} is very large and dominates the decay process.

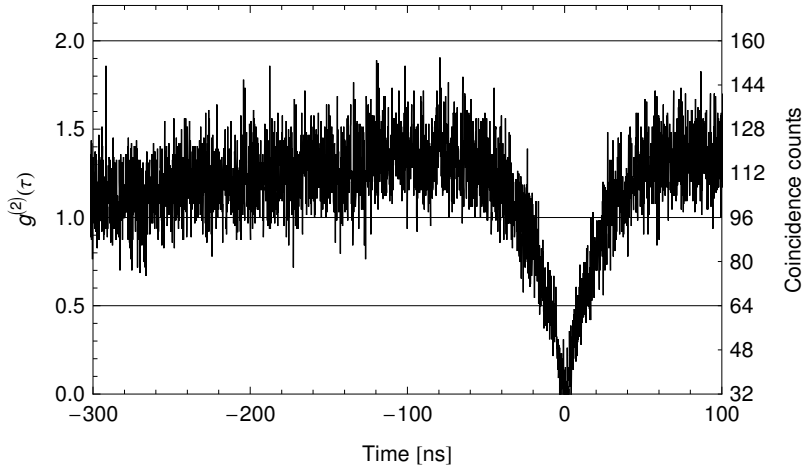

Figure 5.3: A typical $g^{(2)}$-function for single NV center in a DNC. The normalization and background subtraction was carried out in accordance with reference [129]. The correlation function is measured using the optical setup introduced in section 5.4.2. The integration time is 2400 s.

A typical measured $g^{(2)}$-function for a single NV center is shown in figure 5.3. The non-classical emission of the NV center is evident, as $g^{(2)}(\tau = 0) < 0.5$. In addition to the anti-bunching, there is also a bunching effect $g^{(2)}(\tau) > 1$ visible for $\tau > 0$. This is due to the meta stable ^{1}A level, that adds an additional fluctuation to the photon emission. The entire process can be modeled by solving a set of

coupled differential equations for the three individual energy levels [135, 136], leading to a bi-exponential expression for the $g^{(2)}$-function. The bunching is most prominent for high excitation intensities.

Grangier and Weinfurter [115] first showed that the emission from a single NV center in bulk diamond is a non-classical light source. A quantum key distribution (QKD) scheme using NV centers in diamond as single photon sources has successfully been demonstrated [116]. Further, it has been argued [123] that an optical microcavity coupled to an NV center can form a single photon source with a high emission probability of 0.99 following a sub-picosecond pump pulse. Another advantage of this system is the substantially reduced lifetime (70 ps) and high spectral purity (linewidth of 0.01 nm) suggesting applications in QKD systems.

Finally, there are practical reasons that qualify NV centers for quantum information applications. NV-centers can be used at room temperature without the need for extensive vacuum chambers or complicated atoms traps as required in alternative single photon sources.

5.3 Theory of toroidal microresonators

Toroidal microresonators are advantageous for coupling quantum emitters to whispering gallery modes. In comparison to spherical resonators toroidal modes are not degenerate and thus the mode density is smaller. Therefore, an emitter can more easily be coupled controllably to an individual resonator mode. These aspects and the fact that toroidal resonators can be produced with a high standard of reproducibility led to the use of toroidal resonators.

In contrast to spherical microresonators it is not possible to find an analytical solution for the optical modes formed in a toroidal microresonator. The problem results from the inseparability of the scalar wave equation in the local coordinates of the toroid. Therefore there exist two approximate approaches that lead toward a description of the modes within a toroid. The first one relies on finding a numerical solution for the vectorial wave equation using a finite-element method (FEM) solver. The second approach is based on the idea to approximate the toroid as a closed ring made from a thin optical fiber [137].

This section will highlight some of the central properties of toroidal microresonators based on some numerical FEM simulations. The results are obtained using the commercial FEM solver software *Comsol Multiphysics* and a customization for rotational symmetrical resonators [138]. A more in-depth review of toroidal microresonators can be found in [139].

5.3.1 Field distribution and mode structure

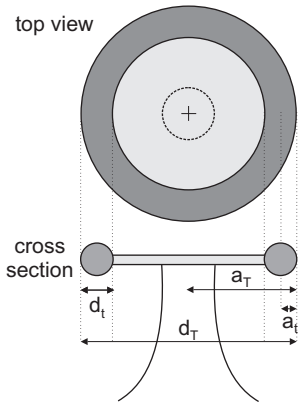

Figure 5.4: Schematic drawing of a toroid indicating the minor diameter d_t and the major diameter d_T. Shown is the top view perspective and a cross section.

The mode structure of a toroid is similar to the modes of a spherical resonator. Therefore it is convenient to adopt a similar naming scheme for the different modes. This can be illustrated by considering the electric field distribution for the lowest modes of a toroid, as shown in figure 5.5. The dimensions of the toroid are defined according to figure 5.4. First of all, the modes are quasi-TE or quasi-TM polarized. A radial mode number n is associated with the number of radial field nodes. The radial mode number

for the selected modes in figure 5.5 is one. Similar to spherical resonators the number of complete wave periods contained within a toroid is denoted by the azimuthal mode number l. Finally, the angular mode number m describes the number of field nodes along the angular direction. It is common to denote the fundamental mode $|l-m|=0$ as shown in figure 5.5 (a) and (b). The next higher modes with $|l-m|=1$ and $|l-m|=2$ are depicted in 5.5 (c),(d) and (e),(f), respectively. Thus an individual mode can completely be described by four mode numbers in the form $\mathrm{TE}_{n,l,|l-m|}$ or $\mathrm{TM}_{n,l,|l-m|}$.

The majority of the field is contained inside the toroid. However, a small fraction is evanescently guided at the surface of the toroid. This field forms the crucial interface for matter-light interactions and thus for applications of toroids in CQED experiments. Figure 5.6 (a) shows the intensity distribution for a toroid with a major diameter of $d_T = 65\,\mu$m. The dashed vertical line in the radial field distribution in figure 5.6 represents the toroid's surface. Only a small fraction of the total electric field energy is guided outside of the toroid. This fraction can be increased by choosing a smaller major and minor toroid diameter [137]. Smaller overall dimensions are limiting the Q factor and thus a trade-off between evanescent field fraction and Q factor has to be made.

Mode spectrum

One of the remarkable features of toroidal microresonators is their mode spectrum. In contrast to spherical resonators the $|l-m|$ modes are not degenerate. This is illustrated by the numerically calculated mode spectrum for a toroid in figure 5.7. The higher $|l-m|$ modes are shown at distinct frequencies different from the fundamental mode. This is of great importance for the coupling of emitters to the toroidal modes. The strong coupling regime is reached more easily, since the coupling of an emitter to other cavity modes is less efficient (as, for instance, in the case of spherical resonators).

5.3.2 Coupling microtoroids to fiber tapers

Phase matching

A requirement for coupling efficiently to a resonator is to achieve phase matching between the excitation field in the coupling fiber taper and the field within the resonator. This requires the mode propagation constant in the fiber, β_f, and in the toroid, β_t, to match, i.e. $\Delta\beta = 0 = \beta_f - \beta_t$. This is illustrated qualitatively in figure 4.8 and discussed in section 4.2.4.

The propagation constant for the toroidal resonator can be deduced using the numerical methods introduced in section 5.3.1. However, for the fundamental toroidal mode it is more convenient to refer to the approximate, closed expression obtained in reference [137] for the mode constant β_t.

The effective propagation constant for the fundamental mode $\mathrm{TM}_{1,l,|l-m|=0}$ or $\mathrm{TE}_{1,l,|l-m|=0}$ is given by

$$\beta_t = \frac{2\pi}{\lambda}\left[N_t - (2-N_t)\left\{1+\zeta\left(\frac{a_t}{\lambda/N_t}\right)^2\right\}\right] \tag{5.2}$$

where N_t is the refractive index, a_t the minor radius of the toroid and the fitting constant $\zeta = 6.8288$. A plot of the propagation constant in terms of the effective refractive index can be seen in figure 5.8 (a).

Simple phase matching (SPM) between a toroid and a fiber can easily be obtained by matching $N_{\mathrm{eff,toroid}} = N_{\mathrm{eff,fiber}}$ using the results for the toroid modes in figure 5.8 (a) and for the fiber modes in figure 2.5. The result of this SPM is shown in figure 5.8 (b). The ideal fiber taper diameter is approximately equal to the minor diameter of the toroid, as expected, considering the similar circular geometry of both structures.

The main drawback of this SPM approach is the lack of consideration for the curvature in the circular waveguide forming the toroid. By transforming the propagation constant β_t in curved coordinates into the straight equivalent $\beta_{\mathrm{t,st}}$ based on equation (4.15) and requiring it to be equal to the propagation constant of the taper β_f the following transcendental equation for the phase matching condition is obtained

$$\beta_f(a_f) = \frac{\lambda}{2\pi}\left(1 - \frac{a_f - a_{\mathrm{T,eff}} + a_T + a_f}{2R_{\mathrm{T,eff}}}\right)\beta_t \tag{5.3}$$

where $a_{\mathrm{T,eff}} = m\lambda/(2\pi)$. The solution for selected wavelengths and toroid diameters is displayed in 5.8 (b). The calculation suggests that a toroid 60 μm in diameter and with a minor diameter of 5 μm would be phase-matched using a taper of 1.8 μm at an operation wavelength of 635 nm.

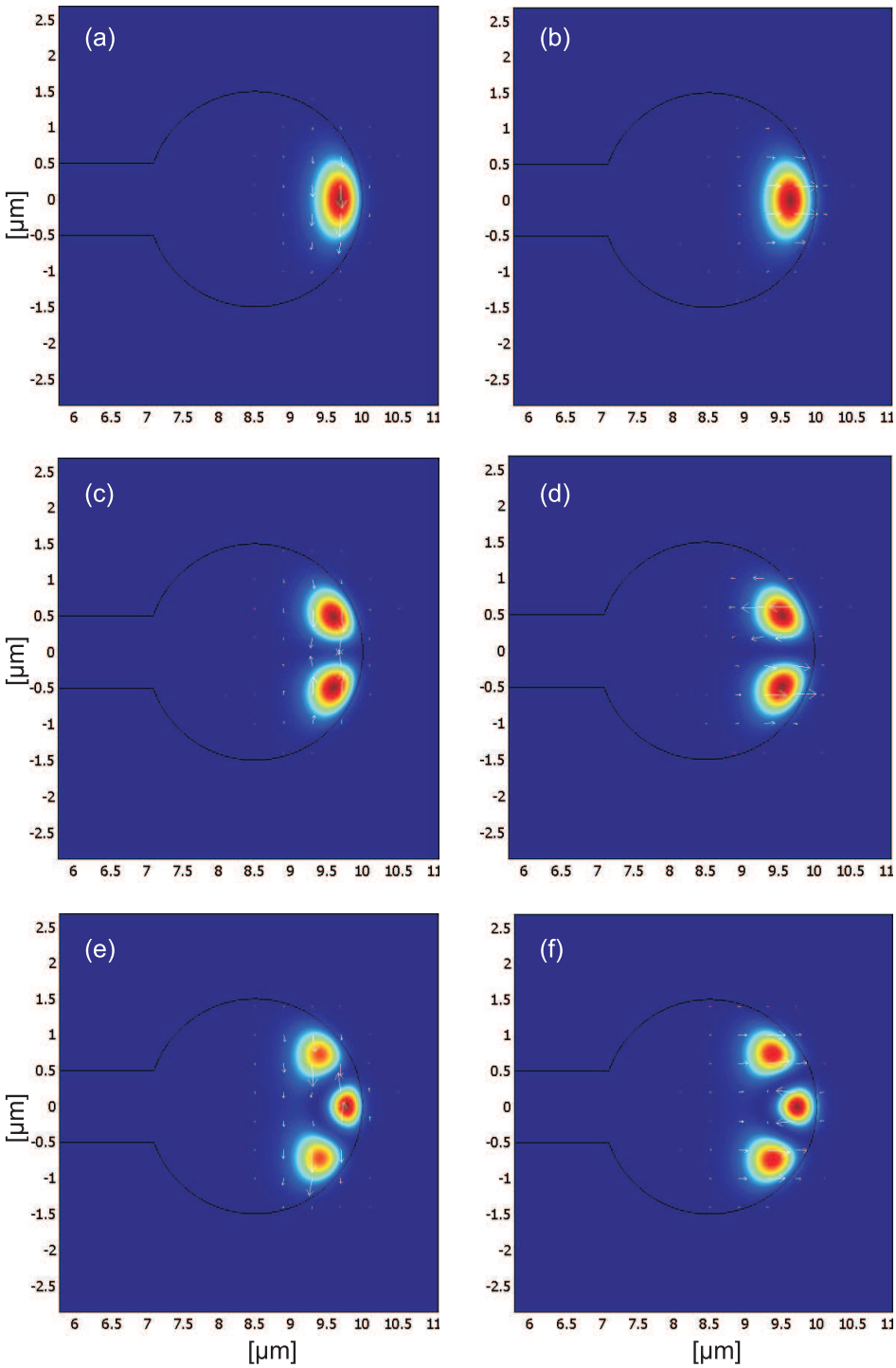

Figure 5.5: Intensity distribution $|E|^2$ for a toroidal microresonator with $a_T = 10\,\mu$m, $a_t = 1.5\,\mu$m, $l = 135$ at a resonance frequency of $\sim 637\,$nm for the modes (a) TE $|l-m| = 0$, (b) TM $|l-m| = 0$, (c) TE $|l-m| = 1$, (d) TM $|l-m| = 1$, (e) TE $|l-m| = 2$, (f) TM $|l-m| = 2$. The intensity is plotted in a normalized linear scale of arbitrary units.

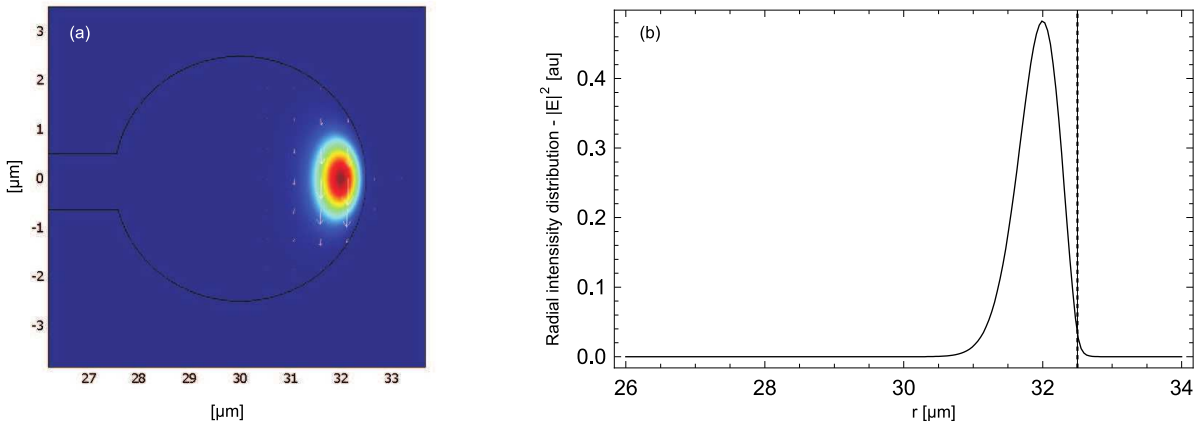

Figure 5.6: (a) Intensity distribution and (b) radial intensity distribution $|E|^2$ for a toroidal microresonator with $d_T = 65\,\mu$m, $d_t = 5\,\mu$m, $l = 450$. The dashed line indicates the surface boundary of the toroid. The relative field intensity outside the toroid is 0.25 %. The intensity distribution is plotted in a normalized linear scale of arbitrary units.

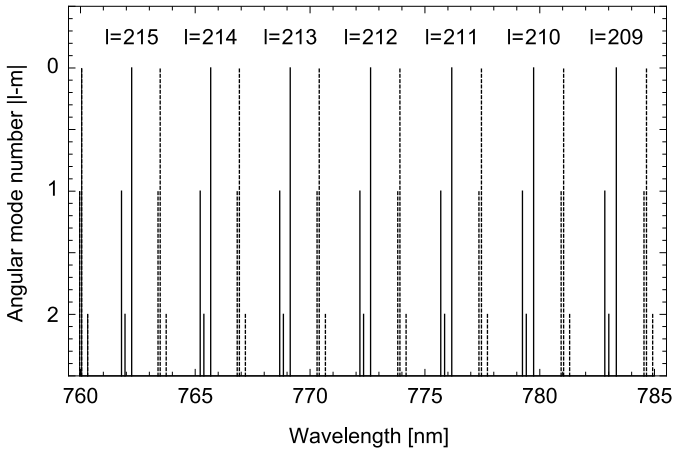

Figure 5.7: Resonance mode structure for a toroid with $d_T = 38\,\mu$m, $d_t = 5\,\mu$m. The TE and TM modes are shown as dashed and solid lines, respectively.

Spectral components of an optical resonance spectrum

In the previous chapter 4.2.4 a simple model of a waveguide coupled resonator system was derived. The transmission spectrum derived as part of this simple resonator model is further investigated in the following.

Experimentally, it is possible to measure the transmission spectrum for a waveguide-coupled resonator system similar to the calculated spectrum as shown in figure 4.7 using a tunable narrow-bandwidth laser (cf. section 4.5.1 and section 5.5.1). This, however, is a sequential process as the laser wavelength is tuned. A different approach is to record the transmission of a white light source (LED) through the system. The advantage is that no additional laser system is needed and the coupled resonator system can be characterized for a wide wavelength region in a single measurement.

A suitable method to analyze a transmission spectrum measured by a spectrometer is to perform a segmented Fourier transform (SFT), as also discussed in appendix C. This allows for visualization of the different frequency components present at different wavelengths.

Figure 5.9 shows the SFT for the calculated transmission spectra in figure 4.7. The colored bands correspond to the presence of individual frequency components in the transmission spectrum where the spacing between the bands is equivalent to the free spectral range of the resonator. Plot (a) in figure 5.9 contains a higher percentage of higher order frequency components than plot (b), which is no surprise considering the nearly sinusoidal-shaped resonance for plot (b) and the nearly Lorentzian-shaped

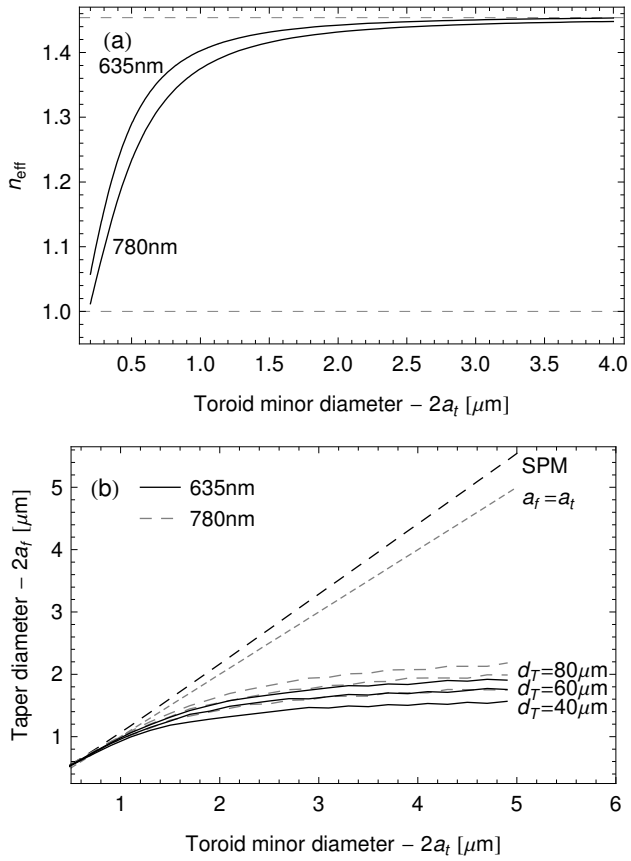

Figure 5.8: (a) Effective refractive index for toroidal microresonators using equation (5.2) for 635 nm and 780 nm. (b) Calculated phase-matched taper diameter using the simple phase matching condition (SPM) and using curvature corrected phase matching (cf. equation(5.3)) for 635 nm (solid) and 780 nm (dashed) at major toroid diameters of $40, 60, 80\,\mu$m. The condition $a_f = a_t$ is drawn as a visual aid.

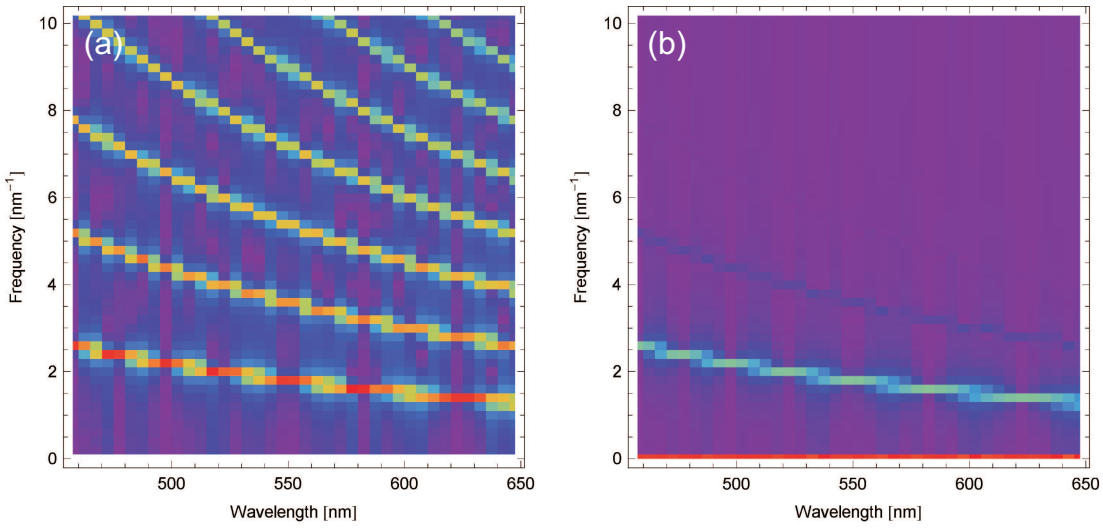

Figure 5.9: SFT of the computed transmission spectrum shown in figure 4.7 for (a) $\alpha = 0.9$, $T = 0.9$ and (b) $\alpha = 0.1$, $T = 0.1$.

resonance for plot (a) in figure 4.7. It can be concluded that the higher Q factor transmission curves do have higher frequency components since the form of the curve deviates more from a perfect sinusoidal curve. Finally, it is important to note that it is possible to apply this method to investigate the broad fluorescence coupled into such a resonator system by a quantum emitter on the surface of the resonator.

5.4 Experimental methods

5.4.1 Fabrication of toroidal resonators

The toroidal cavities are manufactured using a lithographic method similar to the techniques introduced by Armani *et al* [114]. The toroids used in this work are produced as part of a co-operation with the Paul-Drude-Institute for solid state physics in Berlin, Germany. The exact process parameters for our implementation and a much more in depth discussion of the process can be found in the diploma thesis of Tim Schröder [140]. Only a short summary is given at this point to provide an overview of the production method.

Commercially available, thermally oxidized, two inch, bohr-doped silicon wafers (Si-Mat GmbH, Germany) are used. The silica layer has a thickness of $2\,\mu$m and constitutes the silica for the toroids. The lithographic production process involves 9 individual steps:

1. **Wafer cleaning** The wafers are thoroughly cleaned using purified water.
2. **Gold coating** A 50 nm thick gold layer is evaporated onto the wafer. This acts as an additional adhesive for the resist during the hydrofluoric silica etching. (cf. figure 5.10 (a))
3. **Resist coating** A layer of positive resist is spin-coated onto the wafer (cf. figure 5.10 (b)).
4. **Exposure** The photoresist is exposed at 360 nm using a contact mask (cf. figure 5.10 (c)).
5. **Development and removal of gold coating** Then exposed photoresist is removed by a solvent. Then gold on the silica layer of the wafer is chemically removed (cf. figure 5.10 (c)).
6. **HF etching** Hydrofluoric acid (40%) is used to dissolve the silica layer at the exposed regions (cf. figure 5.10 (d)).
7. **Resist and gold coating removal** In this step, the remaining resist and also the gold coating is removed. Afterwards the wafer is cleaned again by purified water. Clean silica and silicon surfaces are obtained (cf. figure 5.10 (e)).
8. **Reactive ion-etching** Smaller pieces of the wafer are placed in a reactive ion-etching chamber. The etching chemical SF_6 is ionized and flushed across the wafer. This isotropic silicon etching method results in undercut silica disks supported by silicon stems since SF_6 does not affect silica (cf. figure 5.10 (f)).
9. **Melting disks to toroids** In the final step, a focused CO_2 laser is used to heat the silica disk. Silicon is a very good heat conductor. Therefore the process is self-terminating as the heat is transferred away from the disc close to the Si-pedestal (cf. figure 5.10 (h)).

By changing the diameter of the lithographically structured silica disks, it is possible to produce a wide range of different sized toroids. The high degree of precision in this lithographic process results in highly reproducible optical toroidal microresonators.

5.4.2 Optical setup

An intricate optical setup is used to support the manipulation and transfer of DNCs from tapers to toroids while at the same time it offers optical access to the assembled system to investigate its optical properties. An overview of the different components can be found in figure 5.11. The flexibility of the setup is guaranteed by the use of flip mirrors that allow for different functionalities to be added without the need for re-alignment of the optical system. In the following the individual subsystems are discussed:

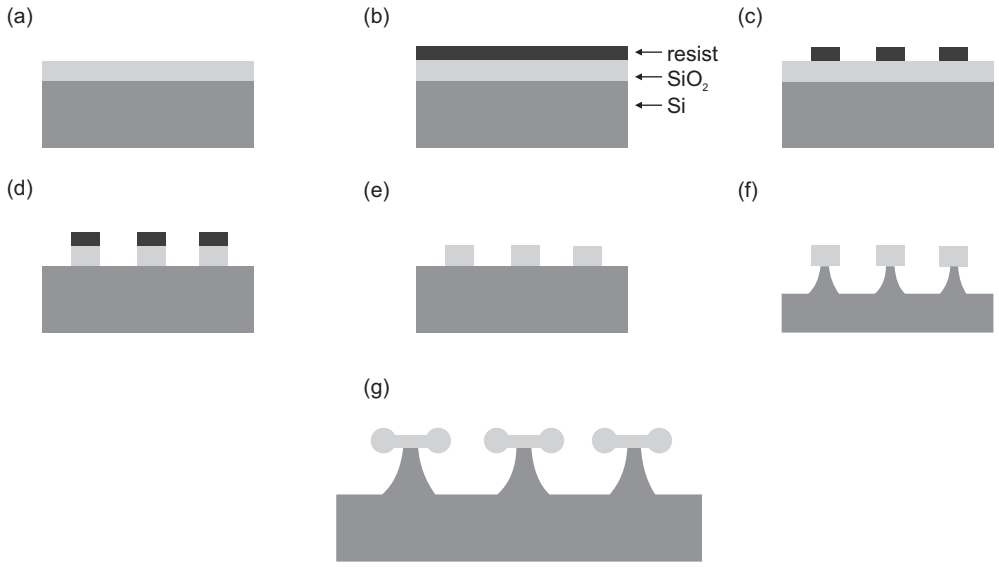

Figure 5.10: Illustration of the individual steps involved in the production of toroidal microresonators.

Sample Chamber: The silicon wafer with the toroids is placed on a 6-axis manipulation stage. The three fundamental axes can be adjusted with piezo precision actuators (miniTritor, Piezo-System-Jena GmbH, Germany). The sample is contained in a perspex enclosure to create a protective environment. The wafer itself is inserted via a small slit into the chamber. Optical access to the toroid is established by a fiber taper contained inside the chamber and also by a microscope objective. A photo of this part of the setup can be found in figure 5.12. The precise alignment of the wafer plane with the taper is vital for successful coupling of the taper to a toroid. A reflective-light microscope is used to aide the coarse alignment process as shown in the photograph.

Imaging: For the manipulation process of individual DNCs it is important to obtain images of high quality. The challenge here is to be able to image an individual DNC with a size of about 100 nm while at the same time being able to identify certain regions on toroids with diameters of about 60 μm or larger. A high quality microscope objective (Zeiss, 100x, NA 0.75, working distance 10.6 mm) is used and allows for resolving structures below 1 μm. The sample is illuminated by a simple Köhler-illumination scheme. In order to reduce chromatic abberations and to increase further the optical resolution, a red LED-based light source is used.
For imaging, two different CCD-cameras have been used. The first camera (WAT-120 N, Wartec) was equipped with an $f = 100$ mm lens barrel resulting in an optical magnification of 50× and a field of view (FOV) of about 100 μm. This camera was ideal for selecting individual toroids from the silicon wafer sample and imaging the overall alignment process of toroid and taper. Additionally, a highly sensitive camera (ORCA-ER, Hamamatsu) is used for fluorescence imaging. A lens barrel of $f = 200$ mm was placed in front of the camera. Increased magnification of up to 100× aids the identification of fluorescing DNCs.

Exitation laser: A fiber coupled pump laser is used to excite fluorescing particles on the sample. Two pump lasers are available emitting at 514 nm (argon-ion gas laser, Spectra Physcis) and 532 nm (Verdi V, Coherent). The pump light is supplied to the setup by a single mode fiber and passed through a set of laser line filters before it is coupled into the detection beam path via an uncoated glass wedge (BK7, Thorlabs). The pump spot size on the sample can be varied from 1 μm to few tens of μm in diameter allowing for wide field fluorescent illumination by changing the distance between the lens and fiber end facet at the fiber coupler.

Beam steering: In addition to the ability to position the sample in front of the microscope objective it is important to be able to fine adjust the pump laser spot. This is achieved by using a precise mirror mount before the microscope objective. This forms a simple yet efficient manual beam steering tool.

By choosing this particular position in the optical setup, the excitation and detection path remain aligned.

Confocal microscope: The fundamental idea of a confocal microscope is to image the sample onto a narrow pinhole, which then acts as a spatial filter. Only light emerging form the focal point (lateral and longitudinal) on the sample may pass through the pinhole. This method dramatically increases the signal to noise ratio, and provides an effective method to suppress substrate fluorescence.
A pinhole (75 μm in diameter) fixed to a flip mount can be inserted between two imaging lenses ($f = 100$ mm) acting as a spatial filter.

Taper access: By placing the optical fiber taper within the sample chamber it is possible to use the taper as an optical probe to excite and collect light from the toroid or DNCs.
It is possible to couple light from a tunable Ti:sapphire laser (899-21 Ring Laser, Coherent) into the taper. At a later stage of the experiment the Ti:sappire laser has been replaced by an external cavity diode laser (Velocity, New Focus, see chapter 4.4.1). By scanning the laser frequency it is possible to investigate resonances of the microresonators. The transmission is monitored on a photodiode behind the taper. Additionally, light scattered by the toroid into the microscope objective is imaged onto another photodiode. This setup can be used to measure the Q factor of the resonator system. Furthermore, if the laser is not coupled into the fiber taper, it is possible to use the fiber taper as an optical probe to collect light from the toroid or fluorescing samples.

Spectral and photon-statistical measurements: The optical setup provides optical access to the sample via the microscope objective and a fiber taper probe. The light collected via both paths is further investigated using a spectrometer (Spectra Pro 500i, Acton Research) and also a Hanbury-Brown Twiss setup (HBT). The HBT setup consists of a non-polarizing 50:50 beamsplitter and two actively quenched avalanche photodiodes (SPCM-AQR-14, Perkin Elmer). The correlation is measured by a PC-based coincidence counter (TimeHarp 200, PicoQuant). For these measurements the scattered pump light is removed by a colored glass edge filter (OG550, Schott Glass).

5.4.3 Cryostat

The low temperature experiments are performed using a cold finger continuous flow cryostat (KONTI-Kryostat Typ Mikro, CryoVac, Germany), as shown in figure 5.13. The liquid helium enters the cryostat and is evaporated in the heat exchanger. The evaporation removes heat from the cold finger that is attached to the heat exchanger. Consequently, it is cooled down to liquid helium temperatures at about 4 K. In order to isolate the cold finger efficiently from the warm lab environment, it is placed within a vacuum. The sample is glued onto a gold-coated sample holder using silver-based conductive paint (Busch GmbH, Germany). It is attached to the cold finger within the vacuum chamber. The optical access is provided by an optical glass window and a microscope objective (Mitutoyo M Plan Apo, 100×, NA 0.7, working distance 6 mm). The optical setup to excite the sample and to investigate its fluorescence is very similar to the setup shown in figure 5.13. There is no optical taper access to the sample due to the small dimensions of the vacuum chamber.

5.5 Investigation of the optical properties of fiber taper-coupled microtoroids

Before a quantum emitter may be attached to a toroidal microresonator, it is important to establish the optical performance of the fiber taper-coupled microresonator system. In the following a couple of techniques are introduced that can be used prior to and during the deposition process.

5.5.1 Typical mode structure of toroids

A narrow-bandwidth tunable external cavity diode laser (ECDL, cf. section 4.4.1) is used to investigate the mode structure of a fiber taper-coupled microtoroid. The laser is scanned over a region of about 17 nm starting from 764.5 nm while the transmission is monitored on a photodiode. The recorded transmission spectrum is shown in figure 5.14.

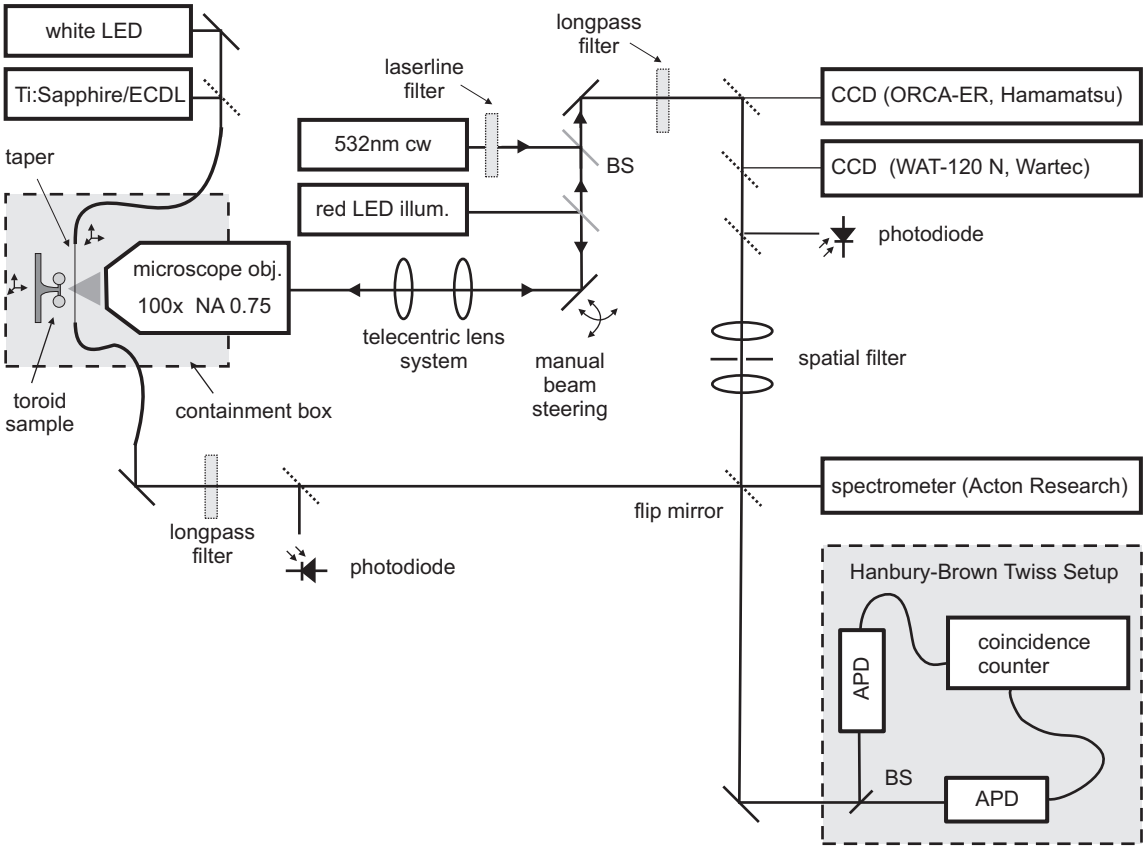

Figure 5.11: Schematic drawing of the optical setup used for coupling single DNCs to toroidal microresonators.

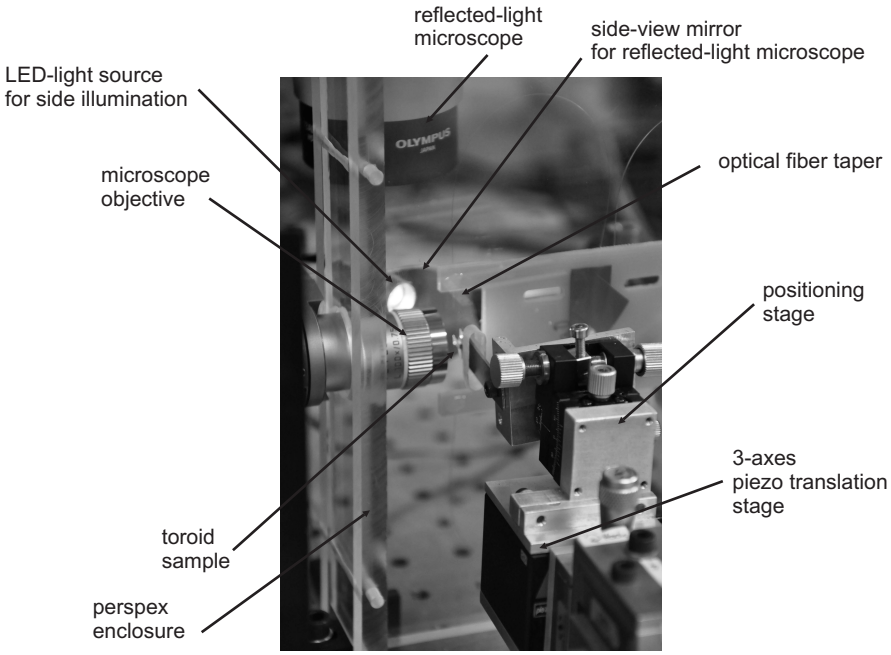

Figure 5.12: Photograph of perspex enclosure containing the optical taper and toroid sample.

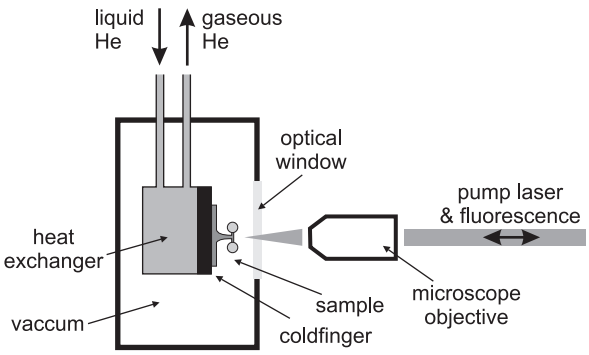

Figure 5.13: Schematic drawing of cryogenic setup used for spectroscopic investigation of DNCs.

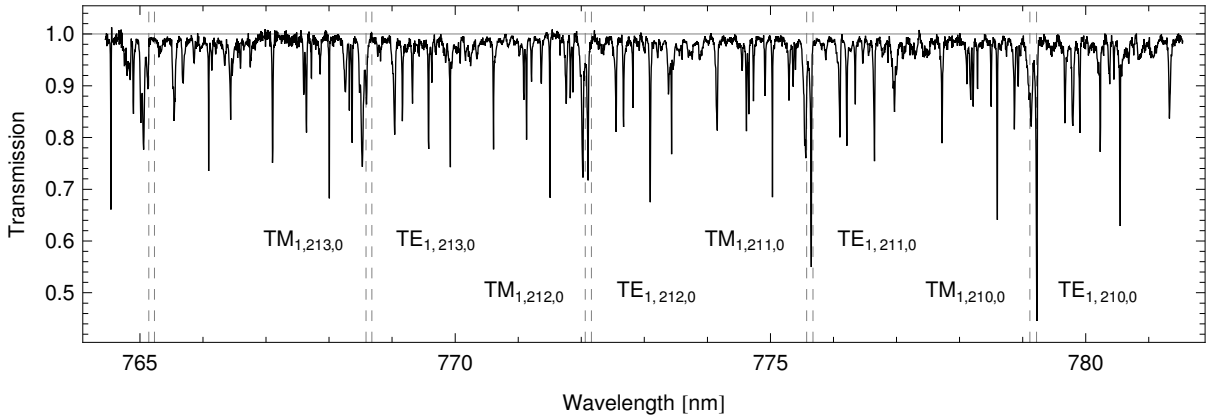

Figure 5.14: Transmission spectrum of a fiber taper-coupled microresonator (shown in figure 5.15) using the ECDL laser. Taper and toroid are not in contact. The spectrum is normalized to the taper transmission. The numerically calculated position of the $n = 1$, $|m - l| = 0$ modes are indicated by the vertically dashed lines and named individually.

The individual resonances corresponding to the optical modes of the toroid can be seen. The exact identification of the individual modes is difficult. An optical measurement of the dimensions of the toroid using a microscope image, as displayed in figure 5.15, can be used to supply the parameters for a numerical simulation. The results of such a simulation for the given toroid are shown in figure 5.7.

The error associated with optical measurements of the toroid's dimensions is far too large to determine the *absolute position* of an individual resonance in the spectrum precisely. The resonance wavelength of an individual resonance may be shifted by an entire free spectral range if the optical path length is varied by a distance as small as a wavelength. For instance, the resonance wavelength would shift over a range of $\lambda_{free} = 3.5\,\text{nm}$ at 779 nm if the optical path length changes by 779 nm.

The most prominent resonances in the transmission spectrum in figure 5.14 are associated with the fundamental TM and TE modes as indicated. The positions of the calculated resonances are shifted slightly to fit the resonance positions (cf. dashed vertical lines). The fit of the calculated resonances with the measured resonances are less precise for smaller wavelengths due to limitations in knowing the precise toroidal dimensions, as discussed in the previous paragraph. For a better fit of the resonance positions an iterative numerical process may be used. The other resonances in the transmission spectrum can be associated to higher optical modes of the toroid.

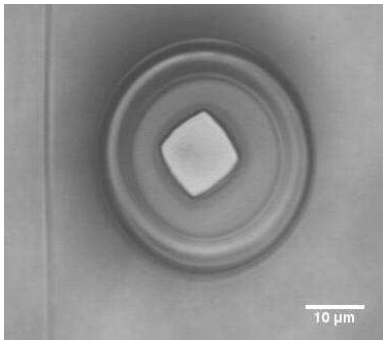

Figure 5.15: Microscope image of a microtoroid and an optical fiber taper corresponding to the recorded transmission spectrum in figure 5.14. Major diameter $d_T = 38\,\mu\text{m}$, minor diameter $d_t = 5\,\mu\text{m}$.

5.5.2 Q factor of selected toroids

Before any quantum emitters can be attached to a toroid a measurement of the Q factor provides crucial information about the quality of the resonator and the resonator-waveguide coupling. This forms a pre-selection criterion for the available resonators.

In principle, the Ti:sapphire laser or the ECDL, as demonstrated in section 5.5.1, can be used. However, the ECDL is much more simple to handle compared to the Ti:saphire laser, since it does not involve any adjustments of laser resonator mirrors in oder to coarse tune the laser wavelength. Additionally, mode-hop free operation is difficult to achieve using the Ti:sapphire laser in this mode of operation. However, during the earlier experiments only the Ti:sapphire laser was available.

Therefore, before deposition of a DNC the optical quality or Q factor of the fiber-coupled toroidal resonator is measured using the Ti:sapphire laser, which is scanned over a frequency range of 20 GHz. Figure 5.16 shows the scan across a narrow resonance with a Q factor of the order of 5×10^5 which is limited by imperfections in fabrication. This value is a typical value for the toroids and tapers used in these experiments. The asymmetric line shape is due to Fano interferences of modes in the toroid and multiple modes in the taper [141].

5.5.3 White light characterization of fiber taper-coupled toroids

As discussed in section 5.3.2 the white light transmission spectrum of a fiber taper-coupled microtoroid provides valuable information about the resonator system. In particular, the quality of the system may be estimated. Additionally, the interferometric effects caused by the toroid and the taper only can be separated. The identification of these two different sources of interference is of particular importance in order to be able to prove the coupling of fluorescence to a toroidal microresonator.

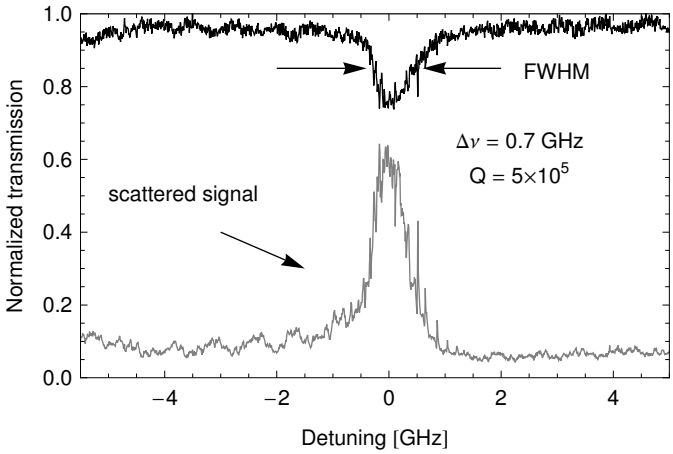

Figure 5.16: Toroid's resonance measured by a tunable Ti:Sapphire laser at 788.75 nm. Taper transmission (top) and scattered signal detected by the confocal microscope (bottom) are shown.

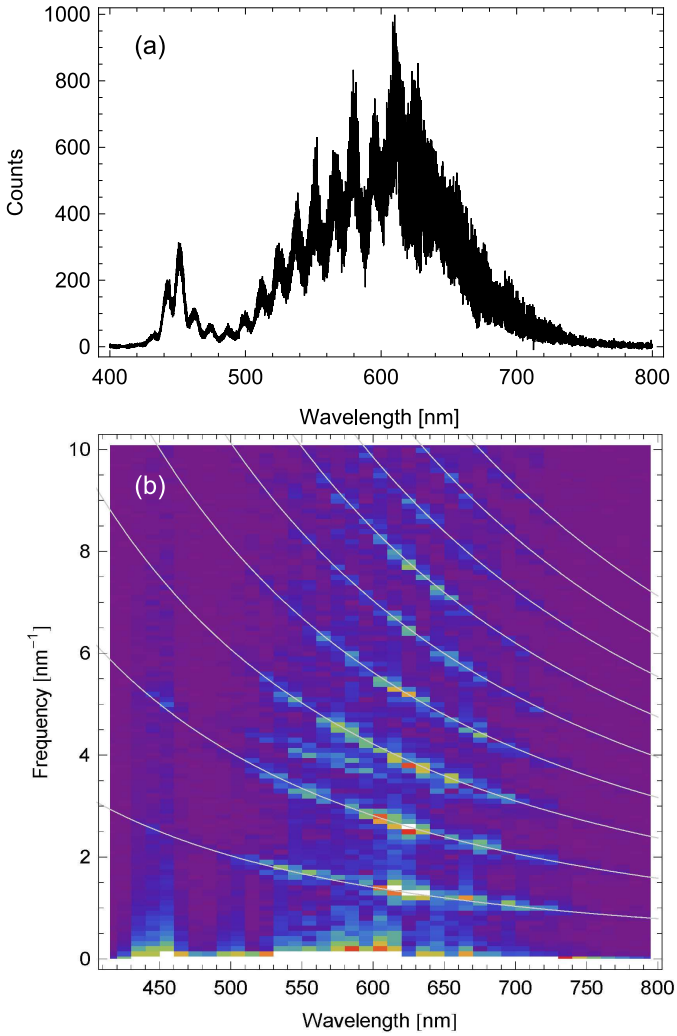

Figure 5.17: (a) White light transmission spectrum of a fiber taper-coupled microtoroid system and (b) the corresponding segmented Fourier transform (SFT). The white lines indicate the fitted free spectral range $\nu_{free} = c/(\pi d_T N_t)$ and multiple orders for a toroidal resonator with a major diameter $d_T = 112\,\mu$m. A white LED is used as the white light source.

Figure 5.17 (a) shows the typical white light transmission spectrum through a fiber taper coupled to a toroid. A white LED light source is coupled into the taper and the transmitted spectrum is dispersed in the spectrometer. The recorded spectrum shows the spectral intensity envelope of the white LED. However, the transmission spectrum shows also a very rapid oscillation. In order to identify the source of this interference effect the SFT technique is applied, as shown in figure 5.17 (b).

Up to eight different bands are visible in the plot corresponding to mode interference within the microtoroid. These bands have a frequency spacing corresponding to an integer multiple of the free spectral range, as indicated by the white lines. By using this fit, it is possible to estimate the optical path length and thus the diameter of the toroid. This value of $112\,\mu$m agrees well with the microscopically measured diameter of $111 \pm 1\,\mu$m, within the resolution of the microscope.

There is an additional interference effect visible between the second and the third band of the toroid interference. This effect originates from interfering taper modes. The same taper used in this experiment is investigated in section 2.5.4. A direct comparison of figure 2.22 which shows only the taper modes, with figure 5.17 clearly identifies the taper modes in both spectra. This technique proves to be valuable in identifying the source of interferometric effects.

5.6 Coupling of quantum emitters to microtoroids

The ability to couple quantum emitters or even single photon sources to toroidal mircoresonators is the first step to be able to observe CQED effects in toroids. In this section, firstly, the placement of a dye-doped fluorescing polystyrene bead is demonstrated. These results form the basis for the deposition of a DNC onto a microtoroid discussed in section 5.6.2.

5.6.1 Coupling a fluorescing bead to resonator modes

A taper is drop-coated using a diluted dispersion of 200 nm dye-doped polystyrene beads (69B1-2 molecular probes, Invitrogen) in ethanol. Small droplets are applied to the taper resulting in sparsely distributed beads on the taper surface. By mounting the taper as shown in figure 5.12 it is possible to transfer beads to the toroid by a sliding a bead on the taper past the rim of the toroid. The transfer procedure can easily be monitored by exciting the beads using the pump laser at 532 nm and imaging the fluorescence light on a CCD camera.

The microscope image in figure 5.18 (c) shows the successful transfer of a bead onto a toroid. The bead is excited using the pump laser and its florescence is coupled into the toroid and can be extracted via a fiber taper. A spectrum of the collected light can be seen in figure 5.18 (a). It shows the typical fluorescence spectrum of the dye that is strongly modulated. An SFT is applied to the spectrum in order to proove that the interferences originate from modes within the resonator. The results displayed in figure 5.18 (b) show clearly the typical band structure associated with the toroidal resonances and their higher frequency components, as discussed in section 5.5.3. The estimated diameter of the toroid according to the recorded spectrum is $95\,\mu$m. This agrees well with a diameter of $95.3 \pm 1\,\mu$m obtained from the microscopic image. This result proves that the fluorescence of the bead indeed couples to resonator modes within the toroid.

5.6.2 Transferring a pre-selected DNC onto a microtoroid

In order to transfer a DNC onto a toroid it is not possible to use the technique successfully used for polystyrene beads, as described in the previous section. Drop-coated DNCs tend to stick together and form small aggregations of DNCs on the taper surface. An additional problem arises in identifying an individual DNC containing a single NV center, since only about one in ten DNCs contain an NV center (100 nm, MicroDiamant, Switzerland). This makes it very unlikely for a single DNC to be suitably positioned on the surface of the taper.

A different transfer scheme is adopted allowing for pre-section of individual DNCs. A donor fiber, acting as a DNC reservoir, is made from a small piece of stripped, standard optical fiber with a diameter of $125\,\mu$m, that was cleaned in an ultrasonic bath of alkaline detergent before being dipcoated with 100 nm DNCs (MicroDiamant, Switzerland).

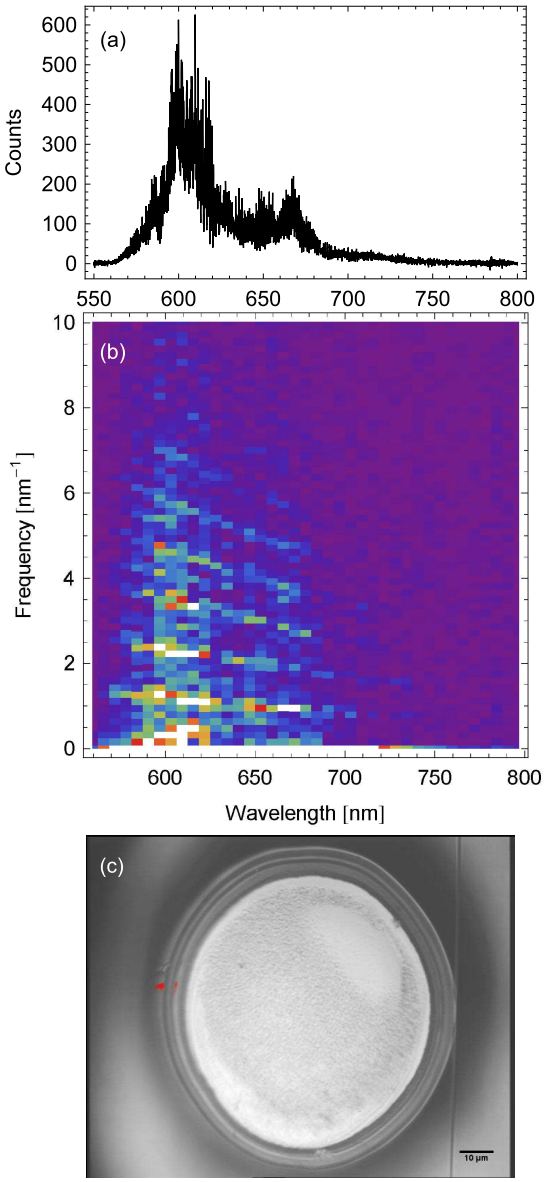

Figure 5.18: (a) Spectrum of coupled fluorescence collected through a fiber taper, (b) segmented Fourier transform (SFT) of coupled fluorescence spectrum, (c) composed microscope image showing the fiber-coupled toroid. The red area in the microscope image shows the position of the beads. The fluorescence from the beads is recorded separately and is superimposed onto the image using a masking technique. The taper can be seen to the right of the toroid.

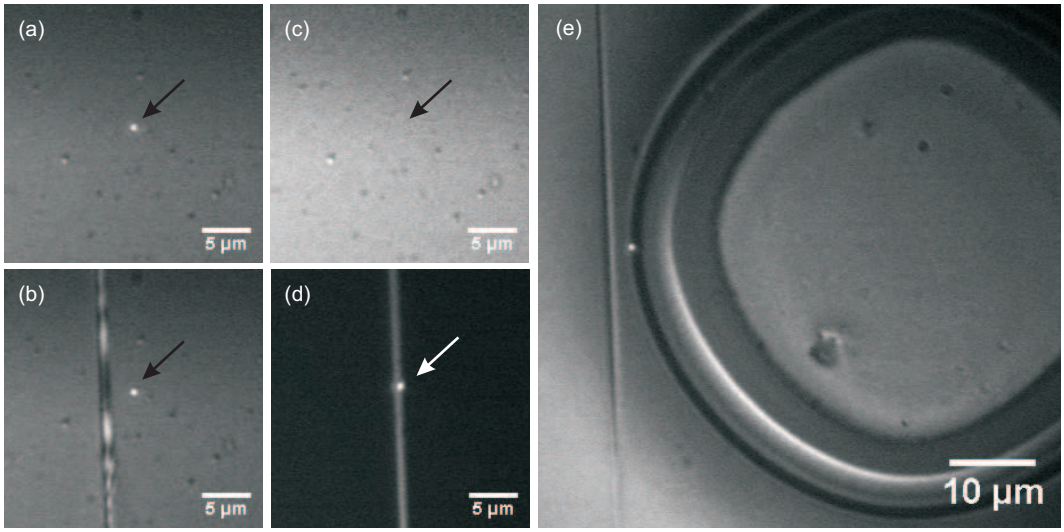

Figure 5.19: Manipulation of a single 100 nm DNC: (a) selected DNC on donor fiber, (b) taper is brought into contact with donor fiber, (c) donor fiber without lifted-off DNC, (d) DNC on fiber taper, (e) DNC placed on toroid. In all images the DNC is optically excited using the pump laser at 532 nm.

Figure 5.19 (a) shows an image of the fiber surface coated with DNCs. By moving and rotating the donor fiber, it is possible to access each DNC on the surface of the fiber, as seen in the cartoon in Figure 5.20. The manipulation process is imaged by the CCD camera in real time. Already at this point it is possible to investigate the optical properties of individual DNCs using the optical setup described in section 5.4.2. The confocal microscope equipped with a spectrometer and a Hanbury-Brown Twiss correlator can be used to analyze the fluorescence and to pre-select individual DNCs. Once a suitable DNC is found the fiber taper is brought into contact with the surface of the donor fiber. The point of contact is indicated by the interference fringes in the fiber taper shown in figure 5.19 (b). By sliding the taper along the donor fiber the DNC can be picked-up as shown in figures 5.19 (c) and (d). Finally, the same technique can be used to deposit the DNC on the outer rim of the toroid (see figure 5.19 (e)).

5.6.3 Coupling NV centers to resonator modes

In order to obtain coupling to modes with highest Q the DNC is placed close to the rim of the toroid. There the overlap with the evanescent field from a fundamental whispering gallery mode is maximal. The corresponding computed radial field distribution for a toroid of the used dimensions is shown in figure 5.6. By integrating the field inside and outside of the toroid it is possible to calculate the evanescent field fraction. For the given toroid the fraction of the mode's intensity is only 0.5%. However, this can be increased for smaller toroid sizes.

The DNC is then excited at 532 nm using the confocal microscope, and its fluorescence is collected by the taper coupler with a diameter of 900 nm, and spectrally dispersed by the spectrometer. The recorded spectrum is displayed as the blue curve in figure 5.21 (a). A clear modulation revealing coupling to individual high-Q modes is apparent. For comparison fluorescence from the DNC which is not collected by the fiber coupler and emitted in free space is detected by the confocal microscope. It is plotted as the red curve in figure 5.21 (a). The lack of modulation in this spectrum shows that the amount of light from the resonator modes scattered by the DNC into the direction of the microscope objective is small compared to the direct fluorescence from the DNC [3].

For a quantitative analysis we divided the spectrum collected via the taper into 10 nm wide segments and performed a Fourier transform. The frequency amplitude for each transform is color coded and plotted in figure 5.21 (b). A number of horizontal bands are visible corresponding to the Fourier components of the toroid's resonances. They are evenly spaced at an integer multiple of the corresponding free spectral range of the toroid, as indicated by the fitted white lines corresponding to a toroid diameter of $d_T = 65\,\mu$m. This is in agreement with the microscopically measured diameter of $64.3 \pm 1\,\mu$m.

In another experiment, light from the Ti:Sapphire laser is coupled via the fiber taper into the toroid,

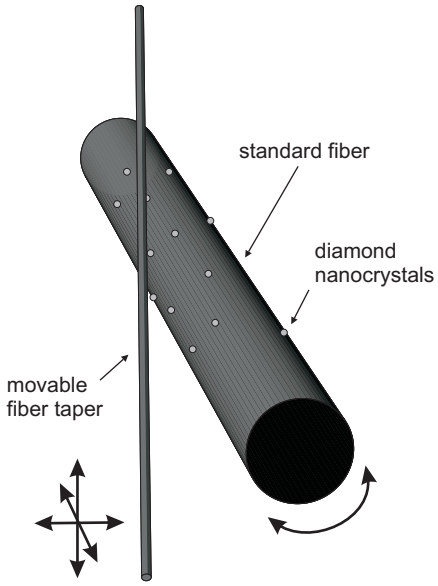

Figure 5.20: Schematic drawing of the mechanical setup used for selecting an individual DNC from the surface of the donor fiber.

as shown in the microscope image in figure 5.22. The laser light is scattered by the DNC on the toroid, indicating that the DNC is interacting with the evanescent fields of the toroid.

These results prove that the fluorescence of the DNC couples to resonator modes within the toroid.

5.6.4 Photon statistics of NV centers

In order to determine the actual number of NV centers in the DNC the second order correlation function $g^{(2)}$ is measured using the HBT setup and shown in figure 5.23. The antibunching indicates that non-classical light is generated by the DNC. The $g^{(2)}$ function for M single photon emitters is given by equation (5.1). By fitting this function to the measured data $M = 6.2 \pm 0.3$ is obtained indicating that at least [134] 6 NV centers are contained inside the DNC.

5.6.5 Low temperature spectroscopy

For a controlled CQED experiment coupling of a single optical transition to a resonator mode is required. In solid-state systems cooling is necessary to reduce homogeneous broadening due to thermal phonons. However, it is worth noting that, similar to single molecule experiments [142], inhomogeneous broadening can be exploited to spectrally select a single emitter out of an ensemble.

In order to demonstrate the feasibility of such an approach, and also to confirm the number of $M = 6$ NV centers in the deposited DNC, we performed fluorescence measurements at cryogenic temperatures. The toroid with the deposited DNC was mounted inside the continuous flow cold finger cryostat discussed in section 5.4.3 and cooled down to approximately liquid helium temperature.

The measured spectrum in figure 5.24 shows the enhancement of the zero phonon lines (ZPLs) compared to the phonon side bands. Five individual lines are clearly distinguishable. The asymmetry of the line at 637.5 nm indicates a possible overlap of two ZPLs not resolvable due to a finite spectrometer resolution. Thus, the number of observed ZPLs is in agreement with 6 NV centers in the DNC. Also, the separation of the individual lines clearly shows that coupling to single resonator modes is possible. This relaxes the requirement to isolate exactly one NV center in a single DNC for a controlled CQED experiment. It is also important to note that cooling of a DNC on a toroid is possible without the need exchange gas to improve thermal coupling.

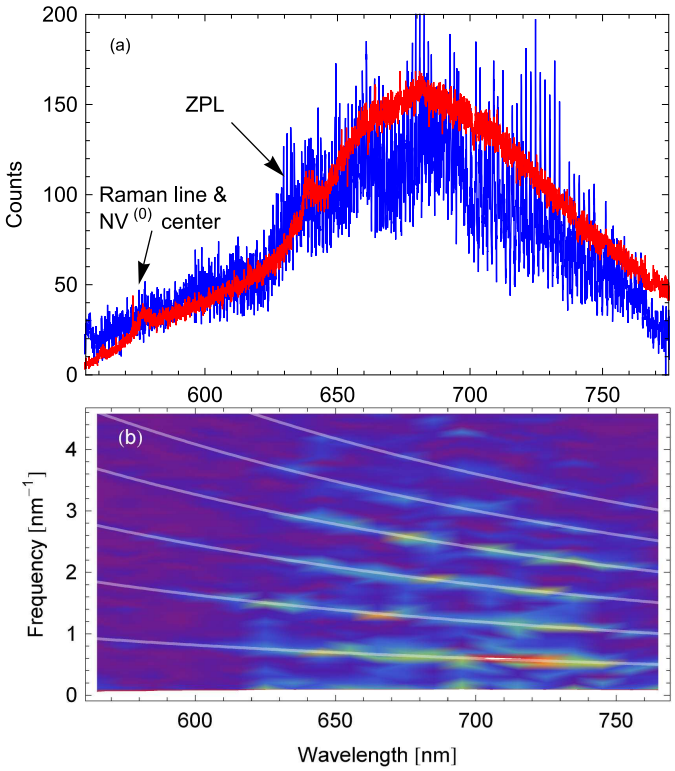

Figure 5.21: (a) Confocal (red, unmodulated, 10 s, 266 μW, scaled by 0.42) and taper-collected (blue, modulated, 60 s, 150 μW) photoluminescence spectra of the DNC on the toroid, (b) segmented Fourier transform (SFT) of the taper collected spectrum with 10 nm segment width. White lines are fits to the free spectral range expected from a toroid with major diameter $d_T = 65\,\mu$m and minor diameter $d_t = 5\,\mu$m.

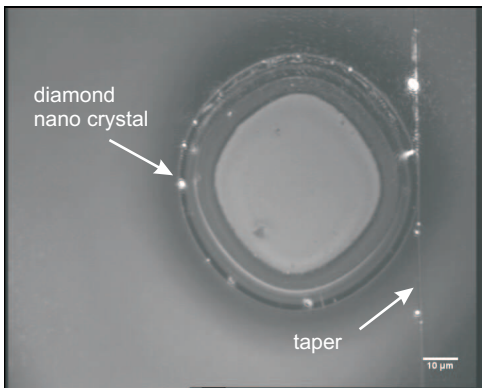

Figure 5.22: Microscope image of diamond scattering light from the mode of the toroid, while the Ti:sapphire laser is coupled to the resonator. Bright spots correspond to scattering centers as imperfections in the glass structure or contaminations.

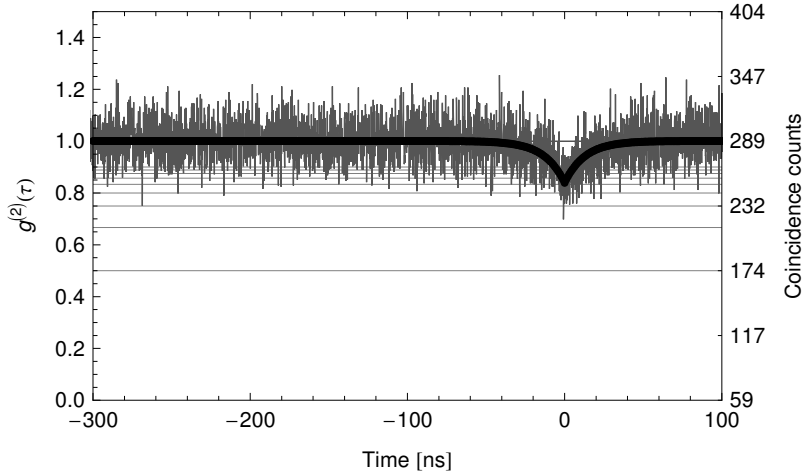

Figure 5.23: Measured second-order correlation $g^{(2)}$- function for the DNC placed on the torroid. The normalization and background subtraction was carried out in accordance with referrence [129] based on the following experimental parameters: integration time of 6120 s, pump power 170 μW, signal to noise ratio of 10 and an average count rate of 20 kcounts/s per detector. The horizontal grid lines are spaced in $1 - 1/M$ distance indicating the number of NV centers.

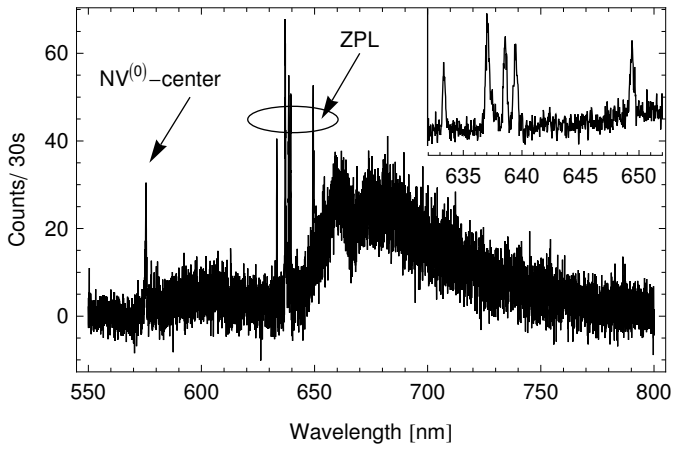

Figure 5.24: Fluorescence spectrum of the deposited DNC at liquid helium temperature. Excitation power was 2 mW. The inset shows a zoom-in around the ZPLs.

5.7 Conclusion

In summary, a technique is demonstrated to select individual DNCs and to position them on-demand on a toroidal microresonator. Coupling of non-classical light emission from 6 NV centers in the DNC to high-Q modes was achieved. It is argued that the typical inhomogeneous broadening in DNCs can be exploited to achieve single mode coupling even with a larger number of NV centers in the DNC. This also relaxes the need to design the mode structure of the resonator for one specific ZPL line.

Chapter 6

Outlook

Fiber tapers are a crucial building block facilitating experiments as well as applications in sensing and cavity quantum electrodynamics. The performed experiments revealed fascinating aspects of optically-coupled microresonator physics that should be pursued. In the following, possible intriguing avenues of future research are highlighted.

6.1 Functionalizing of fiber taper

In principle, a great variety of particles that can be brought into a suspension can be trapped, preselected, and deposited on fiber tapers or on other fragile micro- and nanophotonic components. Therefore, this method allows for a versatile non-contact functionalization of fiber-coupled photonic components with active particles, e.g. for sensing applications or as fundamental light sources, such as single photon sources [20, 3].

In future experiments, it is of great interest to investigate the possibility of depositing particles on more complicated photonic structures, such as microresonators. This can be achieved by using lateral position precision of the Paul trap itself or guided deposition by changing the surface charge distribution using focused UV light.

6.2 Taper-coupled microresonator for sensing application

The main focus for future development lays on the improvement of the coupling of individual spheres. Additionally, it is interesting to investigate the coupling of multiple resonators with each another when multiple spheres are attached to the same taper.

Due to contact coupling and eccentricity splitting the individual modes are difficult to separate. The polystyrene sphere could be chemically coated by a thin layer of a much lower refractive index. This few hundert nanometers thick layer would effectively act as a spacer between the resonator sphere and the taper. It is expected that such measures would improve the mode coupling substantially. An illustration of the geometry is shown in figure 6.1.

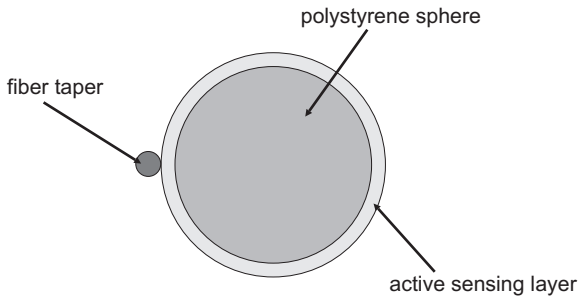

Figure 6.1: Schematic cross-section of a fiber taper-coupled polystyrene sphere that is coated with a thin spacing layer.

This layer could be doped with chemically sensitive substances to indicate certain trace gases [113] or binding events of bio molecules [70]. By attaching multiple spheres sensitive to different substance a very compact integrated highly specific sensor system can be envisioned.

Highly stable optical resonators are a resource for many metrological application, e.g. as a frequency reference. The high frequency stability of the resonator system has been successfully been demonstrated (cf. section 4.5.8). Therefore, is interesting to explore the limits of this stability and in particular the thermal self-locking properties of the microresonator [102].

Finally, it would be possible to couple the modes of the individual spheres to another resonator via the fiber taper. This would allow the study of multiple coupled-resonator physics [143], like dispersion properties or mode-splitting effects.

6.3 CQED with toroidal microresonators

The ability to couple strongly an atomic resonance to an high quality cavity forms the framework for application in quantum information processing. Chip-based micro toroidal resonators are due to their scalability and high quality optical properties a very interesting candidate. First results in this area have already been presented [144, 122]. Caesium atoms have been coupled strongly to a microtoroid. This is an important step to show the feasibility of this approach.

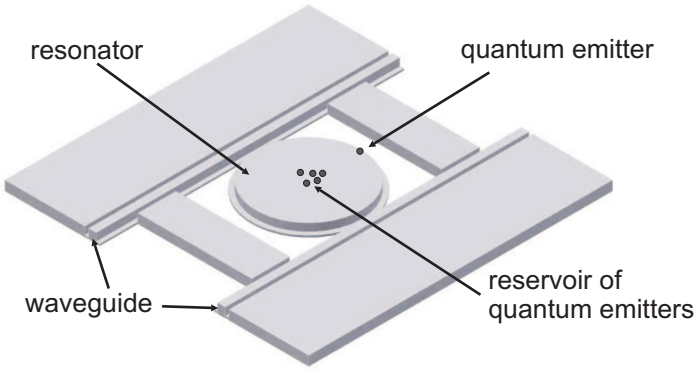

Figure 6.2: Schematic drawing of an integrated silica structure consisting of a disk resonator, waveguides and a coupled quantum emitter. Individual quantum emitters can be manoeuvered to the optimum position (here at the rim of the disc) with probe-based manipulation techniques, e.g. AFM manipulation [64].

However the main drawback is the need for a magnetically optical trap in ultra high vacuum to place the atoms on the toroid. Our approach using DNCs is much more robust. The challenge resides in achieving optimal coupling of the NV center to the resonator mode by precise positioning of the DNC. A rough positioning can be achieved by using a fibre taper, as discussed in section 5.6.2. However, the topology of the toroid poses a difficulty to conventional probe techniques like atomic force microscopes (AFM) for a more precise positioning. AFMs have successfully be used on planar structures [64].

An appealing alternative is to switch to a planar resonator geometry. Figure 6.2 illustrates a possible design of of such an intergraded disk resonator design including waveguides. Since the system would be made from silica on silicon it is possible to rely on advanced manufacturing techniques for silicon. On these planar structure DNCs are expected to be positioned using an AFM, as shown in figure 6.2. However, the achievable Q factors for such new structures are yet unknown.

Apart from such a planar resonator geometry, a DNC-coupled toroid system posses potential for future applications in quantum information application. In order to estimate the coupling efficiency of the NV to the resonator mode, the Pucell factor can be measured. This is achieved by measuring the radiative decay time of the NV center during the manipulation. Such an experiment would ultimately determine the coupling regime the system and thus explore the limits of this resonator-emitter system.

For a significant coupling rate to the resonator the NV center and thus the entire system has to be cooled to liquid helium temperature in order to reduce the linewidth of the NV center to the linewidth of the resonator (cf. section 5.6.5). There are different approaches to shift the atom and cavity resonance to

coincide. For instance, Stark tuning [145] of the zero phonon line of the NV center has been demonstrated. The required electrodes for applying the electric field to the DNC on the rim of the toroid can be placed in a further lithographic step onto the toroid. Additionally it is possible to tune the resonance frequency of the toroid by nitrogen condensation [18]. These would be the next steps for demonstrating the potential of fiber taper-coupled microtorid systems.

Appendix A

Vector field components, normalization constants and mode cut-off diameters

A.1 Field components

In chapter 2 the individual eigenmodes of a step-index fibre are derived. A summary of the vector field components of the TM, TE and hybrid modes are listed below following reference [22].

A.1.1 TM components

	Core	Cladding
e_z	$i\frac{U}{\beta a_{co}}\frac{J_0(Ur/a_{co})}{J_1(U)}$	$-i\frac{N_{co}^2}{N_{cl}^2}\frac{W}{\beta a_{co}}\frac{K_0(Wr/a_{co})}{K_1(W)}$
e_r	$\frac{J_1(Ur/a_{co})}{J_1(U)}$	$\frac{N_{co}^2}{N_{cl}^2}\frac{K_1(Wr/a_{co})}{K_1(W)}$
h_ϕ	$\sqrt{\frac{\epsilon_0}{\mu_0}}\frac{N_{co}^2}{N_{eff}}\frac{J_1(Ur/a_{co})}{J_1(U)}$	$\sqrt{\frac{\epsilon_0}{\mu_0}}\frac{N_{co}^2}{N_{eff}}\frac{K_1(Wr/a_{co})}{K_1(W)}$

By definition, all other components of a TM mode must vanish, i.e. $h_z = e_\phi = h_r = 0$.

A.1.2 TE components

	Core	Cladding
h_z	$i\sqrt{\frac{\epsilon_0}{\mu_0}}\frac{U}{ka_{co}}\frac{J_0(Ur/a_{co})}{J_1(U)}$	$-i\sqrt{\frac{\epsilon_0}{\mu_0}}\frac{W}{ka_{co}}\frac{K_0(Wr/a_{co})}{K_1(W)}$
e_ϕ	$-\frac{J_1(Ur/a_{co})}{J_1(U)}$	$-\frac{K_1(Wr/a_{co})}{K_1(W)}$
h_r	$N_{eff}\sqrt{\frac{\epsilon_0}{\mu_0}}\frac{J_1(Ur/a_{co})}{J_1(U)}$	$N_{eff}\sqrt{\frac{\epsilon_0}{\mu_0}}\frac{K_1(Wr/a_{co})}{K_1(W)}$

By definition, all other components of a TE mode must vanish, i.e. $e_z = e_r = h_\phi = 0$.

A.1.3 Hybrid mode components

	Core	Cladding	ϕ
e_r	$-\left\{\frac{a_1 J_{\nu-1}(Ur/a_{co})+a_2 J_{\nu+1}(Ur/a_{co})}{J_\nu(U)}\right\}$	$-\frac{U}{W}\left\{\frac{a_1 K_{\nu-1}(Wr/a_{co})-a_2 K_{\nu+1}(Wr/a_{co})}{K_\nu(W)}\right\}$	$f_\nu(\phi)$
e_ϕ	$-\left\{\frac{a_1 J_{\nu-1}(Ur/a_{co})-a_2 J_{\nu+1}(Ur/a_{co})}{J_\nu(U)}\right\}$	$-\frac{U}{W}\left\{\frac{a_1 K_{\nu-1}(Wr/a_{co})+a_2 K_{\nu+1}(Wr/a_{co})}{K_\nu(W)}\right\}$	$g_\nu(\phi)$
e_z	$-i\frac{U}{\beta a_{co}}\frac{J_\nu(Ur/a_{co})}{J_\nu(U)}$	$-i\frac{U}{\beta a_{co}}\frac{K_\nu(Ur/a_{co})}{K_\nu(U)}$	$f_\nu(\phi)$
h_r	$\sqrt{\frac{\epsilon_0}{\mu_0}}\frac{N_{co}^2}{N_{\mathit{eff}}}\left\{\frac{a_3 J_{\nu-1}(Ur/a_{co})+a_4 J_{\nu+1}(Ur/a_{co})}{J_\nu(U)}\right\}$	$\sqrt{\frac{\epsilon_0}{\mu_0}}\frac{N_{co}^2}{N_{\mathit{eff}}}\frac{U}{W}\left\{\frac{a_5 K_{\nu-1}(Wr/a_{co})+a_6 K_{\nu+1}(Wr/a_{co})}{K_\nu(U)}\right\}$	$g_\nu(\phi)$
h_ϕ	$-\sqrt{\frac{\epsilon_0}{\mu_0}}\frac{N_{co}^2}{N_{\mathit{eff}}}\left\{\frac{a_3 J_{\nu-1}(Ur/a_{co})+a_4 J_{\nu+1}(Ur/a_{co})}{J_\nu(U)}\right\}$	$-\sqrt{\frac{\epsilon_0}{\mu_0}}\frac{N_{co}^2}{N_{\mathit{eff}}}\frac{U}{W}\left\{\frac{a_5 K_{\nu-1}(Wr/a_{co})-a_6 K_{\nu+1}(Wr/a_{co})}{K_\nu(U)}\right\}$	$f_\nu(\phi)$
h_z	$-i\sqrt{\frac{\epsilon_0}{\mu_0}}\frac{UF_2}{ka_{co}}\frac{J_\nu(Ur/a_{co})}{J_\nu(U)}$	$-i\sqrt{\frac{\epsilon_0}{\mu_0}}\frac{UF_2}{ka_{co}}\frac{K_\nu(Wr/a_{co})}{W_\nu(U)}$	$g_\nu(\phi)$

The parameters are given by

$a_1=\frac{F_2-1}{2}$	$a_2=\frac{F_2+1}{2}$	$a_3=\frac{F_1-1}{2}$
$a_4=\frac{F_1+1}{2}$	$a_5=\frac{F_1-1+2\Delta}{2}$	$a_6=\frac{F_1+1-2\Delta}{2}$
$F_1=\left(\frac{UW}{V}\right)^2\frac{b_1+b_2(1-2\Delta)}{\nu}$	$F_2=\left(\frac{V}{UW}\right)^2\frac{\nu}{(b_1+b_2)}$	
$b_1=\frac{J'_\nu(U)}{UJ_\nu(U)}$	$b_2=\frac{K'_\nu(W)}{WK_\nu(W)}$	$\Delta=\frac{1}{2}\left(1-\frac{N_{cl}^2}{N_{co}^2}\right)$.

The prime denotes the derivative in respect to the argument. All other variables are defined as introduced in chapter 2.

A.2 Normalization constants

A summary of the normalization constants for the TM, TE and hybrid modes are listed below following ref. [22]. The normalization constants for the TM modes are

$$C_{co}=\frac{\pi a_{co}^2}{2}\sqrt{\frac{\epsilon_0}{\mu_0}}\frac{kN_{co}^2}{\beta}\left\{1-\frac{J_0(U)J_2(U)}{J_1^2(U)}\right\}$$
$$C_{cl}=-\frac{\pi a_{co}^2}{2}\frac{N_{co}^2}{N_{cl}^2}\sqrt{\frac{\epsilon_0}{\mu_0}}\frac{kN_{co}^2}{\beta}\left\{1-\frac{K_0(W)K_2(W)}{K_1^2(W)}\right\}.$$

The normalization constants for the TE modes are

$$C_{co}=\frac{\pi a_{co}^2}{2}\sqrt{\frac{\epsilon_0}{\mu_0}}\frac{\beta}{k}\left\{1-\frac{J_0(U)J_2(U)}{J_1^2(U)}\right\}$$
$$C_{cl}=-\frac{\pi a_{co}^2}{2}\sqrt{\frac{\epsilon_0}{\mu_0}}\frac{\beta}{k}\left\{1-\frac{K_0(W)K_2(W)}{K_1^2(W)}\right\}.$$

For the hybrid modes the normalization constant is given by

$$C_{co}=\frac{\pi a_{co}^2}{2}\sqrt{\frac{\epsilon_0}{\mu_0}}\frac{kN_{co}^2}{\beta}\times \left\{\frac{a_1a_3(J_{\nu-1}^2(U)-J_\nu(U)J_{\nu-2}(U))+a_2a_4(J_{\nu+1}^2(U)-J_\nu(U)J_{\nu+2}(U))}{J_\nu^2(U)}\right\}$$
$$C_{cl}=-\frac{\pi a_{co}^2}{2}\sqrt{\frac{\epsilon_0}{\mu_0}}\frac{kN_{co}^2}{\beta}\times \left\{\frac{a_1a_5(K_{\nu-1}^2(W)-K_\nu(W)K_{\nu-2}(W))+a_2a_6(K_{\nu+1}^2(W)-K_\nu(W)K_{\nu+2}(W))}{(W^2/U^2)K_\nu^2(W)}\right\}.$$

A.3 Mode cut-off diameter

As discussed in section 2.2.3 the cut-off frequencies for the individual modes can be calculated. In table A.1 the cut-off frequencies and also the corresponding cut-off taper diameter for selected wavelengths are shown for the first 27 fiber modes.

Table A.1: Cut-off frequencies and corresponding taper diameters for selected wavelengths based on equation (2.2.3) for $\Delta = 0.26$ (air-clad taper). The normalized frequency V for a given solution U can be found by noting that $V = U$ at the cut-off point.

mode	U	a_{co}/λ	$a_{co}/532\,\mathrm{nm}$ [μm]	$a_{co}/637\,\mathrm{nm}$ [μm]	$a_{co}/780\,\mathrm{nm}$ [μm]	$a_{co}/1300\,\mathrm{nm}$ [μm]	$a_{co}/1500\,\mathrm{nm}$ [μm]
HE_{11}	-	-	-	-	-	-	-
TM_{01}, TE_{01}	2.40	0.37	0.20	0.24	0.29	0.48	0.55
HE_{21}	2.75	0.42	0.23	0.27	0.33	0.55	0.63
EH_{11}, HE_{12}	3.83	0.59	0.31	0.37	0.46	0.77	0.88
HE_{31}	4.24	0.65	0.35	0.41	0.51	0.85	0.98
EH_{21}	5.14	0.79	0.42	0.50	0.62	1.03	1.18
TM_{02}, TE_{02}	5.52	0.85	0.45	0.54	0.66	1.10	1.27
HE_{41}	5.57	0.86	0.46	0.54	0.67	1.11	1.28
HE_{22}	5.70	0.88	0.47	0.56	0.68	1.14	1.31
EH_{31}	6.38	0.98	0.52	0.62	0.76	1.27	1.47
HE_{51}	6.83	1.05	0.56	0.67	0.82	1.36	1.57
EH_{12}, HE_{13}	7.02	1.08	0.57	0.69	0.84	1.40	1.62
HE_{32}	7.29	1.12	0.60	0.71	0.87	1.46	1.68
EH_{41}	7.59	1.17	0.62	0.74	0.91	1.52	1.75
HE_{61}	8.05	1.24	0.66	0.79	0.96	1.61	1.85
EH_{22}	8.42	1.29	0.69	0.82	1.01	1.68	1.94
TM_{03}, TE_{03}	8.65	1.33	0.71	0.85	1.04	1.73	1.99
HE_{42}	8.74	1.34	0.71	0.86	1.05	1.75	2.01
EH_{51}, HE_{23}	8.77	1.35	0.72	0.86	1.05	1.75	2.02
HE_{71}	9.24	1.42	0.75	0.90	1.11	1.84	2.13
EH_{32}	9.76	1.50	0.80	0.96	1.17	1.95	2.25

Appendix B

Characteristics of the ceramic heater

As discussed in detail in chapter 2.4.3 a commercial ceramic heater is used to manufacture fiber optical tapers. The axial temperature profile and the performance of the particular heater used for the experiments in this thesis are shown in figure B.1.

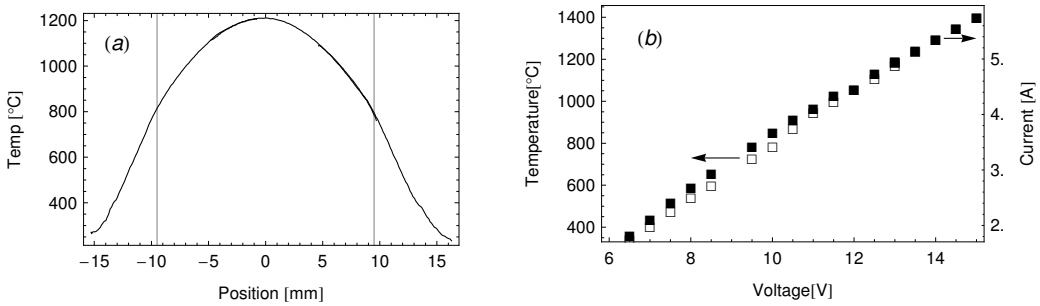

Figure B.1: (a) Axial temperature distribution at 13 V and 6 A. The temperature is recorded by a platinum-rhodium thermocouple (typ-K), which is pulled by the translation stage through the ceramic heater. A 31 mm long protective aluminium oxide ceramic pipe is inserted into the heater during the measurement. (b) Applied voltage versus the maximum measured heater temperature (open squares) and drawn current (solid squares). The temperature is linearly fitted as $T(U) = U \cdot 126.75°C/V - 474.29°C$. Date of measurement 08/29/08.

The specified maximum operational ratings for this type of heater are listed below.

Manufacturing company:	NTT Advanced Technology Co., Ltd., Japan
Heater No:	A4-17-06002
Max. rating:	Max. rating 1550 °C at
	16.6 V, 6.62 A, 2.5 Ω (17.5 Ω at room temperature)
Max. temp. rise speed:	50 °C/min

Appendix C

Segmented Fourier transform

The segmented Fourier transform (SFT) is a technique that is used for the identification of interferometric effects in transmission and fluorescence spectra of optical tapers and optically functionalized microresonator systems.

The central idea is to subdivide a given spectrum into small sections and perform a *discrete Fourier transform* (DFT). The resulting intensity distribution of the individual frequencies is then color-coded and displayed as individual strips representing a wavelength section.

The DFT ν_s of a list of data points u_r and length n is defined as

$$\nu_s = \frac{1}{\sqrt{n}} \sum_{r=1}^{n} u_r \exp\left(\frac{2\pi i(r-1)(s-1)}{n}\right)$$

where $i = \sqrt{-1}$. For illustration purposes a simple example of an SFT is shown in figure C.1.

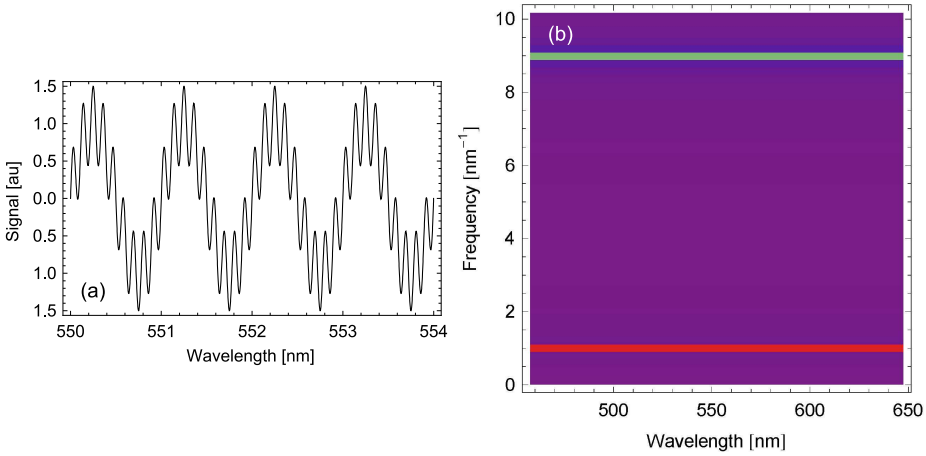

Figure C.1: (a) Transmission spectrum of two interfering frequency components, as $T(\lambda) = \sin(1 \cdot 2\pi\lambda) + 0.5\sin(9 \cdot 2\pi\lambda)$. The corresponding SFT in (b) shows the frequency components of $T(\lambda)$.

The SFT has several advantages for analyzing transmission spectra in wavelength space. Firstly, the oscillations observed in the spectrum may not be present over the entire wavelength region due to cut-off effects. A SFT allows one to identify these wavelength regions clearly. Secondly, the SFT is advantageous with respect to a standard DFT applied to an unsegmented spectrum. For such an approach to work the spectrum in wavelength space has to be translated into frequency space in order to identify frequency components present in the entire spectrum. However, a DFT requires a set of equally spaced data points, which is not available after the transfer from wavelength into frequency space.

Appendix D

Asymptotic expansion of resonance frequencies in Mie scattering

The size parameter $x_l^{(n)}$ for the radial mode n and azimuthal mode l is given by

$$x_l^{(n)} = \frac{l+1/2}{\tilde{N}} - \frac{\zeta_n}{\tilde{N}}\left(\frac{l+1/2}{2}\right)^{1/3} + \sum_{k=0}^{k_{max}} \frac{d_k(\tilde{N},\zeta_n)}{(l+1/2)^{k/3}(\tilde{N}^2-1)^{(k+1)/2}}, \tag{D.1}$$

where ζ_n is the n^{th} zero of the Airy function. The relative refractive index $\tilde{N}$ is defined as in the previous section to be $\tilde{N} = N_s/N_e$.

The first eight coefficients of the expansion result to be [89]

$$\begin{aligned}
d_0 &= -p \\
d_1 &= \frac{2^{1/3}\,3(\tilde{N}^2-1)\,\zeta_n^2}{20\,\tilde{N}} \\
d_2 &= \frac{-2^{2/3}\,\tilde{N}^2\,p(-3+2p^2)\,\zeta_n}{6} \\
d_3 &= \frac{350\,\tilde{N}^4\,(1-p)\,p\,(-1+p+p^2) + (\tilde{N}^2-1)^2\,(10+\zeta_n^3)}{700\,\tilde{N}} \\
d_4 &= \frac{-2^{1/3}\tilde{N}^2\,\zeta_n^2(4-\tilde{N}^2+e_4)}{20} \\
d_5 &= \frac{\zeta_n\left[40(-1+3\,\tilde{N}^2-3\,\tilde{N}^4+351\,\tilde{N}^6) - 479(\tilde{N}^2-1)^3\zeta_n^3 - e_5\right]}{2^{4/3}\,63,000\,\tilde{N}} \\
d_6 &= \frac{5\,\tilde{N}^2(-13-16\,\tilde{N}^2+4\,\tilde{N}^4) + 2\,\tilde{N}^2(128-4\,\tilde{N}^2+\tilde{N}^4)\zeta_n^3 - e_6}{1400} \\
d_7 &= \frac{\zeta_n^2\left[100(-551+2204\,\tilde{N}^2-3306\,\tilde{N}^4-73,256\,\tilde{N}^6+10,229\,\tilde{N}^8) - 20,231(\tilde{N}^2-1)^4\zeta_n^3 + e_7\right]}{2^{2/3}\,16,170,000\,\tilde{N}} \\
d_8 &= \frac{10\,\tilde{N}^2\zeta_n(11,082+44,271\,\tilde{N}^2-288\tilde{N}^4+7060\,\tilde{N}^6)}{2^{10/3}\,14,1750} \\
&\quad - \frac{3\,\tilde{N}^2\zeta_n^4(52,544+48,432\,\tilde{N}^2-11,496\,\tilde{N}^4+2395\,\tilde{N}^6)+e_8}{2^{10/3}\,141,750}.
\end{aligned}$$

For all TE modes $p = 1$ and for all TM modes $p = \tilde{N}^{-2}$. The coefficients e_k are given by $e_k =$

$(\tilde{N}^2-1)\,e'_k$ where e'_k is zero for all TE modes, whereas for TM modes the coefficients are given by,

$$
\begin{aligned}
e'_4 &= (-8+12\,\tilde{N}^4+\tilde{N}^8)/\tilde{N}^8\\
e'_5 &= 7000\,\tilde{N}^{-6}(-28-\tilde{N}^2+56\,\tilde{N}^4-16\,\tilde{N}^6-7\,\tilde{N}^8+2\,\tilde{N}^{10})\\
e'_6 &= \tilde{N}^{-8}[5(-200-32\,\tilde{N}^2+526\,\tilde{N}^4-226\,\tilde{N}^6-99\,\tilde{N}^8+62\,\tilde{N}^{10}+4\,\tilde{N}^{12})\\
&\quad +2\,\zeta_n^3(-400+279\,\tilde{N}^2+744\,\tilde{N}^4-424\,\tilde{N}^6-366\,\tilde{N}^8-2\,\tilde{N}^{10}+\tilde{N}^{12})]\\
e'_7 &= -269,500\,\tilde{N}^{-8}(-232+160\,\tilde{N}^2+543\,\tilde{N}^4-447\,\tilde{N}^6-186\,\tilde{N}^8+165\,\tilde{N}^{10}-15\,\tilde{N}^{12}+4\,\tilde{N}^{14})\\
e'_8 &= \tilde{N}^{-10}\zeta_l[-10(-459,200+286,000\,\tilde{N}^2+1,360,312\,\tilde{N}^4-1,305,476\,\tilde{N}^6-433,952\,\tilde{N}^8+717,562\,\tilde{N}^{10}\\
&\quad -209,039\,\tilde{N}^{12}-21,542\,\tilde{N}^{14}+7060\,\tilde{N}^{16})+3\zeta_n^3(336,000-441,600\,\tilde{N}^2-626,496\,\tilde{N}^4\\
&\quad +891,008\,\tilde{N}^6+306,416\,\tilde{N}^8-505,696\,\tilde{N}^{10}-72,488\,\tilde{N}^{12}-7664\,\tilde{N}^{14}+2395\,\tilde{N}^{16})].
\end{aligned}
$$

Appendix E

Rubidium energy scheme

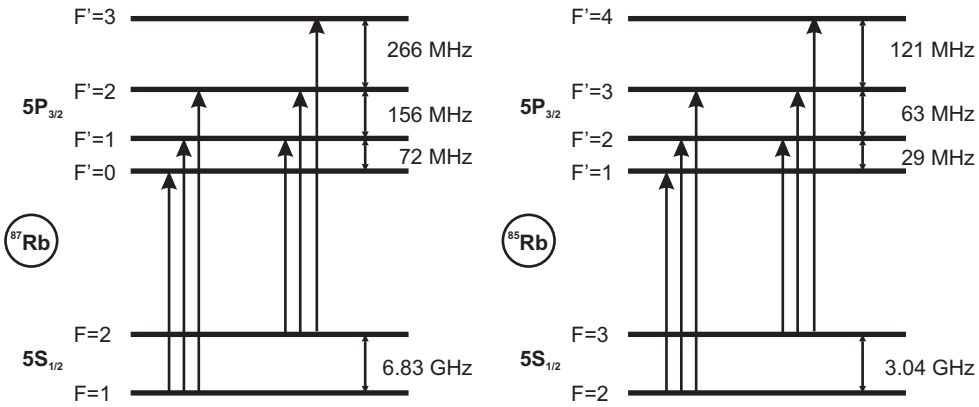

Figure E.1: Energy scheme of the rubidium D_2 line [14, 110].

Bibliography

[1] K. Srinivasan, A. Stintz, S. Krishna, and O. Painter. Photoluminescence measurements of quantum-dot-containing semiconductor microdisk resonators using optical fiber taper waveguides. *Phys. Rev. B*, 72(20):205318, Nov 2005.

[2] K. Srinivasan, O. Painter, A. Stintz, and S. Krishna. Single quantum dot spectroscopy using a fiber taper waveguide near-field optic. *Appl. Phys. Lett.*, 91(9):091102, 2007.

[3] P. E. Barclay, C. Santori, K.-M. Fu, R. G. Beausoleil, and O. Painter. Coherent interference effects in a nano-assembled diamond NV center cavity-QED system. *Opt. Express*, 17(10):8081–8097, 2009.

[4] F. Warken, E. Vetsch, D. Meschede, M. Sokolowski, and A. Rauschenbeutel. Ultra-sensitive surface absorption spectroscopy using sub-wavelength diameter optical fibers. *Opt. Express*, 15(19):11952–11958, 2007.

[5] K. P. Nayak, P. N. Melentiev, M. Morinaga, F. L. Kien, V. I. Balykin, and K. Hakuta. Optical nanofiber as an efficient tool for manipulating and probing atomic fluorescence. *Opt. Express*, 15(9):5431–5438, 2007.

[6] J. Lou, L. Tong, and Z. Ye. Modeling of silica nanowires for optical sensing. *Opt. Express*, 13(6):2135–2140, 2005.

[7] J. Villatoro and D. Monzón-Hernández. Fast detection of hydrogen with nano fiber tapers coated with ultra thin palladium layers. *Opt. Express*, 13(13):5087–5092, 2005.

[8] G. Brambilla and D. N. Payne. The ultimate strength of glass silica nanowires. *Nano Letters*, 9(2):831, 2009.

[9] M. Gregor, A. Kuhlicke, and O. Benson. Soft-landing and optical characterization of a preselected single fluorescent particle on a tapered optical fiber. *Opt. Express*, 17(26):24234–24243, 2009.

[10] S. M. Spillane, T. J. Kippenberg, O. J. Painter, and K. J. Vahala. Ideality in a fiber-taper-coupled microresonator system for application to cavity quantum electrodynamics. *Phys. Rev. Lett.*, 91(4):043902, Jul 2003.

[11] K. J. Vahala. Optical microcavities. *Nature*, 424(6950):839, 2003.

[12] L. Collot, V. Lefévrè-Seguin, M. Brune, J. M. Raimond, and S. Haroche. Very high-Q whispering-gallery mode resonances observed on fused silica microspheres. *EPL (Europhysics Letters)*, 23(5):327–334, 1993.

[13] F. Vollmer, S. Arnold, and D. Keng. Single virus detection from the reactive shift of a whispering-gallery mode. *Proceedings of the National Academy of Sciences*, 105(52):20701–20704, 2008.

[14] A. Chiba, H. Fujiwara, S. T. Jun-ichi Hotta, and K. Sasaki. Resonant frequency control of a microspherical cavity by temperature adjustment. *Japanese Journal of Applied Physics*, 43:6138, 2004.

[15] M. Gregor, C. Pyrlik, R. Henze, A. Wicht, A. Peters, and O. Benson. An alignment-free fiber-coupled microsphere resonator for gas sensing applications. *Appl. Phys. Lett.*, 96(23):231102, 2010.

[16] V. B. Braginsky, M. L. Gorodetsky, and V. S. Ilchenko. Quality-factor and nonlinear properties of optical whispering-gallery modes. *Physics Letters A*, 137(7-8):393 – 397, 1989.

[17] T. J. Kippenberg, A. L. Tchebotareva, J. Kalkman, A. Polman, and K. J. Vahala. Purcell-factor-enhancement scattering from si nanoc in an optical microcavity. *Phys. Rev. Lett.*, 103:027406, 2009.

[18] K. Srinivasan and O. Painter. Linear and nonlinear optical spectroscopy of a strongly coupled mircodisk-quantum dot system. *Nature*, 450:862, 2007.

[19] L.-M. Duan and H. J. Kimble. Scalable photonic quantum computation through cavity-assisted interactions. *Phys. Rev. Lett.*, 92(12):127902, 2004.

[20] M. Gregor, R. Henze, T. Schröder, and O. Benson. On-demand positioning of a preselected quantum emitter on a fiber-coupled toroidal microresonator. *Appl. Phys. Lett.*, 95(15):153110, 2009.

[21] F. Lu and W. H. Knox. Generation of a broadband continuum with high spectral coherence in tapered single-mode optical fibers. *Opt. Express*, 12(2):347, 2004.

[22] J. Bures. *Guided Optics*. Wiley-VCH, 2008.

[23] J. D. L. Allan W. Snyder. *Optical Waveguide Theory*. Chapman and Hall, 1983.

[24] *Corning SMF-28e Optical Fiber Product Informtaion*. Corning Inc., 2007.

[25] D. Jackson. *Classical Electrodynamics*. John Wiley and Sons, New York, 1998.

[26] F. L. Kien, J. Liang, K. Hakuta, and V. Balykina. Field intensity distributions and polarization orientations in a vacuum-clad subwavelength-diameter optical fiber. *Opt. Commun.*, 242(4-6):445–455, 2004.

[27] T. A. Birks and Y. W. Li. The shape of fibre tapers. *Journal of Lightwave Technology*, 10:432, 1992.

[28] F. Orucevic, V. Lefèvre-Seguin, and J. Hare. Transmittance and near-field characterization of sub-wavelength tapered optical fibers. *Opt. Express*, 15(21):13624–13629, 2007.

[29] F. Gonthier, S. Lacroix, X. Daxhelet, R. Black, and J. Bures. Broadband all-fiber filters for wavelength division multiplexing application. *Appl. Phys. Lett.*, 54(14):1290, 1989.

[30] R. H. Doremus. Viscosity of silica. *Journal of Applied Physics*, 92:7619, 2002.

[31] J. M. Ward, D. G. O'Shea, B. J. Shortt, M. J. Morrissey, K. Deasy, and S. G. Nic Chormaic. Heat-and-pull rig for fiber taper fabrication. *Rev. Sci. Instrum.*, 77(8):083105, 2006.

[32] G. Brambilla, V. Finazzi, and D. Richardson. Ultra-low-loss optical fiber nanotapers. *Opt. Express*, 12(10):2258–2263, 2004.

[33] Y. Takeuchi. Characteristics analysis of wavelength-division-multiplexing fiber couplers fabricated with a microheater. *Appl. Opt.*, 35(9):1478, 1996.

[34] F. Warken and H. Giessen. Fast profile measurement of micrometer-sized tapered fibers with better than 50-nm accuracy. *Opt. Lett.*, 29(15):1727–1729, 2004.

[35] A. Ghatak and K. Thyagarajan. *Introduction to fibre optics*. Cambridge University Press, 1998.

[36] private communication with Hideaki Takashima, Hokkaido University, May 2009.

[37] L. Ding, C. Belacel, S. Ducci, G. Leo, and I. Favero. Ultra-low loss single-mode silica tapers manufactured by a microheater. *arXiv:1001.3076v1*, 2010.

[38] J. Corres, J. Bravo, I. Matias, and F. Arregui. Nonadiabatic tapered single-mode fiber coated with humidity sensitive nanofilms. *IEEE Photonics Technology Letters*, 18(8):935, 2006.

[39] L. Zhang, F. Gu, J. Lou, X. Yin, and L. Tong. Fast detection of humidity with a subwavelength-diameter fiber taper coated with gelatin film. *Opt. Express*, 16(17):13349–13353, 2008.

[40] M. Shadaram, J. Martinez, F. Garcia, and D. Tavares. Sensing ammonia with ferrocene-based polymer coated tapered optical fibers. *Fiber and Integrated Optics*, 16(1):115–122, 1997.

[41] W. Paul. Electromagnetic traps for charged and neutral particles. *Rev. Mod. Phys.*, 62:531, 1990.

[42] W. H. Oskay, S. A. Diddams, E. A. Donley, T. M. Fortier, T. P. Heavner, L. Hollberg, W. M. Itano, S. R. Jefferts, M. J. Delaney, K. Kim, F. Levi, T. E. Parker, and J. C. Bergquist. Single-atom optical clock with high accuracy. *Phys. Rev. Lett.*, 97(2):1–4, 2006.

[43] F. Schmidt-Kaler, H. Häffner, S. Gulde, M. Riebe, G. P. T. Lancaster, T. Deuschle, C. Becher, W. Hänsel, J. Eschner, C. Roos, and R. Blatt. How to realize a universal quantum gate with trapped ions. *Applied Physics B: Lasers and Optics*, 77:789–796, 2003.

[44] J. Cirac and P. Zoller. Quantum computations with cold trapped ions. *Phys. Rev. Lett.*, 74(20):4091, 1995.

[45] W. Schnitzler, N. M. Linke, R. Fickler, J. Meijer, F. Schmidt-Kaler, and K. Singer. Deterministic ultracold ion source targeting the heisenberg limit. *Phys. Rev. Lett.*, 102(7):1–4, 2009.

[46] S. Schlemmer, J. Illemann, S. Wellert, and D. Gerlich. Nondestructive high-resolution and absolute mass determination of single charged particles in a three-dimensional quadrupole trap. *Journal of Applied Physics*, 90(10):5410, 2001.

[47] S. Arnold and L. Folan. Fluorescence spectrometer for a single electrodynamically levitated microparticle. *Rev. Sci. Instrum.*, 57:2250, 1986.

[48] A. Kuhlicke. Einfang und Untersuchung von Nanopartikeln in einer Paul-Falle. Master's thesis, Humboldt University in Berlin, Germany, June 2007.

[49] M. Nasse and C. Foot. Influence of background pressure on the stability region of a paul trap. *Euro. J. Phys.*, 22:563–573, 2001.

[50] J. Bures and R. Ghosh. Power density of the evanescent field in the vicinity of a tapered fiber. *J. Opt. Soc. Am. A*, 16(8):1992–1996, 1999.

[51] F. L. Kien, S. D. Gupta, V. I. Balykin, and K. Hakuta. Spontaneous emission of a cesium atom near a nanofiber: Efficient coupling of light to guided modes. *Phys. Rev. A*, 72:032509, 2005.

[52] I. D. Chremmos and N. K. Uzunoglu. Integral equation analysis of scattering by a spherical microparticle coupled to a subwavelength-diameter wire waveguide. *J. Opt. Soc. Am. A*, 23(2):461–467, 2006.

[53] J. D. Prestage, G. J. Dick, and L. Maleki. New ion trap for frequency standard applications. *J. Appl. Phys*, 66(3):1013, 1989.

[54] H. C. Nägerl, W. Bechter, J. Eschner, F. Schmidt-Kaler, and R. Blatt. Ion strings for quantum gates. *Appl. Phys. B: Lasers and Optics*, 66:603–608, 1998.

[55] M. G. Raizen, J. M. Gilligan, J. C. Bergquist, W. M. Itano, and D. J. Wineland. Ionic crystals in a linear paul trap. *Phys. Rev. A*, 45(9):6493, 1992.

[56] D. Kielpinski, C. Monroe, and D. J. Wineland. Architecture for a large-scale ion-trap quantum computer. *Nature*, 417:709, 2002.

[57] S. Schulz, U. Poschinger, K. Singer, and F. Schmidt-Kaler. Optimization of segmented linear paul traps and transport of stored particles. *Fortschr. Phys.*, 54(8-10):648–665, 2006.

[58] S. J. Gaskell. Electrospray: Principles and practice. *Journal of Mass Spectrometry*, 32:677–688, 1997.

[59] P. Kebarle and L. Tang. From ions in solution to ions in the gas phase-the mechanism of electrospray mass spectrometry. *Analytical Chemistry*, 65:972, 1993.

[60] http://www.physik.hu-berlin.de/nano/movie.

[61] B. E. A. Saleh and M. C. Teich. *Fundamentals of Photonics*. John Wiley and Sons, New York, 2nd edition, 2007.

[62] T. van der Sar, E. C. Heeres, G. M. Dmochowski, G. de Lange, L. Robledo, T. H. Oosterkamp, and R. Hanson. Nanopositioning of a diamond nanocrystal containing a single nitrogen-vacancy defect center. *Appl. Phys. Lett.*, 94(17):173104, 2009.

[63] E. Ampem-Lassen, D. A. Simpson, B. C. Gibson, S. Trpkovski, F. M. Hossain, S. T. Huntington, K. Ganesan, and L. C. L. H. S. Prawer. Nano-manipulation of diamond-based single photon sources. *arXiv:0905.2784v1*, 2009.

[64] M. Barth, N. Nüsse, B. Löchel, and O. Benson. Controlled coupling of a single-diamond nanocrystal to a photonic crystal cavity. *Opt. Lett.*, 34(7):1108–1110, 2009.

[65] J. W. S. Rayleigh. The problem of the whispering gallery. *Philosophical Magazine*, XX:1001–1004, 1910.

[66] A. Mazzei, H. Krauter, O. Benson, and S. Götzinger. Influence of a controllable scatterer on the lasing properties of an ultralow threshold raman microlaser. *Appl. Phys. Lett.*, 89(10):101105, 2006.

[67] M. Cai, O. Painter, K. J. Vahala, and P. C. Sercel. Fiber-coupled microsphere laser. *Opt. Lett.*, 25(19):1430–1432, 2000.

[68] N. M. Hanumegowda, C. J. Stica, B. C. Patel, I. White, and X. Fan. Refractometric sensors based on microsphere resonators. *Appl. Phys. Lett.*, 87(20):201107, 2005.

[69] F. Vollmer, D. Braun, A. Libchaber, M. Khoshsima, I. Teraoka, and S. Arnold. Protein detection by optical shift of a resonant microcavity. *Appl. Phys. Lett.*, 80(21):4057–4059, 2002.

[70] F. Vollmer, S. Arnold, D. Braun, I. Teraoka, and A. Libchaber. Multiplexed DNA quantification by spectroscopic shift of two microsphere cavities. *Biophysical Journal*, 85:1974–1979, 2003.

[71] A. Francois and M. Himmelhaus. Whispering gallery mode biosensor operated in the stimulated emission regime. *Appl. Phys. Lett.*, 94(3):031101, 2009.

[72] A. M. Armani, R. P. Kulkarni, S. E. Fraser, R. C. Flagan, and K. J. Vahala. Label-free, single-molecule detection with optical microcavities. *Science*, 317(5839):783–787, 2007.

[73] J. T. Robinson, L. Chen, and M. Lipson. On-chip gas detection in silicon optical microcavities. *Opt. Express*, 16(6):4296–4301, 2008.

[74] A. T. Rosenberger and J. P. Rezac. Whispering-gallery-mode evanescent-wave microsensor for trace-gas detection. *Proc. SPIE*, 4265:102, 2001.

[75] A. Mazzei, S. Götzinger, L. S. Menezes, V. Sandoghdar, and O. Benson. Optimization of prism coupling to high-Q modes in a microsphere resonator using a near-field probe. *Optics Communications*, 250(4-6):428–433, 2005.

[76] S. Schietinger and O. Benson. Coupling single NV-centres to high-Q whispering gallery modes of a preselected frequency-matched microresonator. *J. Phys. B: Atomic, Molecular and Optical Physics*, 42(11):114001 (5pp), 2009.

[77] A. Serpengüzel, S. Arnold, and G. Griffel. Excitation of resonances of microspheres on an optical fibre. *Opt. Lett.*, 20(7):654–656, 1995.

[78] J. M. Ward, P. Féron, and S. Nic Chormaic. A taper-fused microspherical laser source. *IEEE Phot. Tech. Lett.*, 20:392, 2008.

[79] A. Matsko and V. Ilchenko Optical resonators with whispering-gallery modes-part I: basics. *IEEE Journal of Selected Topics in Quantum Electronics*, 12(1):3–14, 2006.

[80] M. L. Gorodetsky, A. A. Savchenkov, and V. S. Ilchenko. Ultimate Q of optical microsphere resonators. *Opt. Lett.*, 21(7):453–455, 1996.

[81] G. Mie. Beiträge zur Optik trüber Medien, speziell kolloidaler Metallösungen. *Annalen der Physik*, 330(3):377–445, 1908.

[82] B. E. Little, J.-P. Laine, H. A. Haus, and L. Fellow. Analytic theory of coupling from tapered fibers and half-blocks into microsphere resonators. *J. Lightwave Technol.*, 17(4):704, 1999.

[83] P. R. Conwell, P. W. Barber, and C. K. Rushforth. Resonant spectra of dielectric spheres. *J. Opt. Soc. Am. A*, 1(1):62–67, 1984.

[84] C. C. Lam, P. T. Leung, and K. Young. Explicit asymptotic formulas for the positions, widths, and strengths of resonances in Mie scattering. *J. Opt. Soc. Am. B*, 9(9):1585–1592, 1992.

[85] J. A. Stratton. *Electomagnetic Theory*. McGraw-Hill Book Company, 1941.

[86] P. Barber and R. K. Chang, editors. *Optical Effects associated with Small Particles*. World Scientific, Singapore, 1988.

[87] S. Schiller and R. L. Byer. High-resolution spectroscopy of whispering gallery modes in large dielectric spheres. *Opt. Lett.*, 16(15):1138–1140, 1991.

[88] C. C. Lam, P. T. Leung, and K. Young. Explicit asymptotic formulas for the positions, widths, and strengths of resonances in Mie scattering. *J. Opt. Soc. Am. B*, 9(9):1585–1592, 1992.

[89] S. Schiller. Asymptotic expansion of morphological resonance frequencies in Mie scattering. *Appl. Opt.*, 32(12):2181–2185, 1993.

[90] H. M. Lai, P. T. Leung, K. Young, P. W. Barber, and S. C. Hill. Time-independent perturbation for leaking electromagnetic modes in open systems with application to resonances in microdroplets. *Phys. Rev. A*, 41(9):5187–5198, 1990.

[91] M. Cai, O. Painter, and K. J. Vahala. Observation of critical coupling in a fiber taper to a silica-microsphere whispering-gallery mode spectrum. *Phys. Rev. Lett.*, 85:74, 2000.

[92] H. A. Haus and W. Huang, editors. *Coupled-mode theory*, volume 79 of *Proc. IEEE*, October 1991.

[93] S. M. Spillane. *Fieber-coupled Ultra-high-Q Microresonators for Nonlinear and Quantum Optics*. PhD thesis, California Institute of Technology, 2004.

[94] D. Rowland and J. Love. Evanescent wave coupling of whispering gallery modes of adielectric cylinder. *IEEE Proceedings.-J: Optoelectronics*, 140(3):177–188, (1993).

[95] M. J. Humphrey, E. Dalea, A. Rosenberger, and D. Bandya. Calculation of optimal fiber radius and whispering-gallery mode spectra for a fiber-coupled microsphere. *Opt. Commun.*, 271(1):124–131, 2007.

[96] C.-H. Dong, L. He, Y.-F. Xiao, V. R. Gaddam, S. K. Ozdemir, Z.-F. Han, G.-C. Guo, and L. Yang. Fabrication of high-Q polydimethylsiloxane optical microspheres for thermal sensing. *Appl. Phys. Lett.*, 94(23):231119, 2009.

[97] S. N. Kasarova, N. G. Sultanova, C. D. Ivanov, and I. D. Nikolov. Analysis of the dispersion of optical plastic materials. *Opt. Mat.*, 29:1481, 2007.

[98] H. N. Subrahmanyam and S. V. Subramanyam. Thermal expansion of irradiated polystyrene. *Journal of Materials Science*, 22:2079, 1987.

[99] N. J. Mills. *Encyclopedia of Polymer Science and Engineering*, volume 10. John Wiley and Sons, New York, 2nd edition, 1987.

[100] C. G. Robertson and G. L. Wilkes. Refractive index: a probe for monitoring volume relaxations during physical againg of glassy polymers. *Polymer*, 39(11):2129, 1998.

[101] V. S. Ilchenko and M. L. Gorodetsky. Thermal nonlinear effects in optical whispering gallery microresonator. *Laser Phys.*, 2:1004, 1992.

[102] T. Carmon, L. Yang, and K. Vahala. Dynamical thermal behavior and thermal self-stability of microcavities. *Opt. Express*, 12(20):4742–4750, 2004.

[103] A. E. Fomin, M. L. Gorodetsky, I. S. Grudinin, and V. S. Ilchenko. Nonstationary nonlinear effects in optical microspheres. *J. Opt. Soc. Am. B*, 22(2):459, 2005.

[104] C. Schmidt, A. Chipouline, T. Pertsch, A. Tünnermann, O. Egorov, F. Lederer, and L. Deych. Nonlinear thermal effects in optical microspheres at different wavelength sweeping speeds. *Opt. Express*, 16(9):6285–6301, 2008.

[105] M. J. Weber. *Handbook of Optical Materials*. CRC Press, 2002.

[106] D. R. Lide, editor. *CRC Handbook of Chemistry and Physics*. Taylor & Francis Group, 83rd edition, 2002-2003.

[107] *Model 6300-LN, The Velocity Tunable Diode Laser, New Focus a devision of Brookham, USA*.

[108] K.Liu and M. Littman. Novel geometry for single-mode scanning of tunable lasers. *Opt. Letters*, 6(3):117, 1981.

[109] private communication with New Focus Inc., USA, 2009.

[110] S. Kraft, A. Deninger, C. Trück, J. Fortagh, F. Lison, and C. Zimmermann. Rubidium spectroscopy at 778-780 nm with a distributed feedback laser diode. *Laser Physics Letters*, 2(2):71–76, 2005.

[111] E. Thornton and W. A. D. Baker. Viscosity and thermal conductivity of binary gas mixtures: Argon-neon, argon-helium, and neon-helium. *Proceedings of the Physical Society*, 80(5):1171–1175, 1962.

[112] E. A. Mason and H. von Ubisch. Thermal conductivities of rare gas mixtures. *The Physics of Fluids*, 3:355, 1960.

[113] R. P. Podgorsek and H. Franke. Selective optical detection of aromatic vapors. *Appl. Opt.*, 41(4):601–608, 2002.

[114] D. K. Armani, T. J. Kippenberg, S. M. Spillane, and K. J. Vahala. Ultra-high-Q toroid microcavity on a chip. *Nature*, 421:925 – 928, 2003.

[115] C. Kurtsiefer, S. Mayer, P. Zarda, and H. Weinfurter. Stable solid-state source of single photons. *Phys. Rev. Lett.*, 85(2):290–293, 2000.

[116] A. Beveratos, R. Brouri, T. Gacoin, A. Villing, J.-P. Poizat, and P. Grangier. Single photon quantum cryptography. *Phys. Rev. Lett.*, 89(18):187901, 2002.

[117] M. Larsson, K. N. Dinyari, and H. Wang. Composite optical microcavity of diamond nanopillar and silica microsphere. *Nano Lett.*, 9(4):1447–1450, 2009.

[118] Y.-S. Park, A. K. Cook, and H. Wang. Cavity QED with diamond nanocrystals and silica microspheres. *Nano Lett.*, 6(9):2075–2079, 2006.

[119] S. Schietinger, T. Schröder, and O. Benson. One-by-one coupling of single defect centers in nanodiamonds to high-Q modes of an optical microresonator. *Nano Lett.*, 8(11):3911–3915, 2008.

[120] C.Monroe. Quantum information processing with atoms and photons. *Nature*, 416:238, 2002.

[121] D. Englund, A. Faraon, I. Fushman, N. Stoltz, P. Petroff, and J. Vuckuvic. Controlling cavity reflectivity with a single quantum dot. *Nature*, 450:857, 2007.

[122] T. Aoki, A. S. Parkins, D. J. Alton, C. A. Regal, B. Dayan, E. Ostby, K. J. Vahala, and H. J. Kimble. Efficient routing of single photons by one atom and a mircotoroidal cavity. *Phys. Rev. Lett.*, 102:083601, 2009.

[123] C.-H. Su, A. D. Greentree, and L. C. L. Hollenberg. Towards a picosecond transform-limited nitrogen-vacancy based single photon source. *Opt. Express*, 16(9):6240–6250, 2008.

[124] F. Jelezko and J. Wrachtrup. Single defect centers in diamond: A review. *Phys. Stat. Sol. A*, 13:3207, 2006.

[125] A. Dräbenstedt, L. Fleury, C. Tietz, F. Jelezko, S. Kilin, A. Nizovtzev, and J. Wrachtrup. Low-temperature microscopy and spectroscopy on single defect centers in diamond. *Phys. Rev. B*, 60(16):11503–11508, 1999.

[126] G. Balasubramanian, I. Y. Chan, R. Kolesov, M. Al-Hmoud, J. Tisler, C. Shin, C. Kim, A. Wojcik, P. R. Hemmer, A. Krueger, T. Hanke, A. Leitenstorfer, R. Bratschitsch, F. Jelezko, and J. Wrachtrup. Nanoscale imaging magnetometry with diamond spins under ambient conditions. *Nature*, 455(7213):648–651, October 2008.

[127] J. R. Maze, P. L. Stanwix, J. S. Hodges, S. Hong, J. M. Taylor, P. Cappellaro, L. Jiang, M. V. G. Dutt, E. Togan, A. S. Zibrov, A. Yacoby, R. L. Walsworth, and M. D. Lukin. Nanoscale magnetic sensing with an individual electronic spin in diamond. *Nature*, 455(7213):644–647, October 2008.

[128] A. T. Collins, M. F. Thomaz, and M. I. B. Jorge. Luminescence decay time of the 1.945 eV centre in type Ib diamond. *Journal of Physics C: Solid State Physics*, 16(11):2177–2181, 1983.

[129] A. Beveratos, R. Brouri, T. Gacoin, J.-P. Poizat, and P. Grangier. Nonclassical radiation from diamond nanocrystals. *Phys. Rev. A*, 64(6):061802, Nov 2001.

[130] S. Schietinger, M. Barth, T. Aichele, and O. Benson. Plasmon-enhanced single photon emission from a nanoassembled metal-diamond hybrid structure at room temperature. *Nano Lett.*, 9(4):1694–1698, 2009. PMID: 19301860.

[131] Y. Mita. Change of absorption spectra in type-Ib diamond with heavy neutron irradiation. *Phys. Rev. B*, 53(17):11360–11364, 1996.

[132] T. Gaebel, I. Popa, A. Gruber, M. Domhan, F. Jelezko, and J. Wrachtrup. Stable single-photon source in the near infrared. *New J. Phys.*, 6:98, 2004.

[133] R. H. Brown and R. Q. Twiss. Correlation between photons in thwo coherent beams of light. *Nature*, 177:27–32, 1956.

[134] Y. Y. Hui, Y.-R. Chang, T.-S. Lim, H.-Y. Lee, W. Fann, and H.-C. Chang. Quantifying the number of color centers in single fluorescent nanodiamonds by photon correlation spectroscopy and monte carlo simulation. *Appl. Phys. Lett.*, 94(1):013104, 2009.

[135] A. Beveratos, R. Brouri, J.-P. Poizat, and P. Grangier. Bunching and antibunching from single NV color centers in diamond. In *QCM&C 3 Proceedings*. See also e-print arXiv:quant-ph/0010044, 2000.

[136] M. Barth. *Hybrid Nanophotonic Elements and Sensing Devices based on Photonic Crystal Structures*. PhD thesis, Humbold University Berlin, Germany, 2010.

[137] B. Min, L. Yang, and K. Vahala. Perturbative analytic theory of an ultrahigh-Q toroidal microcavity. *Phys. Rev. A*, 76(1):013823, Jul 2007.

[138] M. Oxborrow. Ex-house 2D finite-element simulation of the whispering-gallery modes of arbitrarily shaped axisymmetric electromagnetic resonators. *arXiv:quant-ph/0607156v2*, 2007.

[139] K. Vahala, editor. *Optical Microcavities*. World Scientific Publishing Company, 2005.

[140] T. Schröder. Herstellung und Vermessung von toroidalen Microresonatoren. Master's thesis, Humboldt University in Berlin, Germany, 2007.

[141] A. Chiba, H. Fujiwara, J. ichi Hotta, S. Takeuchi, and K. Sasaki. Fano resonance in a multimode tapered fiber coupled with a microspherical cavity. *Appl. Phys. Lett.*, 86(26):261106, 2005.

[142] J. Michaelis, C. Hettich, J. Mlynek, and V. Sandoghdar. Optical microscopy using a single-molecule light source. *Nature*, 405(6784):325–328, 2000.

[143] N. Masaya, K. Eiichi, and T. Takasumi. Large-scale arrays of ultrahigh-Q coupled nanocavities. *Nature Photonics*, 2(12):741–747, 2008.

[144] T. Aoki, B. Dayan, E. Wilcut, W. P. Bowen, A. S. Parkins, T. J. Kippenberg, and H. J. K. K. J. Vahala. Observation of strong coupling between one atom and a monolithic microresonator. *Nature*, 443:761, 2006.

[145] P. Tamarat, T. Gaebel, J. R. Rabeau, M. Khan, A. D. Greentree, H. Wilson, L. Hollenberg, and S. Prawer. Stark shift control of a single optical center in diamond. *Phys. Rev. Lett.*, 97:083002, 2006.

Acknowledgement

So, at last, that's it. It has been a long way and I would like to thank everybody, who accompanied and supported me all this time. Without their help this work would never have been possible.

First of all, I would like to thank Prof. Oliver Benson for the opportunity to work in his group. His tutorship has been extremely helpful. His insight and perspective to the physical problems has been inspiring and guided the way to solving the problems at hand. I always felt comfortable to turn to him.

Prof. Achim Peters and Andreas Wicht from the Ferdinand Braun Institut (FBH) were of great help. Their experience and insight into "stability" and "precision" were of great importance for the success of the experiment.

I am also thankful for the long discussion with Prof. Shigeki Takeuchi and Hideaki Takashima about fiber tapers and different production techniques.

My great gratitude goes to all my colleges who contributed to this work. Rico Henze is the master of the toroids and skillfully produced spotless "glass donuts" for our experiments. I also would like to thank Alexander Kuhlicke for spending so many nights in the lab, trying to manoeuver small trapped particles. Tim Schröder showed a remarkable stamina when it came to finding small nanodiamonds on small toroids at nighttime. My appreciation also goes to Christoph Prylik for many hours of labwork purging a small plastic box with different gas mixtures.

Many fruitful discussions with my colleges Michael Barth, Stefan Schietinger, Gesine Steudle, Thomas Aichele, David Höckel, Lars Koch, Matthias Leifgen, Leonardo de Souza Menezes and Ulrike Herzog contributed to the success of this work. My thanks goes also to all my colleges from the QOM group. Especially the usual 4 o'clock discussion was a highlight of the day and restored productivity and creativity.

I would like to thank Alexander, Rico and Michael for their help of ridding my written words of all littel spelling mistakes.

Where would I have been without the help of Klaus Palis. Whenever there was a technical problem or some advice was needed regarding some piece of electronic I felt comfortable to consult him and was sure that some solution would be found. Sabine Strobel was always very friendly and helpful.

My thanks also goes to the Paul Drude Institut (PDI) for granting us access to their clean room equipment and their very helpful technical staff. Mr Costial and Mrs Wiebeke helped us with their expertise to implement a procedure to produce toroidal microresonators. Mrs Blum was always very forthcoming when scanning electron microscope images were needed.

My gratitude goes to my family for the strong believe in me and their continuous support during all the time. I would like to thank my father for his real interest in my research and his inspirational fascination in physics. Thanks.

Finally, but not last, I want to thank Katrin for her encouragement during the last years. Her understanding and "moral" support whenever the experiments didn't work or took a little longer than anticipated.

I want to thank the Deutsche Studienstiftung for their continues financial support and also for providing a forum to meet interesting people at summer schools and at many other occasions.

And finally, I like to acknowledge the help of the chemical support from differently flavored mixtures of $C_8H_{10}N_4O_2$ and $C_{12}H_{22}O_{11}$, as well as their various suppliers that provided a productive working environment.

List of Own Publications

The following list of articles (in reverse chronological order) have been published by the author. Work that is marked by an asterisk is not part of this thesis.

Peer-reviewed journals

- Markus Gregor, Christoph Pyrlik, Rico Henze, Andreas Wicht, Achim Peters, and Oliver Benson. An alignment-free fiber-coupled microsphere resonator for gas sensing applications. *Applied Physics Letters*, 96(23):231102, 2010.
- Markus Gregor, Alexander Kuhlicke, and Oliver Benson. Soft-landing and optical characterization of a preselected single fluorescent particle on a tapered optical fiber. *Optics Express*, 17(26):24234–24243, 2009.
- Markus Gregor, Rico Henze, Tim Schröder, and Oliver Benson. On-demand positioning of a preselected quantum emitter on a fiber-coupled toroidal microresonator. *Applied Physics Letters*, 95(15):153110, 2009.
- Markus Gregor, Rico Henze, Tim Schröder, and Oliver Benson. On-demand positioning of a preselected quantum emitter on a fiber-coupled toroidal microresonator. *Virtual Journal of Nanoscale Science & Technology*, 20(18), 2009.
- *Martin Ostermeyer, Thomas Waltinger, and Markus Gregor. Frequency stabilization of a q-switched Nd:YAG laser oscillator with stability better 300khz following an rf-sideband scheme. *Optics Communications*, 282(16):3302 – 3307, 2009.

Conference proceedings

- Michael Barth, Markus Gregor, Rico Henze, Tim Schröder, Nils Nüsse, Bernd Löchel, and Oliver Benson. Hybrid approaches toward single emitter coupling to optical microresonators. Volume 7579 of *Proc. SPIE*, 2010.
- Markus Gregor, Rico Henze, Tim Schröder, and Oliver Benson. On-demand positioning of a preselected quantum emitter on a fiber-coupled toroidal microresonator. Poster, *Frühjahrstagung der Deutschen Physikalischen Gesellschaft*, Hannover, March 2010
- Rico Henze, Markus Gregor, Christoph Pyrlik, Andreas Wicht, Achim Peters, and Oliver Benson. Toroidal Microresonators as High-Tech Platform for Applications in Sensor, Analysis, Laser Measurement and Optical Telecommunication Systems. Poster, *Laser Optics Berlin*, March 2010
- Alexander Kuhlicke, Markus Gregor, and Oliver Benson. Soft-Landing of Preselected Single Nanoparticles on Optical Fiber Tapers for Spectroscopy and Detection. *Frontiers in Optics, OSA Technical Digest* , 2009
- Alexander Kuhlicke, Markus Gregor, and Oliver Benson. Detection and Spectroscopy of Preselected Single Nanoparticles Soft-Landed on Optical Fibre Tapers. *Frühjahrstagung der Deutschen Physikalischen Gesellschaft* , Hamburg, 2009

- Rico Henze, Markus Gregor, Tim Schröder, H. Kostial, E. Wiebicke and Oliver Benson. Towards controlled Cavity-QED experiments with toroidal microresonators. Poster, *Frühjahrstagung der Deutschen Physikalischen Gesellschaft* , Darmstadt, 2008
- *Dirk Puhlmann, Markus Gregor, and Martin Ostermeyer. Präparation von photonischen Hohlkernfasern zum selektiven Befüllen mit Materialien hoher optischer Nichtlinearität. Poster, *Frühjahrstagung der Deutschen Physikalischen Gesellschaft*, Darmstadt, 2008
- *Markus Gregor, Martin Ostermeyer, and Ralf Menzel. Generation of Correlated Photons in Photonic Crystal Fibres. Poster, *Frühjahrstagung der Deutschen Physikalischen Gesellschaft*, Frankfurt, 2006
- *Markus Gregor, Axel Heuer, and Ralf Menzel. Ultraschnelles Messverfahren zur Erfassung von dreidimensionalen Oberflächen. *Frühjahrstagung der Deutschen Physikalischen Gesellschaft*, Frankfurt, 2006
- *Markus Gregor, Martin Ostermeyer, Sebastian Bange, and Ralf Menzel. Comparison of frequency stabilisation schemes for pulsed ring oscillators, *Frühjahrstagung der Deutschen Physikalischen Gesellschaft*, Berlin, 2005